The effect of microstructure on micro- and macro-scale corrosion and passivation behaviour of low-alloyed ferrous materials

Yilmaz, A.

DOI
10.4233/uuid:ab648631-4b9a-4c4b-add6-5696b3cf0165

Publication date
2021

Document Version
Final published version

Citation (APA)
Yilmaz, A. (2021). *The effect of microstructure on micro- and macro-scale corrosion and passivation behaviour of low-alloyed ferrous materials*. [Dissertation (TU Delft), Delft University of Technology]. https://doi.org/10.4233/uuid:ab648631-4b9a-4c4b-add6-5696b3cf0165

Important note
To cite this publication, please use the final published version (if applicable).
Please check the document version above.

The effect of microstructure on micro- and macro-scale corrosion and passivation of low-alloyed ferrous materials

Ph.D. thesis

Aytac YILMAZ

This research was carried out under project number F41.3.14546a in the framework of the Partnership Program of the Materials innovation institute M2i (www.m2i.nl) and the Foundation for Fundamental Research on Matter (FOM), which is part of the Netherlands Organisation for Scientific Research NWO (www.nwo.nl).

This research was performed at Delft University of Technology
Department of Materials Science and Engineering
Mekelweg 2, 2628 CD Delft,
The Netherland

The effect of microstructure on micro- and macro-scale corrosion and passivation behaviour of low-alloyed ferrous materials

Proefschrift

Ter verkrijging van de graad van doctor
aan de Technische Universiteit Delft,
op gezag van de Rector Magnificus, Prof. Dr. Ir. T.H.J.J. van der Hagen,
voorzitter van het College voor promoties,
in het openbaar te verdedigen op
maandag 8 November 2021 om 12:30 uur.

door

Aytac YILMAZ

Master of Science in Materials Science and Engineering
University of Florida, U.S.A.
Geboren te Mersin, Turkije

Dit proefschrift is goedgekeurd door de promotor en co-promotor:

Prof. dr. ir. J. Sietsma

Dr. Y. Gonzalez-Garcia

Samenstelling promotiecommissie bestaat uit:

Rector Magnificus, Voorzitter

Prof. dr. ir. J. Sietsma, promotor

Dr. Y. Gonzalez-Garcia, co-promotor

Onafhankelijke leden:

Prof. dr. ir. J.M.C Mol, Delft University of Technology, The Netherlands

Prof. dr. ir. L. Kestens, Delft University of Technology, The Netherlands

Prof. dr. L. Fedrizzi, University of Udine, Italy

Prof. dr. M. Olivier, University of Mons, Belgium

Dr. B. Boelen, Tata Steel, The Netherlands

Keywords: steels, microstructure, corrosion, passivity, grain size, grain boundary density, dislocation density, crystallographic orientation, phases

An electronic version of this dissertation is available at:

http//repository.tudelft.nl

Table of Contents

Summary

The relationship between microstructural features and mechanical properties of metals has been the centre of attention for decades in efforts to improve the mechanical properties of alloys. A significant number of studies have provided insight into the relationship between microstructural features and mechanical properties. However, the knowledge of the relationship between microstructural features and corrosion is still limited. Understanding the specific effect of a microstructural feature on corrosion and passivity properties is a challenging phenomenon. This is mainly due to the intricate combined effects of microstructural features on corrosion behaviour.

In this Ph.D. study, it is aimed to understand the specific effect of microstructural features on corrosion behaviour of low alloyed ferrous materials. The focus is given to grain size/boundary areas, dislocations, crystallographic texture, and phases. To isolate the changes in the microstructural features, several heat treatments or thermomechanical processes were applied. In-depth microstructural characterisation was carried out to ensure that the changes in microstructure are limited to the one investigated. Local and global electrochemical and surface

characterisation techniques were applied to establish a relationship between microstructural features and corrosion/passivity relationships.

In the first part of the thesis (Part A), the effect of microstructural defect density (dislocation density and grain boundary density) on the corrosion and passivity of interstitial free (IF) steels is investigated. Chapter 2 investigates the role of microstructural defect density (dislocation density and grain boundary density) on the properties of passive films formed on interstitial free (IF) steels. The results show that the barrier properties of passive films decrease with rising microstructural density due to increasing donor density and decreasing volume fraction of protective γ-Fe_2O_3 in the passive film. In chapter 3, the effect of dislocation density, induced by cold rolling, on corrosion behaviour is investigated by scanning Kelvin probe force microscopy (SKPFM) and electrochemical measurements. It was observed that the corrosion rate increases by inducing dislocation density, attributed to the increasing degree of galvanic coupling between grain due to an increase in dislocation density. Moreover, it was also observed that the effect of dislocation density dominates the one of crystallographic texture on corrosion behaviour.

Part B (chapters 4-6) focusses on the effect of grain size on corrosion and passive layer behaviour of various low alloyed ferrous materials. Chapter 4 examines the effect of grain size on the passive layer behaviour of iron in an alkaline environment. It was shown that the grain refinement leads to the deterioration of passive films' barrier properties due to an increase in defectiveness and a decrease in γ-Fe_2O_3 volume fraction in the passive film. In chapter 5, the effect of prior austenite grain size (PAGS) on passivity behaviour of a low alloyed fully martensitic steel is investigated. The results show that the grain refinement in the range of 28 to 66 µm leads to a decrease in the barrier properties of the passive film due to a rise in passive films' donor density and lower γ-Fe_2O_3 volume fraction. However, it was observed that further refinement in PAGS leads to the enhancement in the barrier properties of the passive film due to the increase in γ-Fe_2O_3 volume fraction in passive film. This enhancement is attributed to the dominant effect of changes within the complex martensite structure on PAGS refinement. Chapter 6 studies the effect of grain size on the corrosion behaviour of iron. It was found that the grain refinement leads to an increase in the corrosion rate. However, the crystallographic texture

formation dominates the effect of grain size and leads to a decrease in corrosion rate.

Part C (Chapters 7 and 8) compares the passivity and corrosion behaviour of low-alloy steels composed of ferrite-pearlite and ferrite-martensite microstructures. Chapter 7 studies the passivity behaviour of ferrite-martensite and ferrite-pearlite microstructures. It was shown that the passive layer formed on the ferrite-martensite microstructure has lower barrier properties than the one formed on the ferrite-pearlite microstructure. This stems from the higher donor density of passive film formed on ferrite-martensite microstructure. In Chapter 8, the corrosion behaviour of ferrite-pearlite and ferrite-martensite microstructures are assessed. The results show that ferrite-martensite has a higher corrosion rate due to its distorted structure with higher dislocation content and boundaries.

In part D (chapter 9), the effect of crystallographic orientation on Localised corrosion behaviour of IF steel is investigated by combining electron backscatter diffraction (EBSD), scanning Kelvin probe force microscopy (SKPFM), and in-situ atomic force microscopy. It was shown that the

corrosion resistance decreases in the order of (001), (101), and (111) crystallographic orientations with respect to the sample surface.

Chapter 10 gives a general overview, conclusions, and suggestions for future research.

Samenvatting

De relatie tussen microstructurele kenmerken en mechanische eigenschappen van metalen staat al decennia in het middelpunt van de aandacht bij pogingen om de mechanische eigenschappen van legeringen te verbeteren. Een aanzienlijk aantal onderzoeken heeft inzichten opgeleverd in de relatie tussen microstructurele kenmerken en mechanische eigenschappen. De kennis van de relatie tussen microstructurele kenmerken en corrosie en passiviteit is echter nog steeds beperkt. Het begrijpen van het individuele effect van een microstructureel kenmerk op de eigenschappen van corrosie en passiviteit, is uitdagend. Dit komt voornamelijk door het complexe gecombineerde effect van microstructurele kenmerken op het corrosiegedrag.

Dit proefschrift richt zich op het begrijpen van het individuele effect van microstructurele kenmerken op het corrosiegedrag van laaggelegeerde ferro-materialen. De nadruk wordt gelegd op korrelgrootte en korrelgrenzen, dislocaties, kristallografische textuur en fasen. Om de veranderingen in de microstructurele kenmerken te isoleren, werden verschillende warmtebehandelingen en thermomechanische processen toegepast. Er werd een diepgaande microstructurele karakterisering

uitgevoerd om ervoor te zorgen dat de veranderingen in de microstructuur beperkt blijven tot de te onderzoeken kenmerken. Lokale en macroscopische elektrochemische en oppervlaktekarakteriseringstechnieken werden toegepast om een relatie te leggen tussen microstructurele kenmerken en corrosie en passiviteit.

In het eerste deel (Deel A, hoofdstukken 2 en 3) van het proefschrift wordt het effect van microstructurele defectdichtheid (dislocatiedichtheid en korrelgrensdichtheid) op de corrosie en passiviteit van interstitieel-vrije (IF) staalsoorten onderzocht. Hoofdstuk 2 onderzoekt de rol van microstructurele defectdichtheid (dislocatiedichtheid en korrelgrensdichtheid) op de passieve filmeigenschappen gevormd op interstitieel-vrije staalsoorten. De resultaten laten zien dat de barrière-eigenschappen van passieve films afnemen met toenemende microstructurele defectdichtheid, als gevolg van toenemende donordichtheid en afnemende volumefractie van het beschermende γ-Fe_2O_3 in de passieve film. In hoofdstuk 3 wordt het effect van dislocatiedichtheid, geïnduceerd door koudwalsen, op corrosiegedrag onderzocht met scanning Kelvin sondekrachtmicroscopie (SKPFM) en elektrochemische metingen. Er wordt waargenomen dat de

corrosiesnelheid toeneemt door het verhogen van de dislocatiedichtheid, toegeschreven aan de toenemende mate van galvanische koppeling tussen korrels als gevolg van een toename in dislocatiedichtheid. Bovendien wordt waargenomen dat het effect van dislocatiedichtheid het effect van kristallografische textuur op corrosiegedrag domineert.

Deel B (hoofdstuk 4-6) richt zich op het effect van korrelgrootte op corrosie en het gedrag van passieve lagen van verschillende laaggelegeerde ferro-materialen. Hoofdstuk 4 onderzoekt het effect van korrelgrootte op het gedrag van passieve lagen op ijzer in een alkalische omgeving. Er wordt aangetoond dat de korrelverfijning leidt tot een verslechtering van de barrière-eigenschappen van passieve films, als gevolg van een toename van de defecten en een afname van de γ-Fe_2O_3 volumefractie van de passieve film. In hoofdstuk 5 wordt het effect van de voormalige austenietkorrelgrootte (PAGS) op het passiviteitsgedrag van laaggelegeerd martensitisch staal onderzocht. De resultaten laten zien dat de korrelverfijning in het bereik van 28 tot 66 µm leidt tot een afname van de barrière-eigenschappen van de passieve film als gevolg van een toename van de donordichtheid van passieve films en een lagere γ-Fe_2O_3 volumefractie. Er wordt echter opgemerkt dat verdere verfijning van PAGS

leidt tot een verbetering van de barrière-eigenschappen van de passieve film vanwege de toename van de γ-Fe_2O_3 volumefractie. Deze verbetering wordt toegeschreven aan het dominante effect van veranderingen in de complexe martensietstructuur ten opzichte van verfijning van de voormalige austenietkorrels. Hoofdstuk 6 bestudeert het effect van korrelgrootte op het corrosiegedrag van ijzer. Er blijkt dat de korrelverfijning leidt tot een toename van de corrosiesnelheid. De kristallografische textuurvorming domineert echter het effect van korrelgrootte en leidt tot een afname van de corrosiesnelheid.

Deel C (hoofdstukken 7 en 8) vergelijkt de passiviteit en het corrosiegedrag van laaggelegeerde staalsoorten samengesteld uit ferriet-perliet en ferriet-martensiet microstructuren. Hoofdstuk 7 bestudeert het passiviteitsgedrag van ferriet-martensiet en ferriet-perliet microstructuren. Aangetoond wordt dat de passieve laag gevormd op de ferriet-martensiet microstructuur lagere barrière-eigenschappen heeft dan degene die gevormd is op de ferriet-perliet microstructuur. Dit komt voort uit de hogere donordichtheid van passieve film gevormd op ferriet-martensiet microstructuur. In hoofdstuk 8 wordt het corrosiegedrag van ferriet-perliet en ferriet-martensiet microstructuren onderzocht. De resultaten laten zien

dat ferriet-martensiet een hogere corrosiesnelheid heeft, vanwege de vervormde structuur met een hogere dislocatie- en korrelgrensdichtheid.

In deel D (hoofdstuk 9) wordt het effect van kristallografische oriëntatie op gelokaliseerd corrosiegedrag van IF-staal onderzocht door elektronen backscatter diffractie (EBSD), scanning Kelvin sondekrachtmicroscopie (SKPFM) en in-situ atomairekrachtmicroscopie te combineren. Er wordt aangetoond dat de corrosieweerstand afneemt in de orde van (001), (101) en (111) kristallografische oriëntaties t.o.v. het oppervlak van het proefstuk.

Hoofdstuk 10 geeft een algemeen overzicht, conclusies en suggesties voor toekomstig onderzoek.

List of Figures

List of tables

CHAPTER 1

INTRODUCTION

1.1 Introduction

The word steel has its origin from the Proto-Germanic adjectives stahlaz or stahlią, meaning standing firm. The earliest known 'standing firm' products (low-carbon steel fragments) were discovered in a multi-period archaeological site in Anatolia (Kaman-Kalehöyük), approximately 4000 years old, dating back to nearly the 20th century BC [1]. Since then, iron products have formed a basis for human civilization development primarily due to their mechanical properties. However, steel manufacturing was difficult and expensive until discovering the Bessemer process in the second half of the 19th century AD, allowing cheap and fast production of low-carbon steel. Mass production has allowed the application of steel in a wide range of industrial applications. With the increasing number of steel applications, significant steel processing advances have been achieved to continuously improve the steel's strength and toughness for various purposes. Besides its advantageous mechanical properties, the application of steel is suffering from the material's high sensitivity for corrosion.

Whereas significant progress has been achieved in the understanding of the microstructure-strength relations along with the advances in steel processing, we are still seriously lacking knowledge of

relations between microstructure and corrosion resistance. The required corrosion resistance and mechanical properties are generally achieved by employing different grades of steel. Figure 1.1 shows the relationship between tensile strength and corrosion rate for various grades of steel in 3.5 wt.% NaCl solution. Highly alloyed steels (stainless steels (SS) and twinning-induced plasticity (TWIP)) provide high corrosion resistance (mainly due to highly protective oxide formations) and tensile strength simultaneously, whereas mild steels generally provide low corrosion resistance and tensile strength. The corrosion resistance and tensile strength of other steels are between these two extremes. Although Interstitial-Free (IF) steel could be regarded a mild steel, its corrosion resistance is very high. The most plausible explanation of this feature is that IF steel is a single-phase (ferritic) steel, whereas most mild steels contain multiple phases, possibly leading to micro-galvanic coupling between phases [2,7,10,18]. Similarly, the formation of micro-galvanic couplings between phases might decrease the corrosion resistance of TRIP and dual-phase steels, while the alloying elements (e.g. chromium) might increase the corrosion resistance of these steels. The martensitic steels exhibit relatively low corrosion resistance due to the highly distorted structure of

martensite phase (higher strain and higher boundary density) [5,7,13]. The corrosion resistance of ferrous materials can be improved alongside their strength without altering their chemical composition by manipulating the microstructure. To do so, it is crucial to understand the role of microstructural features in corrosion behaviour.

In this work, the effect of various microstructural features on corrosion and passivity behaviour of low-alloy ferrous materials is investigated. In the present chapter, the introduction, the motivation and aim, research approach, and the outline of the thesis are provided. The results of the investigations on microstructural defects on passivity and corrosion behaviour of low-alloyed ferrous steels are given in Part A, chapters 2 and 3, respectively. In Part B, the role of grain size and prior austenite grain sizes on the passivity behaviour of low-alloy ferrous materials are investigated in chapters 4 and 5. Chapter 6 studies the effect of grain size on the corrosion behaviour of pure iron. Chapters 7 and 8 (Part C) investigate the effect of ferrite-pearlite and ferrite-martensite microstructures on passivity and corrosion behaviour, respectively. Chapter 9 investigates the role of grain's crystallographic orientation on corrosion behaviour of interstitial free ferritic steels. Chapter 10 summarizes and

correlates the main results of this work. Furthermore, suggestions are given for future research directions.

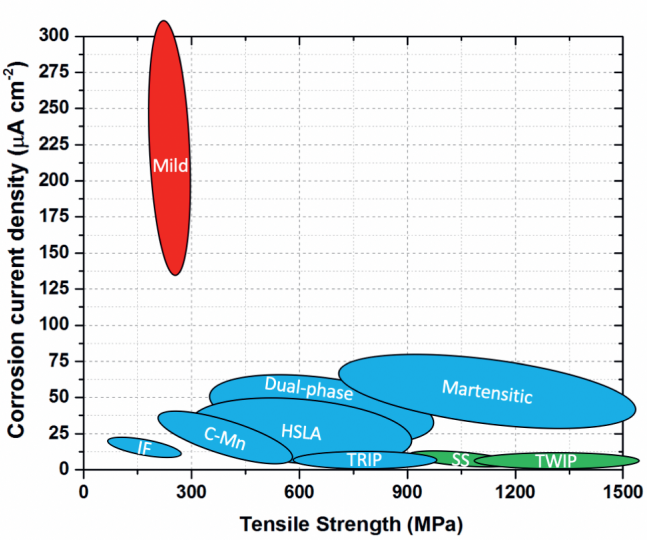

Figure 1.1 The relationship between corrosion current density and tensile strength. The corrosion current density values are obtained from the studies conducted in 3.5 wt.% NaCl solution. The data is obtained from references [2]–[27].

1.2 Research Motivation and Aim

Steels have been widely employed in many applications ranging from infrastructure, oil and gas production and transportation to domestic utensils. Considering the extensive knowledge obtained in the past decades on the relationship between microstructure and mechanical properties [28]–[31], it is possible to control steels' mechanical properties to a very high degree. For instance, it is well known that grain size refinement plays a

crucial role in controlling the mechanical properties since it increases the yield strength and wear resistance while maintaining high ductility. However, well-established relationships between microstructure and corrosion properties do not exist. Corrosion protection methods such as protective coatings, plating, surface treatments, corrosion inhibitors are used to improve the corrosion resistance of low-alloy steels since corrosion is a tremendously important issue in their applications. These corrosion protection methods often not only increase production costs but also lead to environmental and safety problems. These are invariably major problems for industry and significant concerns for engineering communities. Therefore, it is crucial to improve the corrosion resistance of bare metal in efforts to enhance the corrosion protection of ferrous materials. This is possible by understanding the relationship between microstructure and corrosion since the microstructure of metal does affect the corrosion processes and plays a crucial role in the initiation of corrosion, and leads to local differences in protective passive layer properties.

Accomplishing adequate corrosion resistance in bare metals is only possible based on fundamental insight into the microstructure and corrosion relationship. Although a number of studies have investigated the

role of microstructure in the corrosion and passivity behaviour of steels [32]–[51], there has been a limited number of studies on developing a fundamental understanding of the effects of microstructural features on the corrosion behaviour of steels. The existing studies have often reported contradictory results. These contradictions mainly stem from the fact that microstructural features have a complex interaction with each other on the corrosion and passivity behaviour of steels. These microstructural features can enhance or deteriorate each other's effect on corrosion resistance, making it challenging to identify the specific role of particular microstructural features. Several of these microstructural features are dislocation density, grain size, crystallographic orientation, chemical composition, metallurgical phases, and inclusions. This work aims to understand the individual role of grain size, dislocation density, crystallographic orientation, and different phases on both (local) corrosion and passivity behaviour of low alloy ferrous materials.

1.3 Research Approach

A multidisciplinary approach, composed of metallurgy, electrochemistry, and surface science with the application of high-resolution characterisation techniques, is taken in this project to investigate the individual effect of

microstructural features on corrosion and passivity behaviour. Figure 1.2 schematically shows the research approach of this work.

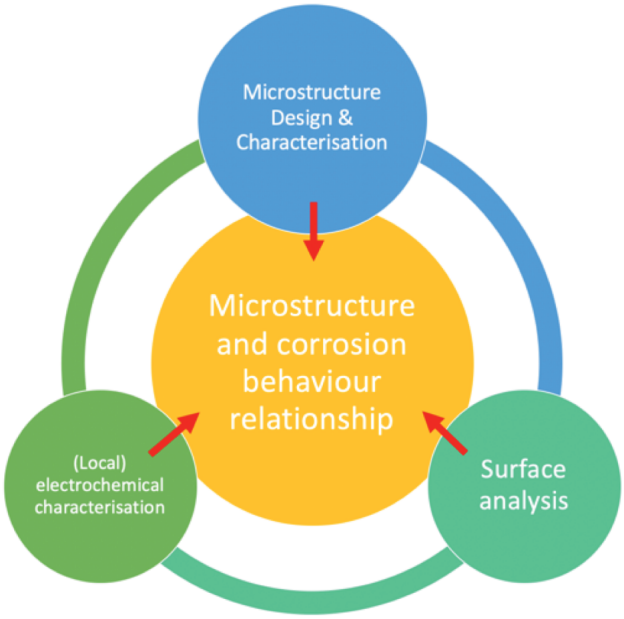

Figure 1.2 Schematic representation of the multidisciplinary approach taken to establish relationships between microstructural features and corrosion behaviour

On the side of microstructure design and characterisation, (model) microstructures were created and employed for the corrosion and passivity investigations to limit the changes in microstructural features only to the one investigated. Different heat treatments and/or thermomechanical processes were used to obtain the model microstructures. Heat treatments were conducted in dilatometry, which allows the precise control of

parameters and monitors the evolution of transformations by observing the dimensional changes in samples. The designed heat treatments provide the opportunity to minimize the changes in dislocation density while allowing grain size manipulations and/or phase formations [52]. Therefore, heat treatments in dilatometry are employed for the studies that investigate the role of grain size and phase combinations. In contrast, thermomechanical processes were employed to manipulate dislocation density and to investigate its role on corrosion and passivity behaviour.

The model microstructure of samples was characterized with different surface analysis techniques. Electron backscatter diffraction (EBSD) and X-ray diffraction (XRD) were employed to characterize the microstructures by obtaining information about phases and crystallographic orientation and dislocation density. In addition, EBSD was used to obtain grain boundary area density and grain size of samples. Optical microscopy was also used to determine the grain size, phase fractions, and phases. Similarly, scanning electron microscopy (SEM) was also used to determine the microstructural features investigated with optical microscopy. Additionally, since the inclusions and phases play an important role in

corrosion and passivity behaviour, SEM characterisation was employed to investigate these features.

On the surface characterisation side, Scanning Kelvin Probe Force Microscopy (SKPFM) was employed to study the local differences of Volta-potential on substrates surface to study both corrosion and passivity behaviour. Scanning Kelvin probe force microscopy is a powerful method that gives information on the electronic properties of the surface (Volta-potential) at the nanoscale (sensitivity of 1 mV and spatial resolution of ~15 nm) [44], [45]. The Volta-potential can provide information on the nobility of the metal surface depending on microstructural features, which can provide perceptive information on local electrochemical processes such as micro-galvanic coupling [33]. Therefore, Volta-potential differences between microstructural features have been employed to understand the corrosion behaviour [46], [53], [54]. Higher surface reactivity is attributed to areas with a higher difference in Volta-potential [33], [46], [53]. Moreover, Scanning Kelvin Probe (SKP) measurements were conducted to investigate surface reactivity through surface work-function measurements. In contrast to SKPFM that provides information about the surface reactivity at nano- to micro-scale, SKP provides information about

the overall surface reactivity in micrometre to millimetre range. In addition, X-ray photoelectron spectroscopy (XPS) was employed to study the chemical composition and the volume fraction of various iron oxides in the passive layer, as well as the thickness of the passive layer since these factors have an effect on the barrier properties. Therefore, the thickness of the passive layer was also investigated with ellipsometry.

Electrochemical characterisation techniques were used to understand the role of microstructural features in corrosion and passivity behaviour. The corrosion kinetics and mechanisms were determined with potentiodynamic polarisation. Potentiodynamic polarisation was also applied to correlate the kinetics in the passive region of potentiodynamic polarisation curves with the substrate's microstructure. Potentiostatic polarisation was used in passivation studies to form the passive layer and investigate the passivation kinetics and mechanisms. Electrochemical impedance spectroscopy (EIS) was applied in corrosion studies to study the relationship between the corrosion resistance and the microstructure of the substrate. Moreover, EIS was employed to investigate the effect of microstructure on passive films' barrier properties. Using Mott-Schottky analysis, the semi-conductor behaviour of passive films was investigated by

correlating the space-charge capacitance and the applied potential. This analysis reveals the donor and/or acceptor density of semi-conductor passive films. In addition to the electrochemical characterisation, in-situ atomic force microscopy (AFM) measurements were employed to study the local corrosion behaviour.

1.4 Research Outline

In figure 1.3, the structure of this Ph.D. thesis is shown schematically. A general introduction, research motivation, and aim, as well as the research approach, are given in the sections 1.1 through 1.3. The rest of the thesis is divided into four main parts.

Part A focuses on the effect of dislocation density and grain boundary areas on passivity and corrosion behaviour. It consists of two chapters. Chapter 2 studies the role of microstructural defects (dislocation density and grain boundary density) on the passivity behaviour of cold- and hot-rolled interstitial free (IF) steels. Electrochemical measurements are employed to investigate the effect of microstructural defect density on the passive layer's electrochemical properties. The defect density, chemical composition, and thickness of iron (hydr)oxides are correlated to the passive film's barrier properties, depending on the microstructural defect

density in the substrate. Additionally, Scanning Kelvin Probe (SKP) is employed to measure the work function, which is associated with the kinetics of passivity. In chapter 3, the role of dislocation density in the corrosion behaviour of IF ferritic steels is studied. The effect of dislocation density on corrosion kinetics and mechanisms is investigated with potentiodynamic polarisation. To assess the degree of galvanic coupling between grains depending on the substrate's dislocation density, the Volta-potential is evaluated. The differences in corrosion rate are associated with differences in the degree of galvanic coupling.

In Part B, the focus is on the effect of grain size on passivity and corrosion behaviour. It is composed of chapters 4, 5, and 6. Chapter 4 investigates the effect of grain size on the passive layer behaviour of pure iron in an alkaline environment. In this work, samples with various grain sizes at the micrometre scale were created by applying different heat treatments in dilatometry while controlling the other microstructural features such as dislocation density, inclusions, phases and texture. The effect of grain size on passive films' barrier properties was investigated with potentiostatic polarisation and EIS. Passive films' barrier properties are correlated with the defect density, chemical composition, and volume

fractions of iron (hydr)oxides of the passive films. In Chapter 5, the role of prior austenite grain size (PAGS) on passive layer properties of martensitic steels is studied. In this chapter, various heat treatments by dilatometry were applied to obtain samples with varying PAGS. Prior austenite grain size, dislocation density and features within the martensite structure are characterized by EBSD. The barrier properties of passive layers were studied through potentiodynamic and potentiostatic polarisation as well as with electrochemical impedance spectroscopy. The changes in the barrier properties with PAGS and the differences in martensite structure are associated with the defect density measured with Mott-Schottky analysis and the fraction of (hydr)oxides in the passive film. Chapter 6 investigates the role of grain size and crystallographic orientation on corrosion behaviour of pure iron samples. Potentiodynamic polarisation and EIS measurements evaluate the effect of grain size and crystallographic orientation on corrosion kinetics. Topography measurements obtained with atomic force microscopy (AFM) investigate the local corrosion behaviour at grain boundaries.

Part C studies the effect of phase combinations (ferrite-pearlite and ferrite-martensite) on passivity and corrosion behaviour. Chapter 7

compares pearlite's and martensite's role in their combination with ferrite in two-phase microstructures in passivity behaviour. Heat treatments with different transformation temperatures and durations were applied to obtain ferrite-pearlite and ferrite-martensite steels with similar ferrite volume fractions, characterized by optical microscopy and SEM. The barrier properties of the passive film were investigated with potentiostatic polarisation and EIS measurements. Furthermore, Mott-Schottky analysis was applied to correlate donor density and the microstructural phase combinations. Chapter 8 compares the corrosion behaviour of low-alloyed steels with ferrite-martensite and ferrite-pearlite microstructures. The corrosion behaviour of these phase combinations is investigated with potentiodynamic polarisation and EIS measurements.

Part D investigates the role of crystallographic orientation in the localised corrosion behaviour of IF ferritic steels. In chapter 9, the influence of crystallographic orientation on localised corrosion behaviour of interstitial free steels is investigated. The differences in the susceptibility for corrosion of grains with different crystallographic orientations were measured with in-situ AFM measurements. The differences in dissolution rates are

correlated with the variations in Volta-potentials between grains with different crystallographic orientations.

A general overview, conclusions and suggestions for future research are given in Chapter 10.

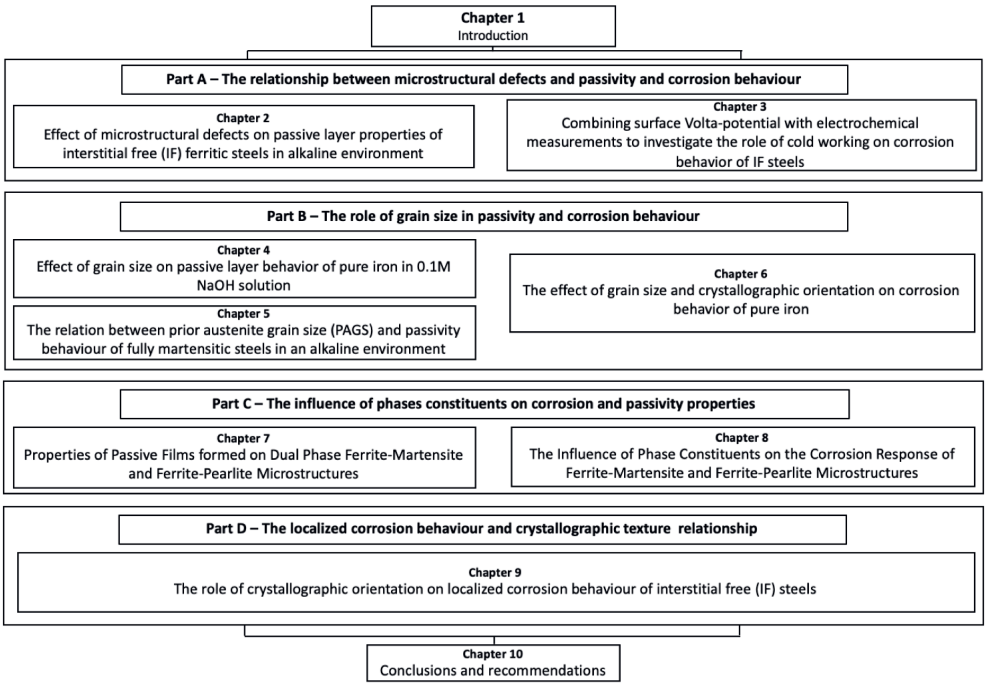

Figure 1.3 Schematic of the thesis structure

1.4 References

[1] H. Akanuma, “The significance of the composition of excavated iron fragments taken from Stratum III at the site of Kaman-Kalehöyük, Turkey,” *Anatol. Archaeol. Stud.*, vol. 14, pp. 147–158, 2005.

[2] G. P. Singh, A. P. Moon, S. Sengupta, G. Deo, S. Sangal, and K. Mondal, “Corrosion Behavior of IF Steel in Various Media and Its Comparison with Mild Steel,” *J. Mater. Eng. Perform.*, vol. 24, no. 5, pp. 1961–1974, 2015.

[3] B. Hadzima, M. Janeček, Y. Estrin, and H. S. Kim, “Microstructure and corrosion properties of ultrafine-grained interstitial free steel,” *Mater. Sci. Eng. A*, vol. 462, no. 1–2, pp. 243–247, 2007.

[4] C. T. Kwok, F. T. Cheng, and H. C. Man, “Synergistic effect of cavitation erosion and corrosion of various engineering alloys in 3.5% NaCl solution,” *Mater. Sci. Eng. A*, vol. 290, no. 1, pp. 145–154, 2000.

[5] W. Kingkam, C. Zhao, H. Li, H. Zhang, and L. Zhiming, “Effect of temperature during hot deformation on the electrochemical behavior of HSLA pipeline steels,” *Int. J. Electrochem. Sci.*, vol. 13, no. 3, pp. 2766–2778, 2018.

[6] Q. Yan, Q. Yin, J. Cui, X. Wang, Y. Qiao, and H. Zhou, “Effect of

temperature on corrosion behavior of E690 steel in 3.5 wt.% NaCl solution," *Mater. Res. Express*, vol. 8, no. 1, p. 16528, 2021.

[7] T. A. N. Remmerswaal, "The influence of microstructure on the corrosion behaviour of ferritic-martensitic steel,", Master Thesis, TU Delft, p. 106, 2015.

[8] Y. Shadangi, K. Chattopadhyay, S. B. Rai, and V. Singh, "Effect of laser shock peening on microstructure, mechanical properties and corrosion behavior of interstitial free steel," *Surf. Coatings Technol.*, vol. 280, pp. 216–224, 2015.

[9] W. R. Osório, L. C. Peixoto, L. R. Garcia, and A. Garcia, "Electrochemical corrosion response of a low carbon heat treated steel in a NaCl solution," *Mater. Corros.*, vol. 60, no. 10, pp. 804–812, 2009.

[10] P. K. Katiyar, S. Misra, and K. Mondal, "Corrosion Behavior of Annealed Steels with Different Carbon Contents (0.002, 0.17, 0.43 and 0.7% c) in Freely Aerated 3.5% NaCl Solution," *J. Mater. Eng. Perform.*, vol. 28, no. 7, pp. 4041–4052, 2019.

[11] Y. Raghupathy, A. Kamboj, M. Y. Rekha, N. P. Narasimha Rao, and C. Srivastava, "Copper-graphene oxide composite coatings for corrosion

protection of mild steel in 3.5% NaCl," *Thin Solid Films*, vol. 636, pp. 107–115, 2017.

[12] W. Xu, E.-H. Han, and Z. Wang, "Effect of tannic acid on corrosion behavior of carbon steel in NaCl solution," *J. Mater. Sci. Technol.*, vol. 35, no. 1, pp. 64–75, 2019.

[13] T. V. Shibaeva, V. K. Laurinavichyute, G. A. Tsirlina, A. M. Arsenkin, and K. V. Grigorovich, "The effect of microstructure and non-metallic inclusions on corrosion behavior of low carbon steel in chloride containing solutions," *Corros. Sci.*, vol. 80, pp. 299–308, 2014.

[14] M. A. M. Ibrahim, S. S. Abd El Rehim, and M. M. Hamza, "Corrosion behavior of some austenitic stainless steels in chloride environments," *Mater. Chem. Phys.*, vol. 115, no. 1, pp. 80–85, 2009.

[15] P. Boonsa and A. Rodchanarowan, "Virtual corrosion testing on stainless steel AISI 304 welded pipe with Hydroxyethyl Cellulose in 3.5% NaCl solution and turbulent flow," *Mater. Res. Express*, vol. 7, no. 6, p. 66519, 2020.

[16] P. P. Sarkar, P. Kumar, M. K. Manna, and P. C. Chakraborti, "Microstructural influence on the electrochemical corrosion behaviour of dual-phase steels in 3.5% NaCl solution," *Mater. Lett.*,

vol. 59, no. 19–20, pp. 2488–2491, 2005.

[17] A. P. Moon, S. Sangal, S. Layek, S. Giribaskar, and K. Mondal, "Corrosion Behavior of High-Strength Bainitic Rail Steels," *Metall. Mater. Trans. A*, vol. 46, no. 4, pp. 1500–1518, 2015.

[18] H. Gerengi, N. Sen, I. Uygur, and E. Kaya, "Corrosion behavior of dual-phase 600 and 800 steels in 3.5 wt.% NaCl environment," *J. Adhes. Sci. Technol.*, vol. 34, no. 8, pp. 903–915, 2020.

[19] L. Onyeji and G. Kale, "Preliminary Investigation of the Corrosion Behavior of Proprietary Micro-alloyed Steels in Aerated and Deaerated Brine Solutions," *J. Mater. Eng. Perform.*, vol. 26, no. 12, pp. 5741–5752, 2017.

[20] Y. Guo, J. Hu, J. Li, L. Jiang, T. Liu, and Y. Wu, "Effect of annealing temperature on the mechanical and corrosion behavior of a newly developed novel lean duplex stainless steel," *Materials (Basel).*, vol. 6, no. 9, pp. 6604–6619, 2014.

[21] E. A. Ariza, M. Masoumi, and A. P. Tschiptschin, "Improvement of tensile mechanical properties in a TRIP-assisted steel by controlling of crystallographic orientation via HSQ&P processes," *Mater. Sci. Eng. A*, vol. 713, pp. 223–233, 2018.

[22] J. Yang, Y. Lu, Z. Guo, J. Gu, and C. Gu, “Corrosion behaviour of a quenched and partitioned medium carbon steel in 3.5wt.% NaCl solution,” *Corros. Sci.*, vol. 130, pp. 64–75, 2018.

[23] X. Yuan, Y. Zhao, X. Li, and L. Chen, “Effect of Cr on mechanical properties and corrosion behaviors of Fe-Mn-C-Al-Cr-N TWIP steels,” *J. Mater. Sci. Technol.*, vol. 33, no. 12, pp. 1555–1560, 2017.

[24] J. Bosch, U. Martin, W. Aperador, J. M. Bastidas, J. Ress, and D. M. Bastidas, “Corrosion Behavior of High-Mn Austenitic Fe–Mn–Al–Cr–C Steels in NaCl and NaOH Solutions,” *Materials* , vol. 14, no. 2. 2021.

[25] P. K. Katiyar, S. Misra, and K. Mondal, “Effect of Different Cooling Rates on the Corrosion Behavior of High-Carbon Pearlitic Steel,” *J. Mater. Eng. Perform.*, vol. 27, no. 4, pp. 1753–1762, 2018.

[26] L. D. Paolinelli, T. Pérez, and S. N. Simison, “The effect of pre-corrosion and steel microstructure on inhibitor performance in CO2 corrosion,” *Corros. Sci.*, vol. 50, no. 9, pp. 2456–2464, 2008.

[27] T. Haisch, E. J. Mittemeijer, and J. W. Schultze, “On the influence of microstructure and carbide content of steels on the electrochemical dissolution process in aqueous NaCl-electrolytes,” *Mater. Corros.*, vol. 53, no. 10, pp. 740–755, 2002.

[28] S. Zaefferer, J. Ohlert, and W. Bleck, “A study of microstructure, transformation mechanisms and correlation between microstructure and mechanical properties of a low alloyed TRIP steel,” *Acta Mater.*, vol. 52, no. 9, pp. 2765–2778, 2004.

[29] K. L. Murty, M. D. Mathew, Y. Wang, V. N. Shah, and F. M. Haggag, “Nondestructive determination of tensile properties and fracture toughness of cold worked A36 steel,” *Int. J. Press. Vessel. Pip.*, vol. 75, no. 11, pp. 831–840, 1998.

[30] J. P. Chu, J. M. Rigsbee, G. Banaś, and H. E. Elsayed-Ali, “Laser-shock processing effects on surface microstructure and mechanical properties of low carbon steel,” *Mater. Sci. Eng. A*, vol. 260, no. 1–2, pp. 260–268, 1999.

[31] C. C. Tasan *et al.*, “An Overview of Dual-Phase Steels: Advances in Microstructure-Oriented Processing and Micromechanically Guided Design,” *Annu. Rev. Mater. Res.*, vol. 45, no. 1, pp. 391–431, 2015.

[32] K. H. Anantha, C. Örnek, S. Ejnermark, A. Medvedeva, J. Sjöström, and J. Pan, “In Situ AFM Study of Localized Corrosion Processes of Tempered AISI 420 Martensitic Stainless Steel: Effect of Secondary Hardening,” *J. Electrochem. Soc.*, vol. 164, no. 13, pp. C810–C818,

2017.

[33] C. Örnek and D. L. Engelberg, “SKPFM measured Volta potential correlated with strain localisation in microstructure to understand corrosion susceptibility of cold-rolled grade 2205 duplex stainless steel,” *Corros. Sci.*, vol. 99, pp. 164–171, 2015.

[34] K. Yanagisawa, T. Nakanishi, Y. Hasegawa, and K. Fushimi, “Passivity of dual-phase carbon steel with ferrite and martensite phases in pH 8.4 boric acid-borate buffer solution,” *J. Electrochem. Soc.*, vol. 162, no. 7, pp. C322–C326, 2015.

[35] K. Fushimi, K. Miyamoto, and H. Konno, “Anisotropic corrosion of iron in pH 1 sulphuric acid,” *Electrochim. Acta*, vol. 55, no. 24, pp. 7322–7327, 2010.

[36] K. Fushimi, K. Azumi, and M. Seo, “Evaluation of Heterogeneity in Thickness of Passive Films on Pure Iron by Scanning Electrochemical Microscopy,” *ISIJ Int.*, vol. 39, no. 4, pp. 346–351, 1999.

[37] J. Lv and H. Luo, “Effects of strain and strain-induced α’-martensite on passive films in AISI 304 austenitic stainless steel,” *Mater. Sci. Eng. C*, vol. 34, no. 1, 2014.

[38] L. Jinlong and L. Hongyun, “The effects of cold rolling temperature on

corrosion resistance of pure iron," *Appl. Surf. Sci.*, vol. 317, pp. 125–130, 2014.

[39] K. D. Ralston and N. Birbilis, "Effect of grain size on corrosion: A review," *Corrosion*, vol. 66, no. 7, pp. 0750051–07500513, 2010.

[40] A. Fattah-Alhosseini and S. Vafaeian, "Influence of grain refinement on the electrochemical behavior of AISI 430 ferritic stainless steel in an alkaline solution," *Appl. Surf. Sci.*, vol. 360, pp. 921–928, 2016.

[41] A. Schreiber, J. W. Schultze, M. M. Lohrengel, F. Kármán, and E. Kálmán, "Grain dependent electrochemical investigations on pure iron in acetate buffer pH 6.0," *Electrochim. Acta*, vol. 51, no. 13, pp. 2625–2630, 2006.

[42] T. Suter, T. Peter, and H. Böhni, "Microelectrochemical Investigations of MnS Inclusions," *Mater. Sci. Forum*, vol. 192–194, pp. 25–40, 1995.

[43] R. A. Perren *et al.*, "Corrosion resistance of super duplex stainless steels in chloride ion containing environments: Investigations by means of a new microelectrochemical method. II. Influence of precipitates," *Corros. Sci.*, vol. 43, no. 4, pp. 727–745, 2001.

[44] C. Örnek, C. Leygraf, and J. Pan, "Passive film characterisation of duplex stainless steel using scanning Kelvin probe force microscopy

in combination with electrochemical measurements," *npj Mater. Degrad.*, vol. 3, no. 1, pp. 1–8, 2019.

[45] C. Örnek, J. Walton, T. Hashimoto, T. L. Ladwein, S. B. Lyon, and D. L. Engelberg, "Characterisation of 475°C Embrittlement of Duplex Stainless Steel Microstructure via Scanning Kelvin Probe Force Microscopy and Magnetic Force Microscopy," *J. Electrochem. Soc.*, vol. 164, no. 6, pp. C207–C217, 2017.

[46] V. Guillaumin, P. Schmutz, and G. S. Frankel, "Characterisation of Corrosion Interfaces by the Scanning Kelvin Probe Force Microscopy Technique," *J. Electrochem. Soc.*, vol. 148, no. 5, p. B163, 2001.

[47] L. C. Yule *et al.*, "Nanoscale Active Sites for the Hydrogen Evolution Reaction on Low Carbon Steel," *J. Phys. Chem. C*, vol. 123, no. 39, pp. 24146–24155, 2019.

[48] L. C. Yule *et al.*, "Nanoscale electrochemical visualization of grain-dependent anodic iron dissolution from low carbon steel," *Electrochim. Acta*, vol. 332, p. 135267, 2020.

[49] Y. Takabatake, K. Fushimi, T. Nakanishi, and Y. Hasegawa, "Grain-Dependent Passivation of Iron in Sulfuric Acid Solution," *J. Electrochem. Soc.*, vol. 161, no. 14, pp. C594–C600, 2014.

[50] K. Fushimi, K. Yanagisawa, T. Nakanishi, Y. Hasegawa, T. Kawano, and M. Kimura, “Microelectrochemistry of dual-phase steel corroding in 0.1 M sulfuric acid,” *Electrochim. Acta*, vol. 114, pp. 83–87, 2013.

[51] K. Fushimi, Y. Takabatake, T. Nakanishi, and Y. Hasegawa, “Microelectrode techniques for corrosion research of iron,” *Electrochim. Acta*, vol. 113, pp. 741–747, 2013.

[52] C. García De Andrés, F. G. Caballero, C. Capdevila, and L. F. Álvarez, “Application of dilatometric analysis to the study of solid-solid phase transformations in steels,” *Mater. Charact.*, vol. 48, no. 1, pp. 101–111, 2002.

[53] M. Rohwerder and F. Turcu, “High-resolution Kelvin probe microscopy in corrosion science: Scanning Kelvin probe force microscopy (SKPFM) versus classical scanning Kelvin probe (SKP),” *Electrochim. Acta*, vol. 53, no. 2, pp. 290–299, 2007.

[54] W. Li, M. Cai, Y. Wang, and S. Yu, “Influences of tensile strain and strain rate on the electron work function of metals and alloys,” *Scr. Mater.*, vol. 54, no. 5, pp. 921–924, 2006.

Part A

The relationship between microstructural defects and passivity/corrosion behaviour

CHAPTER 2

Effect of microstructural defects on passive layer properties of interstitial free (IF) ferritic steels in an alkaline environment

This chapter is based on a published scientific paper:

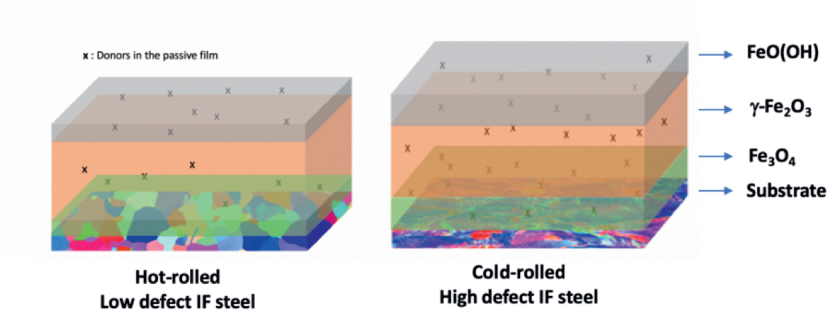

A.Yilmaz, K. Traka, S. Pletincx, T. Hauffman, J. Sietsma, and Y. Gonzalez-Garcia, "Effect of microstructural defects on passive layer properties of interstitial free (IF) ferritic steels in alkaline environment," *Corros. Sci.*, vol. 182, 2021, 109271.

Abstract

The role of microstructural defect density (dislocation density and grain boundary density) on the passive film properties formed on interstitial free (IF) steels is investigated in 0.1 M NaOH solution. To obtain varied defect density between the studied samples, cold-rolled and hot-rolled samples were employed. The microstructure of samples was characterized by electron backscatter diffraction (EBSD) measurements. Cold-rolled samples exhibit higher dislocation density and grain boundary density. No alloy segregation, inclusion formation, and phase transformation are observed after cold rolling, preventing the interaction between defect density and other microstructural features on passive layer properties. Potentiodynamic polarisation (PDP) shows the increased current density in the passive region with increasing defect density. Electrochemical impedance spectroscopy (EIS) results show that the passive layer formed on samples with a higher defect density has lower barrier properties. Mott-Schottky analysis reveals that the donor density of the passive layer increases with higher substrate defect density. X-ray Photoelectron Spectroscopy (XPS) shows that the chemical composition of passive layers formed by potentiostatic polarisation consists of Fe_3O_4, γ-Fe_2O_3 and FeO(OH) for both materials, but also that the

relative quantity of protective γ-Fe_2O_3 in passive film decreases with the rise in defect density. Ellipsometry measurements show that the passive film formed on samples with higher dislocation density is thicker. This is attributed to increased donor density and a lower work function, measured with Scanning Kelvin Probe (SKP). This work shows that the increased microstructural defect density induced by cold rolling decreases the passive layer's barrier properties due to higher donor density and lower protective γ-Fe_2O_3 ratio in passive film.

Keywords: Interstitial free (IF) steels, dislocation density, passive layer, EIS, Mott-Schottky analysis, XPS, SKP

2.1 Introduction

Cold working is commonly applied on steels in many industries, varying from automotive to oil and gas in order to increase the strength and hardness of materials during fabrication procedures [1]. The improved mechanical properties mainly stem from the higher defect density (dislocation and grain boundary density) achieved after cold working. A significant number of studies has widely investigated the relationship between defect density and mechanical properties [2]–[4]. However, the understanding of the relationship between defect density and passivity is still to be improved. During the processes to manipulate the defect density, other changes in the microstructure of the substrate material also occur [5]–[7]. These other microstructural changes, e.g. segregation of alloying elements, phase transformation, the formation of inclusions, affect passive layer properties with different defect density.

The effect of these microstructural features might interfere with or dominate the impact of defect density on the passive layer properties. This leads to contradictory reports on the effect of dislocation density on the passivity behaviour in the existing literature. Both improvement and deterioration in the barrier properties of the passive film with an increase

in defect density are reported [8]–[12]. Jinlong and Hongyun [8] studied the effect of pre-deformation, resulting in the rise in both dislocation density and the volume fraction of α'-martensite, on passive layer properties of AISI 304 stainless steel. They reported the deterioration of passive layer barrier properties with an increase in pre-deformation. Yamamoto et al. [11] investigated the role of different degrees of cold working on the passivation behaviour of pure iron. They observed first a decrease and then an enhancement in the barrier properties of the passive film with increasing cold working degrees, leading to an increase in the defect density. Wang and Li [12] compared the electrochemical behaviour of nanocrystalline and as received 304 stainless steels. The nanocrystalline material was obtained with sandblasting, leading to a significant increase in dislocation density and decrease in grain size. They observed better passive layer properties in nanocrystalline material after sandblasting. These existing studies show that it is not straightforward to establish a relationship between defect density and passive layer properties due to the changes in other microstructure features, occurring during the processes used to change the defect density. Considering the contradictory results presented in the

literature, it is only possible to understand the sole role of defect density on the passive layer properties by designing and controlling the microstructure.

Furthermore, the majority of the abovementioned studies focused on the passivity behaviour of stainless steels [8]–[10], [12]. Very few studies investigated the role of microstructural defect density on passive layer properties of low alloyed steels [11]. The existing literature explained the changes in electrochemical properties of passive films are associated to the variations in the donor/acceptor density in the passive films due to the presence of substrate microstructural defects [8]–[11]. Yet, very little attention has been given to the alterations in the chemical composition and thickness of the passive layer with variations in microstructural defect density, that change the barrier properties of passive films.

The goal of this work is to deepen the understanding of the relation between microstructural defect density and passive layer behaviour of high-strength steels. For this purpose, controlled alloys of hot- and cold-rolled interstitial free (IF) steels were employed to minimize the changes in microstructural features other than the defect density. The effect of microstructural defect density on the barrier properties of passive films was investigated with potentiodynamic polarisation (PDP) and electrochemical

impedance spectroscopy (EIS) in 0.1 M NaOH. The donor density of passive films was characterized by Mott-Schottky analysis. The chemical composition and thickness of the passive films were evaluated by X-ray photoelectron spectroscopy (XPS) and ellipsometry, respectively. Scanning Kelvin Probe (SKP) measurements were conducted to determine the effect of microstructural defect density on surface reactivity. The experimental results form the basis for a discussion on the role of defect density on the properties of the passive film.

2.2 Experimental

2.2.1 Material

Hot and cold-rolledinterstitial-free (IF) ferritic steels (provided by Tata Steel, the Netherlands) were investigated. The chemical composition of IF steel employed is given in Table 2.1. The thickness reduction at the last pass of hot-rolling was approximately 85% and the cold-rolling reduction was approximately 78%. Hot-rolled and cold- rolled samples are indicated as low defect density (LD) and high defect density (HD) samples, respectively. The thickness of hot- and cold-rolled samples were 3.4 and 0.76 mm, respectively. Both samples

were laser-cut to the dimension of 10 mm x 5 mm.

2.2.1.Microstructure Characterisation

Electron backscatter diffraction (EBSD) analysis was employed to characterize the microstructures, by obtaining information about crystallographic phases and orientation, grain boundary area fraction and

	Fe	C	Mn	Al	N	Ti	S	Cr
wt%	99.78	0.002	0.095	0.05	0.002	0.045	0.006	0.02

Table 2.1 Chemical Composition of the IF- ferritic steel specimens

dislocation density. The calculation of Geometrically Necessary Dislocations (GND) density was performed with OIM v7.3 software using the function described in [13]. The method approximates the dislocation content ρ_{GND} by its relation to the dislocation tensor (known as Nye's tensor[14]) which is calculated as the tensorial summation of the lattice curvature (i.e. orientation's $curl$) and the elastic strain tensor's divergence, as it was initially proposed by Nye in [14]. To prepare the samples for electron backscatter diffraction (EBSD) analysis, the samples were ground with SiC papers of 80 to 4000 grit. Afterwards, the samples were polished with a diamond particle slurry with particle sizes of 3 and 1 μm (Struers DiaDuo-2), respectively. The samples were finally polished with a standard colloidal silica suspension with a 0.04 μm particle size. Then, the samples were

cleaned in an ultrasonic bath with ethanol for 10 min and dried with compressed air. The high-resolution EBSD measurements were conducted with a JEOL JSM 6500F FEG-SEM microscope with an EDAX/TSL detector. A working distance of 17 mm and a step size of 0.5 μm were used for all EBSD measurements. The post-processing of the EBSD data was conducted both in TSL-OIM version 7.3 and in Matlab with the use software tool provided by MTEX [15].

2.2.2 Scanning Kelvin probe measurements

Scanning Kelvin probe measurements were conducted to investigate the relationship between microstructural defect density and surface reactivity. The samples for Scanning Kelvin Probe (SKP) measurements were prepared as follows. The samples were mechanically ground with SiC grinding papers, from 80 to 4000 grit. Following grinding, the samples were polished with alcohol-based, high-performance diamond slurry, having particles size of 3 μm (Struers DP-Suspension a), and polishing cloth (Struers DP-Mol). Finally, the samples were polished with a 1 μm alcohol based-high performance diamond slurry (Struers DP-Suspension a) and polishing cloth (Struers DP-Nap) until obtaining mirror-like surface finishing. The samples were cleaned in an ultrasonic bath in ethanol for 10 min and dried with compressed air

before the SKP measurements. A height-regulated scanning Kelvin probe (SKP5050) from KM Soft Control was employed to conduct potential measurements right after the sample preparation. The SKP probe consisted of an SAE 304 stainless steel tip with a diameter of approximately 550 μm. Before the measurements, the probe was calibrated against $Cu/CuSO_4$ reference. The experiments with the IF-steel samples were conducted on freshly polished samples at a controlled relative humidity of ambient air, ~43% and room temperature (23 ^{o}c). The potential was measured as a function of time. Point measurements were repeated three times for each sample to ensure reproducibility of the results.

2.2.3 Electrochemical Measurements

Electrochemical measurements (potentiodynamic polarisation, electrochemical impedance spectroscopy) were employed to investigate the effect of microstructural density on the electrochemical properties of passive film formed on both LD and HD samples.

Type-K chromel-alumel thermocouple wire was spot welded on the bottom of the samples to ensure a good connection of the working electrode to the electrochemical cell. Prior to electrochemical measurements, the samples were embedded in an epoxy resin (Struers

ClaroCit). The resin was cured for 1 hour under 2 bar pressure. Subsequently, the samples were mechanically ground and polished by the same procedure for samples preparation for SKP measurements. Afterwards, the samples were cleaned in an ultrasonic bath in ethanol for 10 min and dried with compressed air. To prevent crevice corrosion, the gap between the resin and the sample was masked by a thin layer of sealing lacquer (Electrolube Bloc Lube Red).

The electrolyte used for the electrochemical measurements was an aerated 0.1 M NaOH solution with a pH of 12.7. The solution was prepared with distilled water at room temperature. A conventional three-electrode electrochemical cell was used for the electrochemical measurements. The setup is composed of the sample as the working electrode, a graphite rod as counter electrode and an Ag/AgCl (Sat. KCl) reference electrode. A Biologic SP 300 potentiostat was used. The potentials were measured versus Ag/AgCl (Sat. KCl). The electrochemical tests were conducted three times to verify the reproducibility of the results.

Before conducting the electrochemical tests, the open circuit potential (OCP) was measured for 1800 seconds at which steady-state is achieved. For potentiodynamic polarisation, a potential range between -

0.25 V to 1.25 V (vs OCP) and a scan rate of 0.167 mV/s were chosen. Before EIS measurements, potentiostatic polarisation was conducted at 0.2 V (vs. Ag/AgCl) for 3 hours at which steady-state was observed for both samples to form the passive layer. Then, EIS measurements were obtained between 30 kHz and 10 mHz with an A.C. signal, having an amplitude of 10 mV peak to peak. Zview software (v3.5) was employed for analysing the EIS data.

Capacitance measurements (Mott-Schottky analysis) were conducted to correlate the microstructural defect density with the electronic properties of the passive film after forming the passive layer with potentiostatic polarisation at 0.2 V (vs. Ag/AgCl) for 3 hours. Capacitance measurements (Mott-Schottky analysis) were performed at the frequency of 1 kHz with an amplitude of 10 mV peak to peak for the AC signal. The potential sweeps were conducted from 0.6 V to -1V with the potential step size of 50 mV. To analyse data from polarisation and capacitance measurements, ECLab software (v11.33) was used.

2.2.4 Passive Layer Analysis

X-ray photoelectron spectroscopy (XPS) measurements were conducted to analyse the chemical composition and relative fractions of different (hydr)oxide layers in the passive layer, depending on the substrate defect

density. Before XPS measurements, the passive layer was formed by potentiostatic polarisation at 0.2 V for 3 hours in 0.1 M NaOH solution. Subsequently, the samples were rinsed with ethanol and dried with compressed air. A PHI5000 Versa probe II photoelectron spectrometer (Physical Electronics) with an Al K alpha monochromatic X-ray source (1486.71 eV photon energy) was employed to collect XPS spectra. The pressure in the analysis chamber was maximum of 5 x 10^{-9} Torr during measurements. The chosen take-off angle and X-ray spot size were 45 degrees and 200 µm for high-resolution scans of Fe 2p and O 1s core electron peaks, respectively. A pass energy of 23.5 eV and an energy step size of 0.1 eV were employed. Casa XPS software was used for fitting the acquired XPS data, using a Shirley background.

Ellipsometry measurements were conducted to measure the thickness of the passive layers of both samples. The passive layers were formed by potentiostatic polarisation at 0.2 V for 3 hours in a 0.1 M NaOH solution. A visual variable angle spectroscopic ellipsometry (M2000X VIS-VASE) provided by J. A. Woollam Co., Inc. with Xenon lamp source was used for the measurements. WVASE software was employed to analyse the ellipsometry data.

2.3 Results and Discussion

2.3.1 Analysis of microstructural features

High-resolution electron backscatter diffraction (EBSD) measurements were performed to determine the spatially resolved crystallographic orientations and consequently the defect density (grain boundary area fraction and dislocation density) through the local orientation distributions. The EBSD measurements were conducted in several longitudinal sections perpendicular to transverse direction (TD), rolling direction (RD) and normal direction (ND) to trace possible differences in these various planes. The results on the ND-TD plane are only shown due to the plane of interest for the current study. Furthermore, the same step size for the EBSD measurements performed on LD and HD samples were employed to prevent the effect of step size on the calculation of boundaries and dislocation density [16].

Figures 2.1a and 2.1b show the EBSD inverse pole figures (IPF) in ND-TD plane of the low defect (LD) and high defect (HD) samples, respectively. The LD microstructure consists of equiaxed grains while having a mild preferential orientation for <111>//ND, <100>//ND and <112>//ND, <113>//ND, <114>//ND planes which is a result of the β fibre texture of

austenite to ferrite transformation [17]. However, a stronger preferential crystallographic orientation in <111>//ND and <100>//ND (Fig. 2.1b) and also components in <112>//ND, <113>//ND, <114>//ND planes is observed in HD material. In this case, the components mentioned above appeared as a result of the α and γ fibre rolling textures [18], [19]. Therefore, the intensity (magnitude) and the exact components which are preferred are different. However, both samples have a similar distribution of preferential crystal orientations with respect to the crystal direction, which is parallel to ND. Furthermore, in Fig 2.1a and 2.1b, the microstructure of both LD and HD samples belongs only in the BCC crystal structure. It shows that both materials consist of only the ferritic phase. Both materials do not exhibit carbides in IPF maps, showing the negligible volume fraction of carbides due to the very low alloyed nature of the material.

In Figures 2.1c and 2.1d, the geometrically necessary dislocation (GND) maps of LD and HD samples are given, respectively. It is observed that dislocations in LD samples (Figure 1c) are homogeneously distributed with very low density. In Figure 2.1d, it is shown that the HD exhibits a much higher dislocation density, consisting of topological heterogeneities (e.g. the largest GND density is observed at highly distorted regions while other

regions do not contain large orientation gradients). The mean dislocation density values are 3.6 ± 0.4 x 10^{12} m^{-2} and 147 ± 14 x 10^{12} m^{-2} for the low defect (LD) and high defect (HD) samples, respectively. It shows that there are almost two orders of magnitude differences in dislocation density between both samples. Concerning the defect density, as it was previously mentioned, the quantification of the dislocation density refers to only the structural dislocations (GNDs) and not to statistically stored dislocation (SSD) density. Although SSDs can highly contribute to the material's dislocation content, the studied material is characterized by a high Stacking-Fault Energy (SFE), and in such metals, sub-cell structures would be expected to be prevalent [20]–[22]. This occurs due to the dislocations' cross-slip during deformation which results in the formation of favourable (lower) energy arrangements of the dislocation content (mechanism of dynamic recovery – a phenomenon known as polygonisation [23], [24]). Hence, in such metals the largest contribution of the dislocation density can be reasonably expected to be located at the substructure's boundaries.

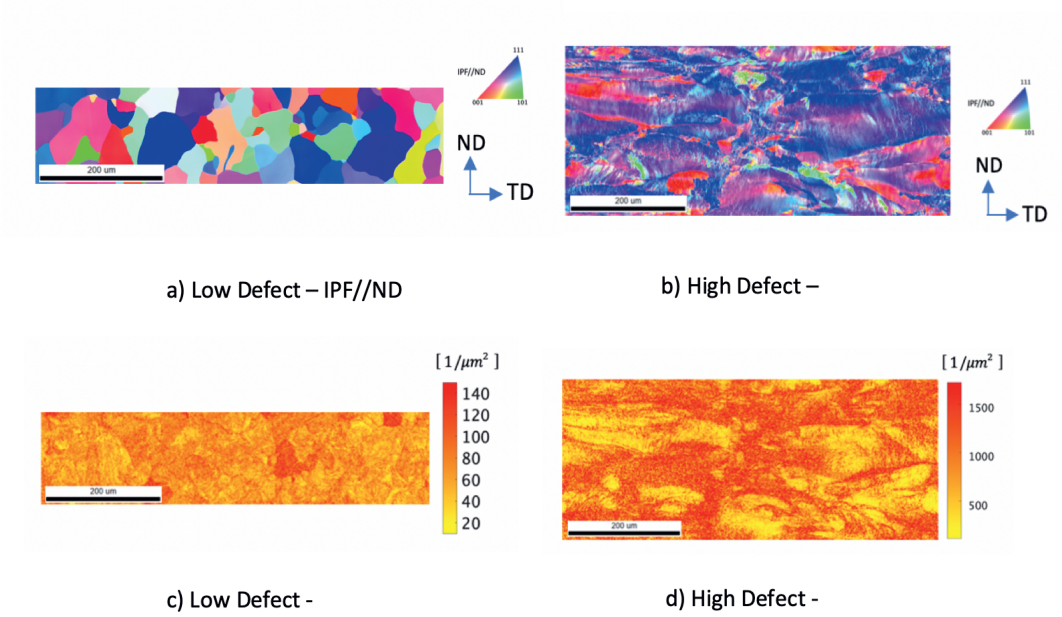

Figure 2.1EBSD maps of the hot- and cold- rolled samples.a) and b) are the Inverse Pole Figure (IPF) maps show the spatially resolved crystallographic orientations parallel to the normal direction of the sheets for the low- Defect (HD) and b) the high- Defect (LD) samples, respectively. (c) and d) are the Geometrically Necessary Dislocation (GND) maps (measured with the same step size of 0.5 μm) for LD and HD samples.The GNDs were calculated for a maximum angle of 10° and up to the 3rd neighbour pixel

Similar to geometrically necessary dislocation density, the grain boundary fraction is much higher in HD samples. Considering the threshold angle for high angle grain boundaries (HAGB) as 15°, the HAGB densities for HD and LD samples are 0.152 ± 0.002 and 0.029 ± 0.001 μm^{-1}, respectively. HD samples also exhibit higher low-angle grain boundary density in comparison with LD samples. The LAGB density for HD samples is 2.44 ± 0.14 μm^{-1} whereas the LAGB density for LD samples is 0.006 ± 0.002 μm^{-1}.

2.3.2 Reactivity of the surface – SKP experiments

To elucidate the effect of microstructural defects on the reactivity of the surface, SKP point measurements were conducted on freshly polished surfaces of both low (LD) and high defect (HD) density samples. Figure 2.2a shows the work function changes over time at the measured points. On both samples, an initial increase in the work function is observed and associated with the evaporation of absorbed water layer on the surface and the growth of natural passive layer [25]. The further increase in the work function probably results from the further growth of a natural passive layer. In Figure 2.2b, the work function values at three selected exposure times after reaching the stability are given. It is observed that the work function is lower for HD samples than for LD samples at all times. The decrease in work function with increasing defect density agrees with the existing literature that report decreases in work function with an increase in microstructural defect density, introduced by plastic deformation on steel samples [10], [26], [27]. The work function is defined as the minimum necessary work to take an electron from the sample to a point outside of sample where its contribution from image forces are eliminated [28]. Therefore, the HD samples that have lower work function are more electrochemically reactive.

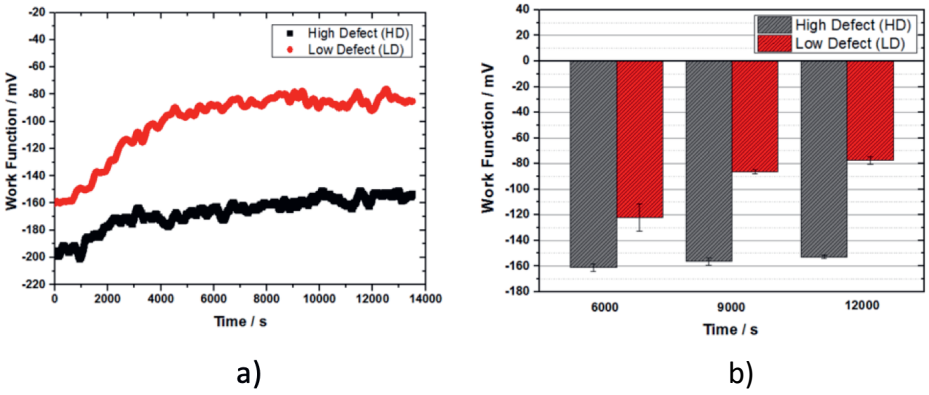

Figure 2.2 a) SKP point measurements on fresh polished samples with 550 µm stainless steel probe, at ambient temperature and 43% RH as a function of time b) Work function values measured at selected exposure times

2.3.3 Passive Layer Analysis

Chemical composition - X-ray photoelectron spectroscopy (XPS) measurements were conducted to investigate the chemical composition of the passive layers. High-resolution Fe $2p_{3/2}$ photoelectron spectra between 704 and 717 eV of both high defect (HD) and low defect (LD) samples are given in Figure 2.3. Multiplet-split fitting was applied for fitting the Fe $2p_{3/2}$ photoelectron spectra since multiplet splitting occurs due to unpaired d-orbital electrons in high-spin Fe^{+2} and Fe^{+3} species [29]. The reported optimized fitting parameters by Biesinger et al. [30] were used for the fitting of data and represented as single peaks for Fe^{0}, Fe^{+2} and Fe^{+3} after background subtraction. From the fitting analysis of the Fe 2p 3/2 and O 1/2

spectrum, composition of the passive layer consists of Fe_3O_4, γ-Fe_2O_3 and FeO(OH). Based on previous studies [31]–[35], we assumed that the passive layer consists of a bi-layered oxide layer (Fe_3O_4 and γ-Fe_2O_3) and an outer FeO(OH) layer. The differences in peak intensities show that the fractions of the oxides differ between HD and LD samples. The phase fractions are calculated according to fitting parameters and given in Table 2.2. The lower ratio of Fe^{+3}/Fe^{+2} peak intensity in HD samples indicates that the fraction of γ-Fe_2O_3 in the passive layer is lower for HD samples. The γ-Fe_2O_3 fraction in HD samples is approximately 66 % of the total passive layer versus 75% observed on the LD samples.

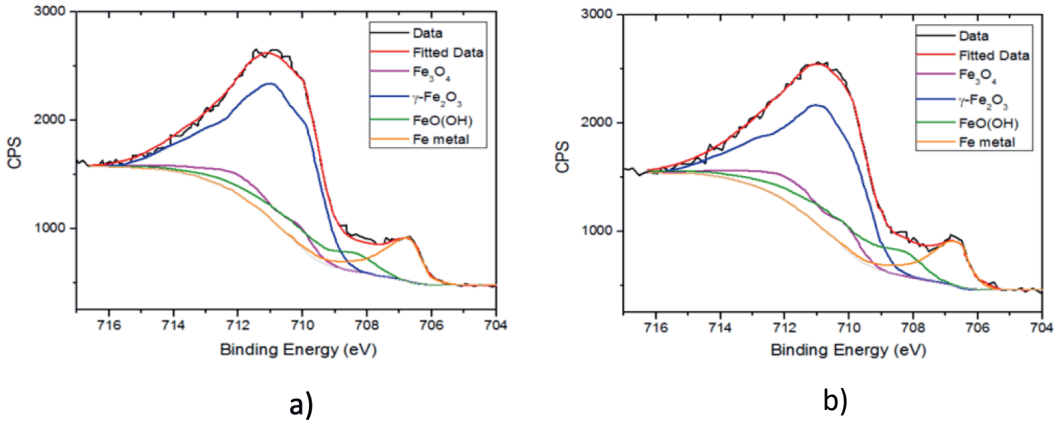

Figure 2.3 Experimental Fe 2p spectrum from the XPS measurement and corresponding fitting of the spectrum for the passivated a) LD and b) HD samples. Passive layer formed after potentiostatic polarisation for 3 hours at 0.2 V (vs. Ag/AgCl) in 0.1 M NaOH solution

	γ-Fe_2O_3(%)	Fe_3O_4(%)	FeO(OH)(%)
Low Defect (LD)	74.8	13.4	11.8
High Defect (HD)	65.9	18.8	15.3

Table 2.1 Oxide fractions of the passive layers calculated from the fitting XPS Fe 2p spectrum

Passive layer thickness – Ellipsometry measurements were conducted after potentiostatic passivation of the samples. The following optical constants of 3.18 – 3.85i for the iron substrate and 2.55 – 0.35i for the thin iron oxide film (Fe_3O_4 and γ-Fe_2O_3) were used into in the model to estimate the oxide thickness [36]. The thicknesses of the passive layers formed on HD and LD samples are 2.54 ± 0.11 and 1.67 ± 0.07 nm, respectively. From SKP results, the elucidated high-reactivity of the HD samples can explain a faster kinetic of the passive layer growth resulting in a thicker passive film.

2.3.4 Electrochemical Characterisation

Potentiodynamic polarisation (PDP) – Potentiodynamic polarisations were conducted in a 0.1 M NaOH solution, which ensures the formation of a passive layer due to alkaline environment. In Figure 2.4a, potentiodynamic polarisation curves obtained from both HD and LD samples are given. Both samples show similar curves with the main difference in the passivity current densities. It is observed that current density values are higher for

HD samples comparison to LD samples. Figure 2.4b shows the values at the potentials of 0, 0.25 and 0.5 V for both samples. For all the potentials, the current density values are approximately 1.5 times higher in HD samples than in LD samples, indicating higher electronic and/or ionic conductivity of the passive film in HD samples.

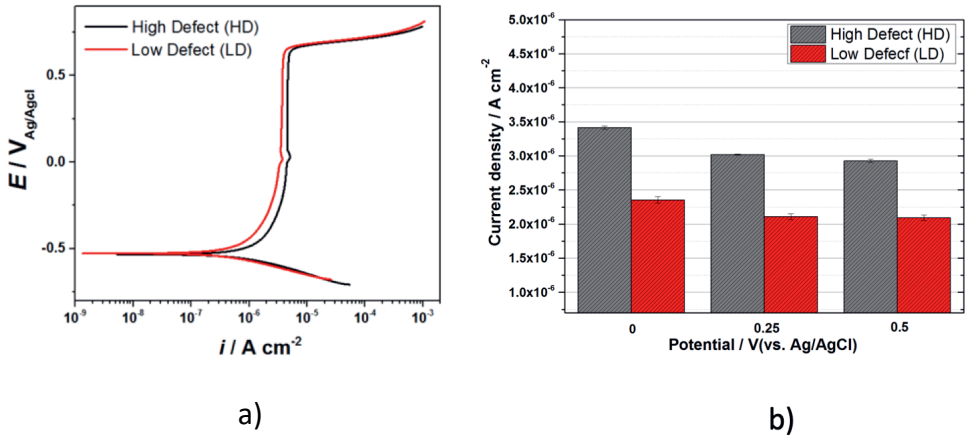

Figure 2.4 a) Potentiodynamic polarisation curves of LD and HD samples in 0.1 M NaOH solution b) Current density values from PD curves at the potentials 0, 0.25 and 0.5 V (vs. Ag/AgCl)

Potentiostatic polarisation – Figure 2.5a shows the current density transients of both samples during potentiostatic polarisation at 0.2V in 0.1 M NaOH solution. The initial current density values are associated with the charging of the double layer on both samples [37]. The sharp decrease in current density values on both samples in the first few seconds of measurements stems from the initial formation of the insulating passive

layer. The further decline in current density values is due to the growth of the passive film. After 3 hours of polarisation, the current density transients of both samples approach to steady state, at which the rates of formation and dissolution of the passive film are equal. Figure 5b shows the current density values measured after 3 hours of polarisation. It is observed that the current density of values HD samples is more than 1.5-fold higher than the one of LD samples. This suggests that the conductivity of passive film HD samples are higher than the passive film formed on LD samples, in agreement with the current density trends observed in the passive region of potentiodynamic polarisation curves.

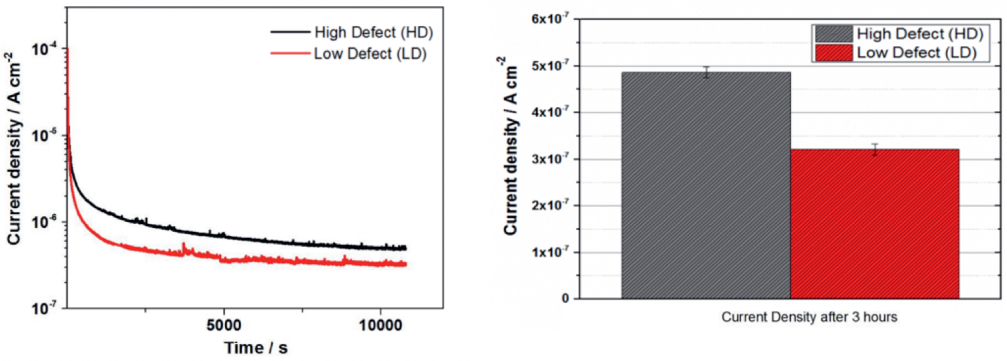

a) b)

Figure 2.5 a) Current vs time curves during potentiostatic polarisation at 0.2 V (vs. Ag/AgCl) in 0.1 M NaOH solution b) Current density values of samples after 3 hours of potentiostatic polarisation

Electrochemical Impedance Spectroscopy (EIS) – EIS data were collected after passivating both samples. The Nyquist plots of both samples (Fig. 2.6a) show that a larger arc is produced in LD samples in comparison to HD samples. It indicates the lower barrier properties of the passive layer formed on HD samples, in agreement with the current-density values observed in the passive region of the potentiodynamic polarisation curves.

The equivalent electrical circuit (EEC) fitting of EIS data was conducted with the circuit shown in Fig. 2.6b with a constant phase element (CPE) instead of a pure capacitor in line with the literature [11], [37]–[39]. The deviation from the ideal capacitive behaviour can be associated with the inhomogeneities in the passive film [40][32]. In the EEC, R_1 is attributed to the resistivity of the solution. R_2 and CPE_2 are related to resistive and capacitive behaviour of the passive film, respectively. The values obtained from the fitting are given in Table 2.2. The resistance values of passive layer R_2 are higher for LD samples in comparison to HD samples.

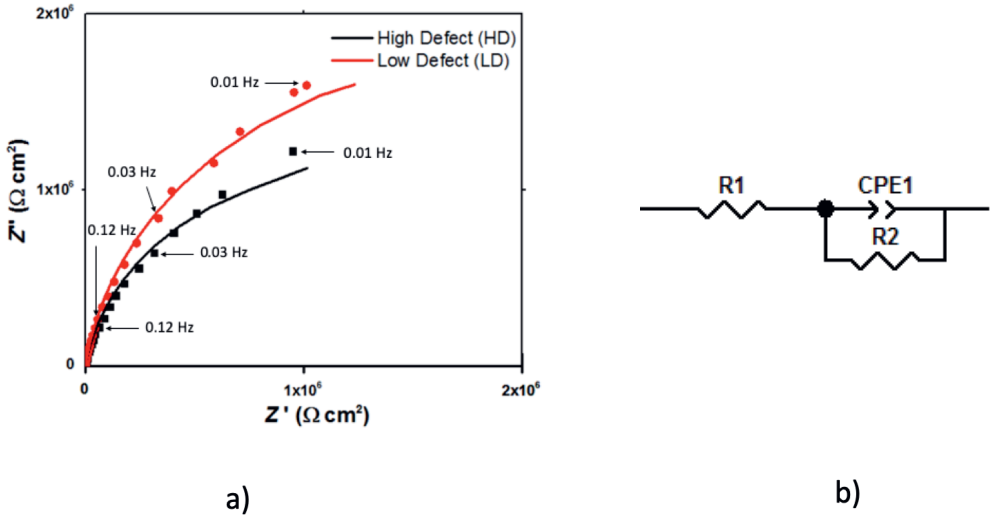

Figure 2.6 a) Nyquist plots of LD and HD samples collected after passivation with potentiostatic polarisation at 0.2 V (vs. Ag/AgCl) for 3 hours in 0.1 M NaOH solution c) Equivalent electrical circuit (EEC) used to interpret the EIS data for HD and LD samples. Solid lines show the fitted curves by the proposed equivalent circuit.

The capacitance values were calculated using the Hsu and Mansfeld formula [41]:

$$C = R^{\frac{(1-n)}{n}} Q^{\frac{1}{n}} \qquad \text{[Eqn. 2.1]}$$

The calculated values (C_1) are presented in Table 2.3. From them, the thickness of the passive film can be estimated from [42]

$$d_f = \frac{\varepsilon \varepsilon_o}{C_f} \qquad \text{[Eqn. 2.2]}$$

where d_f is the passive layer thickness, C_f is the capacitance value of the passive film, $\varepsilon = 40$ [43], [44] and ε_o are the dielectric constant of passive film on low carbon steel and permittivity in vacuum, respectively. The thickness obtained from the capacitance values is 2.21±0.01 nm and 1.87±0.01 nm for HD and LD samples, respectively. These values are in reasonable agreement with the values obtained from ellipsometry measurements.

	R_1 (Ω cm^2)	R_2 (Ω cm^2) $x10^6$	CPE_1-Q (Ω^{-1} $s^n cm^2$ $x10^{-6}$)	CPE_1-n	C_1 ($\mu F/cm^2$)
Low Defect (LD)	184±10	3.55±0.04	5.17±0.04	0.91±0.01	6.90±0.07
High Defect (HD)	176±10	2.77±0.01	4.57±0.01	0.91±0.01	5.83±0.01

Table 2.2 Equivalent circuit parameters obtained by fitting the collected EIS data of LD and HD samples

Capacitance measurements – Mott-Schottky (M-S) analysis was applied to characterize the semi-conductive properties of passive films. From M-S analysis, it is possible to quantify the defect density in an oxide film.

The total capacitance of the passive film is generally considered as the combination of two capacitors in series, representing the space charge capacitance region and the Helmholtz layer. The contribution of the Helmholtz layer on the capacitance of the passive layer (much larger than the space charge layer) is negligible due to the strong presence of the passive layer. Thus, the capacitance of passive film can be considered as the capacitor of the space charge layer. Therefore, the Mott-Schottky relationship (Eqn. 2.3) can be applied to quantify the number of defects in the passive layer:

$$\frac{1}{C^2} = 2(E - E_{FB} - kT/q)/\varepsilon\varepsilon_o q\,\mathrm{N}_d \qquad \text{[Eqn. 2.3]}$$

where T is the temperature, k the Boltzmann constant, E_{FB} the flat band potential, N_d the donor density, q the electron charge, ε_0 the permittivity of vacuum and $\varepsilon = 40$ [43] the dielectric constant of the iron oxide films formed on carbon steels. Experiments were carried out at the frequency of 1 kHz. At this value, the capacitance of iron oxide is not significantly affected by the applied frequency, and the electronic part of the space charge capacitance can be evaluated [45].

Figure 2.7 shows the Mott-Schottky plots obtained after forming the passive layer at 0.2 V for 3 hours. The positive slope in the Mott-Schottky

plots illustrates n-type semi-conductor behaviour of the passive layer [43], [46]. This slope is inversely proportional to the donor density, the higher slope meaning a lower donor density. The deviation from linearity above 0 V can be associated with the changes in passive film structure/composition [47]. The donor density values calculated from the linear slopes in the Mott-Schottky plots are given in Table 2.3. The donor density values are in the same order of magnitude with the previously reported for low carbon steels [48] and pure iron [38], [49]. It is shown that the donor density values are approximately 1.5 times higher in HD samples than in LD ones, showing that the donor density increases with an increase in the defect density. The donor population in the passive film mainly consists of oxygen vacancies and cation interstitials [50]. The lower donor density in LD samples that have a lower defect density indicates the decrease of the concentration of Fe^{+2} in the passive layer due to the oxidation of Fe^{+2} to Fe^{+3} [45]. Furthermore, the differences in flat band potential also indicate differences in the fractions of Fe_3O_4, γ-Fe_2O_3 and FeO(OH) in passive films. These are in line with a higher concentration of Fe^{+2} in the passive layers as measured with XPS when the defect density increased.

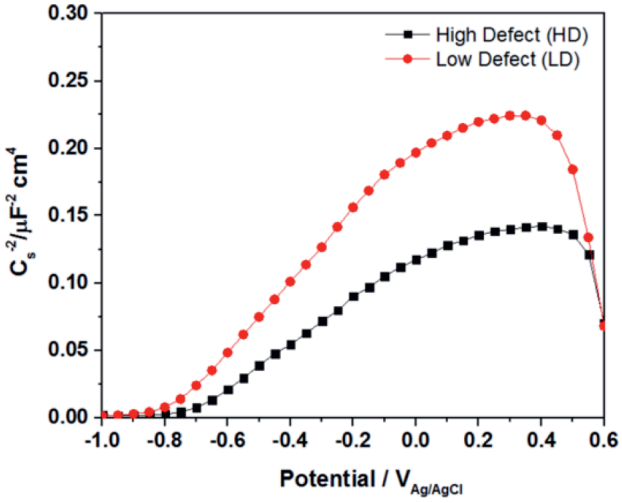

Figure 2.7 Mott-Schottky plot of samples collected after forming passive layer at 0.2 V (vs. Ag/AgCl) for 3 hours

	Donor Density N_d (10^{20} cm^{-3})	***Flat Band Potential (vs Ag/AgCl)/V***
Low Defect (LD)	4.6 ± 0.1	-0.73 ± 0.03
High Defect (HD)	6.8 ± 0.4	-0.79 ± 0.02

Table 2.3 Donor density values after passivating of 3 hours at 0.2 V (vs Ag/AgCl)

To understand the role of defect density on passive layer properties, it is required to prevent the combined effect of other microstructural features with defect density. The very low alloyed nature of the interstitial-free ferritic steels allows preventing the effect of chemical composition that might lead to alloying element segregation after cold rolling. Furthermore, the low alloying content also excludes the formation of inclusions and

different phases. In this way, these microstructural features do not play a role in the passive layer properties and only the microstructural defect density is the main influencing feature. The crystallographic orientation is also a feature that may influence the formation of the passive layer. The EBSD measurements reveal the formation of stronger preferential orientation in <111>//ND and <100>//ND in HD samples than in LD samples. However, in our other research on the effect of cold rolling in the corrosion behaviour of IF steels, it is demonstrated that the dislocation density is still the dominant feature versus the effect of the crystallographic orientation [51]. In conclusion, no other microstructural features are influencing significantly the passive layer properties than the difference in microstructural defect densities between the samples, HD and LD. The microstructural defects relate to geometrically necessary dislocation (GND) and grain boundary densities.

SKP measurements demonstrate that the sample with higher defect density (HD sample) shows more negative surface potential and a faster kinetic to achieve stability of the potential. It indicates that the significant difference of microstructural defect densities leads to higher reactivity of the surface. These results explain the formation of thicker passive films in

the HD sample measured by ellipsometry experiments. Polarisation and EIS measurements show that the barrier properties of passive film worsen with the increase in microstructural defect density in the IF steel substrate. The passive layer consists of the oxides, Fe_3O_4 and γ-Fe_2O_3 and the presence of FeO(OH) . The protective properties of the passive layer are mainly attributed to the presence of γ-Fe_2O_3. The band gap of Fe_3O_4 is 0.1 eV [52] whereas the band gap of γ-Fe_2O_3 is 2.3 eV [53]. Since the lower band gap leads to easing in electron transfer, Fe_3O_4 has significantly higher conductivity. Moreover, FeO(OH) layer has a less dense and more porous structure than γ-Fe_2O_3. Hence, it is considered that Fe_3O_4 and FeO(OH) layers do not have a significant contribution to the protection properties of the passive film. XPS analysis shows slightly lower fraction of γ-Fe_2O_3 in the passive film of the sample with higher microstructural defect density (HD sample). However, this result cannot solely explain the difference in the resistances of the passive films from the EIS analysis, with a decrease of approximately 20% on the value of the resistance for the HD sample when compared to the LD sample. Taking also into consideration that the sample with higher defect density forms a thicker passive film that usually is associated with better protective properties.

The capacitance measurements and Mott-Schottky analysis uncover differences in the donor density in the passive films. The donor density in the passive films increases with the increasing of microstructural defect density. This increase probably stems from the fact that the increase in microstructural defect density leads to higher density of active sites, i.e. kinks, jogs, inducing the formation of a defective passive layer at these active sites [11]. In terms of the electronic conductivity, the increase in donor density leads to a smaller band gap in metal oxides [54], [55], increasing the electronic conductivity by easing electron transfer. From the ionic conductivity point of view, the donors in the passive film carry ionic charges in iron oxides [56], [57], and therefore the higher donor density leads to larger ionic conductivity.

Yamamoto et al. [11] showed that most of the donors in the passive film of pure iron are oxygen vacancies instead of cation interstitials in highly deformed samples. Since the formation of passive film and the semi-conductive properties of passive film are governed by the reaction inducing the formation of oxygen vacancies, a thicker passive layer with higher donor density occurs in HD samples. On the side of LD samples, the existing donors arise due to incomplete film ageing [11] since the very low density of

substrate's microstructural defect density has a minimal effect on the formation of donors in passive film, as opposed to HD samples. Ageing the film further in time, potentiostatic polarisation would result in a passive film with a lower donor density and better passive layer properties. These results demonstrate that the microstructural defects, dislocation density and grain boundary area, influence the properties of the passive layer. Nevertheless, further investigation is necessary to differentiate and quantify the influence of the single features.

2.4 Conclusions

In this work, the role of microstructural defect density on the passive layer properties formed on IF steels are investigated in a 0.1 M NaOH solution. The sample with higher defect density presents higher reactivity indicated by the more negative work function. This results in the formation of a thicker passive layer when compared to the specimen with lower defect density. XPS measurements on passive layers formed by potentiostatic polarisation, show that the passive layer consists of Fe_3O_4,γ-Fe_2O_3 and FeO(OH), regardless of the defect density. However, the volume fraction of γ-Fe_2O_3 passive film slightly decreases with increasing defect density. Electrochemical results from potentiodynamic polarisation and EIS

experiments indicate that the passive film of the higher defective sample has worse barrier properties. In conclusion, the presence of higher microstructural defect density on the IF steel substrate enhances the growth of thicker but highly defective passive layers.

2.5 References

[1] A. D.R., *Strain Hardening and Annealing*. Boston, MA: The Science and Engineering of Materials, 1996.

[2] S. Zaefferer, J. Ohlert, and W. Bleck, "A study of microstructure, transformation mechanisms and correlation between microstructure and mechanical properties of a low alloyed TRIP steel," *Acta Mater.*, vol. 52, no. 9, pp. 2765–2778, 2004.

[3] K. L. Murty, M. D. Mathew, Y. Wang, V. N. Shah, and F. M. Haggag, "Nondestructive determination of tensile properties and fracture toughness of cold worked A36 steel," *Int. J. Press. Vessel. Pip.*, vol. 75, no. 11, pp. 831–840, 1998.

[4] J. P. Chu, J. M. Rigsbee, G. Banaś, and H. E. Elsayed-Ali, "Laser-shock processing effects on surface microstructure and mechanical properties of low carbon steel," *Mater. Sci. Eng. A*, vol. 260, no. 1–2, pp. 260–268, 1999.

[5] W. Karlsen and S. Van Dyck, "The effect of prior cold-work on the deformation behaviour of neutron irradiated AISI 304 austenitic stainless steel," *J. Nucl. Mater.*, vol. 406, no. 1, pp. 127–137, 2010.

[6] S. Takahashi, J. Echigoya, T. Ueda, X. Li, and H. Hatafuku, "Martensitic

transformation due to plastic deformation and magnetic properties in SUS 304 stainless steel," *J. Mater. Process. Technol.*, vol. 108, no. 2, pp. 213–216, 2001.

[7] M. Takahashi and H. K. D. H. Bhadeshia, "Model for transition from upper to lower bainite," *Mater. Sci. Technol.*, vol. 6, no. 7, pp. 592–603, 1990.

[8] Jinlong Lv and L. Hongyun, "Electrochemical investigation of passive film in pre-deformation AISI 304 stainless steels," *Appl. Surf. Sci.*, vol. 263, no. 0, pp. 29–37, 2012.

[9] J. Lv and H. Luo, "Effects of strain and strain-induced α'-martensite on passive films in AISI 304 austenitic stainless steel," *Mater. Sci. Eng. C*, vol. 34, no. 1, 2014.

[10] J. Lv, W. Guo, and T. Liang, "The effect of pre-deformation on corrosion resistance of the passive film formed on 2205 duplex stainless steel," *J. Alloys Compd.*, vol. 686, pp. 176–183, 2016.

[11] T. Yamamoto, K. Fushimi, S. Miura, and H. Konno, "Influence of Substrate Dislocation on Passivation of Pure Iron in pH 8 . 4 Borate Buffer Solution," *J. Electrochem. Soc.*, vol. 157, no. 7, pp. 231–237, 2010.

[12] X. Y. Wang and D. Y. Li, “Mechanical and electrochemical Behaviour of nanocrystalline surface of 304 stainless steel,” *Electrochim. Acta*, vol. 47, no. 24, pp. 3939–3947, 2002.

[13] B. L. Adams and J. Kacher, “EBSD-based microscopy: Resolution of dislocation density,” *Comput. Mater. Contin.*, vol. 14, no. 3, pp. 183–194, 2009.

[14] F. Nye, “Some geometrical relations in dislocated crystals,” *Acta Metall.*, vol. 1, pp. 153–162, 1953.

[15] F. Bachmann, R. Hielscher, and H. Schaeben, “Texture analysis with MTEX- Free and open source software toolbox,” *Solid State Phenom.*, vol. 160, pp. 63–68, 2010.

[16] J. Jiang, T. B. Britton, and A. J. Wilkinson, “Measurement of geometrically necessary dislocation density with high resolution electron backscatter diffraction: Effects of detector binning and step size,” *Ultramicroscopy*, vol. 125, pp. 1–9, 2013.

[17] L. A. I. Kestens and H. Pirgazi, “Texture formation in metal alloys with cubic crystal structures,” *Mater. Sci. Technol. (United Kingdom)*, vol. 32, no. 13, pp. 1303–1315, 2016.

[18] B. B. Hutchinson, “Deformation Microstructures and textures in

steels," *Philos. Trans. R. Soc. Lond. Ser. Math. Phys. Eng. Sci*, vol. 357, pp. 1471–1485, 1999.

[19] R. K. Ray, J. J. Jonas, and R. E. Hook, "Cold rolling and annealing textures in low carbon and extra low carbon steels," *Int. Mater. Rev.*, vol. 39, no. 4, pp. 129–172, Jan. 1994.

[20] Y. Inokuti and R. D. Doherty, "Transmission kossel study of the structure of compressed iron and its recrystallization behaviour," *Acta Metall.*, vol. 26, no. 1, pp. 61–80, 1978.

[21] B. Hutchinson, "Deformation Microstructures and Textures in Steels," *Philos. Trans. R. Soc. Lond. Ser. Math. Phys. Eng. Sci*, vol. 357, no. 1756, 1999.

[22] B. Hutchinson, "Nucleation of recrystallisation," *Scr. Met. Mater.*, vol. 27, no. 11, pp. 1471–1475, 1992.

[23] R. W. Cahn, "Recrystallization of single crystals after plastic bending," *J. Inst. Met.*, vol. 76, no. 2, p. 121, 1949.

[24] R. W. Cahn, "Internal Strains and Recrystallization," *Prog. Met. Phys.*, vol. 2, pp. 151–176, 1950.

[25] Ö. Özkanat, B. Salgin, M. Rohwerder, J. M. C. Mol, H. De Wit, and H. Terryn, "Scanning Kelvin probe study of (Oxyhydr)oxide surface of

aluminum alloy," *J. Phys. Chem. C*, vol. 116, no. 2, pp. 1805–1811, 2012.

[26] W. Li, M. Cai, Y. Wang, and S. Yu, "Influences of tensile strain and strain rate on the electron work function of metals and alloys," *Scr. Mater.*, vol. 54, no. 5, pp. 921–924, 2006.

[27] A. Nazarov and D. Thierry, "Application of Volta-potential mapping to determine metal surface defects," *Electrochim. Acta*, vol. 52, no. 27 SPEC. ISS., pp. 7689–7696, 2007.

[28] M. Rohwerder and F. Turcu, "High-resolution Kelvin probe microscopy in corrosion science: Scanning Kelvin probe force microscopy (SKPFM) versus classical scanning Kelvin probe (SKP)," *Electrochim. Acta*, vol. 53, no. 2, pp. 290–299, 2007.

[29] R. P. Gupta and S. K. Sen, "Calculation of multiplet structure of core *p* -vacancy levels," *Phys. Rev. B*, vol. 10, no. 1, pp. 71–77, 1974.

[30] M. C. Biesinger, B. P. Payne, A. P. Grosvenor, L. W. M. Lau, A. R. Gerson, and R. S. C. Smart, "Resolving surface chemical states in XPS analysis of first row transition metals, oxides and hydroxides: Cr, Mn, Fe, Co and Ni," *Appl. Surf. Sci.*, vol. 257, no. 7, pp. 2717–2730, 2011.

[31] M. P. Strehblow H, "X-ray photoelectron spectroscopy in corrosion

research. In: Marcus P, Mansfeld F (eds) Analytical methods in corrosion science and engineering.," *CRC Press Taylor Fr.*, 2006.

[32] L. Freire, X. R. Nóvoa, M. F. Montemor, and M. J. Carmezim, "Study of passive films formed on mild steel in alkaline media by the application of anodic potentials," *Mater. Chem. Phys.*, vol. 114, no. 2–3, pp. 962–972, 2009.

[33] I. V. Sieber, H. Hildebrand, S. Virtanen, and P. Schmuki, "Investigations on the passivity of iron in borate and phosphate buffers, pH 8.4," *Corros. Sci.*, vol. 48, no. 11, pp. 3472–3488, 2006.

[34] Y. Li and Y. F. Cheng, "Passive film growth on carbon steel and its nanoscale features at various passivating potentials," *Appl. Surf. Sci.*, vol. 396, pp. 144–153, 2017.

[35] H. H. Strehblow, "Passivity of Metals Studied by Surface Analytical Methods, a Review," *Electrochim. Acta*, vol. 212, pp. 630–648, 2016.

[36] G. O. and N. S. K. Kudo, T. Shibata, "Ellipsometric and radiotracer measurements of the passive oxide film on fe in neutral solution," *Corros. Sci.*, vol. 8, pp. 809–814, 1968.

[37] K. Yanagisawa, T. Nakanishi, Y. Hasegawa, and K. Fushimi, "Passivity of Dual-Phase Carbon Steel with Ferrite and Martensite Phases in pH

8.4 Boric Acid-Borate Buffer Solution," *J. Electrochem. Soc.*, vol. 162, no. 7, pp. C322–C326, 2015.

[38] Y. Takabatake, K. Fushimi, T. Nakanishi, and Y. Hasegawa, "Grain-Dependent Passivation of Iron in Sulfuric Acid Solution," *J. Electrochem. Soc.*, vol. 161, no. 14, pp. C594–C600, 2014.

[39] K. Fushimi, Y. Takabatake, T. Nakanishi, and Y. Hasegawa, "Microelectrode techniques for corrosion research of iron," *Electrochim. Acta*, vol. 113, pp. 741–747, 2013.

[40] M. Büchler, P. Schmuki, and H. Böhni, "Iron passivity in borate buffer: Formation of a deposit layer and its influence on the semiconducting properties," *J. Electrochem. Soc.*, vol. 145, no. 2, pp. 609–614, 1998.

[41] C. H. Hsu and F. Mansfeld, "Concernng the conversion of the constant phase element parameter Y_0 into a capacitance," *Corrosion*, vol. 57, no. 9, pp. 747–748, 2001.

[42] A. J. Bard and L. R. Faulkner, *Electrochemical Methods: Fundamentals and Applications*, 2nd. ed. John Wiley & Sons, 2001.

[43] K. Azumi, "Mott-Schottky Plot of the Passive Film Formed on Iron in Neutral Borate and Phosphate Solutions," *J. Electrochem. Soc.*, vol. 134, no. 6, p. 1352, 1987.

[44] K. Azumi, T. Ohtsuka, and N. Sato, “Impedance of Iron Electrode Passivated in Borate and Phosphate Solutions,” *J. Electrochem. Soc.,* vol. 27, no. 5, pp. 382–392, 1986.

[45] S. J. Ahn and H. S. Kwon, “Effects of solution temperature on electronic properties of passive film formed on Fe in pH 8.5 borate buffer solution,” *Electrochim. Acta*, vol. 49, no. 20, pp. 3347–3353, 2004.

[46] J. H. Kennedy and K. W. Frese, “Flatband Potentials and Donor Densities of Polycrystalline α -Fe2O3 Determined from Mott-Schottky Plots,” *J. Electrochem. Soc.*, vol. 125, no. 5, pp. 723–726, 1978.

[47] E. M. A. Martini and I. L. Muller, “Characterisation of the film formed on iron borate solution by electrochemical impedance spectroscopy,” *Corros. Sci.*, vol. 42, no. 3, pp. 443–454, 2000.

[48] M. Sánchez, J. Gregori, C. Alonso, J. J. García-Jareño, H. Takenouti, and F. Vicente, “Electrochemical impedance spectroscopy for studying passive layers on steel rebars immersed in alkaline solutions simulating concrete pores,” *Electrochim. Acta*, vol. 52, no. 27 SPEC. ISS., pp. 7634–7641, 2007.

[49] S. P. Harrington, F. Wang, and T. M. Devine, “The structure and

electronic properties of passive and prepassive films of iron in borate buffer," *Electrochim. Acta*, vol. 55, no. 13, pp. 4092–4102, 2010.

[50] J. Liu and D. D. Macdonald, "The Passivity of Iron in the Presence of Ethylenediaminetetraacetic Acid. II. The Defect and Electronic Structures of the Barrier Layer," *J. Electrochem. Soc.*, vol. 148, no. 11, p. B425, 2001.

[51] A.Yilmaz, C.Örnek, K.Traka, J. Sietsma, Y. Gonzalez-Garcia"Combining surface Volta-potential with electrochemical measurements to investigate the role of cold working on corrosion Behaviour of interstitial free (IF) steels," *To be Publ.*

[52] R. M. Cornell and U. Schwertmann, *The iron oxides; Structure Properties, Reactions, Occurrences and Uses*. 2003.

[53] L. Hamadou, A. Kadri, and N. Benbrahim, "Characterisation of passive films formed on low carbon steel in borate buffer solution (pH 9.2) by electrochemical impedance spectroscopy," *Appl. Surf. Sci.*, vol. 252, no. 5, pp. 1510–1519, 2005.

[54] J. Wang *et al.*, "Oxygen vacancy induced band-gap narrowing and enhanced visible light photocatalytic activity of ZnO," *ACS Appl. Mater. Interfaces*, vol. 4, no. 8, pp. 4024–4030, 2012.

[55] S. A. Ansari, M. M. Khan, M. O. Ansari, S. Kalathil, J. Lee, and M. H. Cho, “Band gap engineering of CeO2 nanostructure using an electrochemically active biofilm for visible light applications,” *RSC Adv.*, vol. 4, no. 32, pp. 16782–16791, 2014.

[56] T. Sato, Norio ; Noda, “Ion Migration in Anodic Barrier Oxide Films on Iron in Acidic Phosphate Solutions,” *Electrochim. Acta*, vol. 22, no. 839–843, 1976.

[57] S. C. Hendy, N. J. Laycock, and M. P. Ryan, “Atomistic Modeling of Cation Transport in the Passive Film on Iron and Implications for Models of Growth Kinetics,” *J. Electrochem. Soc.*, vol. 152, no. 8, p. B271, 2005.

CHAPTER 3

Combining surface Volta-potential with electrochemical measurements to investigate the role of cold working on corrosion behaviour of IF steels

This chapter is based on a scientific paper:

A. Yilmaz, C. Örnek, K. Traka, J. Sietsma, Y. Gonzalez-Garcia, (2021) Understanding the effect of cold rolling on corrosion behaviour of interstitial free (IF) ferritic steels by SKPFM and electrochemical measurements. (In preparation)

Abstract

*This work investigates the role of cold-rolling on the corrosion behaviour of interstitial free (IF) steels. The microstructures of hot- and cold-rolled samples (dislocation density, grain boundary area and texture) were investigated wit*h *electron backscatter diffraction analysis. Scanning Kelvin probe force microscopy (SKPFM) measurements show increased Volta-potential gradients between grains with different crystallographic orientations after cold-rolling, while no Volta-potential gradients were observed at grain boundary areas. The potentiodynamic polarisation measurements show a higher corrosion rate of cold-rolled material in a 0.1M HCl solution, stemming from the higher micro-galvanic interaction between grains due to the increase in dislocation density.*

Keywords: Interstitial free (IF) steels, dislocation density, corrosion rate, Volta-potential, SKPFM, cold-rolling

3.1 Introduction

A wide range of industries has applied cold working on IF steels mainly in efforts to improve their mechanical properties such as hardness and strength [1]–[3]. Generally, the improvement in mechanical properties of IF steels is attributed to an increase in dislocation density, a phenomenon known as work hardening resulting in impeding the movement of dislocations. The relationship between cold rolling and mechanical properties has been extensively studied in various ferrous materials such as pure iron [4], [5], low alloyed steels [6], [7], and different types of stainless steels [8]–[11]. Nevertheless, the relationship between cold rolling and corrosion behaviour of steels is still yet to be deepened. The previous studies reported varying results on the relationship between cold rolling and corrosion properties of steels [12]–[17].

Jinlong et al. [15] reported higher corrosion rates of pure iron in 0.5 M H_2SO_4 solution when cold-rolled by 95.83% thickness reduction. However, they also reported that the cold-rolling leads to a significant grain size refinement and texture formation, besides increasing the dislocation density. This leads to the interaction of the dislocation density, grain size, and grain's crystallographic orientation on corrosion resistance instead of

the sole effect of the increase in dislocation density. In contrast, Foroulis and Uhlig [17] studied the role of cold rolling on the corrosion behaviour of pure iron and low-alloyed steels in 0.1 M HCl solution. They observed no difference in corrosion rate between the annealed and cold-rolled iron. Yet, they observed a higher corrosion rate in cold-rolled low alloy steels than the annealed ones. The increase in corrosion rate is attributed to the formation of carbides and nitrides with cold-rolling, dominating the effect of other microstructural changes (dislocation density, crystallographic orientation and grain size) on corrosion rate. Another study investigated the effect of plastic deformation on the corrosion rate of iron and low-alloyed steels in deaerated H_2SO_4 and HCl solutions [16]. It was observed that the corrosion rate of both iron and low-alloyed steels is higher for cold-rolled materials than the annealed ones, attributed to more active sites formed due to solely increase in dislocation density. These varying reports in the literature show that there is no direct relationship established between cold-rolling and corrosion resistance. This mainly stems from several microstructural features changes during cold rolling depending on the substrate and cold-rolling processes. These microstructural features are namely dislocation density, grain size/boundary area, grain orientation, phase transformation,

and alloy segregation. These features have a complex interaction with each other on corrosion behaviour.

Understanding the effect of cold rolling on the corrosion behaviour of low-alloyed steels requires knowledge about the individual behaviour of microstructural features, which might change when the material is subjected to cold-rolling. The microstructure has crucial importance in determining the corrosion resistance of IF steels, as any microstructural heterogeneity can impose susceptibility to corrosion. The conventional electrochemical methods' resolution limits the study of the correlation between singular microstructure features and corrosion response. The SKPFM is a powerful method that offers nanoscale resolution and can provide information about the electronic properties of the surface (Volta-potential). High Volta-potential suggests a high electrochemical nobility or vice versa, and, therefore, Volta-potential can be used as a reliable parameter reflecting corrosion susceptibility of material [18]–[21]. The decrease in the Volta-potential is considered as an increase in propensity for electron transfer, leading to the enhancement of electrochemical reactions. This information can be associated with the local reactivity of metals. In general, Volta-potential differences are indicative of possible

micro-galvanic couplings in the microstructure. The possibilities of combining SKPFM and EBSD analyses to understand the local effect of cold-rolling in duplex stainless steels were investigated by Örnek et al. [12]. It was shown that the degree of galvanic couplings in between phases changes with cold-rolling. Furthermore, the local extremes differences in Volta-potential was reported after cold-rolling, leading to localised attacks in high relative humidity conditions due to the formation of strong micro-galvanic couplings in these sites.

This work investigates how the microstructural changes induced by cold-rolling affect the local reactivity and general corrosion behaviour. The interstitial free (IF) ferritic steels are employed due to their low alloyed nature, minimizing the effect of high alloying elements, secondary phases, and inclusions on corrosion behaviour. The differences in microstructural features of hot and cold-rolled IF steels are studied by electron backscatter diffraction (EBSD) analysis. The differences in Volta-potential are investigated by SKPFM measurements. The general corrosion resistance of samples is measured by potentiodynamic polarisation in a 0.1 M HCl solution.

3.2 Experimental

3.2.1 Material

The material investigated was interstitial-free (IF) ferritic steel (provided by Tata Steel, The Netherlands) with the chemical composition shown in Table 3.1. The cold-rolling samples were subsequent to the hot deformation of a former sheet, namely with a thickness reduction of approximately 77.6 %. The cold-rolled and hot-rolled sheets were laser-cut to the dimensions of 4 cm x 4 cm. The thicknesses for cold-rolled and hot-rolled samples are 0.76 mm and 3.4 mm, respectively.

	Fe	C	Mn	Al	N	Ti	S	Cr
wt%	bal.	0.002	0.095	0.05	0.002	0.045	0.006	0.02

Table 3.1 Chemical composition of the as received IF steel

3.2.2 Microstructure Characterisation

The geometrically necessary dislocation density, grain size/boundary area, and crystallographic orientation were determined by EBSD. Before EBSD analysis, the samples were mechanically ground with the automated grinding- and polishing machine (Struers Rotopol 31/ Rotoforce 4, Struers A/S) with abrasive SiC papers 80 to 4000 grit. All grinding steps were conducted at the constant disc rotation frequency of 40 rpm and applied

pressure of 0.5 MPa. After grinding, the samples were polished with diamond slurries with particle sizes of 3 μm and 1 μm (Struers DiaDuo-2). The samples were finally polished with standard colloidal silica suspension with 0.04 μm particle size. The samples were ultrasonically cleaned in ethanol for 10 minutes. Then, the samples were rinsed with ethanol and dried with compressed air. The high-resolution EBSD measurements were obtained with a JEOL JSM 6500F FEG-SEM microscope with an EDAX/TSL detector. The measurements were conducted at a working distance of 17 mm. The same step-size of 0.5 μm was used for all measurements. The reason to perform a high-resolution measurement with the same step size also on a recrystallized microstructure is simply due to the apparent effect of the step size on calculating local misorientations (boundaries) and particularly on the dislocation content [22], [23]. The EBSD data's post-processing was performed with TSL-OIM (version 7.3) software and in Matlab using MTEX routines [24]. The Geometrically Necessary Dislocation (GND) density calculation was performed with the TSL-OIM software using the function described in [25]. The method approximates the density of GNDs (ρ_{GND}) by its relation to the dislocation tensor (known as Nye's tensor [23]), as it was initially proposed by Nye [23]. The dislocation tensor is

calculated as the tensorial summation of the lattice curvature (i.e., orientation's $curl$) and the elastic strain tensor's divergence.

3.2.3 Scanning Kelvin Probe Force Microscopy (SKPFM) measurements

Scanning Kelvin Probe Force Microscopy (SKPFM) measurements were conducted to determine the nobility differences within the samples depending on their microstructure. A Dimension Icon atomic force microscopy from Bruker was employed. Before experiments, the samples were ground and polished, as explained in Section 3.2.2. SKPFM measurements were conducted in the frequency modulation (FM-KPFM) mode, in which obtaining a Volta-potential map took approximately 10 min. The pixel resolution and scan rate were 256 x 256 and 0.6 Hz, respectively. The measurements were conducted in ambient air at a temperature of 22.4 °C and ~43 % relative humidity. The measurements were performed on the same day consequently to avoid changes in ambient conditions. An OSCM-Pt R3 n-Si doped Pt-coated tip from Bruker was employed for the measurements. The sample was biased with a voltage of 6 V in all measurements. The inversion of Volta-potential maps was not applied and to meet the polarity convention of electrochemistry, showing high potentials as cathodic and low values as active [18]. It should be noted

that the measured Volta-potentials in the air do not reflect the true corrosion potential in an electrolyte but rather provides a local characterisation of the microstructure. However, anodic potentials measured in ambient air suggest higher electron reactivity as opposed to cathodic regions.

The Volta-potential is a surface and material-intrinsic property, which exists in all environments. So, a local description of the Volta-potential can provide a unique insight into understanding Localised corrosion, which, by other means, may not be accessible. More detailed information about the fundamental meaning of the Volta-potential and its relevance to corrosion can be found elsewhere [12], [18], [26]–[31]. The used tip was calibrated, as described elsewhere [18]. The software Gwydion V 2.55 was used for analysing the data. The measurements were repeated three times on different regions in the microstructure to ensure reproducibility. The average Volta-potential values for every grain, which will be given in section 3.3.2, are calculated by averaging the Volta-potential in each grain.

3.2.4 Electrochemical Measurements

Potentiodynamic polarisation was applied to determine the corrosion rate of the hot-rolled and cold-rolled specimens. Before conducting electrochemical measurements, the samples were embedded in non-conductive epoxy resin (Struers ClaroCit) that was cured for 1 hour under the pressure of 2 bars. The embedded samples were mechanically ground with abrasive SiC grinding papers from 80 to 4000 grit. Afterwards, the samples were polished with diamond suspension pastes with particle sizes of 3 μm and 1 μm until obtaining a mirror-like surface. Alcohol-based diamond pastes (Struers DP-Suspension a) were employed to minimize the effect of polishing on electrochemical behaviour. Polishing cloths Struers DP-Mol and Struers DP-Nap were used for 3 μm and 1 μm polishing, respectively. The samples were cleaned in an ultrasonic bath for 10 min in ethanol and dried with compressed air before the electrochemical measurements.

The potentiodynamic polarisation measurements were conducted in a 0.1 M HCl solution. The solution was prepared at room temperature with distilled water. A conventional three-electrode cell consisting of a working electrode (samples), a counter electrode (a graphite rod), and a reference

electrode (Ag/AgCl, KCl (sat)) was employed. A Biologic SP 300 potentiostat was used for the measurements. Before potentiodynamic polarisation, open circuit potential (OCP) was measured for 1800 seconds, at which stabilization was achieved. Subsequently, PDP was conducted in the potential range from -0.25 V to 0.25 V (vs. OCP) with a scan rate of 0.167 mV/s. The corrosion potential and current were determined by applying Tafel fit via EC-Lab® v11.33 software. The measurements were repeated three times to estimate the uncertainty of the experiments.

3.3. Results & Discussion

3.3.1 Microstructure Characterisation

EBSD measurements were conducted to obtain the spatially resolved crystallographic orientations and thenceforth to assess the defect density through the local misorientations. EBSD measurements were performed in various longitudinal sections and particularly in Rolling Direction (RD) - Transverse Direction (TD) (the surface on which the electrochemical and SKPFM measurements were conducted) and in Rolling Direction (RD) - Normal Direction (ND). The reason for the multiple measurements and the different cross-sections is to investigate the extent of reproducibility, especially deformation heterogeneities through the thickness or along the

sample's transverse direction could yield different results. Heterogeneities can be present both after hot-rolling, mainly since the microstructure results from austenite recrystallization and phase transformation, which are typically not homogeneous phenomena after cold-deformation due to the macroscopic deformation's boundary conditions. In Figure 3.1 only the two samples that were equally resolved are shown for comparison purposes.

Figures 3.1a and 3.1b show that the crystal direction along the sample's Normal Direction (ND) is shown (spatially resolved) for hot and cold-rolled samples, respectively. The hot-rolled samples consist of equiaxed grains, and orientation gradients are absent, indicating a recrystallized (almost deformation-free) state. Additionally, a mild preference of crystallographic orientation is observed, consisting of components with plane normals <111>//ND and <100>//ND. Furthermore, it is also shown in figures 3.1a and 3.1b that the microstructure has identified orientations in BCC crystal structure, and hence only the ferritic phase has been identified.

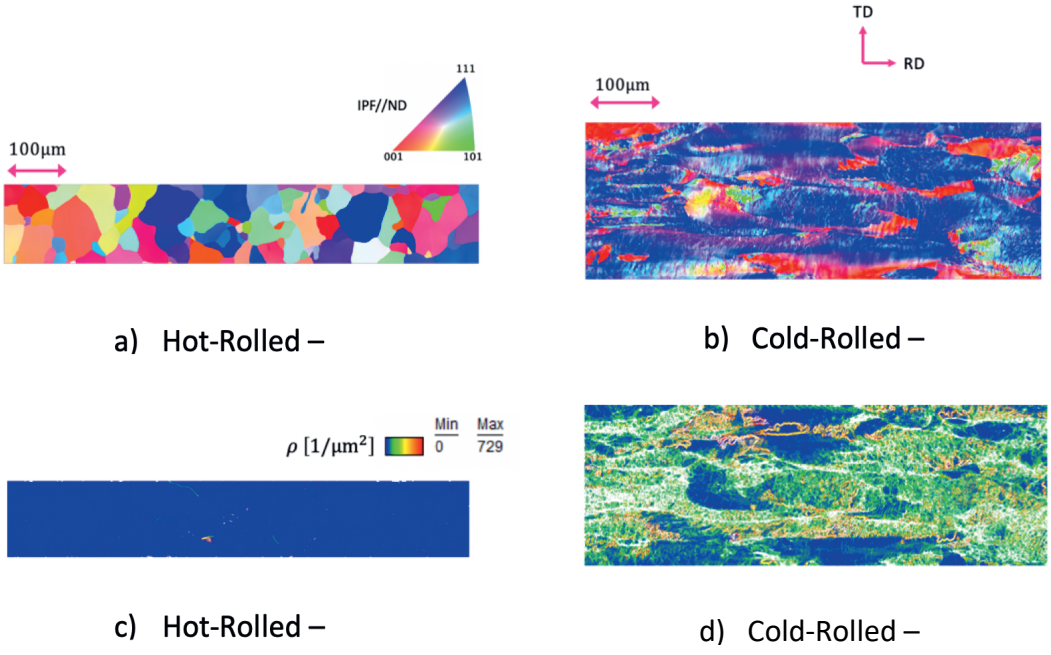

Figure 3.2 Microstructures obtained through EBSD for the samples. The maps show the spatially resolved crystal directions parallel to the sheet's normal direction (ND) in accord with the conventional colour coding with Inverse Pole Figure (IPF) for a) the Cold-Rolled sample and b) the Hot-Rolled sample. The maps in c) and d) show the Geometrically Necessary Dislocations (GND) calculated for a maximum angle $10°$ *and up to the* 3^{rd} *neighbour pixel, for the Cold and Hot-Rolled samples, respectively. The GNDs are shown in the same colour bar. The two EBSD scans were measured in the same resolution– namely* $0.5\mu m$

In figures 3.1c and 3.1d, the GND maps are shown for the hot- and cold-rolled samples, respectively. It was observed that dislocations in hot-rolled samples were homogenously distributed and very small in number. In contrast, the cold-rolled samples exhibit a much larger dislocation content with pronounced topological heterogeneities. The largest GND

density is found at highly distorted regions while other regions do not contain large orientation gradients. The calculated average dislocation density values from GND maps are 147 ± 14 and 3.6 ± 0.4 μm^{-2} for the cold- and hot-rolled samples, respectively. This shows that the GND values are two orders of magnitude higher in the cold-rolled samples than the hot-rolled samples. It should be mentioned that the EBSD gives information for the spatially resolved crystallographic orientation. Hence, only the dislocations related to the orientation gradient can be quantified, whereas the total defect density consists of structural dislocations (GNDs) and Statistically Stored Dislocations (SSD). The only portion of SSDs which can be detected from the EBSD refers to opposite dislocations that were spatially separated enough to be captured in adjacent pixels instead of cancelling out [22], [23].

As expected from the aforementioned GND calculations, the grain boundary density in the cold-rolled samples is much more pronounced than in the hot-rolled samples. The cold-rolled samples consist of large grain boundary density, particularly low-angle-grain-boundaries (LAGBs). The hot-rolled samples mainly contain a high-angle grain boundary with lower density in comparison to cold-rolled samples. This is expected since, as said

earlier, the hot-rolled sample seems to be fully recrystallized, and hence the only misorientations would be deduced from the regions that two grains meet. Oppositely, the cold-rolled samples exhibit much larger orientation gradients (as indicated from the GND density) due to the immense deformation energy (here expressed as structural dislocations) that is stored. Defining as a threshold minimum angle to consider a HAGB the value of $15°$, the calculated average HAGB per unit length in the hot-rolled samples was 0.058 ± 0.002 μm^{-1}. In contrast, the average LAGB per unit length in the hot-rolled samples was 0.012 ± 0.004 μm^{-1}. In contrast to this, the cold-rolled samples have an average HAGB per unit length was 0.304 ± 0.004 μm^{-1}, and the average LAGB per unit length in the cold-rolled samples was 4.9 ± 0.3 μm^{-1}.

Regarding the crystallographic texture shown in figure 3.2, this corresponds to the most extensive areas we scanned due to the insufficient number of orientations present in the scans shown in Fig. 3.1 and the variability that can occur due to deformation heterogeneities along the transverse and normal direction. Hence, we decided to present the crystallographic texture, which was the most representative of our materials' crystal orientations. To quantify the crystallographic texture in

the samples, we calculated the Orientation Distribution Function (ODF) [32] and MTEX [24] routine was employed using a de La Valle Poussin kernel with a half-width of $10°$. From Fig. 3.2, it is clear that both sheets exhibit preferred crystallographic orientations. The cold-rolled samples are characterized by a strong α fibre (components with a plane normal <110>//RD) and thenceforth γ fibre (components with a plane normal <111>//ND) and θ fibre (components with a plane normal <100>//ND). The hot-rolled samples exhibit a milder crystallographic texture yet with relatively similar preferred components (the only difference is a more pronounced maximum in a particular element of α fibre, namely {112} <110>). Although the two sheets have a more or less similar distribution of preferred crystal orientations, the intensity (magnitude of preference concerning the random texture) of the overall texture is nonetheless different. That is due to the origin of the texture in each microstructure. While the cold-rolled exhibits these preferences due to crystal rotations during rolling, the hot-rolled gives rise to these components either due to austenite recrystallization and afterwards phase transformation or phase transformation while austenite is still deformed [32]. The exact

phenomenon responsible for the crystallographic texture is not in the scope of the present work.

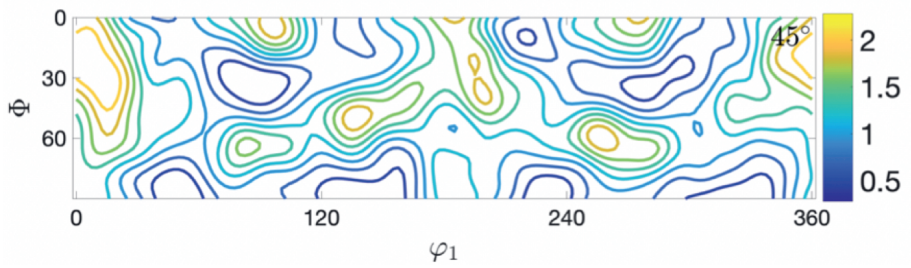

a) Hot-rolled – ODF (from large

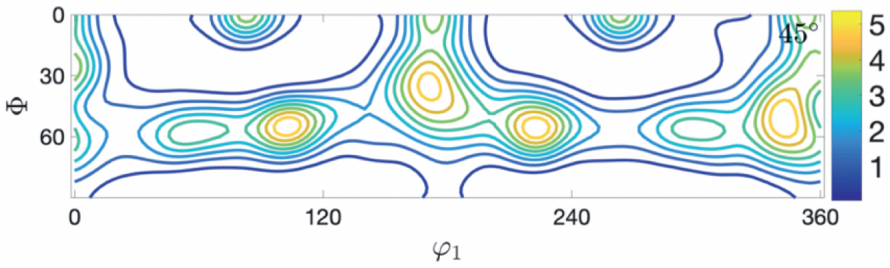

b) Cold-rolled – ODF (from large

Figure 3.3 Texture calculated from EBSD measurements in Large Scanned Areas of the samples used in the analysis. The texture is represented as Orientation Distribution Function (ODF) with a half-width of 10° for a) the Cold-Rolled and b) the Hot-Rolled material

3.3.2 Volta-potential assessment

The Volta-potential and EBSD Inverse Pole Figure (IPF) maps of a hot-rolled sample are given in Fig. 3.3a and 3.3b. The Volta-potential varies depending on the crystallographic orientation in hot-rolled samples. The Volta-

potential of the (001) plane exhibits distinctively more noble (cathodic) behaviour than the one in (111) and (101) planes. In contrast, no difference in terms of Volta-potential is observed between grains in (111) and (101) planes. This indicates a lower electrochemical activity of (001) than (111) and 101 planes in the hot-rolled samples. This is in agreement with previously reported by Fushimi et al. [33], who investigated the reactivity of several planes of iron samples with SECM (scanning electrochemical microscopy) in sulphuric acid solution and reported the lower reactivity of passive layer formed on grains in (001) in comparison to (111) and (101) planes.

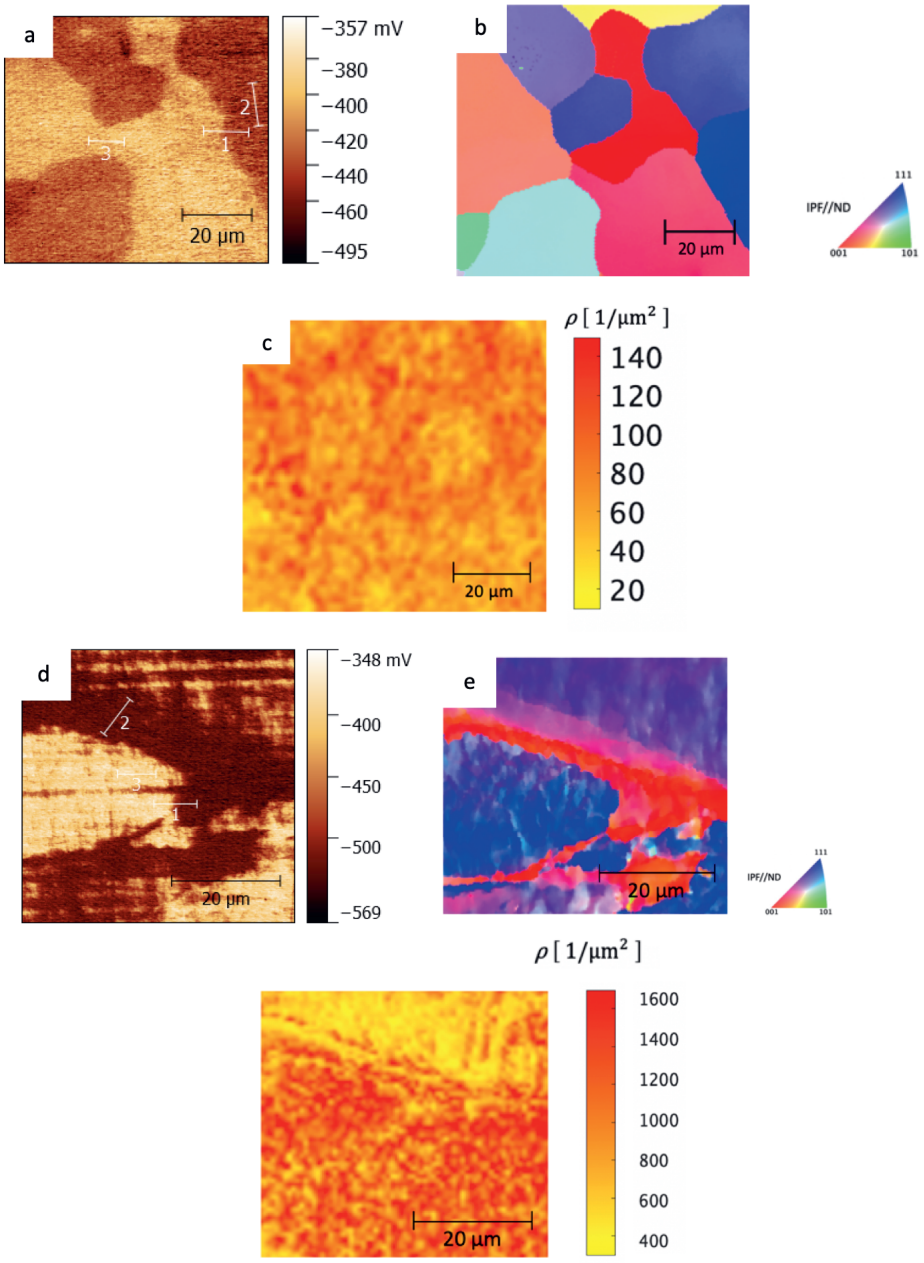

Figure 3.4 a) SKPFM Volta-potential map of hot-rolled material, showing differences of Volta-potential between grains with different orientations, and regions of HAGB and LAGB areas b) the corresponding EBSD Inverse pole figure map, and c) Geometrically necessary dislocation map d) SKPFM Volta-potential map of cold-rolledmaterial, showing differences of Volta-potential between grains with different orientations, and regions of HAGB and LAGB areas e) the corresponding EBSD Inverse pole figure map, and d) Geometrically necessary dislocation map

Mean Volta-potential (mV)	***(001) planes***	***(111) planes***	***(101) planes***
Hot-rolled	-424 $\pm$ 6	-464 $\pm$ 6	-462 $\pm$ 4
Cold-rolled	-529 $\pm$ 3	-392 $\pm$ 5	-

Table 3.2 Mean Volta-potential values of HR and CR samples of entire measurement area and grains in different planes

Furthermore, GND maps (Fig. 3.3c) of the corresponding areas in hot-rolled samples show uniform and very low GND values (almost strain-free). Therefore, this suggests the minimal effect of GND on measured Volta-potential in hot-rolled samples. The Volta-potential and EBSD- IPF maps of the cold-rolled specimen are presented in Fig. 3.3a and 3.3b. The grain orientation (Fig. 3.3b) corresponds to Volta-potential distribution. In contrast to the hot-rolled samples, in Fig 3.3d, the grains in the (001) plane presents less noble character than (111) planes in the cold-rolled samples. Fig. 3.3c shows that geometrically necessary dislocation density is two orders of magnitude higher in (111) planes than (001), indicating that dislocations are preferentially piled-up in (111) planes. Hence, the dislocation pile-up at grains in (111) planes leads to nobility inversion between (001) and (111) planes. In Table 3.2, the mean Volta-potential values of grains in different crystallographic planes are given for both samples. The mean Volta-potential values are calculated (001), (111), and

(101) in planes for hot-rolled and cold-samples in (001) and (111) planes after three measurements. The Volta-potential measurements could not be performed on grains in (101) planes due to texture formation in (001) and (111) planes, leading to a very limited volume fraction of (101) in cold-rolled samples. In hot-rolled samples, it is shown that the mean Volta-potential of (001) planes is approximately 40 mV more noble character than (111) and (101) planes. In contrast, no significant difference in mean Volta-potential values (limited to 2 mV) between (111) and (101) planes are observed. In cold-rolledsamples, it is shown that the polarity between grains in (001) and (111) planes are inverted. The mean Volta-potential of (001) orientation is approximately 140 mV less noble than (111) orientation. Since the differences in Volta-potential generally suggests the presence and degree of driving force for galvanic coupling [12], [19], [20], the higher Volta-potential difference in cold-rolledmaterial indicates a higher degree of galvanic coupling in cold-rolled material. Furthermore, the entire measurement area's mean potential in cold-rolled material is approximately 60-70 mV less noble (anodic) than the one of hot-rolled material. This Volta-potential decrease in cold-rolled material indicates more susceptibility to corrosion in cold-rolled material [12] [21].

Figure 3.4a and 3.4b show the Volta-potential variations across the line profiles given in fig. 3.3a and 3.3b for hot- and cold-rolled materials, respectively. In fig. 3.4a, the line profile 1 shows that the grain in the (001) plane has approximately 40 mV than the one in the (111) plane. The line profile 2 and 3 show no Volta-potential variations between different grains in (111) and (001) orientations, respectively. The line profile 1 in figure 3.4b illustrates that the grain in the (111) plane exhibits approximately 130 mV more cathodic behaviour in comparison with the grain in (111) plane. The line profile 2 shows no significant Volta-potential variations between the grains in (001) plane and the line profile 3 between the grains in (111) plane in cold-rolled material. On the side of grain boundaries, no change in Volta-potential was observed in both low and high angle grain boundaries (indicated in figure 3.4a and 3.4b) in this resolution/scale of SKPFM measurements, implying no/very limited effect of grain boundaries on Volta-potential in both samples. Moreover, the line profiles of both materials show that the Volta-potential variations within each grain are small and limited to a maximum of 10 mV, in agreement with previously reported [12]. Volta-potential variation is most likely associated with GND's

inhomogeneous distribution within each grain, affecting Volta-potential values.

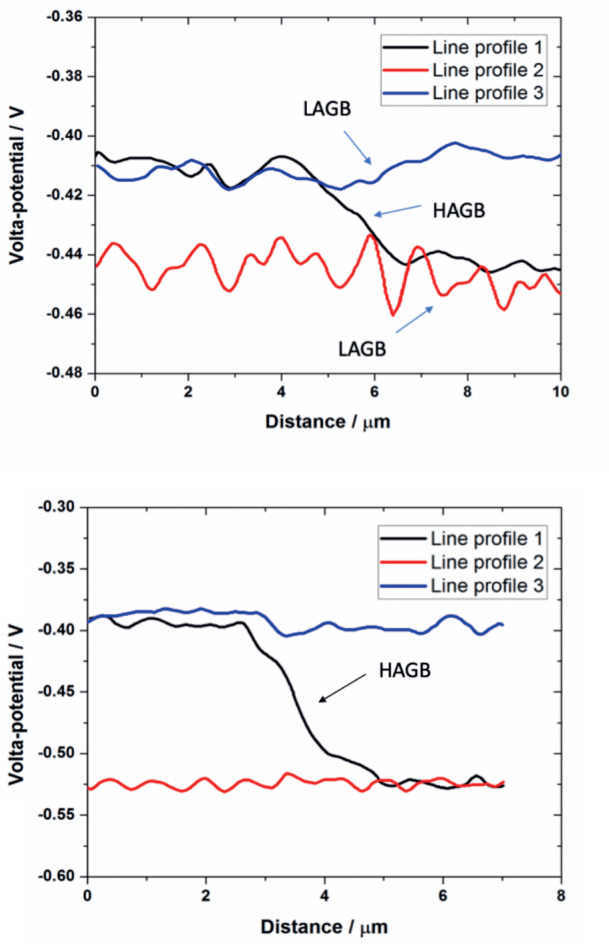

Figure 3.5 Line profiles corresponding to a) Hot-rolled material (Fig 3.3a) and b) Cold-rolled material (Fig. 3.3d). The transition zones formed at HAGB and the differences between grains with different orientations are shown

No local steep potential gradients (high Volta-potential differences at limited areas) are observed in hot-rolled samples, indicating no susceptible spots (such as inclusions) for localised corrosion [34]. Similar to

hot-rolled material, no sharp increase in Volta-potential is also observed in cold-rolledsamples, shows that cold-rolling does not lead to the formation of inclusions.

3.3.3 Electrochemical Characterisation

The potentiodynamic polarisation curves of both cold and hot-rolled materials, carried out in 0.1 M HCl solution, are shown in Fig. 3.5. The anodic and cathodic parts of the curves show the kinetics of anodic dissolution of the metal and cathodic hydrogen evolution reactions (HER), respectively. It is observed that the anodic branch of the polarisation curves of cold-rolled samples shifts towards higher current density values (arrow 1 in Fig. 3.5), showing an increase in anodic dissolution kinetics. However, no difference in anodic slope is observed between both materials. This indicates that the anodic dissolution mechanisms are independent of the substrate microstructure, in line with previously reported [35]. Similar to the shift in the anodic branch of polarisation curves, the cathodic branch of the polarisation curves also exhibits a right shift (arrow 2 in Fig. 3.5), revealing an increase in HER's kinetics. Furthermore, the higher slope of cathodic reactions observed in cold-rolled material shows faster HER kinetics in the

cold-rolled sample, indicating that HER is governed by the substrate microstructure.

The corrosion current density and corrosion potentials, determined by Tafel extrapolation of potentiodynamic polarisation curves, are given in Table 3.2. The cold-rolled material shows approximately 1.5 times higher corrosion current density, exhibiting a faster corrosion rate of cold-rolled material than the hot-rolled material. Furthermore, the cold-rolled material shows about 30 mV more cathodic corrosion potential than the hot-rolled material, which is in line with previous reports [16]. The corrosion potential shifts towards more cathodic potential in cold-rolled material, probably due to the larger shift of anodic dissolution reactions. This stems from the fact that the higher degree of galvanic coupling occurs in cold-rolled material, shown as the higher Volta-potential difference between grains with different orientations of cold-rolled samples.

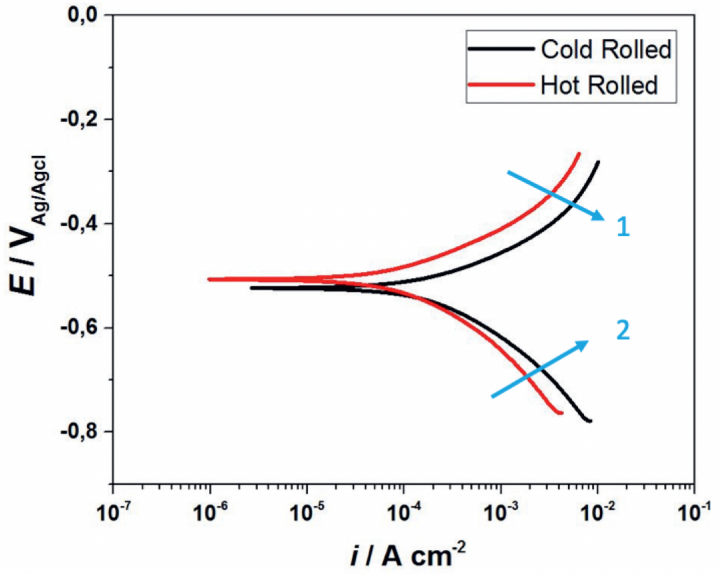

Figure 3.6 Potentiodynamic polarisation curves of hot-rolled and cold-rolledmaterial in 0.1 M HCl solution

	E_{corr} (mV)	I_{corr} (µA/cm²)
ColdRolled	-527 ± 4	147 ± 6
Hot-rolled	-503 ± 8	84 ± 14

Table 3.3 Corrosion potential and corrosion values obtained by Tafel extrapolation of potentiodynamic polarisation curves

The low-alloyed nature of the IF steel allows preventing any alloy segregation, inclusion formation after cold-rolling. Furthermore, both samples consist of only a ferritic phase. These allow avoiding the effect of these microstructural features on corrosion behaviour. Therefore, the individual effect of dislocation density changes, grain boundary density, and texture after cold-rolling on corrosion behaviour could be investigated. In hot-rolled samples, Volta-potential gradients solely depend on the crystallographic orientation due to the absence of dislocation density. In contrast, in cold-rolled material, the polarity between crystallographic orientation is inverted in between (001) and (111) orientation, and the difference of Volta-potential in between these orientations increases about 100 mV. This is attributed to the diffusion of carbon atoms towards dislocations due to the lowered strain energy of crystal structure [36]–[38], leading to a Volta-potential shift to more noble values at dislocation sites. This shows that dislocation density dominates the effect of crystallographic orientation in cold-rolled material. No variations of Volta-potential at grain boundaries was not observed, indicating that no or possibly very limited effect on galvanic interaction compared to dislocation density. Therefore, the galvanic interaction is governed by the dislocation density increase. The

electrochemical measurements discussed above show that the corrosion rate depends on the substrate microstructure and are higher in cold-rolledmaterial. In general, the larger gradients in Volta-potential leads to a higher galvanic interaction [12], [19], [20], which might lead to an increase in the corrosion rate. In cold-rolled material, the higher degree of galvanic coupling occurs (the higher gradient in Volta-potential in between grains in (001) and (111) planes) due to the increase in dislocation density, leading to a higher corrosion rate.

3.4 Conclusions

In this work, the effect of microstructural changes induced by cold rolling on overall corrosion behaviour and the local reactivity was investigated. The following conclusions were drawn.

1. In hot-rolled material, the galvanic interaction in hot-rolled material is governed by the Volta-potential gradient (~40 mV) stemming from the different crystallographic orientations. In cold-rolled material, the nobility between grains in (001) and (111) planes is inverted. The grains in the (001) plane show less noble Volta-potential (~140 mV) than the ones in the (111) planes, contrary to hot-rolled material. Hence, the higher Volta-potential gradient shows higher galvanic

interaction between grains in cold-rolled material. Furthermore, the increase in Volta-potential gradient and the inversion in nobility are attributed to the increase in dislocation density since the effect of crystallographic orientation and grain boundaries on Volta-potential are dominated by the influence of dislocation density on Volta-potential.

2. Potentiodynamic polarisation exhibited a higher corrosion rate in cold-rolled materials, attributed to a higher degree of galvanic interaction in cold-rolledmaterial. Since the higher Volta-potential gradient stems from the main increase in dislocation density, leading to a higher corrosion rate in cold-rolled material.

   From the results given above, it is concluded that the increase in dislocation density leads to increase in corrosion rate due to the increasing degree of micro-galvanic interaction between grains.

3.5 References

[1] W. L. Roberts, *Cold rolling of steel*. New York : M. Dekker, 1978.

[2] Yu Wei-Wen, *Cold-Formed Steel Design*, 5th ed. New York: John Wiley and Sons Inc, 2000.

[3] R. A. Degarmo, E. Paul, J. Black. T. Kohser, ''*Materials and Processes in Manufacturing*, 9th ed. Wiley, 2003.

[4] H. J. Raven and E. Nes, “Structure and properties of heavily cold-rolledIron and high strength low alloy and low carbon steels,” *Met. Sci.*, vol. 18, no. 11, pp. 515–520, Nov. 1984.

[5] M. J. Roberts and W. Jolley, “Influence of cold work and recovery on the strength and toughness of iron,” *Metall. Mater. Trans. B*, vol. 1, no. 5, pp. 1389–1398, 1970.

[6] R. Ueji, N. Tsuji, Y. Minamino, and Y. Koizumi, “Ultragrain refinement of plain low carbon steel by cold-rolling and annealing of martensite,” *Acta Mater.*, vol. 50, no. 16, pp. 4177–4189, 2002.

[7] S. Tagashira, K. Sakai, T. Furuhara, and T. Maki, “Deformation microstructure and tensile strength of cold-rolledpearlitic steel sheets,” *ISIJ Int.*, vol. 40, no. 11, pp. 1149–1155, 2000.

[8] M. Ashraf, L. Gardner, and D. A. Nethercot, “Strength enhancement

of the corner regions of stainless steel cross-sections," *J. Constr. Steel Res.*, vol. 61, no. 1, pp. 37–52, 2005.

[9] S. Ueda, "Effect of Pre-cold-working on Diffusional Reversion of Deformation Induced Martensite in Metastable Austenitic Stainless Steel," *ISIJ Int.*, vol. 34, no. 6, pp. 522–527, 1994.

[10] I. Shakhova, V. Dudko, A. Belyakov, K. Tsuzaki, and R. Kaibyshev, "Effect of large strain cold rolling and subsequent annealing on microstructure and mechanical properties of an austenitic stainless steel," *Mater. Sci. Eng. A*, vol. 545, pp. 176–186, 2012.

[11] M. Eskandari, A. Najafizadeh, and A. Kermanpur, "Effect of strain-induced martensite on the formation of nanocrystalline 316L stainless steel after cold rolling and annealing," *Mater. Sci. Eng. A*, vol. 519, no. 1–2, pp. 46–50, 2009.

[12] C. Örnek and D. L. Engelberg, "SKPFM measured Volta-potential correlated with strain localisation in microstructure to understand corrosion susceptibility of cold-rolled grade 2205 duplex stainless steel," *Corros. Sci.*, vol. 99, pp. 164–171, 2015.

[13] A. Barbucci, G. Cerisola, and P. L. Cabot, "Effect of cold-working in the passive Behaviour of 304 stainless steel in sulfate media," *J.*

Electrochem. Soc., vol. 149, no. 12, pp. 534–542, 2002.

[14] B. R. Kumar, R. Singh, B. Mahato, P. K. De, N. R. Bandyopadhyay, and D. K. Bhattacharya, "Effect of texture on corrosion Behaviour of AISI 304L stainless steel," *Mater. Charact.*, vol. 54, no. 2, pp. 141–147, 2005.

[15] L. Jinlong and L. Hongyun, "The effects of cold rolling temperature on corrosion resistance of pure iron," *Appl. Surf. Sci.*, vol. 317, pp. 125–130, 2014.

[16] G. A. S. N. D. Greene, "Effect of Plastic Deformation On the Corrosion of Iron and Steel," *Corrosion*, vol. 20, no. 9, 1964.

[17] Z. A. Foroulis and H. H. Uhlig, "Effect of Cold-Work on Corrosion of Iron and Steel in Hydrochloric Acid," no. 2, pp. 522–528, 1964.

[18] C. Örnek, C. Leygraf, and J. Pan, "On the Volta-potential measured by SKPFM–fundamental and practical aspects with relevance to corrosion science," *Corros. Eng. Sci. Technol.*, vol. 54, no. 3, pp. 185–198, 2019.

[19] M. Rohwerder and F. Turcu, "High-resolution Kelvin probe microscopy in corrosion science: Scanning Kelvin probe force microscopy (SKPFM) versus classical scanning Kelvin probe (SKP),"

Electrochim. Acta, vol. 53, no. 2, pp. 290–299, 2007.

[20] V. Guillaumin, P. Schmutz, and G. S. Frankel, "Characterisation of Corrosion Interfaces by the Scanning Kelvin Probe Force Microscopy Technique," *J. Electrochem. Soc.*, vol. 148, no. 5, p. B163, 2001.

[21] W. Li, M. Cai, Y. Wang, and S. Yu, "Influences of tensile strain and strain rate on the electron work function of metals and alloys," *Scr. Mater.*, vol. 54, no. 5, pp. 921–924, 2006.

[22] J. Jiang, T. B. Britton, and A. J. Wilkinson, "Measurement of geometrically necessary dislocation density with high resolution electron backscatter diffraction: Effects of detector binning and step size," *Ultramicroscopy*, vol. 125, pp. 1–9, 2013.

[23] P. J. Konijnenberg, S. Zaefferer, and D. Raabe, "Assessment of geometrically necessary dislocation levels derived by 3D EBSD," *Acta Mater.*, vol. 99, pp. 402–414, 2015.

[24] F. Bachmann, R. Hielscher, and H. Schaeben, "Texture analysis with MTEX- Free and open source software toolbox," *Solid State Phenom.*, vol. 160, pp. 63–68, 2010.

[25] B. L. Adams and J. Kacher, "EBSD-based microscopy: Resolution of dislocation density," *Comput. Mater. Contin.*, vol. 14, no. 3, pp. 183–

194, 2009.

[26] M. Iannuzzi, K. L. Vasanth, and G. S. Frankel, “Unusual Correlation between SKPFM and Corrosion of Nickel Aluminum Bronzes,” *J. Electrochem. Soc.*, vol. 164, no. 9, pp. C488–C497, 2017.

[27] A. B. Cook, Z. Barrett, S. B. Lyon, H. N. McMurray, J. Walton, and G. Williams, “Calibration of the scanning Kelvin probe force microscope under controlled environmental conditions,” *Electrochim. Acta*, vol. 66, pp. 100–105, 2012.

[28] C. Örnek, C. Leygraf, and J. Pan, “Passive film characterisation of duplex stainless steel using scanning Kelvin probe force microscopy in combination with electrochemical measurements,” *npj Mater. Degrad.*, vol. 3, no. 1, pp. 1–8, 2019.

[29] C. Örnek, J. Walton, T. Hashimoto, T. L. Ladwein, S. B. Lyon, and D. L. Engelberg, “Characterisation of 475°C Embrittlement of Duplex Stainless Steel Microstructure via Scanning Kelvin Probe Force Microscopy and Magnetic Force Microscopy,” *J. Electrochem. Soc.*, vol. 164, no. 6, pp. C207–C217, 2017.

[30] P. Schmutz and G. S. Frankel, “Characterisation of AA2024-T3 by Scanning Kelvin Probe Force Microscopy,” *J. Electrochem. Soc.*, vol.

145, no. 7, pp. 2285–2295, 1998.

[31] H.J. Bunge, "*Texture analysis in materials science: mathematical methods*", Cuvillier Verlag, 1993.

[32] L. A. I. Kestens and H. Pirgazi, "Texture formation in metal alloys with cubic crystal structures," *Mater. Sci. Technol. (United Kingdom)*, vol. 32, no. 13, pp. 1303–1315, 2016.

[33] K. Fushimi, K. Azumi, and M. Seo, "Evaluation of Heterogeneity in Thickness of Passive Films on Pure Iron by Scanning Electrochemical Microscopy," *ISIJ Int.*, vol. 39, no. 4, pp. 346–351, 1999.

[34] M. Femenia, J. Pan, and C. Leygraf, "Characterisation of Ferrite-Austenite Boundary Region of Duplex Stainless Steels by SAES," *J. Electrochem. Soc.*, vol. 151, no. 11, p. B581, 2004.

[35] K. Fushimi, K. Miyamoto, and H. Konno, "Anisotropic corrosion of iron in pH 1 sulphuric acid," *Electrochim. Acta*, vol. 55, no. 24, pp. 7322–7327, 2010.

[36] A. H. Cottrell and B. A. Bilby, "Dislocation theory of yielding and strain ageing of iron," *Proc. Phys. Soc. Sect. A*, vol. 62, no. 1, pp. 49–62, 1949.

[37] G. Da Rosa, P. Maugis, J. Drillet, V. Hebert, and K. Hoummada, "Co-

segregation of boron and carbon atoms at dislocations in steel," *J. Alloys Compd.*, vol. 724, pp. 1143–1148, 2017.

[39] L. Ventelon *et al.*, "Dislocation core reconstruction induced by carbon segregation in bcc iron," *Phys. Rev. B - Condens. Matter Mater. Phys.*, vol. 91, no. 22, pp. 1–5, 2015.

Part B

Role of grain size on passivity and corrosion behaviour

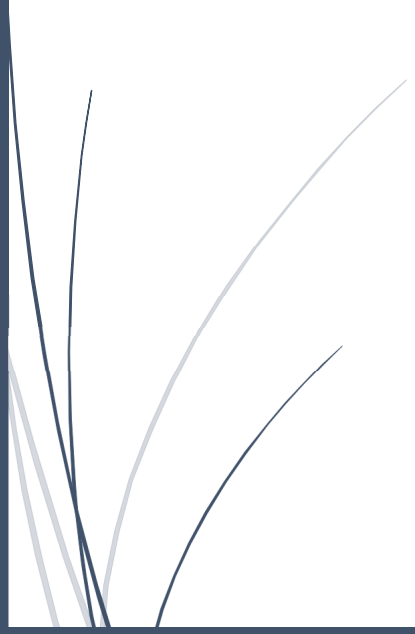

CHAPTER 4

Effect of grain size on passive layer properties of pure iron in 0.1 M NaOH solution

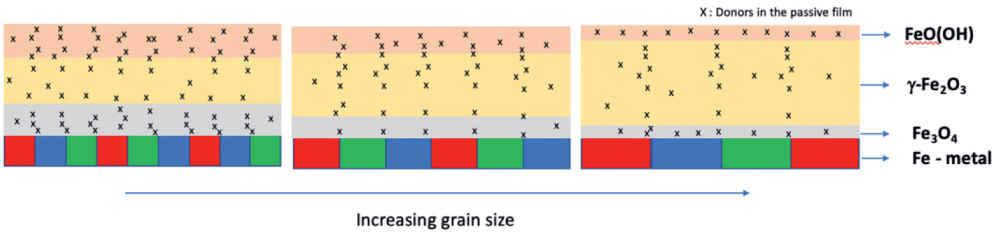

This chapter is based on the scientific paper:

A. Yilmaz, K. Traka, S. Kar, J. Sietsma, Y. Gonzalez-Garcia (2021) Role of grain size and crystallographic orientation on the corrosion and passivation behaviour of pure iron (Under review)

Abstract

In this work, the role of grain size on passive layer properties of pure iron is investigated in 0.1 M NaOH solution. Electron backscatter diffraction analysis was performed to characterize the microstructure of heat-treated samples. Samples with mean grain sizes of 26, 53 and 87 µm are obtained after heat treatments. Potentiostatic polarisation and electrochemical impedance spectroscopy (EIS) measurements show the deterioration in the passive layer's barrier properties with grain refinement. This stems from the decrease in the fraction of protective γ-Fe_2O_3 in the passive film and the increase in the passive layer's donor density with grain refinement.

Keywords: Grain size, iron, passivity, EIS, Mott-Schottky analysis, EBSD, XPS

4.1 Introduction

Grain size is an important parameter that influences mechanical properties such as strength, ductility and wear resistance without altering the material's chemical composition. In the past decades, the relationship between grain size and ferrous alloys' mechanical properties has been significantly developed [1]–[7]. However, the knowledge of the effect of grain size on ferrous alloys' passive layer properties is still limited. Ralston and Birbilis [8] reviewed the existing literature very comprehensively. This review shows that the studies reported contradictory results on grain size's effect on passive layer properties. The contradictions in literature stem from the fact that the processing routes used to achieve different grain sizes lead to variations in microstructural features besides grain size, such as dislocation density, texture, alloy segregations, inclusions. These microstructural modifications have a complex interaction with the effect of grain size on passive layer properties, making it impossible to relate microstructural features and subsequent passive layer properties directly. Furthermore, a reasonable number of studies investigated the grain size and passive layer properties in stainless steels [9]–[14], whereas there are

very few studies on low-alloyed ferrous materials in grain size in micrometre range [15], [16].

The effect of grain refinement induced by cold rolling on pure iron's passivity behaviour was investigated in a borate buffer solution [15]. It was reported that the barrier properties of the passive film improve with grain refinement, attributed to a decrease in donor density in the passive film. However, besides grain refinement, the formation of preferred crystallographic orientation, and the increase in dislocation density induced by cold rolling was also observed. In previous work, the role of prior austenite grain size (PAGS) on passive layer properties formed on fully martensitic high-strength steels was investigated [16]. The different PAGS was achieved by applying other heat treatments. It was reported that the grain refinement is the dominant factor down to the certain grain size (~30 μm) and leads to a worsening of the barrier properties of the passive layer. However, further refinement leads to improved barrier properties due to the changes within the martensite structure. The passive film's deterioration was attributed to a decrease in the fraction of protective γ-Fe_2O_3 and an increase in donor density in the passive film.

This work aims to investigate the relationship between grain size and the passive layer properties of pure iron. Different heat treatments are employed in the design of samples with varying sizes of grain while preventing the effect of other microstructural features. Electron backscatter diffraction (EBSD) analysis is used to determine grain size and dislocation density throughout the crystallographic orientation of each material volume. The chemical composition and thickness of the passive layers are investigated by X-ray photoelectron spectroscopy (XPS). Potentiostatic polarisation and electrochemical impedance spectroscopy (EIS) are employed to examine the effect of grain size on the barrier properties of the passive film in 0.1 M NaOH solution. The semiconductor properties of passive films are studied with capacitance measurements (Mott-Schottky analysis).

4.2 Experimental

4.2.1 Material

As-received Armco® pure iron samples (AK Steel, The Netherlands) were employed. The sheets of iron with a thickness of 2.2 mm were laser-cut to the dimensions of 5 x 10 mm^2. The samples' chemical composition was evaluated with a JEOL JXA 8900R microprobe with an electron beam having

an energy of 10 keV and beam current of 100 nA using wavelength dispersive spectrometry (WDS). The X-ray intensities of the constituent elements were used to evaluate the chemical composition at every measurement location after conducting a background correction to the X-ray intensities relative to the corresponding intensities of reference materials. The samples' chemical composition is given in Table 4.1, showing very high purity

(> 99% Fe) of the samples.

	Fe	***C***	***Si***	***Mn***	***P***	***S***	***Cr***	***Cu***	***N***	***Ni***	***Sn***
wt%	Bal.	0.001	0.003	0.04	0.003	0.003	0.014	0.007	0.003	0.012	0.002

Table 4.1 Chemical composition (wt.%) of iron samples

4.2.2 Microstructure Design & Characterisation

Different heat treatments, given in Fig. 4.1, were employed on as-received iron samples in order to obtain samples with different grain sizes. A Bähr DIL 805 A/D dilatometer was used for the heat treatment. The samples were heated at a rate of 10 $^{o}C\ s^{-1}$ to the annealing temperatures. The annealing temperatures of 700, 950 and 1100 ^{0}C were used for heat treatment S, M, and L, respectively. Subsequently, the samples were quenched to room temperature with helium gas.

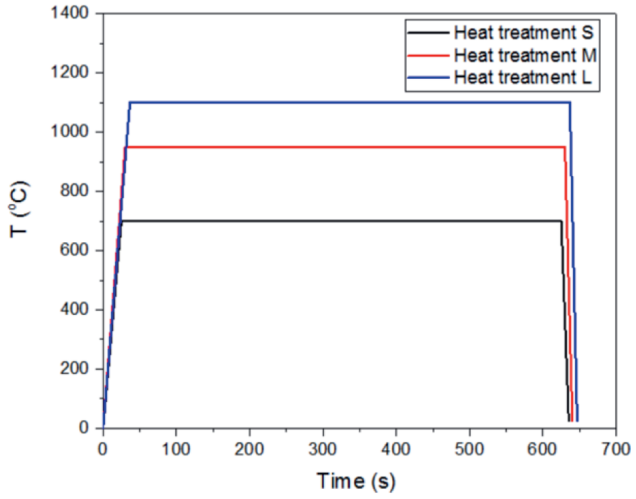

Figure 4.1 Heat treatment processes followed to obtain iron samples with different grain sizes.

Electron backscatter diffraction (EBSD) measurements were conducted to characterize samples' microstructure after heat treatments by extracting crystallographic orientation, geometrically necessary dislocation (GND) density, grain boundary area, and grain size. The samples were prepared for EBSD measurements by grinding with SiC papers from 80 to 4000 grit, followed by mirror-like polishing using diamond particle slurry (Struers DiaDuo-2) with particle sizes of 3 and 1 μm, and finalized with an OP-S polishing. Subsequent to polishing, the samples were cleaned in an ultrasonic bath with ethanol for 10 min, followed by drying with compressed air. A JEOL JSM 6500F FEG-SEM microscope with an EDAX/TSL detector was employed for EBSD measurements. The step size and working distance of

measurements were 1 and 17 mm, respectively. The same step size was used in all measurements to prevent its effect on dislocation density calculations [17]. The GND densities are determined as described elsewhere [17]–[19]. The data post-processing was carried out with TSL-OIM v7.3 software and Matlab using MTEX routines [20]. To obtain a sufficiently large statistical sample size with respect to the grain size, an area of 1.44 mm^2 per sample was investigated.

The grain size was calculated after grain identification was performed. In particular, a grain is identified as the volume that is circumscribed by a closed-loop. All boundary segments have a larger misorientation angle than the lower threshold (here 5^o). The mathematical decomposition of the crystallographic orientation data into grains was performed according to the method described in [21]. Thenceforth, the average grain diameter was calculated as the equivalent circular area's diameter, which was equal to the average grain area.

4.2.3 Electrochemical Measurements

Potentiostatic polarisation and electrochemical impedance spectroscopy (EIS) experiments were carried out to determine the effect of grain size on the passive film's barrier properties on iron samples. The electrolyte

solution employed was aerated 0.1 M NaOH solution, prepared with distilled water in ambient conditions. The samples were embedded in an epoxy resin (Struers ClaroCit) and cured for 1 hour under 2 bar pressure. The samples were prepared for electrochemical measurements by mechanically grinding with SiC abrasive papers from 80 to 4000 grit. Subsequently, mechanical polishing with alcohol-based high-performance diamond slurry with the particle sizes of 3 and 1 μm. Following polishing, the samples were cleaned in an ultrasonic bath of ethanol and dried with compressed air. The space between the sample and epoxy resin was covered by applying a thin layer of sealing lacquer (Electrolube Bloc Lube Red) to prevent the possible formation of crevice corrosion during electrochemical measurements.

The electrochemical measurements were conducted just after the sample preparation with a three-electrode system, compromised of the reference electrode (Ag/AgCl, KCl (Satd.)), the counter electrode (graphite rod), and the working electrode (the sample). A Biologic SP300 potentiostat was used for the electrochemical measurements. Before all electrochemical measurements, the open circuit potential (OCP) was measured for 1800 seconds, in which stabilization of the potential was realized. Potentiostatic

polarisations were carried out at a potential of 0.2 V (vs. Ag/AgCl) for 3600 seconds. EIS spectra of the samples passivated with potentiostatic polarisation were collected in the frequency range from 30 kHz to 0.01 Hz by applying a perturbation amplitude of 10 mV. The EIS data were analysed with Zview software.

The Mott-Schottky analysis was conducted to investigate the effect of grain size on the passive film's semiconductor behaviour formed on samples. The capacitance measurements were conducted on the pre-passivated samples with potentiostatic polarisation for 3600 seconds at 0.2 V (vs. Ag/AgCl). The measurements are conducted at 1 kHz with an AC voltage of 10 mV. A potential step size of 50 mV was employed to sweep the potential range from 0.6 V to -1 V (vs. Ag/AgCl).

4.2.3 Passive Layer Analysis

X-ray photoelectron spectroscopy (XPS) analysis was used in order to determine the chemical composition of passive films after growing the passive films with potentiostatic polarisation at 0.2 V (vs. Ag/AgCl) for 3600 s in 0.1 M NaOH solution. XPS spectra were collected by a PHI5000 Versaprobe II photoelectron spectroscope (Physical Electronics) with an Al K-α monochromatic X-ray source (1486.71 eV photon energy). The high-

resolution Fe-2p core electrons scans were collected with a take-off angle of 45º and a photoelectron detection diameter of 200 µm. The pass energy and energy step size were 23.5 eV and 0.1 eV, respectively. To fit the obtained XPS data, Casa XPS V2.3.22 software was used by employing Shirley background and a mixed Gaussian-Lorentzian line shape.

4.3 Results & Discussion

4.3.1 Microstructure Characterisation

EBSD analysis was carried out to determine the microstructural characteristics (grain size/boundary area, the spatially resolved crystallographic orientation, and dislocation density) of samples that underwent the different heat treatments. In Figure 4.2, EBSD inverse pole figures (IPF) along Normal Direction (ND) are given for all samples. It was observed that the samples are composed of equiaxed grains. All samples consist of only the BCC crystal structure, thus revealing a 100% ferritic microstructure. The former also indicates that the samples do not contain any inclusions in the resolution limits of EBSD measurements. The microstructure consisting of a single-phase without inclusions formation is attributed to the very high purity of samples.

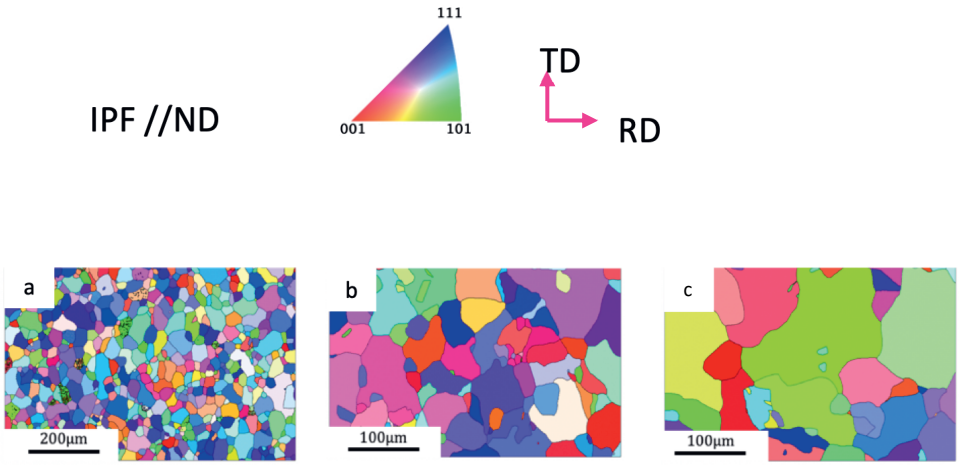

Figure 4.2 Microstructures obtained through EBSD measurements for all samples with different grain sizes. The Inverse Pole Figure (IPF) maps show the spatially resolved crystal directions parallel to the normal direction (ND) a) Sample S, b) Sample M and c) Sample L

The overview of the microstructural features of all samples is given in Table 4.2. Different heat treatments lead to distinct changes in the average grain size of samples. The average grain sizes increase with the increase in the annealing temperature. While sample S, annealed at 700 ^{o}C for 10 min, has an average grain size of 26 µm, the sample L, annealed at 1100 ^{o}C for 10 min, has an average grain size of 87 µm. Annealing at an intermediate temperature of 900 ^{o}C for 10 min leads to the average grain size of 53 µm in Sample M.

	Grain size (μm)	***Grain boundary density (μm^{-1})***	***Geometrically necessary dislocation density (m^{-2})***
Sample S	26 ± 2	0.101 ± 0.008	$2.3 \pm 0.4 \cdot 10^{13}$
Sample M	53 ± 4	0.051 ± 0.004	$7.9 \pm 0.2 \cdot 10^{12}$
Sample L	87± 12	0.027 ± 0.004	$4.4 \pm 0.2 \cdot 10^{12}$

Table 4.2 Overview of the grain size, grain boundary density and geometrically necessary dislocation density of Sample S, M and L

In Figure 4.3, GND density maps of all samples are shown. It is observed that the GND densities are below 10^{13} m^{-2} and uniform within the grains in all samples. In contrast, the grain boundary areas exhibit higher GND densities, showing that the dislocations accumulate at grain boundaries. The mean GND values are $2.3 \pm 0.4 \cdot 10^{13}$ m^{-2} for Sample S, $7.9 \pm 0.2 \cdot 10^{12}$ m^{-2} for Sample M and $4.4 \pm 0.2 \cdot 10^{12}$ m^{-2} for Sample L. The GND values are relatively close, considering the very small order of magnitude in all samples, and the slight differences between samples follow the order of grain boundary density areas. This stems from the fact that abutting grains of close crystallographic orientation will be separated by LAGBs and hence by GNDs. The small values of GND density, as well as the equiaxed grains shown in Fig. 4.1, indicate a fully strain-free grain structure, which renders all samples equal in terms of dislocation density (other than grain boundaries).

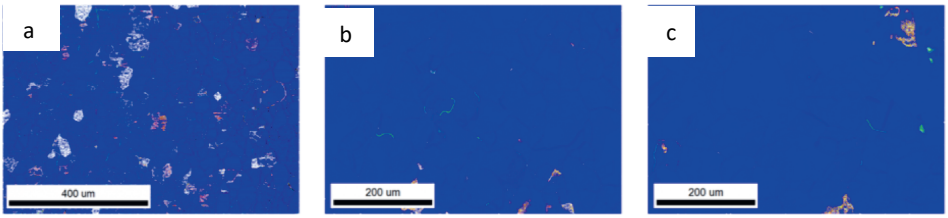

Figure 4.3 GND density maps obtained from EBSD analysis with same resolution for a) Sample S: Average $\rho_{GND} = 2.3 \cdot 10^{13}\mathrm{m}^{-2}$, b) Sample M: Average $\rho_{GND} = 7.9 \cdot 10^{12}\mathrm{m}^{-2}$ and c) Sample L: Average $\rho_{GND} = 4.4 \cdot 10^{12}\mathrm{m}^{-2}$. The GND is determined for a maximum angle 10° and up to the 1st neighbour pixels.

4.3.2 Passive layer analysis

X-ray photoelectron spectroscopy (XPS) analysis was used to determine the chemical composition and the fractions of oxide and hydroxides of the passive films as a function of substrate grain size. In Figure 4.4, high-resolution curves Fe-$2p_{3/2}$ photoelectron spectra between 716 and 705 eV for all samples are given. The data were fitted with the optimized parameters reported by Biesinger et al. [22], applying a Shirley-type background subtraction. Multiplet structure fitting was employed due to the occurrence of multiplet splitting in high-spin Fe^{+2} and Fe^{+3} species [23], providing accurate quantification of the fractions of oxides and hydroxides. It is suggested that the passive layers are composed of inner iron oxide layers (Fe_3O_4 and γ-Fe_2O_3) with an outer layer of hydroxide (FeO(OH)) layer, in line with the previously reported studies [24]–[30]. The analysed peaks

for each oxidation state are represented as single peaks for Fe^{0}, $Fe^{+2,}$ and Fe^{+3} species in Figure 4.4. The differences in the relative peak intensities of Fe_3O_4, γ-Fe_2O_3 and FeO(OH) between all samples suggest that the fractions of oxides and hydroxides depend on the grain size, which is summarized in Table 4.3. The fraction of γ-Fe_2O_3 in the passive layer for samples S, M, and L are 53 %, 60%, and 66 %, respectively. This shows that the γ-Fe_2O_3 fraction decreases with grain refinement. In opposite, the fraction of Fe_3O_4 in the passive film is 25.2% for sample S, 21.9% for Sample M and 18.3% for Sample L, and the fraction of FeO(OH) is 22.9% for sample S, 17.7% for Sample M and 15.6% for Sample L. This shows that the fractions of both Fe_3O_4 and FeO(OH) increase with grain refinement.

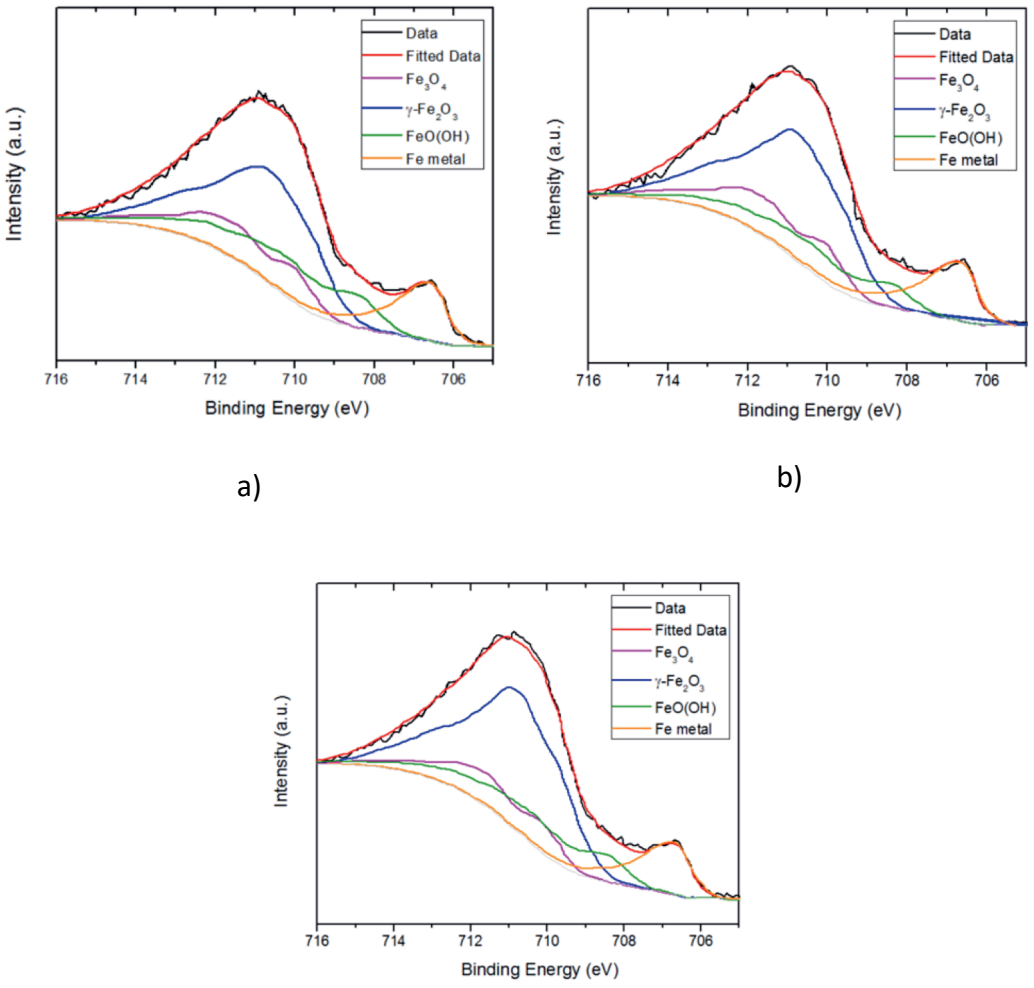

Figure 4.4 High resolution XPS Fe 2p spectra and the corresponding fitting of a) Sample S, b) Sample M and c) Sample L.

	γ-Fe₂O₃ (%)	***Fe₃O₄ (%)***	***FeO(OH) (%)***
Sample S	52.9±2.3	25.2±1.4	22.9±2.1
Sample M	60.4±1.1	21.9±1.5	17.7±1.3
Sample L	66.1±1.4	18.3±1.3	15.6±1.1

Table 4.3 The fractions of Fe_3O_4, γ-Fe_2O_3 and FeO(OH) in the passive films depending on the substrate grain size

The passive layer thickness is calculated using the intensity ratio between metal and oxide peaks, as described in detail elsewhere [31], [32]. The thickness of the passive film, assuming that the entire passive layer consists of γ-Fe_2O_3, is calculated as follows:

$$d = \lambda_{ox} cos\theta \ln\left(\frac{N_{Fe}\lambda_{Fe}}{N_{ox}\lambda_{ox}} \frac{I_{ox}}{I_{Fe}} + 1\right) \qquad \text{[Eqn. 4.1]}$$

where d is oxide thickness, I_{Fe} is the photoelectron intensity of metallic iron, I_{ox} is the intensity of γ-Fe_2O_3, N_i is the number of atoms per unit volume in phase i, λ_{Fe} (1.10 nm) is the inelastic mean free electron path in metallic iron, λ_{ox} (1.42 nm) is the inelastic mean free electron path in γ-Fe_2O_3, θ (45º) is detection angle. Inelastic mean free paths are calculated as described by Shinotsuka et al. [32]. The calculated thickness estimations of the passive layers are 1.4 nm for sample S, 1.5 nm for Sample M and 1.5 nm for Sample L, showing no major difference in the thickness of the passive layer for samples with different grain sizes.

4.3.3 Electrochemical Characterisation

Potentiostatic polarisation – Potentiostatic polarisation was carried out in 0.1 M NaOH solution for 3600 seconds at 0.2 V (vs. Ag/AgCl), at which

the formation of a passive layer is ensured. In Figure 4.5, the current density changes of all samples during potentiostatic polarisation are given. The initial current density values are related to the double layer's charging formed on the samples [33]. The decrease in current density with time in all samples shows the formation of a passive layer, limiting the charge transfer. All samples approach a steady state after approximately 1500 seconds of polarisation, and the steady-state is achieved after 3600 seconds. The current density values at the steady-state are 3.2 ± 0.4 μA/cm^2 for Sample S, 1.9 ± 0.2 μA/cm^2 for Sample M and 1.3 ± 0.2 μA/cm^2 for Sample L. The increase in current density values at steady-state from Sample L to Sample S shows that the passive film's conductivity increases with grain refinement.

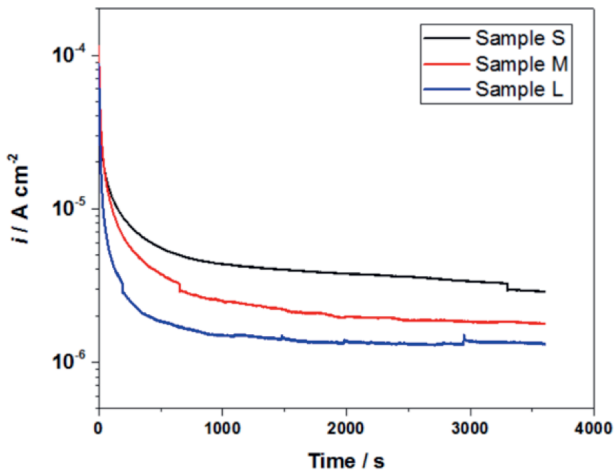

Figure 4.5 Potentiostatic polarisation plot of all samples showing the current transients at 0.2 V (vs. Ag/AgCl) for 3600 seconds in 0.1 M NaOH

Electrochemical Impedance Spectroscopy (EIS) – Figures 4.6a show the Nyquist and plots of all samples after passivation. The diameter of the arc in Nyquist plots decreases with grain refinement. This indicates that passive films' barrier properties deteriorate with grain refinement, in line with the trend in current density values at steady state at potentiostatic polarisation. The equivalent electrical circuit (EEC) (Fig. 4.6b) with two-time constants is employed to fit the EIS data of all samples. The employed circuit has already been used to fit the EIS data of low carbon steels in alkaline NaOH solutions [25], [34], [35]. Constant phase elements are employed in the EEC because of non-ideal capacitive behaviour, probably caused by the passive film's inhomogeneities [36]. The solution resistance is represented with R_1. R_2 and CPE_2 are associated with resistive and capacitive behaviour of double layer at higher frequencies, respectively. At lower frequencies, R_3 and CPE_3 represent the resistive and capacitive behaviour of passive film, respectively. Capacitance values, *C*, were determined by using CPE parameters and the resistance values as follows [37]:

$$C = R^{\frac{(1-n)}{n}} Q^{\frac{1}{n}} \quad \text{[Eqn. 4.2]}$$

where *Q* is the CPE constant, *n* is the CPE coefficient, and *R* is the resistance. The EEC fitting results and calculated capacitance values are summarized in Table 4.4. It is shown that the resistance values of the double layer are two-orders of magnitude lower than the ones of passive layer. The resistance values representing the passive layer (R_3) of Samples S are approximately half the value for Sample M and 20% of the value for sample L, in agreement with the trend in the current density values of potentiostatic polarisation curves. This shows that the grain refinement leads to lower barrier properties in the passive layer.

Moreover, considering the passive layer consisting of parallel capacitors, the total thickness of the passive film is inversely proportional to capacitance values and calculated as follows [38]:

$$d_p = \frac{\varepsilon \varepsilon_o}{C_p} \qquad \text{[Eqn. 4.3]}$$

where d_p is the thickness of the passive layer, C_f is the passive film's capacitance, $\varepsilon = 40$ [39] and ε_o are the dielectric constant of passive film formed on low carbon steels and permittivity in a vacuum, respectively. The passive layer thickness formed on samples S, M and L are 2.11 ± 0.03 nm, 2.08 ± 0.03 nm and 1.89 ± 0.11 nm, showing no significant difference in

passive layer thickness between samples. This is in line with the passive layer thickness calculated from XPS data and shows that the passive layer thickness is independent of substrate grain size, in agreement with our other work [16].

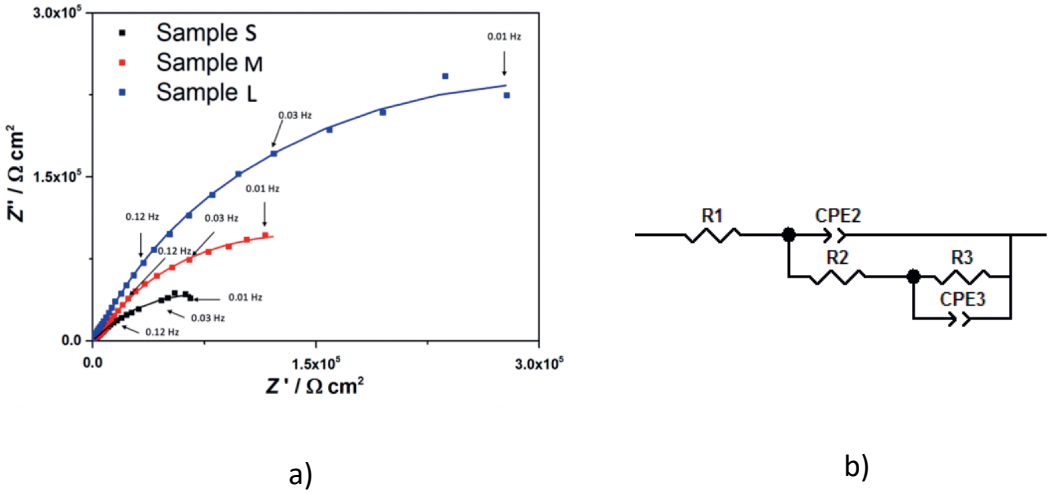

a) b)

Figure 4.6 Nyquist plots of all samples passivated potentiostatically at 0.2 V (vs. Ag/AgCl) for 3600 seconds. b) the equivalent circuit used to fit EIS data

	R_2 Ω cm^2 x10^3	**CPE_2-Q** Ω^{-1} s^{n}cm^2 x10^{-5}	**CPE_2-n**	**C_2** μF cm^{-2}	**R_3** Ω cm^2 x10^5	**CPE_3-Q** Ω^{-1} s^{n}cm^2 x10^{-5}	**CPE_2-n**	**C_3** μF cm^{-2}
Sample S	6.5±0.2	1.04±0.02	0.91± 0.01	48±3	1.1±0.2	8.26±0.02	0.79± 0.02	18.35± 0.06
Sample M	5.8±0.2	1.05±0.08	0.91± 0.01	41±4	2.7±0.6	6.28±0.01	0.81± 0.03	19.05± 0.11
Sample L	26 ±7	0.96±0.02	0.91± 0.01	31.6±0.4	5.7±0.4	3.70±0.02	0.81± 0.02	19.2± 0.42

Table 4.4 Equivalent circuit parameters determined by fitting the collected EIS data of all samples

Capacitance measurements – Mott-Schottky (M-S) analysis was carried out to determine the relationship between substrate grain size and passive films' semi-conductive properties. In Figure 4.7, the Mott-Schottky plots of all samples are given after passivation. The curves of all samples exhibit a positive slope, showing the n-type semiconductor behaviour in passive layers on all samples, as expected for iron oxides [39], [40]. The donor density values are obtained from extrapolating the slope of M-S plots to the potential axis to extract the flat band potential. The flat band potentials for Sample S, Sample M, and Sample L are -0.68 ± 0.02 V, -0.64 ± 0.03 V, and -0.62 ± 0.02 V. The extracted lowest slope is observed in sample S, and the largest slope in Sample L. Since the slope is inversely proportional to the donor density, the order of the slope indicates that the donor density increases with grain refinement. The Mott-Schottky relationship for n-type semiconductors was employed to determine the donor density of the passive layer as follows [41]:

$$\frac{1}{C^2} = \frac{2(E - E_{FB} - \frac{kT}{q})}{\varepsilon \varepsilon_o q \, \mathrm{N}_d} \qquad \text{[Eqn. 4.4]}$$

where T is the temperature, k is the Boltzmann constant, E_{FB} is the flat band potential, N_d is the donor density, q is the electron charge, ε_0 is the

permittivity of vacuum, and $\varepsilon = 40$ is the dielectric constant of the iron oxide films [39]. The donor density values in all samples are in the order of 10^{20} cm^{-3}, in agreement with previous reports for the passive layers formed in pure iron [42]. The donor density values are $14.5 \pm 0.8 \times 10^{20}$ cm^{-3} for Sample S, $9.6 \pm 0.4 \times 10^{20}$ cm^{-3} for Sample M and $7.2 \pm 0.1 \times 10^{20}$ cm^{-3} for Sample L. This shows that the defect density in the passive layer increases with grain refinement. Grain boundaries accommodate a high number of lattice defects, more dominantly at high-angle grain boundaries. These lattice defects probably lead to the formation of more defective passive layers at grain boundaries, as also reported by Yanagisawa et al. [33] for the passive layer formed at ferrite and martensite phase boundaries with a high density of lattice defects. Therefore, the increase in grain boundary area (grain refinement) leads to the formation of a more defective passive layer.

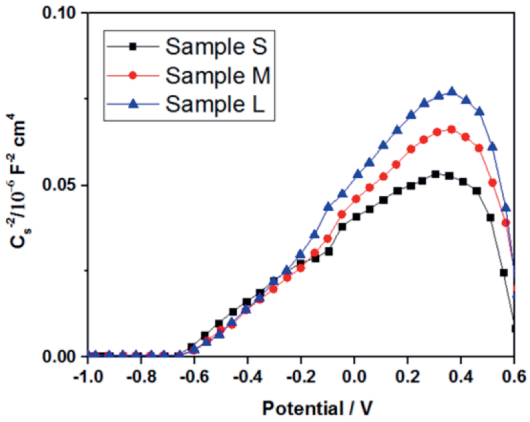

Figure 4.7 Mott-Schottky plots of samples passivated with potentiostatic polarisation at 0.2 V for 3600 seconds

For unambiguous identification of the effects of grain size, it is important to limit the changes in the microstructure to grain size manipulation to avoid the interaction between grain size and other microstructural features in their effect on passive layer properties. In contrast to the vast majority of literature that employed thermomechanical processes to manipulate grain size to investigate passive layer and grain size relationship, applying different heat treatments in the present work permits obtaining different grain sizes manipulation without causing differences in crystallographic orientation and phases, inclusions and dislocation density, as confirmed by the EBSD analysis performed. Therefore, the microstructural changes are only limited to grain size changes, and the sole effect of grain size on passive layer properties of pure iron is thus identified.

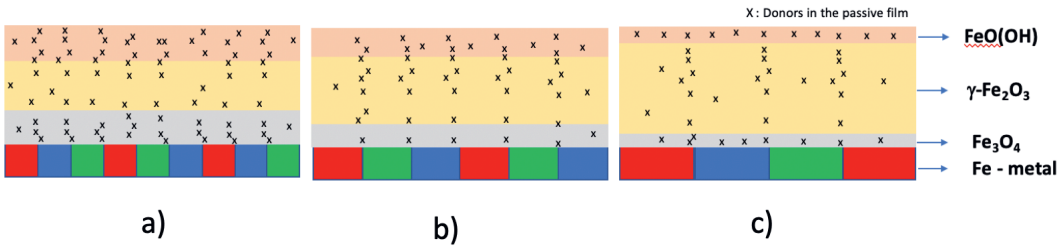

Figure 4.8 Schematic diagram of the passive films for a) Sample S, b) Sample M and c) Sample L, showing the changes in the structure of passive film depending on substrate grain size

Electrochemical measurements show that the grain refinement leads to a worsening of the barrier properties of passive layers. In Figure 4.8, the passive layer structures composed of Fe_3O_4 and γ-Fe_2O_3 and FeO(OH) are schematically shown in their dependence on grain size. The lowest fraction of γ-Fe_2O_3 in the passive layer is observed in the sample with the smallest grain size, accounting for the deterioration in barrier properties of the passive layer with grain refinement due to the stronger protection of γ-Fe_2O_3 in comparison to Fe_3O_4 and FeO(OH). As discussed previously, FeO(OH) provides very limited barrier properties due to its porous structure. Moreover, Fe_3O_4 (0.1 eV) [43] has much lower band gap than γ-Fe_2O_3 (2.3 eV) [44], leading to higher conductivity. Therefore, most barrier properties of the passive film are provided by γ-Fe_2O_3. The defect density is another factor responsible for the deterioration in passive layer properties. The defects in the passive film affect the conductivity due to the changes in both electronic and ionic resistance. An increase in the donor density narrows down the band-gap of metal oxides [45], [46]. This narrowing of the band gap facilitates the electron transfer and eventually decreases the electronic resistance of the passive film. From the ionic resistance point of view, the higher number of ionic defects in the passive film permits the passage of a

larger ionic current [33]. Therefore, the higher density of defects in the passive film leads to higher conductivity due to decreased electronic and ionic resistance.

4.4 Conclusions

In this paper, the role of grain size on the passive layer properties of pure iron is investigated in 0.1 M NaOH solution. The following conclusions are drawn.

1. The samples with variations only in grain size (26, 53, and 87 μm) are achieved after different heat treatments while limiting the changes in any other microstructural features. This allows to limit the complex interaction between microstructural features in their effects on the formation of passive layers and understand the sole role of grain size on passive layer properties.
2. The passive layers on all samples are composed of Fe_3O_4, γ-Fe_2O_3, and FeO(OH) with different fractions. The fraction of protective γ-Fe_2O_3 decreases with grain refinement. Passive films' donor density increases with grain refinement, leading to a more

defective passive layer formation on the substrates having a smaller grain size.

3. The current density at steady-state in potentiostatic polarisation increases with grain refinement. Furthermore, the resistance values of passive layers obtained from EIS measurements decrease with grain size reduction.

From these results, it is concluded that the passive film's barrier properties deteriorate with grain size refinement due to the decrease in the fraction of protective γ-Fe_2O_3 and the increase in the defect density in the passive layer.

4.5 References

[1] J. M. Hyzak and I. M. Bernstein, "The role of microstructure on the strength and toughness of fully pearlitic steels," *Metall. Trans. A*, vol. 7, no. 8, pp. 1217–1224, 1976.

[2] C. Peng-Heng and A. G. Preban, "The effect of ferrite grain size and martensite volume fraction on the tensile properties of dual-phase steel," *Acta Metall.*, vol. 33, no. 5, pp. 897–903, 1985.

[3] S. Takaki, K. Kawasaki, and Y. Kimura, "Mechanical properties of ultra fine grained steels," *J. Mater. Process. Technol.*, vol. 117, no. 3, pp. 359–363, 2001.

[4] B. Mintz and D. V. Wilson, "Strain ageing during the fatigue of carbon steels," *Acta Metall.*, vol. 13, no. 9, pp. 947–956, 1965.

[5] M. Srinivas, G. Malakondaiah, R. W. Armstrong, and P. Rama Rao, "Ductile fracture toughness of polycrystalline armco iron of varying grain size," *Acta Metall. Mater.*, vol. 39, no. 5, pp. 807–816, 1991.

[6] T. Hanamura, F. Yin, and K. Nagai, "Ductile-brittle transition temperature of ultrafine ferrite/cementite microstructure in a low carbon steel controlled by effective grain size," *ISIJ Int.*, vol. 44, no. 3, pp. 610–617, 2004.

[7] T. Hanamura, S. Torizuka, S. Tamura, S. Enokida, and H. Takechi, "Effect of Austenite Grain Size on Transformation Behaviour, Microstructure and Mechanical Properties of 0.1C–5Mn Martensitic Steel," *ISIJ Int.*, vol. 53, no. 12, pp. 2218–2225, 2013.

[8] K. D. Ralston and N. Birbilis, "Effect of grain size on corrosion: A review," *Corrosion*, vol. 66, no. 7, pp. 0750051–07500513, 2010.

[9] M. Pisarek, P. Kędzierzawski, M. Janik-Czachor, and K. J. Kurzydłowski, "Effect of hydrostatic extrusion on passivity breakdown on 303 austenitic stainless steel in chloride solution," *J. Solid State Electrochem.*, vol. 13, no. 2, pp. 283–291, 2009.

[10] A. Abbasi Aghuy, M. Zakeri, M. H. Moayed, and M. Mazinani, "Effect of grain size on pitting corrosion of 304L austenitic stainless steel," *Corros. Sci.*, vol. 94, pp. 368–376, 2015.

[11] A. Di Schino and J. M. Kenny, "Effect of grain size on the corrosion resistance of a high nitrogen-low nickel austenitic stainless steel," *J. Mater. Sci. Lett.*, vol. 21, no. 24, pp. 1969–1971, 2002.

[12] A. Di Schino, M. Barteri, and J. M. Kenny, "Grain size dependence of mechanical, corrosion and tribological properties of high nitrogen stainless steels," *J. Mater. Sci.*, vol. 38, no. 15, pp. 3257–3262, 2003.

[13] X. Y. Wang and D. Y. Li, "Mechanical, electrochemical and tribological properties of nano-crystalline surface of 304 stainless steel," *Wear*, vol. 255, no. 7–12, pp. 836–845, 2003.

[14] V. Afshari and C. Dehghanian, "Effects of grain size on the electrochemical corrosion behaviour of electrodeposited nanocrystalline Fe coatings in alkaline solution," *Corros. Sci.*, vol. 51, no. 8, pp. 1844–1849, 2009.

[15] L. Jinlong and L. Hongyun, "The effects of cold rolling temperature on corrosion resistance of pure iron," *Appl. Surf. Sci.*, vol. 317, pp. 125–130, 2014.

[16] Y. Yilmaz, A; Li, Xi; Pletincx, S; Hauffman, T; Sietsma, J; Gonzalez-Garcia, "The effect of prior austenite grain size (PAGS) on passive layer properties of fully martensitic steel," *To be Publ.*

[17] J. Jiang, T. B. Britton, and A. J. Wilkinson, "Measurement of geometrically necessary dislocation density with high resolution electron backscatter diffraction: Effects of detector binning and step size," *Ultramicroscopy*, vol. 125, pp. 1–9, 2013.

[18] P. J. Konijnenberg, S. Zaefferer, and D. Raabe, "Assessment of geometrically necessary dislocation levels derived by 3D EBSD," *Acta*

Mater., vol. 99, pp. 402–414, 2015.

[19] B. L. Adams and J. Kacher, "EBSD-based microscopy: Resolution of dislocation density," *Comput. Mater. Contin.*, vol. 14, no. 3, pp. 183–194, 2009.

[20] F. Bachmann, R. Hielscher, and H. Schaeben, “Texture analysis with MTEX- Free and open source software toolbox,” *Solid State Phenom.*, vol. 160, pp. 63–68, 2010.

[21] F. Bachmann, R. Hielscher, and H. Schaeben, "Grain detection from 2d and 3d EBSD data-Specification of the MTEX algorithm," *Ultramicroscopy*, vol. 111, no. 12, pp. 1720–1733, 2011.

[22] M. C. Biesinger, B. P. Payne, A. P. Grosvenor, L. W. M. Lau, A. R. Gerson, and R. S. C. Smart, "Resolving surface chemical states in XPS analysis of first row transition metals, oxides and hydroxides: Cr, Mn, Fe, Co and Ni," *Appl. Surf. Sci.*, vol. 257, no. 7, pp. 2717–2730, 2011.

[23] R. P. Gupta and S. K. Sen, “Calculation of multiplet structure of core p-vacancy levels,” *Phys. Rev. B*, vol. 10, no. 1, pp. 71–77, 1974.

[24] M. P. Strehblow H, "X-ray photoelectron spectroscopy in corrosion research. In: Marcus P, Mansfeld F (eds) Analytical methods in corrosion science and engineering.," *CRC Press Taylor Fr.*, 2006.

[25] L. Freire, X. R. Nóvoa, M. F. Montemor, and M. J. Carmezim, "Study of passive films formed on mild steel in alkaline media by the application of anodic potentials," *Mater. Chem. Phys.*, vol. 114, no. 2–3, pp. 962–972, 2009.

[26] I. V. Sieber, H. Hildebrand, S. Virtanen, and P. Schmuki, "Investigations on the passivity of iron in borate and phosphate buffers, pH 8.4," *Corros. Sci.*, vol. 48, no. 11, pp. 3472–3488, 2006.

[27] Y. Li and Y. F. Cheng, "Passive film growth on carbon steel and its nanoscale features at various passivating potentials," *Appl. Surf. Sci.*, vol. 396, pp. 144–153, 2017.

[28] H.-H. Strehblow, *Passivity of Metals: Advances in Electrochemical Science and Engineering*. Wiley-VCH Weinheim, 2003.

[29] P. M. H.-H. Strehblow, V., Maurice, *Passivity of Metals, in Corrosion Mechanisms in Theory and Practise*. Boca Raton: Taylor and Francis, 2011.

[30] H. H. Strehblow, "Passivity of Metals Studied by Surface Analytical Methods, a Review," *Electrochim. Acta*, vol. 212, pp. 630–648, 2016.

[31] A. A. Herzing *et al.*, "Determination of the oxide layer thickness in core-shell zerovalent iron nanoparticles.," *Langmuir*, vol. 24, no. 8,

pp. 4329–34, 2008.

[32] H. Shinotsuka, S. Tanuma, C. J. Powell, and D. R. Penn, "Calculations of electron inelastic mean free paths. X. Data for 41 elemental solids over the 50 eV to 200 keV range with the relativistic full Penn algorithm " *Surf. Interface Anal.*, vol. 47, no. 12, p. 871– 888, 2015.

[33] K. Yanagisawa, T. Nakanishi, Y. Hasegawa, and K. Fushimi, "Passivity of dual-phase carbon steel with ferrite and martensite phases in pH 8.4 boric acid-borate buffer solution," *J. Electrochem. Soc.*, vol. 162, no. 7, pp. C322–C326, 2015.

[34] S. Joiret, M. Keddam, X. R. Nóvoa, M. C. Pérez, C. Rangel, and H. Takenouti, "Use of EIS, ring-disk electrode, EQCM and Raman spectroscopy to study the film of oxides formed on iron in 1 M NaOH," *Cem. Concr. Compos.*, vol. 24, no. 1, pp. 7–15, 2002.

[35] C. Andrade, M. Keddam, X. R. Nóvoa, M. C. Pérez, C. M. Rangel, and H. Takenouti, "Electrochemical behaviour of steel rebars in concrete: Influence of environmental factors and cement chemistry," *Electrochim. Acta*, vol. 46, no. 24–25, pp. 3905–3912, 2001.

[36] M. Büchler, P. Schmuki, and H. Böhni, "Iron passivity in borate buffer: Formation of a deposit layer and its influence on the semiconducting

properties," *J. Electrochem. Soc.*, vol. 145, no. 2, pp. 609–614, 1998.

[37] C. H. Hsu and F. Mansfeld, "Concerning the conversion of the constant phase element parameter Y0 into a capacitance," *Corrosion*, vol. 57, no. 9, pp. 747–748, 2001.

[38] A. J. Bard and L. R. Faulkner, *Electrochemical Methods: Fundamentals and Applications*, 2nd. ed. John Wiley & Sons, 2001.

[39] K. Azumi, "Mott-Schottky Plot of the Passive Film Formed on Iron in Neutral Borate and Phosphate Solutions," *J. Electrochem. Soc.*, vol. 134, no. 6, p. 1352, 1987.

[40] J. H. Kennedy and K. W. Frese, "Flatband Potentials and Donor Densities of Polycrystalline α -Fe2O3 Determined from Mott-Schottky Plots," *J. Electrochem. Soc.*, vol. 125, no. 5, pp. 723–726, 1978.

[41] P. Schmuki and H. Böhni, "Illumination effects on the stability of the passive film on iron," *Electrochim. Acta*, vol. 40, no. 6, pp. 775–783, 1995.

[42] Y. Takabatake, K. Fushimi, T. Nakanishi, and Y. Hasegawa, "Grain-Dependent Passivation of Iron in Sulfuric Acid Solution," *J. Electrochem. Soc.*, vol. 161, no. 14, pp. C594–C600, 2014.

[43] R. M. Cornell and U. Schwertmann, *The iron oxides; Structure*

Properties, Reactions, Occurrences and Uses. 2003.

[44] L. Hamadou, A. Kadri, and N. Benbrahim, "Characterisation of passive films formed on low carbon steel in borate buffer solution (pH 9.2) by electrochemical impedance spectroscopy," *Appl. Surf. Sci.*, vol. 252, no. 5, pp. 1510–1519, 2005.

[45] J. Wang *et al.*, "Oxygen vacancy induced band-gap narrowing and enhanced visible light photocatalytic activity of ZnO," *ACS Appl. Mater. Interfaces*, vol. 4, no. 8, pp. 4024–4030, 2012.

[46] S. A. Ansari, M. M. Khan, M. O. Ansari, S. Kalathil, J. Lee, and M. H. Cho, "Band gap engineering of CeO2 nanostructure using an electrochemically active biofilm for visible light applications," *RSC Adv.*, vol. 4, no. 32, pp. 16782–16791, 2014.

CHAPTER 5

Passive film properties of martensitic steels in alkaline environment: influence of the prior austenite grain size

This chapter is based on the scientific paper:

A. Yilmaz, K. Traka, S. Pletincx, T. Hauffman, J. Sietsma, Y. Gonzalez-Garcia Passive film properties of martensitic steels in alkaline environment: influence of the prior austenite grain size (Under review)

Abstract

The influence of the prior austenite grain size (PAGS) on the passivity of martensitic steels has been studied in an alkaline environment. Martensitic steel samples with prior austenite grain size (PAGS) ranging between 5 to 66 µm were prepared by heat treatments. Potentiodynamic (PD) polarisation reveals that the current density values in the passive region increase with PAGS refinement until reaching a critical PAGS of 28 µm, while further refinement in PAGS leads to a decrease in the current density values. EIS results of passive layers formed after potentiostatic polarisation show the same trend as the current density values in PD measurements for the charge transfer resistance values. However, capacitance measurements (Mott-Schottky analysis) reveal a continuous increase in donor density with PAGS refinement. X-ray Photoelectron Spectroscopy (XPS) analysis shows that the passive layers formed potentiostatic polarisation consists of Fe_3O_4, γ-Fe_2O_3, and FeO(OH). The oxide ratio differs as a function of PAGS. γ-Fe_2O_3 fraction decreases with PAGS refinement until PAGS of 28 m, while further PAGS refinement to 5 µm leads to an increase in γ-Fe_2O_3 volume fraction in passive layers. The worsening in passive layers' electrochemical properties with PAGS refinement from 66 to 28 µm is attributed to the decrease in γ-Fe_2O_3

fraction and donor density. However, the enhancement in passive layers' electrochemical properties with further PAGS refinement is observed due to the increase in γ-Fe_2O_3 fraction. The enhancement in passive layer properties with further PAGS refinement to 5 µm is attributed to the dominance of changes within the complex martensite structure on PAGS.

Keywords: *Martensitic steels, grain-size, Passivity, EIS, Mott-Schottky, XPS*

5.1 Introduction

High-strength steels are of significant interest to both engineering and scientific societies because of their good mechanical properties [1]. Hence, they have found a wide range of applications varying from infrastructure, automotive to oil and gas industries. Engineering the microstructure of high strength steels to enhance their properties is therefore of enormous relevance. Grain refinement is of special significance since it generally improves the mechanical properties of the steel. Although quantitative relations are available for mechanical properties such as strength and hardness, this is not the case for the corrosion properties. This fact has been highlighted in the recent review by Ralston and Birbilis [2]. In this review, a holistic review of current literature related to the relationship between grain size and corrosion resistance for a wide range of metals was presented. For the case of steels, it is possible to find literature that reported contradictory results on the relationship between grain size and both corrosion behaviour and passive layer properties.

The effect of grain refinement on the passive layer properties of ferritic stainless steels was investigated [3]. It was reported that the barrier properties of the passive layer worsen with grain refinement. This is

attributed to the increase in both acceptor and donor density with grain refinement. In another research, the role of grain refinement on passive layer properties of austenitic stainless steels is studied in a borate buffer solution containing chloride [4]. An increase in the current density values at the passive region of potentiodynamic polarisation and a decrease in breakdown potential was observed with grain refinement, also showing that the barrier properties of passive film deteriorate with grain refinement. However, it was also reported that the size of non-metallic inclusions changes, and dislocation density increases during hydrostatic extrusion, used for achieving different grain sizes. In our other research, the role of grain size on the passive layer of pure iron was investigated for grain sizes in the micron range [5]. It was observed that grain refinement leads to an increase in the passivity current density in the potentiodynamic polarisation curves and lower resistance values in the electrochemical impedance spectroscopy (EIS) analysis. This deterioration in the barrier properties of the passive film stems from the increase in donor density and decrease in the fraction of protective γ-Fe_2O_3 in the passive film.

In contrast to these studies, the improvement in the barrier properties of the passive layer with grain refinement is also reported. The effect of

grain refinement induced by cold rolling on the passivity behaviour of pure iron was studied in a borate buffer solution [6]. An improvement in the barrier properties of the passive film with grain refinement was observed, associated with the decrease in donor density in the passive film. However, the formation of texture was also reported besides grain refinement after the cold rolling used for manipulating the grain size.

These contradictory reports show that no straightforward relationship between grain size and passive layer properties has been established. These discrepancies arise because the processes applied for grain refinement may lead to other variations within the microstructure, such as dislocation density, crystallographic orientation, inclusions and segregation of alloying elements. All these microstructural features might have a combined effect on passive layer properties, causing discrepancies on the results if no systematic approach is followed on the processing of the microstructure. This shows that the major challenge still lies in the great difficulty to isolate the effect of each microstructural feature on the corrosion properties of the steel.

In this work, the effect of prior austenite grain size (PAGS) on the passive layer properties of fully martensitic steels is investigated. Several heat

treatments were applied to obtain samples with different PAGS while minimizing the changes in other microstructural features. Low alloyed carbon steel was employed to minimise the presence of secondary phases and possible alloy segregation. Electron backscatter diffraction (EBSD) analysis was conducted to provide a detailed analysis of the microstructural differences after heat treatments. X-ray photoelectron spectroscopy (XPS) was performed to determine the chemical composition and thickness of passive films. The barrier properties of passive films for the specimens with different PAGS were evaluated with potentiodynamic polarisation (PDP) and electrochemical impedance spectroscopy (EIS). The electronic properties of passive films were determined with capacitance measurements (Mott-Schottky analysis). These experimental results form the basis for discussing the effect of the prior-austenite grain size on the properties of passive films formed on fully martensitic steels.

5.2. Experimental

5.2.1 Material

5.1 Material

The as-received material was dual-phase steel sheets with a thickness of 1 mm (DP600 provided by Tata Steel, IJmuiden, The Netherlands). The

chemical composition of the material is given in Table 5.1. Samples were laser cut to the dimensions of 10 mm x 5 mm. The chemical composition of the steel samples was determined with a JEOL JXA 8900R microprobe that applies an electron beam with energy of 10 keV and beam current of 100 nA using Wavelength Dispersive Spectrometry (WDS). The composition at each analysis location of the sample was determined using the X-ray intensities of the constituent elements after background correction relative to the corresponding intensities of reference materials.

	Fe	***C***	***Si***	***Mn***	***Al***	***Cr***	***N***	***Ni***	***Ti***
wt.%	bal.	0.095	0.248	1.776	0.032	0.574	0.008	0.026	0.003

Table 5.1 Chemical composition (wt.%) of the low alloyed steel specimens

5.2.2 Design of microstructure

In order to obtain the desired martensitic microstructures with different prior austenite grain sizes, the as-received material was heat treated at different temperatures for specific times. The Thermo-Calc software was used to determine the single-austenite phase range to choose the appropriate annealing temperature and time. Four different heat treatment

strategies (Fig. 5.1) were followed to create martensitic steels with varying PAGS. The heat treatments were as follows:

- Heat treatment 1 (HT-1) - Samples were heated to the austenitisation temperature of 900 ^{o}C, held for 10 min. under vacuum and quenched to room temperature.
- Heat treatment 2 (HT-2) - Higher austenitisation temperature of 1000 ^{o}C was chosen. Samples were held at austenitisation temperatures for 4 min. Subsequently, samples were quenched to room temperature.
- Heat treatment 3 (HT-3) - Samples were heated to the austenitisation temperature of 1000 ^{o}C, held for 60 min. under vacuum, then quenched to room temperature.
- Heat Treatment 4 (HT-4) - Samples were heated to 1200 ^{o}C and held 48 hours in a furnace and cooled to room temperature. Subsequently, the samples were annealed at the austenitisation temperature of 1000 ^{o}C for 30 min. under vacuum in the dilatometer, then quenched to room temperature.

The heat treatments were conducted under vacuum in a dilatometer (Bähr DIL 805 A/D). Samples were heated with a heating rate of 10 ^{o}C/s and

quenched with helium gas to room temperature with a cooling rate of 50 ^{o}C/s.

.

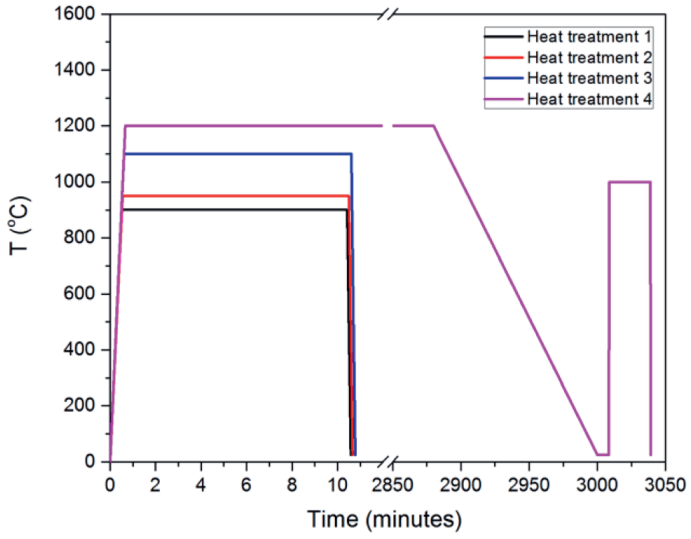

Figure 5.1 Heat treatment operations that were applied to obtain fully martensitic steels with various prior austenite grain sizes

5.2.3 Characterisation of microstructure

The optical micrographs were taken with a Keyence VHX-5000 digital optical microscope after etching with the agent Nital 2%, rinsing with ethanol and drying with compressed clean air.

Electron backscatter diffraction (EBSD) imaging was applied to identify and measure the PAGSs and estimate the geometrically necessary dislocation (GND) density of the samples after the corresponding heat treatments. The samples were ground from 80 to 2000 grit SiC papers and

subsequently polished with diamond particle slurry with the particle diameters of 3 and 1 μm. Then, standard colloidal silica suspension with 0.04 μm particles was employed for the final polishing of the surface. A JEOL JSM-6500F field emission gun scanning electron microscope (FEG-SEM) operating at an acceleration voltage of 20 kV was used for EBSD imaging. For EBSD mapping, a work distance of 10 mm was used. The step size was 50 nm. The geometrically necessary dislocation (GND) distribution was determined with the help of the electron backscatter diffraction (EBSD). TSL OIM v8 analysis software was used for the EBSD data analysis. For GND density calculation, the function in OIM v7.3 software described in [7] was employed. To identify the PAGS, clean-up was done by applying neighbour orientation correlation as well as grain dilatation tools provided with the OIM v7.3 software, as described in [8]. Then, the linear intercept method was used for measuring the size of the prior austenite grains.

5.2.4 Electrochemical measurements

The samples were embedded in Struers ClaroCit resin and cured for 1 hour under 2 bar pressure. Subsequently, the samples were ground from 80 to 2000 grit SiC paper, then polished with 3 and 1 μm diamond particle slurry h until obtaining a mirror-like polished surface. The samples were cleaned

ultrasonically within an ultrasonic bath for 10 min in ethanol before the electrochemical measurements. The resin/metal interface was covered with a thin layer of sealing lacquer (Electolube Bloc Lube Red) to avoid crevice corrosion.

All electrochemical measurements were conducted in aerated 0.1 M NaOH solution with a pH of 12.75 prepared with Milli-Q® ultra pure water. Measurements were carried out at room temperature. A conventional three-electrode electrochemical cell setup, consisting of the sample as working electrode, graphite rod as counter electrode and Ag/AgCl (sat. KCl) as the reference electrode, was employed. The polarisation and electrochemical impedance spectroscopy experiments were carried out using a Solartron 1257 potentiostat combined with SI 1255 HF frequency response analyser (FRA). Pre-passivation of the samples and subsequent capacitance measurements (Mott-Schottky analysis) were carried out with a Biologics SP300 potentiostat. Open Circuit Potential (OCP) was measured for 30 min. before all electrochemical measurements.

Potentiodynamic polarisation measurements were carried out within the potential range of -0.25 V to 1.25 V (vs OCP) with a scan rate of 0.167 mV/sec. Before EIS and capacitance experiments, samples were

passivated by potentiostatic polarisation for 6 hours. Two passivation potentials were studied: 0.2 and 0.4 V. EIS data were acquired in the frequency range from 30 kHz to 10 mHz with an amplitude of 10 mV peak to peak for the AC signal. Capacitance measurements (Mott-Schottky analysis) were conducted at the frequency of 1 kHz with an amplitude of 10 mV peak to peak for the AC signal and 50 mV potential step size. The potential sweep was conducted from 0.6 V to -1 V.

For the data analysis, CorrView software was used for potentiodynamic and potentiostatic polarisation measurements and Zview for EIS and ECLab for capacitance measurements.

5.2.5 Passive layer analysis

X-ray photoelectron spectroscopy (XPS) studies were performed to analyse the chemical composition of passive films. The samples were passivated with potentiostatic polarisation at both 0.2 V and 0.4 V for 6 hours. Before XPS measurements, pre-passivated samples were rinsed with ethanol and dried with compressed clean air. XPS spectra were recorded using a PHI5600 photoelectron spectrometer (Physical Electronics) with an Al K monochromatic X-ray source (1486.71 eV photon energy). The low pressure in the analysis chamber was at a maximum of 5 x 10^{-9} Torr during

measurements. A take-off angle of 45° was chosen for the measurements. A variation of the angle to 90° allowed to elucidate the build-up of the oxides on the surface. A spot diameter of 0.8 mm was used for the high-resolution scans of the Fe 2p and O 1s core electron peaks. An energy of 0.1 eV and pass energy of 23.5 eV were applied. PHI Multipak software (V9.5) was used for XPS data analysis. The XPS data were fitted with CasaXPS software.

5.3 Results and Discussion

5.3.1 Microstructure characterisation of the martensitic steels

Low alloyed steel was chosen to minimise the formation of secondary phases and alloy segregation that may influence the passive layer properties. In Figure 5.2, optical micrographs of the resulting microstructures after the different heat treatments are given. Micrographs show the fully martensitic steel structure composed of very complex sub-grain structures in all samples. High-resolution electron backscatter diffraction (EBSD) measurements were conducted to determine the average PAGS. The results from the EBSD analysis are summarised in Table 5.2. The heat treatment with the lowest austenitisation temperature (HT-1) shows the finest average grain size, 5 µm. The application of higher austenitisation

temperatures results in larger average PAGS, 28 µm and 38 µm for HT-2 and HT-3, respectively. To obtain even larger grains, pre-annealing in a furnace at 1200 ^{o}C was conducted in HT-4. In this case, samples present an average grain size of 66 µm. The prior-austenite grain size increases with increasing austenitisation temperature, which agrees with previous studies of fully martensitic steels [9].

Additionally, from the EBSD measurements, the geometrically necessary dislocation (GND) density was obtained through the local orientation distribution analysis. Figure 3 shows the selected GND density map of sample 2 (PAGS 28 µm). Local differences in the distribution of the GND in fine (block width smaller than 5 µm) and coarse martensite (block width larger than 5 µm) are observed. The coarse martensite (shown with arrows in Figure 5.3) shows lower dislocation density values in comparison with fine martensite. The average GND values are given in Figure 5.4. The GND densities for fine and coarse martensite are in the same order for all samples, with a variation between 10^{14} and 2 x 10^{14} m^{-2}, showing that the average GND density is not significantly affected by the grain size.

Concerning dislocation density, only the geometrically necessary dislocations (GNDs) are considered. Statistically stored dislocation (SSD)

density can also contribute to the total dislocation density in the material, but their density cannot be derived from the present observations.

	Sample 1	***Sample 2***	***Sample 3***	***Sample 4***
PAG Size	5.2 ± 1.5 µm	28 ± 3 µm	38 ± 4 µm	66 ± 6 µm

Table 5.2 Prior Austenite Grain Sizes (PAGS) of the samples after undergoing the heat treatments

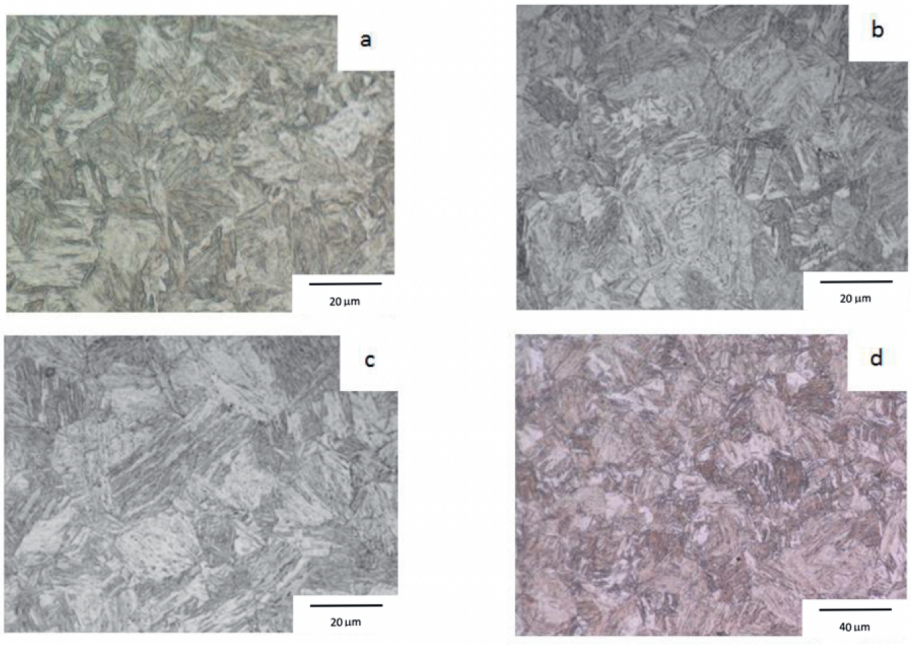

Figure 5.2 Optical images corresponding to a) Sample1 b) Sample 2 c) Sample 3 and d) Sample 4

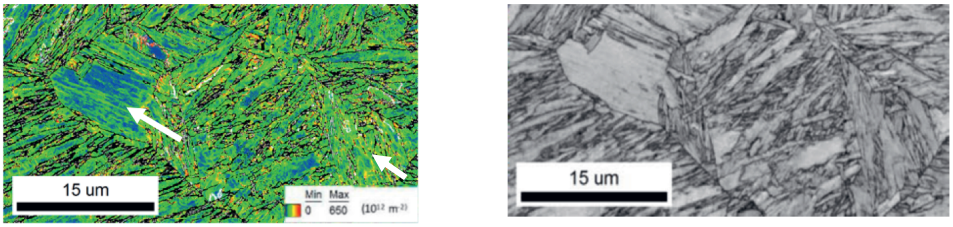

Figure 5.3 EBSD a) Geometrically Necessary Dislocation (GND) density and b) Band-contrast maps of Sample 2. The GNDs were calculated for a maximum angle of 10° and up to the 3rd neighbor pixel.

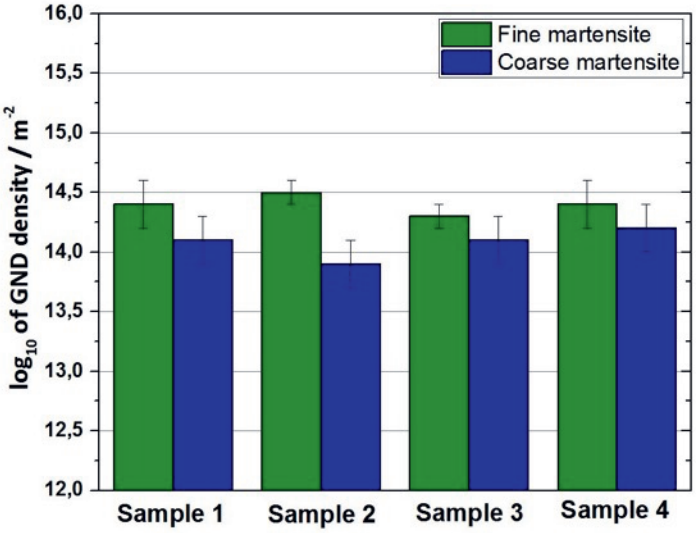

Figure 5.4 Geometrically Necessary Dislocation (GND) density values of all samples

5.3.2 Passive layer analysis

The chemical composition of passive layers was investigated using X-ray Photoelectron Spectroscopy (XPS). Figure 5.5a shows the selected high-resolution Fe $2p_{3/2}$ spectrum of sample 4 (66 μm PAGS) after pre-passivation

at a potential of 0.4 V. To identify the composition of the passive layer, the Fe 2p spectra were fitted by using the multiplet-splitting fitting [10]–[12]. Multiplet splitting occurs for Fe since high-spin Fe(II) and Fe(III) species contain unpaired *d*-electrons, which leads to coupling between a photoionized core electron vacancy and an unpaired outer *d* orbital electron [10]. This leads to several energy states with close binding energies. The fitting of the close binding energies provides accurate quantification of (hydr)oxides. Multiplet-splitting fitting was applied with the reported fitting parameters [12]. The fitting corresponds to fractions of Fe_3O_4, γ-Fe_2O_3 and FeOOH, in agreement with the research that indicates the same passive layer build-up in low-alloyed carbon steels [12]–[15]. In Figure 5b, the high-resolution O 1s spectrum of sample 4 is presented. From the fitting the presence of hydroxide lattice, OH^-, and oxides lattice, O^{-2}, peaks. Furthermore, a low contribution of adsorbed water (H_2O adsorption peak) is observed. The ratio between the contributions of lattice O^{-2} (iron oxides) and lattice OH^- varies, depending on the PAGS of samples and passivation potential (not shown here).

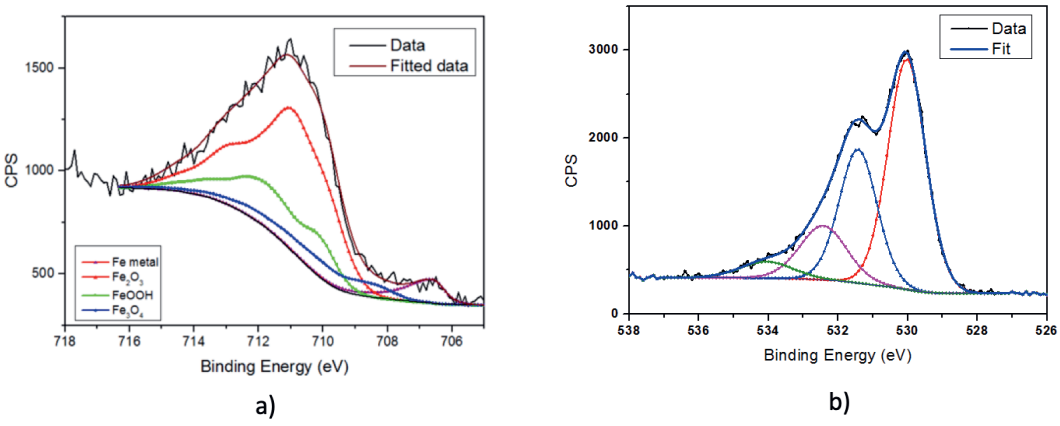

Figure 5.5 High-resolution XPS a) Fe 2p and b) O 1s spectrum of Sample 4. Passive layer is formed with potentiostatic polarisation for 6 hours at 0.4 V (vs. Ag/AgCl) in 0.1 M NaOH solution

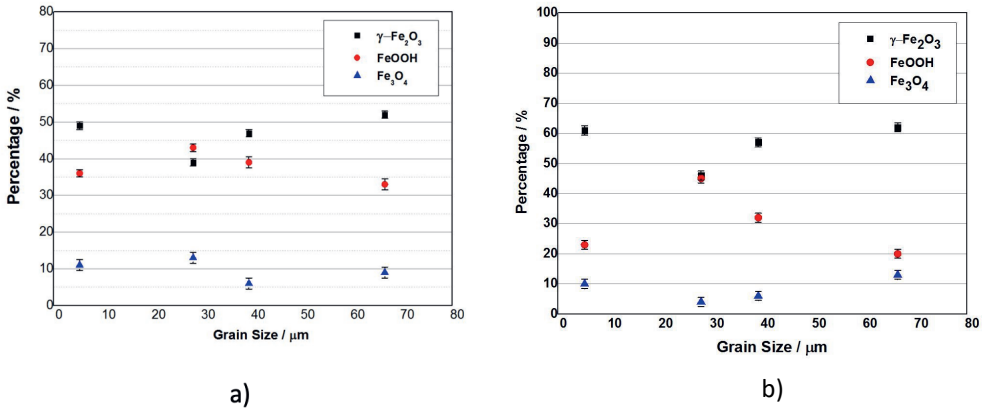

Figure 5.6 The fractions of oxides and hydroxide depending on PAGS for samples passivated with potentiostatic polarisation at a) 0.2 V and b) 0.4 V (vs. Ag/AgCl)

Figures 5.6a and 5.6b present the fractions of Fe_3O_4, γ-Fe_2O_3 and FeOOH in the passive film for all samples after passivation at 0.2 V and 0.4 V, respectively. Firstly, it is possible to observe the differences between oxides and hydroxide ratios between both potentials. The volume fractions of γ-Fe_2O_3 oxide are higher for the case of 0.4 V, with values between 45 and 62%, they are in the range of 40-50% for 0.2 V. For the case of Fe_3O_4 oxides, there are small variations between potentials, with Fe_3O_4 content in the range of 5-12%. For the case of FeOOH, at 0.2V, passive layers show content between 30 and 43%. But for the more positive potential, the content of hydroxide is on average lower. However, the magnitude of the variation depends on the PAGS, fluctuating from 20 to 45 %. At 0.2 V passivation potential, a decrease in γ-Fe_2O_3 percentage from 53 to 39% is observed with the refinement of PAG of 66 to 28 µm. However, further refinement of the grains leads to an increase in γ-Fe_2O_3 percentage, reaching a value of 49% for the sample with 5 µm PAGS. A similar trend is observed for the samples passivated at 0.4 V. A gradual decrease of γ-Fe_2O_3 from 63 to 46% was observed with PAGS refinement from 66 to 28 µm, while further refinement in PAGS to 5 µm leads to an increase in γ-Fe_2O_3 percentage to 61%. A higher contribution of oxide than hydroxide species at the more positive potential

0.4 V is observed for all samples, which agrees with previously reported results by Li et al. [16].

The thickness of the oxide layers was estimated from the analysis of the Fe 2p spectra data by applying the equation proposed by Herzing et al. [17]:

$$d = \lambda_{ox} cos\theta \ln\left(\frac{N_{Fe}\lambda_{Fe}}{N_{ox}\lambda_{ox}} \frac{I_{ox}}{I_{Fe}} + 1\right) \text{[Eqn. 1]}$$

where d is oxide thickness, I_{Fe} is the photoelectron intensity of metallic iron (209.7), I_{ox} is the intensity of γ-Fe_2O_3 (3654.1), N is the number of atoms per unit volume, λ_{Fe} is the inelastic mean free electron path in metallic iron (1.1 nm), λ_{ox} is the inelastic mean free electron path in γ-Fe_2O_3 (1.1 nm), and θ is the detection angle (45º). In this equation, it is assumed that the passive layer is composed of only γ-Fe_2O_3. In Table 5.3, the calculated thickness for all samples is presented. For both potentials, the variation of thickness for the different PAGS is limited to ±0.1 nm. For the 0.2 V potential, the passive layers formed have an average thickness of 3.02 ± 0.09 nm. In the case of 0.4V, passive layers are slightly thicker, with an average thickness of 3.27 ± 0.05 nm.

	Passive layer thickness/ nm			
Passivation Potential/ V	***Sample 1***	***Sample 2***	***Sample 3***	***Sample 4***
0.2	3.0 ± 0.2	2.9 ± 0.1	3.1 ± 0.2	3.1 ± 0.2
0.4	3.2 ± 0.2	3.3 ± 0.2	3.3 ± 0.2	3.3 ± 0.2

Table 5.3 Passive layer thickness values of all samples acquired from XPS data

5.3.3 Electrochemical investigation

Potentiodynamic Polarisation - Figure 5.7a shows the potentiodynamic polarisation curves of all samples with different PAGS during immersion in 0.1 M NaOH solution. The cathodic branch is attributed to the reduction of oxygen dissolved in the solution. After reaching the corrosion potential, the anodic current increases until reaching a plateau corresponding to the passivity region. Figure 5.7b shows the passivity current densities measured from the polarisation curves at two selected potentials, 0.2 and 0.4 V. At both potentials, the current density values increase by a factor 4 with PAGS refinement from 66 to 28 µm. However, further refinement in grain size to 5 µm causes a decrease in current density by a factor 2. The significant difference in the passivity current density values shows that the electrochemical properties of passive layers are affected by the prior

austenite grain size. Interestingly, the current differences do not follow a monotonous dependency with the refinement of the grains.

Moreover, it is observed that the current density values for all samples are higher for passive layers formed at 0.4 V in comparison to layers formed at 0.2 V. This indicates that the passive layers formed at more positive potentials are less conductive than the ones formed at lower potentials, in line with previous research [3], [18], [19].

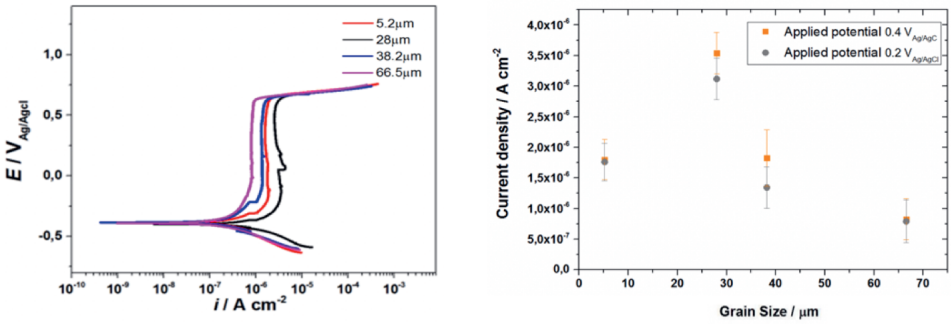

Figure 5.7 a) Potentiodynamic polarisation curves in 0.1 M NaOH solution b) Current density values measured at 0.2 and 0.4 V (vs. Ag/AgCl) as a function of PAGS

EIS measurements – EIS data was acquired from the passivated samples at both 0.2 and 0.4 V in 0.1M NaOH solution. Fig. 5.8a shows the Nyquist plots of the pre-passivated samples at 0.4 V. The impedance values are highest for the sample with 66 µm grain size. With PAGS refinement to

28 µm, the impedance values decrease, while further refinement to 5 µm causes an increase in the impedance. This behaviour is observed for both pre-passivation potentials.

A quantitative analysis of the equivalent electrical circuit fitting was carried out for EIS data. An equivalent circuit with two *R-CPE* (resistance – Constant Phase Element) elements in parallel (Fig. 9b) provides the best fitting for EIS data. *CPEs* are employed instead of a capacitance element C since no fully capacitive behaviour is observed as indicated by *CPE* coefficients lower than 1. R_1 is associated with the resistance of the solution. R_2 and CPE_2 are associated with the resistive and capacitive behaviour of the double layer, respectively. The resistive and capacitive behaviour of the passive layer is represented by R_3 and CPE_3, respectively. This equivalent circuit has been proposed in previous research to describe the passive layer of similar systems [13], [20]–[23]. The fitting results are summarized in Fig. 5.9a and 5.9b.

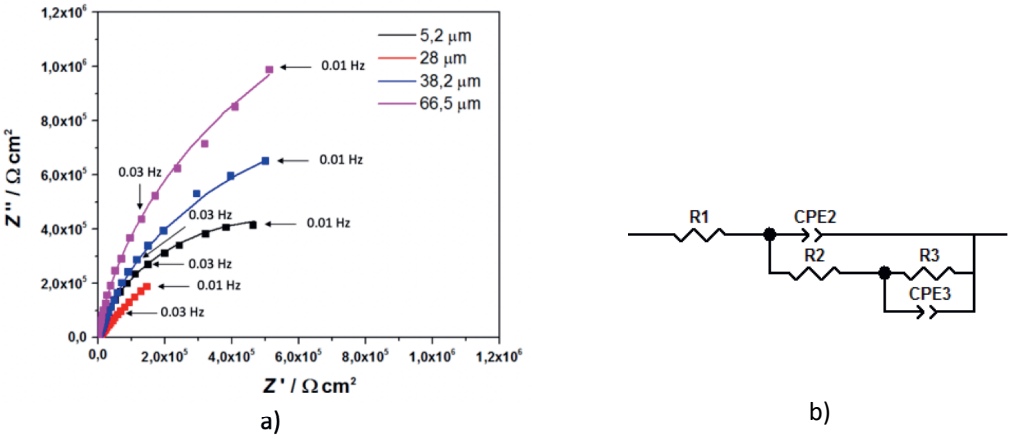

Figure 5.8 a) Nyquist plots of samples collected after passivation with potentiostatic polarisation at 0.4 V for 6 hours in 0.1 M NaOH solution b) Equivalent electrical circuit (EEC/) used to interpret the EIS-data for all samples. Solid lines represent the fitted data.

Fig. 5.9a and 5.9b show the charge transfer resistance values of the double layer (R_2) and passive layer (R_3), respectively, for both pre-passivation potentials, 0.2 and 0.4 V. R_2 is two orders of magnitude lower than R_3, indicating that the protective capacity of the double layer is much lower than that of the passive layers. Fig. 10b shows that the resistance of the passive layer (R_3) decreases by a factor 2 at both potentials upon PAGS refinement from 66 to 28 µm. However, the resistance values of oxide layers (R_3) increases with further refinement to 5 µm. These results agree with the trends in passivity currents observed in the potentiodynamic experiments. Furthermore, the resistance values of the oxide layers (R_3) are higher in all

samples at pre-passivation potential 0.4 V in comparison with 0.2 V, which agrees with the trend observed in the passivity current densities from the polarisation results.

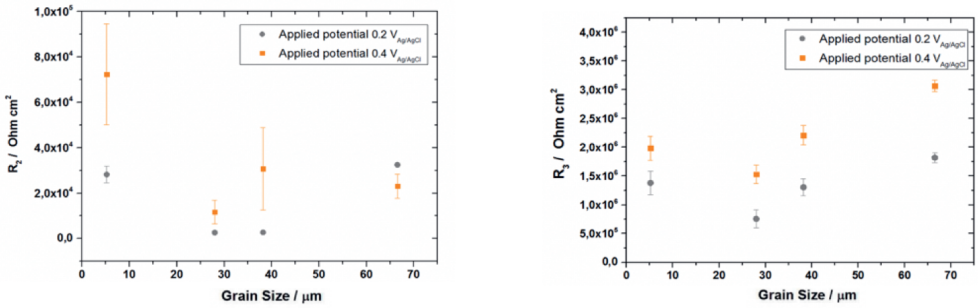

a) b)

Figure 5.9 Resistance values of a) R_2 corresponding to the double layer and b) R_3 corresponding to passive layer

Capacitance measurements - Mott-Schottky analysis was applied to evaluate the semi-conductive behaviour of the passive layers. This analysis allows to assess the electronic properties of the oxides and correlate them with the electrochemical properties as a function of the prior austenite grain size. The Mott-Schottky relationship

$$\frac{1}{C^2} = 2(E - E_{FB} - kT/q)/\varepsilon\varepsilon_o q\, N_d \quad \text{[Eqn. 2]}$$

can be applied for calculating the donor density. In this equation ε is the dielectric constant of the passive film reported for carbon steels [24], ε_0 the

permittivity of free space, q the electron charge, N_d the donor density, E_{FB} the flat band potential, k the Boltzmann constant and T the absolute temperature. Fig. 5.10a shows the variations in the Mott-Schottky plot (C^{-2} vs potential) of the pre-passivated samples at 0.4 V. For n-type semiconductor behaviour, C^{-2} vs. V in the Mott-Schottky plot has a positive slope that is inversely proportional to the donor density of the passive layer. Hence, the passive layer formed on all samples shows n-type semiconductor behaviour. However, non-linear behaviour (two positive slopes with a transition at -0.1 V) is observed in Mott-Schottky plots. This non-linear behaviour is attributed to donors' inhomogeneous distribution within the passive layer [35,36]. It is proposed that the band gap contains a deep donor level stemming from changes in chemical states within the passive layer, leading to structural changes in the passive layer [27], [28]. The deep donor level occurs in the band gap and the potential at which sharp changes in the slope of the Mott-Schottky plot are observed, corresponds to the ionisation of the deep donor level in the band gap. It is suggested to calculate the donor density levels from the two slopes with [24]:

$$S_1 = \frac{2}{\varepsilon\varepsilon_0 e N_1} \text{ for } E<E_c \text{ (Eqn. 5.3a)}$$

$$S_2 = \frac{2}{\varepsilon\varepsilon_0 e (N_1+N_2)} \text{ for } E>E_c \text{(Eqn. 5.3b)}$$

where E_c is the potential at which the slope change occurs and is considered as the critical potential for the ionization of deeper donor density, N_1 is the donor density level that has an energy level close to the conduction band and N_2 is the deep donor density level that occurs deeper in the band gap.

Fig. 5.10b shows the donor density values (N_1 and N_2) obtained at samples passivated at both 0.2 and 0.4 V (vs. Ag/AgCl). The donor density values (Fig. 10b), in the order of 10^{21} cm^{-3}, are comparable with the previous work on passive layer properties of martensitic steels in an alkaline environment [22] and shows that passive layer is highly defective. The donor density level N_1 (the donor density level that has an energy level closer to the conduction band) is higher than N_2 (the deeper donor density level) for all samples and agrees with previously reported results [27]. Furthermore, it is observed that both donor density values are at lower values for samples passivated at more positive potentials. From the results in Fig. 5.10b, it is elucidated that both donor density values depend on PAGS and show an increasing trend with decreasing PAGS. The donor population in the passive layer affects both ionic and electronic resistivity of the passive layer. The higher donor density in the passive layer leads to a more narrow band gap in metal oxides [31], [32]. Therefore, the electron transfer in a

passive layer becomes easier, leading to lower electronic resistivity in the passive layer. In terms of ionic resistivity of the passive layer, the ionic charges in iron oxide are carried by the donors in iron oxide films [33], [34]. Hence, an increase in donor density facilitates the charge transfer, lowering the passive film's ionic resistivity. Considering the decrease in passive film's electronic and ionic conductivity, an increase in donor density leads to higher conductivity in the passive film.

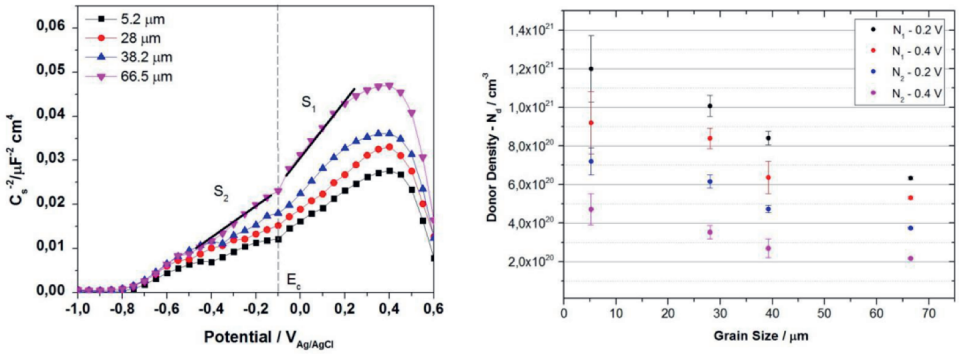

Figure 5.10 a) Mott-Schottky plot of samples after forming passive layer at 0.4 V (vs. Ag/AgCl) for 6 hours. b) Donor density values of the passive layers formed at both 0.2 and 0.4 V (vs. Ag/AgCl) for 6 hours

The electrochemical measurement results discussed above show that the electrochemical properties of passive films formed on martensitic steels are dependent on prior austenite grain size and worsen with

decreasing PAG size from 66 µm to 28 µm. One of the factors of the deterioration in the passive layer's barrier properties is the increase in donor density with PAG refinement. The decreased PAGS causes an increased grain boundary density, leading to higher donor density in passive layers. This agrees with previous studies reporting the donor density to increase with increasing grain boundary density [35]. This probably stems from the crystal lattice mismatch at grain boundaries, leading to higher donor formation of passive film formed at these sites. The donor population in the passive layer affects both ionic and electronic resistivity of the passive layer. The higher amount of donors in a passive layer leads to a more narrow band gap in metal oxides [31], [32]. Therefore, the electron transfer in the passive layer eases with the increase in donor density. In terms of ionic resistivity of passive film, the ionic charges in iron oxide are carried by the donors in iron oxide films [33], [34]. Hence, an increase in donor density facilitates the charge transfer, lowering the passive film's ionic resistivity. Considering the decrease in the passive film's electronic and ionic resistivity, the increase in donor density with PAG refinement leads to higher conductivity in passive film. Another factor in the deterioration of passive film's barrier properties is the changes in the fraction of γ-Fe_2O_3 in the

passive film with PAG refinement. Most barrier properties of the passive film are provided by γ-Fe_2O_3 since Fe_3O_4 has almost metallic conductivity due to a very small band gap of (0.1 eV) [36], whereas the large band gap of γ-Fe_2O_3 (2.3 eV) [37] provides lower conductivity. Furthermore, FeO(OH) has a less dense and porous structure, leading to high conductivity. Therefore, the decrease in γ-Fe_2O_3 in the passive film and the increase in donor density leads to the deterioration in the passive film's barrier properties with PAG refinement up to 28 μm.

Nevertheless, the further refinement in PAGS lower than 28 μm leads to improvement in the passive layer's electrochemical properties, although the donor density keeps increasing with PAG refinement. The increase in donor density can again be attributed to the formation of more defective passive film at grain boundaries due to the further increase in crystal mismatch at grain boundaries and higher misorientation angle between grains. However, PAGS refinement has other consequences within the complex martensite structure. The refinement in PAGS leads to the reduction in packet and block sizes [8] and changes the lath width-to-length ratio. It was reported that the refinement of PAG lower than a grain size of 14 μm in low carbon steels leads to significant changes within the

martensite in terms of reducing packet and block sizes [8] and martensite lath width-to-length ratio [9]. These changes within the martensite structure dominate the effect of PAG refinement on the passive layer's properties due to a significant increase in lath stored energy. This increase in lath stored energy probably affects the surface reactivity, leading to a more resistive passive layer due to an increase in the amount of protective γ-Fe_2O_3 layer.

5.4 Conclusions

This study investigates the role of prior austenite grain size on the passive layer properties formed on martensitic steels in 0.1 M NaOH solution. PAGS refinement from 66 to 28 µm leads to increased current density values in polarisation measurements and a decrease in charge transfer resistance values in EIS measurements. This deterioration in passive layer properties stems from increased donor density and decreased γ-Fe_2O_3 fraction. In this PAG size range, grain refinement is the dominant factor, controlling the passive layer properties. On the other hand, further refinement in PAGS to 5 µm leads to the decrease in current density values in polarisation measurements and the increase in charge transfer resistance values in EIS measurements. This improvement in electrochemical properties of passive

films is due to the increase in γ-Fe_2O_3 fraction. With further PAGS refinement to 5 µm, alterations within the complex martensite structure occur and have a dominance on PAGS refinement, governing the enhancement in passive layer properties.

5.5 References

[1] C. C. Tasan, M. Dieh, D. Yan, M. Bechtold, F. Roters, L. Schemmann, C. Zheng, N. Peranio, D. Ponge, M. Koyama, K. Tsuzaki, and D. Raabe "An Overview of Dual-Phase Steels: Advances in Microstructure-Oriented Processing and Micromechanically Guided Design," *Annu. Rev. Mater. Res.*, vol. 45, no. 1, pp. 391–431, 2015.

[2] K. D. Ralston and N. Birbilis, "Effect of grain size on corrosion: A review," *Corrosion*, vol. 66, no. 7, pp. 0750051–07500513, 2010.

[3] A. Fattah-Alhosseini and S. Vafaeian, "Influence of grain refinement on the electrochemical behaviour of AISI 430 ferritic stainless steel in an alkaline solution," *Appl. Surf. Sci.*, vol. 360, pp. 921–928, 2016.

[4] M. Pisarek, P. Kędzierzawski, M. Janik-Czachor, and K. J. Kurzydłowski, "Effect of hydrostatic extrusion on passivity breakdown on 303 austenitic stainless steel in chloride solution," *J. Solid State Electrochem.*, vol. 13, no. 2, pp. 283–291, 2009.

[5] A. Yilmaz, K. Traka, S. Pletincx, T. Hauffman, J. Sietsma, Y. Gonzalez-Garcia, "The effect of grain size on passive layer properties of pure iron," *To be Published.*

[6] L. Jinlong and L. Hongyun, "The effects of cold rolling temperature on corrosion resistance of pure iron," *Appl. Surf. Sci.*, vol. 317, pp. 125–130, 2014.

[7] B. L. Adams and J. Kacher, "EBSD-based microscopy: Resolution of dislocation density," *Comput. Mater. Contin.*, vol. 14, no. 3, pp. 183–194, 2009.

[8] J. Hidalgo and M. J. Santofimia, "Effect of Prior Austenite Grain Size Refinement by Thermal Cycling on the Microstructural Features of As-Quenched Lath Martensite," *Metall. Mater. Trans. A Phys. Metall. Mater. Sci.*, vol. 47, no. 11, pp. 5288–5301, 2016.

[9] C. Celada-Casero, J. Sietsma, and M. Jesus Santofimia, "The role of the austenite grain size in the martensitic transformation in low carbon steels," *Mater. Des.*, vol. 167, 2019.

[10] Y. Inokuti and R. D. Doherty, "Transmission kossel study of the structure of compressed iron and its recrystallization behaviour," *Acta Metall.*, vol. 26, no. 1, pp. 61–80, 1978.

[11] B. Hutchinson, "Deformation Microstructures and Textures in Steels," *Philos. Trans. R. Soc. Lond. Ser. Math. Phys. Eng. Sci*, vol. 357, no. 1756, 1999.

[12] B. Hutchinson, "Nucleation of recrystallisation," *Scr. Met. Mater.*, vol. 27, no. 11, pp. 1471–1475, 1992.

[13] R. P. Gupta and S. K. Sen, "Calculation of multiplet structure of core p-vacancy levels," *Phys. Rev. B*, vol. 10, no. 1, pp. 71–77, 1974.

[14] K. D. B. J.F. Moulder, W.F. Stickle, P.E. Sobol, "Handbook of X-ray Photoelectron Spectroscopy," *Perkin-Elmer Corp., Eden Prairie, MN*, 1992.

[15] M. C. Biesinger, B. P. Payne, A. P. Grosvenor, L. W. M. Lau, A. R. Gerson, and R. S. C. Smart, "Resolving surface chemical states in XPS analysis of first row transition metals, oxides and hydroxides: Cr, Mn, Fe, Co and Ni," *Appl. Surf. Sci.*, vol. 257, no. 7, pp. 2717–2730, 2011.

[16] L. Freire, X. R. Nóvoa, M. F. Montemor, and M. J. Carmezim, "Study of passive films formed on mild steel in alkaline media by the application of anodic potentials," *Mater. Chem. Phys.*, vol. 114, no. 2–3, pp. 962–972, 2009.

[17] M. P. Strehblow H, "X-ray photoelectron spectroscopy in corrosion

research. In: Marcus P, Mansfeld F (eds) Analytical methods in corrosion science and engineering.," *CRC Press Taylor Fr.*, 2006.

[18] W. Xu, K. Daub, X. Zhang, J. J. Noel, D. W. Shoesmith, and J. C. Wren, "Oxide formation and conversion on carbon steel in mildly basic solutions," *Electrochim. Acta*, vol. 54, no. 24, pp. 5727–5738, 2009.

[19] Y. Li and Y. F. Cheng, "Passive film growth on carbon steel and its nanoscale features at various passivating potentials," *Appl. Surf. Sci.*, vol. 396, pp. 144–153, 2017.

[20] A. A. Herzing *et al.*, "Determination of the oxide layer thickness in core-shell zerovalent iron nanoparticles.," *Langmuir*, vol. 24, no. 8, pp. 4329–34, 2008.

[21] J. J. Kim and Y. M. Young, "Study on the passive film of type 316 stainless steel," *Int. J. Electrochem. Sci.*, vol. 8, no. 10, pp. 11847–11859, 2013.

[22] K. Yanagisawa, T. Nakanishi, Y. Hasegawa, and K. Fushimi, "Passivity of Dual-Phase Carbon Steel with Ferrite and Martensite Phases in pH 8.4 Boric Acid-Borate Buffer Solution," *J. Electrochem. Soc.*, vol. 162, no. 7, pp. C322–C326, 2015.

[23] M. Sánchez, J. Gregori, C. Alonso, J. J. García-Jareño, H. Takenouti,

and F. Vicente, "Electrochemical impedance spectroscopy for studying passive layers on steel rebars immersed in alkaline solutions simulating concrete pores," *Electrochim. Acta*, vol. 52, no. 27 SPEC. ISS., pp. 7634–7641, 2007.

[24] M. Sánchez, H. Mahmoud, and M. C. Alonso, "Electrochemical response of natural and induced passivation of high strength duplex stainless steels in alkaline media," *J. Solid State Electrochem.*, vol. 16, no. 3, pp. 1193–1202, 2012.

[25] S. Joiret, M. Keddam, X. R. Nóvoa, M. C. Pérez, C. Rangel, and H. Takenouti, "Use of EIS, ring-disk electrode, EQCM and Raman spectroscopy to study the film of oxides formed on iron in 1 M NaOH," *Cem. Concr. Compos.*, vol. 24, no. 1, pp. 7–15, 2002.

[26] C. Andrade, M. Keddam, X. R. Nóvoa, M. C. Pérez, C. M. Rangel, and H. Takenouti, "Electrochemical behaviour of steel rebars in concrete: Influence of environmental factors and cement chemistry," *Electrochim. Acta*, vol. 46, no. 24–25, pp. 3905–3912, 2001.

[27] L. Hamadou, A. Kadri, and N. Benbrahim, "Characterisation of passive films formed on low carbon steel in borate buffer solution (pH 9.2) by electrochemical impedance spectroscopy," *Appl. Surf. Sci.*, vol. 252,

no. 5, pp. 1510–1519, 2005.

[28] B. G. Schoonman, J. Vos. K, "Donor Densities in TiO[sub 2] Photoelectrodes," *J. Electrochem. Soc.*, vol. 128, no. 5, p. 1154, 1981.

[29] G. Horowitz, "Capacitance-voltage measurements and flat-band potential determination on Zr-doped α-Fe2O3 single-crystal electrodes," *J. Electroanal. Chem. Interfacial Electrochem.*, vol. 159, no. 2, pp. 421–436, 1983.

[30] M. J. Carmezim, A. M. Simoes, M. O. Figueiredo, and M. da Cunha Belo, "Electrochemical behaviour of thermally treated Cr-oxide films deposited on stainless steel," *Corros. Sci.*, vol. 44, no. 3, pp. 451–465, 2002.

[31] J. Wang *et al.*, "Oxygen vacancy induced band-gap narrowing and enhanced visible light photocatalytic activity of ZnO," *ACS Appl. Mater. Interfaces*, vol. 4, no. 8, pp. 4024–4030, 2012.

[32] S. A. Ansari, M. M. Khan, M. O. Ansari, S. Kalathil, J. Lee, and M. H. Cho, "Band gap engineering of CeO2 nanostructure using an electrochemically active biofilm for visible light applications," *RSC Adv.*, vol. 4, no. 32, pp. 16782–16791, 2014.

[33] T. Sato, Norio ; Noda, "Ion Migration in Anodic Barrier Oxide Films on

Iron in Acidic Phosphate Solutions," *Electrochim. Acta*, vol. 22, no. 839–843, 1976.

[34] S. C. Hendy, N. J. Laycock, and M. P. Ryan, "Atomistic Modeling of Cation Transport in the Passive Film on Iron and Implications for Models of Growth Kinetics," *J. Electrochem. Soc.*, vol. 152, no. 8, p. B271, 2005.

[35] A. B. Chwang and C. D. Frisbie, "Temperature and gate voltage dependent transport across a single organic semiconductor grain boundary," *J. Appl. Phys.*, vol. 90, no. 3, pp. 1342–1349, 2001.

[36] U. Stimming and J. W. Schultze, "A semiconductor model of the passive layer on iron electrodes and its application to electrochemical reactions," *Electrochim. Acta*, vol. 24, no. 8, pp. 859–869, 1979.

[37] R. M. Cornell and U. Schwertmann, *The iron oxides; Structure Properties, Reactions, Occurrences and Uses*. 2003.

CHAPTER 6

Role of grain size and crystallographic orientation on the corrosion behaviour of pure iron

This chapter is based on the scientific paper:

A. Yilmaz, K. Traka, S. Kar, J. Sietsma, Y. Gonzalez-Garcia Role of grain size and crystallographic orientation on the corrosion and passivation behaviour of pure iron (Under review)

Abstract

This work investigates the roles of grain size and crystallographic orientation on corrosion properties of pure iron in 0.1 m sulphuric acid solution. Heat treatments were applied to obtain samples with various grain sizes (26, 53, and 87 µm). Electron backscatter diffraction (EBSD), optical microscopy, and X-ray diffraction (XRD) analysis were performed to characterize the microstructure of the heat-treated samples. The EBSD analysis shows that the samples have a single-phase structure (ferrite), with no inclusions, and similar geometrically necessary dislocation (GND) density values. The XRD analysis exhibit that the sample with 25 µm grain size has a higher volume fraction of grains in (111) crystallographic orientation with respect to sample surface. The results from potentiodynamic polarisation and electrochemical impedance spectroscopy show that the grain refinement from 87 to 52 µm worsens the corrosion resistance of the samples. However, the further refinement in grain size from 52 to 25 µm improves the corrosion resistance. This stems from the dominant effect of preferential crystallographic orientation on grain size for the sample with 25 µm grain size.

Keywords: Grain size, crystallographic orientation, iron, corrosion, EIS, EBSD, XRD

6.1 Introduction

Grain size and crystallographic orientation of grains are important factors that affect the mechanical properties of ferrous materials. The effects of grain size [1]–[7] and crystallographic orientation [8]–[10] have been extensively investigated in the existing literature. Yet, the individual and synergistic effects of grain size and crystallographic orientation on corrosion behaviour of ferrous materials are yet to be explored. On the effect of the grain size on corrosion behaviour, Ralston and Birbilis [11] extensively reviewed the existing literature. Their literature review shows that there is little consensus on the relationship between grain size and corrosion behaviour. This originates from the microstructural changes besides grain size (dislocation density, phase and inclusion formation, alloy segregation, texture) that occur during the processes used to manipulate the grain size of studied samples. These microstructural features have interdependent relationships of their effects on corrosion behaviour, leading to the difficulty in isolating the effect of grain size on corrosion properties.

In a recent study, the effect of grain size on the corrosion behaviour of low alloyed steel is investigated in NaCl and HNO_3 solutions [12]. It is reported that the grain refinement from 35 to 4 μm leads to enhancement

in corrosion resistance in both environments. Another study investigates the effect of grain size on the corrosion behaviour of pure iron in sulphuric acid solution [13]. It is suggested that the corrosion resistance of pure iron deteriorates with grain refinement. However, the study also reports that the samples' dislocation density increases with grain refinement, which interferes with the effect of grain size on corrosion properties. In contrast to the above-mentioned studies, other studies that investigate the role of grain size on corrosion behaviour of iron in HCl [14] and H_2SO_4 [15] solutions show that the corrosion resistance increases with grain refinement.

On the side of crystallographic orientation, there is no united view on crystallographic orientation-dependent corrosion in the literature [16]–[20]. This mainly stems from the fact that the studies are conducted in different environments, and employed both polycrystalline and single-crystal low alloyed ferrous materials. The literature shows that the corrosion behaviour of grains in certain crystallographic orientations (with respect to the surface) differs depending on the environment. In an acetate buffer solution with pH 6, Schreiber et al. [17] show that the dissolution rate of grains in (111) and (101) orientations are higher than the ones in (001) orientation. In a borate buffer solution with pH 8.4, it was reported that the

corrosion rate is higher for the grains in (101) orientation than the ones in (001) orientation [21]. In more aggressive solutions with lower pH values, there is more consensus on the crystallographic orientation and corrosion behaviour relationship. In a study conducted in sodium sulphate solution with pH 2.3, it was reported that the corrosion rate of grains in (001) orientation is higher than the ones in (111) and (101) orientations [18]. Similarly, Yule et al. [20] and Fushimi et al. [16] reported that the corrosion rate of grains in (001) is higher than the ones in (111) and (101) orientations in sulphuric acid solutions.

In this work, it is aimed to investigate the role of grain size and crystallographic orientation on the corrosion behaviour of the iron samples. Moreover, the interrelated effect of grain size and crystallographic orientation is also investigated. Heat treatments were applied to manipulate the samples' grain sizes and crystallographic orientations. Electron backscatter diffraction (EBSD), optical microscopy, and X-ray diffraction (XRD) were employed to characterize the microstructure of the sample. Electrochemical impedance spectroscopy (EIS) measurements and potentiodynamic polarisation in 0.1 M sulphuric acid solution were conducted to investigate the electrochemical behaviour of samples.

6.2 Experimental

6.2.1 Material

A cold-rolled sheet of Armco iron (supplied by AK Steel, Netherlands) is employed in this work. The samples with a thickness of 2 mm were laser cut to the dimensions of 10 x 5 mm^2. The chemical analysis of the sample is performed by wavelength dispersive spectroscopy using a JEOL JXA 8900R microprobe with an electron beam energy of 10 keV and a beam current of 100 nA. Following background correction, the measured X-ray intensities of constituent elements are compared to those of a reference standard to estimate the chemical composition. The chemical composition of samples is given in table 6.1.

	Fe	***C***	***Si***	***Mn***	***P***	***S***	***Al***	***Cr***	***Cu***	***Ni***
wt%	Bal.	0.001	0.003	0.04	0.003	0.003	0.004	0.014	0.007	0.012

Table 6. 1 Chemical composition of employed samples

6.2.2 Microstructure Design & Characterisation

Several different heat treatments were applied on the cold-rolled as-received iron samples with a Bähr DIL 805 A/D dilatometer to vary samples' grain sizes. The details of the heat treatment operations are given in Section 4.2.2. The samples annealed at 700, 950, and 1100 ^{0}C are named as Sample

S, M, and L, respectively, according to their small, medium and large grain sizes.

The microstructure of samples after undergoing the heat treatments was analysed through optical microscopy, electron backscatter diffraction, and X-ray diffractometry (XRD). For microstructural Characterisation, the samples were ground with P80 to P4000 grit SiC paper. Following grinding, the samples were mechanically polished with diamond particle slurry (Struers DiaDuo-2) with particle sizes of 3 and 1 μm. Then, the samples were cleaned with isopropanol in an ultrasonic bath for 10 minutes and dried with airflow.

The optical images were employed to determine the grain sizes of samples by using the line intercept method on three images for each sample and to observe the microstructure after corrosion. For obtaining optical images, the samples were etched with a 2% Nital solution after polishing. The optical images were attained with a digital microscope (Keyence VHX-5000).

Electron backscatter diffraction analysis was conducted to extract the information about microstructural features of samples such as grain size, grain boundary density, the fraction of high-angle and low-angle grain

boundaries, and geometrically necessary dislocation (GND) density. The experimental information of EBSD measurements is given in section 4.2.3.

The macro-texture analysis was carried out on the polished sample surface by employing Bruker D8 Discover X-ray diffractometer with Eulerian cradle and parallel beam geometry. The X-ray radiation employed is Co Kα (λ= 0.179 nm) with an accelerating voltage of 45 kV and a current of 25 mA. The XRD Data processing and analysis were performed by Bruker's software Texture Edit, Texture Evaluation, and DiffracSuite EVA 5.2.

6.2.3 Electrochemical Characterisation

Electrochemical measurements (potentiodynamic polarisation and electrochemical impedance spectroscopy (EIS)) measurements were carried out in a deaerated 0.1 M H_2SO_4 solution. The solution was prepared at room temperature with distilled water. For the deaeration, nitrogen gas is purged through the solution for 1 hour before the electrochemical measurements. The electrochemical measurements were performed at room temperature. The samples were embedded in epoxy resin (Struers ClaroCit) and cured at room temperature and under 2 bar pressure for one hour. Subsequent to embedding, the samples were ground from 80 to 4000 grit SiC paper. Then, the samples were mechanically polished using diamond particle slurry

(Struers DiaDuo-2) with particle sizes of 3 and 1 μm, respectively. The gap between the samples and the embedding resin is covered with sealing lacquer (Electrolube Bloc Lube Red) to prevent any crevice corrosion.

The electrochemical measurements were conducted right after the sample preparation. A three-electrode cell, compromised of the reference electrode (Ag/AgCl, KCl (Satd.)), the counter electrode (graphite rod), and the working electrode (the sample), was employed for the electrochemical measurements. A Biologic SP300 potentiostat was used for the experiments. Before all electrochemical measurements, the open circuit potential (OCP) was measured for 3600 seconds. Following OCP measurements, the EIS spectra of the samples were collected in the frequency range from 30 kHz to 0.01 Hz with a perturbation amplitude of 10 mV. The EIS data were analysed with Zview software. The potentiodynamic polarisation was conducted at a scan rate of 0.167 mV/s in the potential range of 0.25 V to 0.25 V (vs. OCP). For the analysis of the potentiodynamic polarisation data, ECLab software (v11.33) was used.

6.3 Results and Discussion

6.3.1 Microstructure Characterisation

In Fig. 6.1, the optical microscopy images of the samples are given. Considering that the grain sizes increases in parallel with increasing annealing temperatures, the grain sizes of the samples increase in the order of Sample S, M, and L. The grain sizes of the samples, calculated by the line intercept method from optical images and by the EBSD measurements, are summarized in table 6.2.

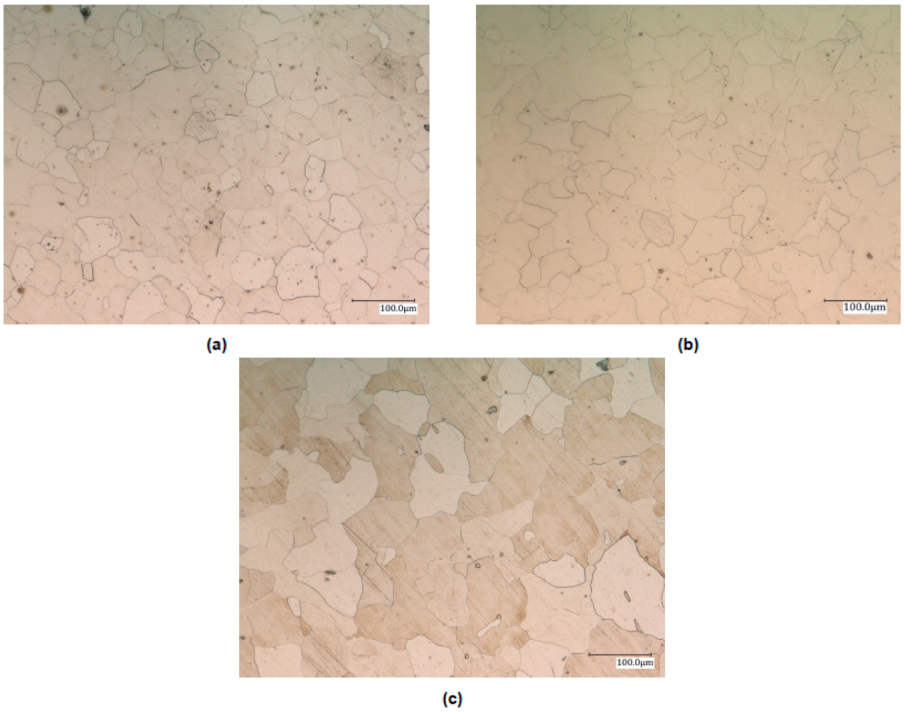

Figure 6. 1 Optical microscope images of a) Sample S, b) Sample M and c) Sample L after etching with 2% Nital solution

	Grain size (µm)	
	Optical microscope	***EBSD***
Sample S	30 ± 2	26 ± 2
Sample M	49 ± 4	53 ± 4
Sample L	76 ± 9	87 ± 12

Table 6.2 The overview of grain size of samples obtained using the line intercept method

The grain size, grain boundary density, and geometrically necessary dislocation density of the samples are investigated through electron backscatter diffraction analysis. Fig 6.2 and 6.3 show the EBSD inverse pole figure and geometrically necessary dislocation maps of the samples, respectively.

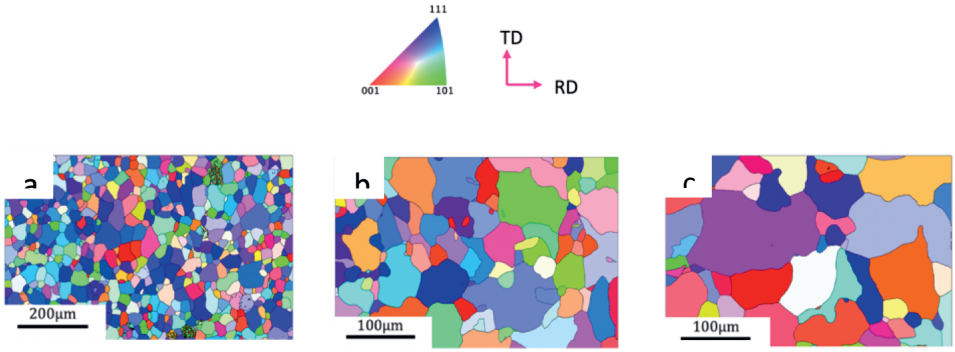

Figure 6. 2 The Inverse Pole Figure (IPF) maps of samples with varying grain sizes a) Sample S, b) Sample M and c) Sample L

The grain sizes of the samples calculated by EBSD are in good agreement with the ones calculated from optical images through the line intercept method. The grain boundary density is inversely proportional to grain size and increases with a grain size refinement. The grain boundary density is 0.101 ± 0.008 μm^{-1} for Sample S, 0.051 ± 0.004 μm^{-1} for Sample M, 0.027 ± 0.004 for μm^{-1} for Sample L.

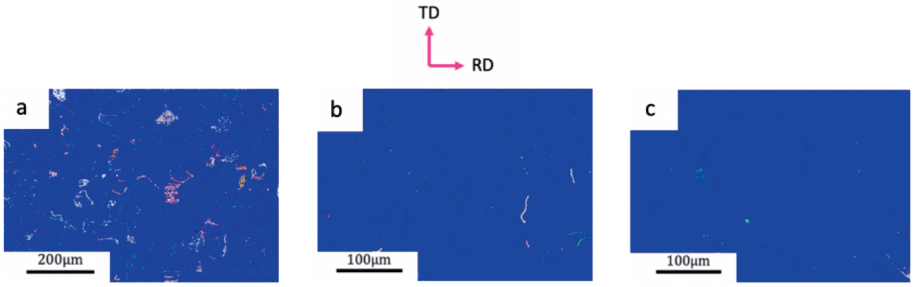

Figure 6. 3 GND density maps extracted from EBSD analysis with same resolution for samples with varying grain sizes a) Sample S, b) Sample M and c) Sample L

GND density maps (Fig 6.3) of all samples show that the dislocations are uniformly distributed throughout the grain's matrix. The grain boundary areas show higher dislocation density, exhibiting that the dislocations accumulate at grain boundaries. The samples have a low density of dislocations. The mean GND density values are $2.3 \pm 0.4 \cdot 10^{13}$ m^{-2} for Sample S, $7.9 \pm 0.2 \cdot 10^{12}$ m^{-2} for Sample M and $4.4 \pm 0.2 \cdot 10^{12}$ m^{-2} for Sample L. The slight differences in GND densities between samples are attributed to the variations in grain boundary density, leading to an increase in GND density with an increase in grain boundary density. The GND densities values below 10^{13} m^{-2} show that samples are nearly strain-free.

Although EBSD inverse pole figure maps reveal the crystallographic orientation of grains for all samples, XRD macro-texture analysis is carried

out due to the limited amount of grains in EBSD analysis. Fig. 6.4 shows the constant ϕ_2 = 45°section of the crystallographic orientation distribution function (ODF) plots of all samples together with a representative ODF plot, exhibiting the characteristics of texture components seen in BCC materials [22]. The Bunge notation is used to represent the ODF plots.

The horizontal section around ϕ = 0° shows the grains in (001) crystallographic orientation parallel to the rolling direction applied to the samples in the ODF plots. Sample S has limited intensity in this section, whereas Sample M and L have a relatively higher density of the iso-intensity lines. This indicates that Sample M and L have a higher intensity of grains in (001) crystallographic orientation in comparison to Sample S. The horizontal section around the ϕ = 50° to 60° shows the grains in (111) crystallographic orientation parallel to the rolling direction of the samples. In this section, Sample S has a higher density of horizontal iso-intensity lines than Samples M and L, showing that Samples S higher intensity of grains in (111) crystallographic orientation. In the ODF plots, the horizontal section near Phi=90° shows the intensity of grains in (110) crystallographic orientation parallel to the rolling direction of the samples. Sample S has a lower density of iso-intensity lines in this region in comparison to the Samples M and L.

This shows that the intensity of grains in (110) orientation is lower in the Sample S than the Samples M and L.

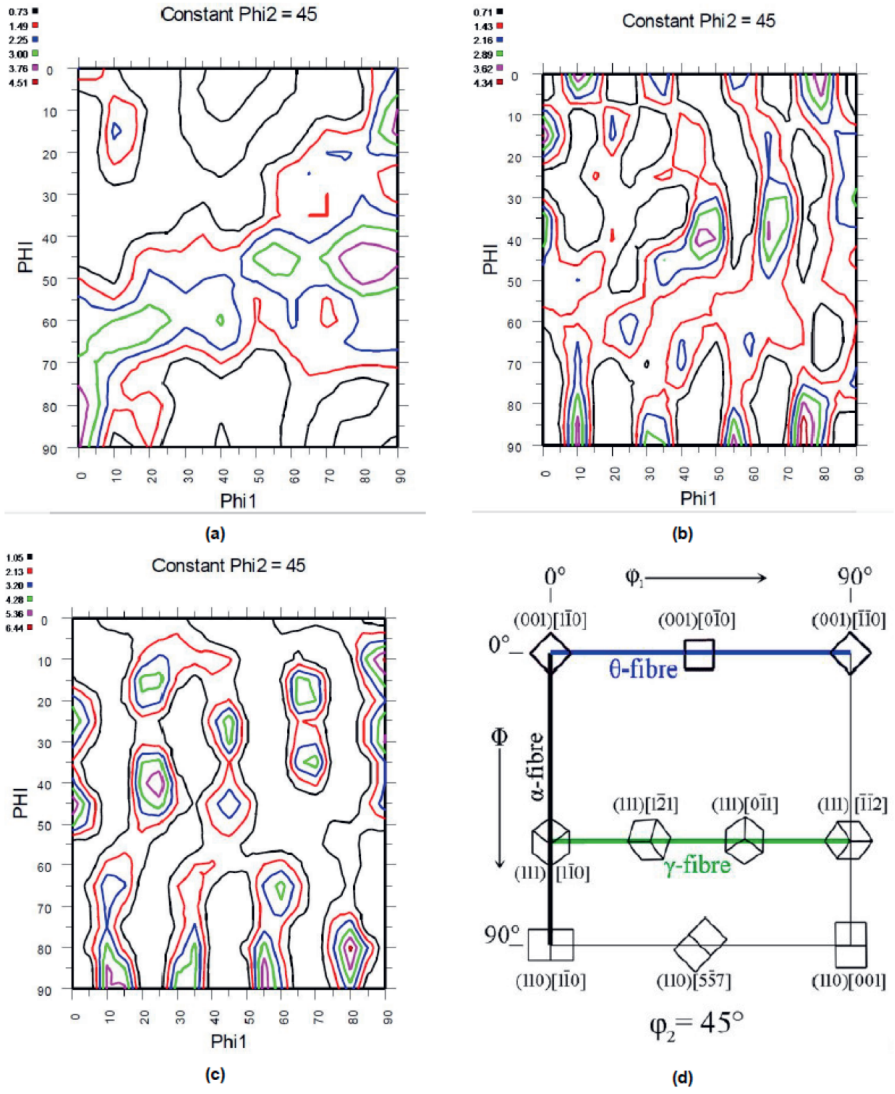

Figure 6.4 ODF section phi2 = 45° of a) Sample S b) Sample M and c) Sample L d) Illustrative $\varphi_2 = 45°$ ODF section representing the characteristic texture components in BCC metals

6.3.2 Electrochemical Characterisation

Electrochemical Impedance Spectroscopy (EIS) – EIS measurements were carried out in deaerated 0.1 M H_2SO_4 solution after measuring open circuit potential for 1 hour. Fig 6.5 shows the Nyquist plots for all samples. The Nyquist plots of all samples show depressed arcs. At low frequencies, the observed capacitive loops in all samples are related to the charge transfer resistance across the double layer. The diameters of arcs are associated with the corrosion resistance [13]–[15], [23]. Therefore, the arc diameters indicate that the corrosion resistance of samples decreases in the order of Sample L, Sample S, and Sample M, considering that the arc diameters decrease in the same order. At low frequencies, an inductive loop was observed for all samples. The inductive loop is attributed to the relaxation of adsorbed species on the electrode surface. These absorbed species are probably composed of iron sulphides and oxides such as FeS, $FeSO_4$, $Fe_2(SO_4)_3$, Fe_2O_3, and FeO(OH) or H_2, based on similar observations in other studies conducted in sulphuric acid solutions [13], [24-26].

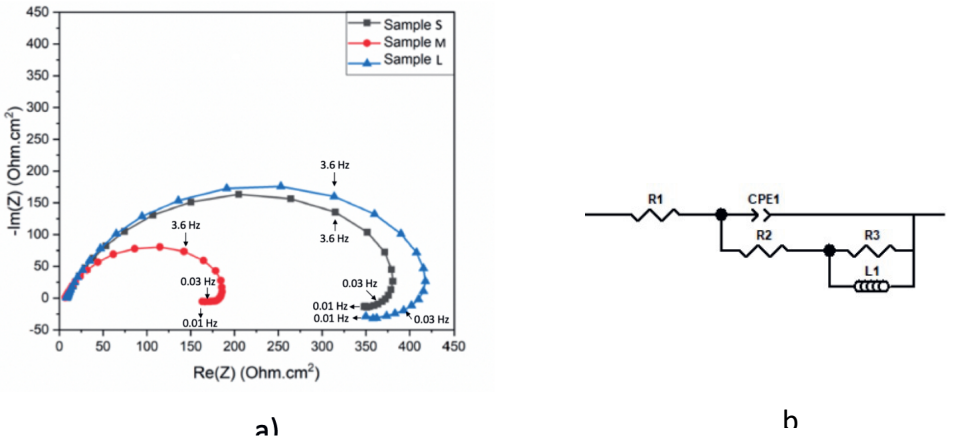

Figure 6.5 a) Nyquist plots of samples in 0.1 M sulphuric acid solution after immersion in open circuit conditions for 1 hour b) Equivalent electrical circuit employed for fitting the EIS data

The equivalent electrical circuit (EEC) fitting was carried out to fit the experimental EIS data. The proposed circuit is given in Fig in 6.5b, in agreement with the similar studies that used EEC fitting for EIS data [13], [27]. R_1 represents the electrolyte's resistance, R_2 the charge transfer resistance, CPE the double layer capacitance, R_3 the resistance and inductance of the adsorbed species, L is the equivalent inductance stemming from the relaxation process of the absorbed species [13]. The mean values of the fitted values for circuit elements are given in table 4.3. The charge transfer resistance values for Sample L are largest with a close value to Sample S, whereas the charge transfer resistance of Sample M is more than 50% smaller than Samples S and L. Considering that the charge transfer resistance is a measure of the corrosion resistance of the samples,

the charge transfer resistance values suggest that the Sample L has the highest corrosion resistance. Sample S has slightly lower corrosion resistance than Sample L, whereas Sample M has the lowest corrosion resistance.

Sample	***R_1 (Ωcm^2)***	***R_2 (Ωcm^2)***	***CPE-Y_0 (Ω^{-1} $cm^{-2}s^n$ 10^{-5})***	***n***	***R_3 (Ωcm^2)***	***L (Hcm^2)***
Sample S	7 ± 2	375 ± 38	1.6 ± 0.1	0.80 ± 0.01	90 ± 28	26 ± 9
Sample M	7 ± 1	218 ± 50	2.3 ± 0.3	0.84 ± 0.02	58 ± 22	9 ± 4
Sample L	11 ± 3	470 ± 42	1.7 ± 0.2	0.83 ± 0.01	127 ± 33	49 ± 7

Table 6. 3 The fit values of the equivalent circuit components for Sample S, M, and L in 0.1 M (pH 1.0) sulphuric acid solution

Potentiodynamic polarisation – Fig 6. 6 shows the potentiodynamic polarisation plots of the samples in 0.1 M sulphuric acid solutions after measuring open circuit potential for 1 hour. The cathodic branches of potentiodynamic polarisation exhibit the cathodic hydrogen evolution reactions (HER), while the anodic branches show the metal's anodic dissolution behaviour. The anodic branches of all curves overlap, indicating that the anodic dissolution and mechanisms are independent of the

samples' grain size. In the cathodic part of the curves, all samples exhibit similar cathodic slopes, indicating that the mechanisms of cathodic reaction are also independent of the samples' grain size. In contrast, the cathodic branch of Sample M is shifted towards higher current density values in comparison to Sample S and L. This indicates that the corrosion kinetics are dependent on the grain size of samples and are the highest in Sample M.

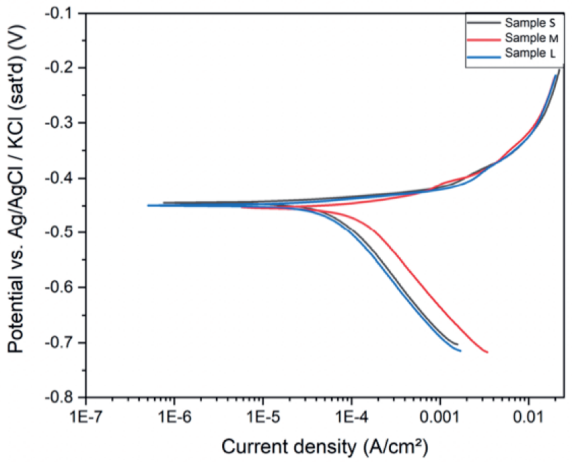

Figure 6. 6 Potentiodynamic polarisation curves of the samples measured in 0.1 M sulphuric acid solution

Tafel extrapolations are applied to the potentiodynamic polarisation curves of all samples to extract corrosion current density (i_{corr}) and corrosion potential (E_{corr}). The calculated values through Tafel extrapolation are given in table 6.4. The E_{corr} values show no significant differences (limited to 3mV) between samples. The i_{corr} values are comparable for Sample S and Sample L. Sample M exhibits about 100% higher corrosion current density values

than Sample S and Sample L. The corrosion current density values show that the corrosion rate increases in the order of Sample L, Sample S, and Sample M, in agreement with the charge-transfer resistance values obtained from EIS curves.

Sample	***i_{corr} ($\mu A.cm^{-2}$)***	***E_{corr} (mV vs. Ag/AgCl)***
Sample S	83±5	-467±7
Sample M	148±4	-466±4
Sample L	73±1	-465±8

Table 6.4 Corrosion current density and corrosion potential values obtained for Sample S, M, and L from the potentiodynamic polarisation experiments in 0.1 M sulphuric acid solutions

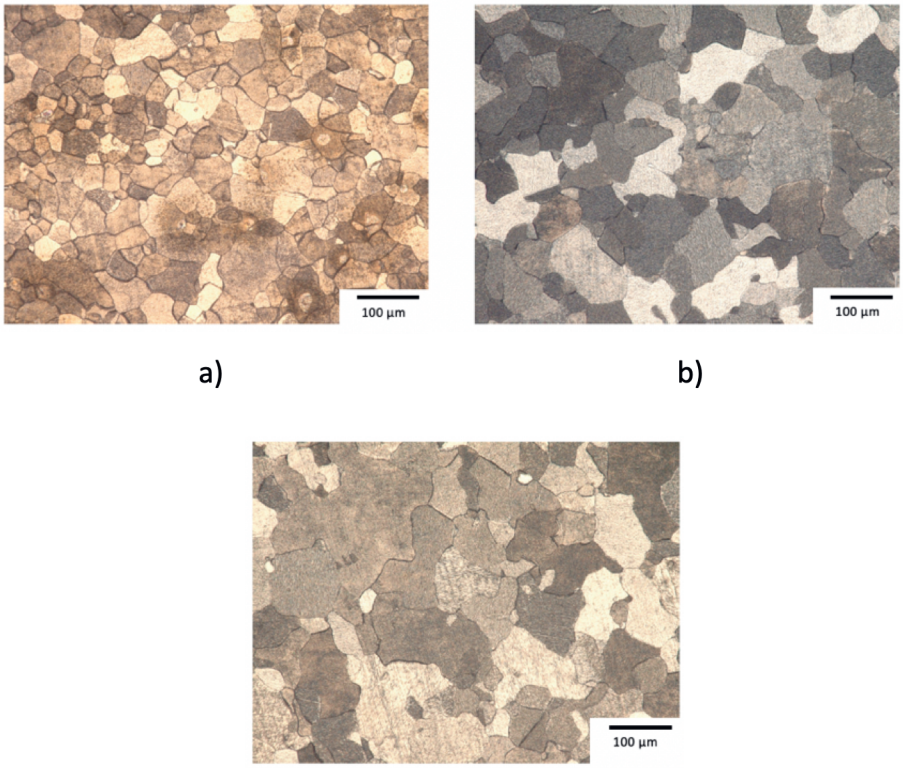

Figure 6.7 Optical images illustrating the surface of samples a) Sample S, b) Sample M and c) Sample L after potentiodynamic polarisation in 0.1 M sulphuric acid solution

Figure 6.7 shows the optical micrographs of all samples after undergoing the potentiodynamic polarisation in 0.1 M sulphuric acid solution. For all samples, it is observed that some of the grain boundaries are severely corroded, while some others have less severe attacks. This is probably due to the fact that high-angle boundaries form more active sites

than low-angle boundaries, leading to more severe attacks at high-angle grain boundary sites [28], [29]. Moreover, it is also observed that the grains dissolve heterogeneously in all samples due to micro-galvanic coupling between grains having different crystallographic orientations. This stems from the fact that the grains with different crystallographic orientations have different corrosion behaviour [16], [17], [19].

To understand the effect of microstructural features, it is necessary to consider the complex interaction of microstructural features on corrosion behaviour. The samples employed in this work have very high purity, allowing to avoid the effect of chemical composition, possible elemental segregations, phases, and inclusions formation on corrosion behaviour. Moreover, the very close geometrically necessary dislocation density values between samples show that the effect of dislocation density on corrosion behaviour is also limited in this study.

The electrochemical measurements show that the corrosion resistance of Sample L is significantly higher than Sample M. This shows that the grain size refinement leads to a decrease in corrosion resistance, considering that the main difference between Sample M and L is grain size. The decrease in corrosion resistance with grain refinement is attributed to

the grain boundaries forming active sites that facilitate the hydrogen evolution reactions and lead to an increase in corrosion rate [12], [30]. On the other hand, Sample S has higher corrosion resistance in comparison to Sample M, although the grain size of Sample S is smaller than the one of Sample M. However, Sample S has a higher volume fraction of grains in (111) crystallographic orientation. Localised studies were conducted by Fushimi et al. [16] on polycrystalline pure iron in sodium sulphate solution and Yule et al. [20] on the polycrystalline low-carbon steels in sulphuric acid solution to investigate the role of crystallographic orientation of grains in corrosion behaviour. These studies show that the corrosion resistance of grains in (110) and (111) crystallographic orientations are similar, whereas the corrosion resistance of grains in (001) crystallographic orientation is lower than the ones in (110) and (111) orientations. The higher corrosion resistance of the grains in (111) and (110) crystallographic orientations is attributed to the slower hydrogen evolution reaction kinetics occurring on the grains in this orientation.

Considering that the Sample S has a higher volume fraction of grains in (111) orientation that has higher corrosion resistance, the higher corrosion resistance in Sample S in comparison to Sample M is attributed to

the effect of crystallographic orientation, which is dominant over the grain size effect in the grain size range between 25 and 52 µm. This shows that the grain size and crystallographic orientation have a complex interaction on corrosion behaviour. The effect of crystallographic orientation is dominating the effect of size on corrosion behaviour while refining the grain size from 52 to 25 µm.

6.4 Conclusions

In this work, the effect of grain size and crystallographic orientation on the corrosion behaviour of pure iron is investigated in 0.1 M sulphuric acid solution. The obtained results lead to the following conclusions.

- Three samples with different grain sizes (Sample S (25 µm), Sample M (52 µm), and Sample L (87 µm)) were obtained after undergoing various heat treatments. The changes in the microstructure between samples M and L is limited to only grain size, whereas Sample S has finer grain size than the two other samples and a higher volume fraction of grains in (111) crystallographic orientation. The changes in microstructural features other than grain size and crystallographic orientation are avoided. These permit investigating

the effects of grain size and crystallographic orientation on corrosion behaviour.

- The grain refinement from Sample L to Sample M leads to an increase in corrosion current density in potentiodynamic polarisation and a decrease in charge transfer resistance in electrochemical impedance spectroscopy results. These results show that grain refinement leads to a decrease in corrosion resistance. However, the further grain refinement from Sample M to Sample S leads to a decrease in corrosion current density and charge transfer resistance. This stems from that Sample S has a higher volume fraction of grains in (111) crystallographic orientation that has higher corrosion resistance in comparison to the grains (001) and (101) orientations, leading to an increase in corrosion resistance in Sample S.

From the above-mentioned results, it is concluded that the grain size refinement leads to increase in corrosion rate. However, the grain size and crystallographic orientation have a synergistic effect on corrosion behaviour in which the effect of crystallographic orientation dominates the effect of grain size while the grain size is refined from 52 to 25 µm.

6.5 References

[1] J. M. Hyzak and I. M. Bernstein, “The role of microstructure on the strength and toughness of fully pearlitic steels,” *Metall. Trans. A*, vol. 7, no. 8, pp. 1217–1224, 1976.

[2] C. Peng-Heng and A. G. Preban, “The effect of ferrite grain size and martensite volume fraction on the tensile properties of dual-phase steel,” *Acta Metall.*, vol. 33, no. 5, pp. 897–903, 1985.

[3] S. Takaki, K. Kawasaki, and Y. Kimura, “Mechanical properties of ultra fine grained steels,” *J. Mater. Process. Technol.*, vol. 117, no. 3, pp. 359–363, 2001.

[4] B. Mintz and D. V. Wilson, “Strain ageing during the fatigue of carbon steels,” *Acta Metall.*, vol. 13, no. 9, pp. 947–956, 1965.

[5] M. Srinivas, G. Malakondaiah, R. W. Armstrong, and P. Rama Rao, “Ductile fracture toughness of polycrystalline armco iron of varying grain size,” *Acta Metall. Mater.*, vol. 39, no. 5, pp. 807–816, 1991.

[6] T. Hanamura, F. Yin, and K. Nagai, “Ductile-brittle transition temperature of ultrafine ferrite/cementite microstructure in a low carbon steel controlled by effective grain size,” *ISIJ Int.*, vol. 44, no. 3, pp. 610–617, 2004.

[7] T. Hanamura, S. Torizuka, S. Tamura, S. Enokida, and H. Takechi, "Effect of Austenite Grain Size on Transformation Behaviour, Microstructure and Mechanical Properties of 0.1C–5Mn Martensitic Steel," *ISIJ Int.*, vol. 53, no. 12, pp. 2218–2225, 2013.

[8] E. A. Ariza, M. Masoumi, and A. P. Tschiptschin, "Improvement of tensile mechanical properties in a TRIP-assisted steel by controlling of crystallographic orientation via HSQ&P processes," *Mater. Sci. Eng. A*, vol. 713, pp. 223–233, 2018.

[9] S.-H. Choi, E.-Y. Kim, W. Woo, S. H. Han, and J. H. Kwak, "The effect of crystallographic orientation on the micromechanical deformation and failure Behaviours of DP980 steel during uniaxial tension," *Int. J. Plast.*, vol. 45, pp. 85–102, 2013.

[10] X. Wang, J. A. Muñiz-Lerma, M. Attarian Shandiz, O. Sanchez-Mata, and M. Brochu, "Crystallographic-orientation-dependent tensile behaviours of stainless steel 316L fabricated by laser powder bed fusion," *Mater. Sci. Eng. A*, vol. 766, p. 138395, 2019.

[11] K. D. Ralston and N. Birbilis, "Effect of grain size on corrosion: A review," *Corrosion*, vol. 66, no. 7, pp. 51–73, 2010.

[12] P. K. Rai, S. Shekhar, and K. Mondal, "Development of gradient

microstructure in mild steel and grain size dependence of its electrochemical response," *Corros. Sci.*, vol. 138, no. July 2017, pp. 85–95, 2018.

[13] L. Jinlong and L. Hongyun, "The effects of cold rolling temperature on corrosion resistance of pure iron," *Appl. Surf. Sci.*, vol. 317, pp. 125–130, 2014.

[14] S. G. Wang, C. B. Shen, K. Long, H. Y. Yang, F. H. Wang, and Z. D. Zhang, "Preparation and Electrochemical Corrosion Behaviour of Bulk Nanocrystalline Ingot Iron in HCl Acid Solution," *J. Phys. Chem. B*, vol. 109, no. 7, pp. 2499–2503, 2005.

[15] S. G. Wang, C. B. Shen, K. Long, T. Zhang, F. H. Wang, and Z. D. Zhang, "The electrochemical corrosion of bulk nanocrystalline ingot iron in acidic sulfate solution," *J. Phys. Chem. B*, vol. 110, no. 1, pp. 377–382, 2006.

[16] K. Fushimi, K. Miyamoto, and H. Konno, "Anisotropic corrosion of iron in pH 1 sulphuric acid," *Electrochim. Acta*, vol. 55, no. 24, pp. 7322–7327, 2010.

[17] A. Schreiber, J. W. Schultze, M. M. Lohrengel, F. Kármán, and E. Kálmán, "Grain dependent electrochemical investigations on pure

iron in acetate buffer pH 6.0," *Electrochim. Acta*, vol. 51, no. 13, pp. 2625–2630, 2006.

[18] K. Fushimi and M. Seo, "An SECM observation of dissolution distribution of ferrous or ferric ion from a polycrystalline iron electrode," *Electrochim. Acta*, vol. 47, no. 1, pp. 121–127, 2001.

[19] G. P. Cammarota, L. Felloni, G. Palombarini, and S. S. Traverso, "Optical Microscopy Studies of Anodic Dissolution of Iron in Sulfuric and Hydrochloric Acid Solutions: Influence of Metal Purity, Structure, Heat Treatment," *Corrosion*, vol. 26, no. 6, pp. 229–240, Jan. 2013.

[20] L.C. Yule, V. Shkirskiy, J. Aarons, G. West, B.A. Shollock, C.L. Bentley, P.R. Unwin, "Nanoscale electrochemical visualization of grain-dependent anodic iron dissolution from low carbon steel," *Electrochim. Acta*, vol. 332, p. 135267, 2020.

[21] M. Seo and M. Chiba, "Nano-mechano-electrochemistry of passive metal surfaces," *Electrochim. Acta*, vol. 47, no. 1, pp. 319–325, 2001.

[22] L. A. I. Kestens and H. Pirgazi, "Texture formation in metal alloys with cubic crystal structures," *Mater. Sci. Technol. (United Kingdom)*, vol. 32, no. 13, pp. 1303–1315, 2016.

[23] W. R. Osório, L. C. Peixoto, L. R. Garcia, and A. Garcia,

"Electrochemical corrosion response of a low carbon heat treated steel in a NaCl solution," *Mater. Corros.*, vol. 60, no. 10, pp. 804–812, 2009.

[24] X. Q. Cheng, F. L. Sun, S. J. Lv, and X. G. Li, "A new steel with good low-temperature sulfuric acid dew point corrosion resistance," *Mater. Corros.*, vol. 63, no. 7, pp. 598–606, 2012.

[25] L. Bai and B. E. Conway, "{AC} Impedance of Faradaic Reactions Involving Electrosorbed Intermediates: Examination of Conditions Leading to Pseudoinductive Behaviour Represented in Three-Dimensional Impedance Spectroscopy Diagrams," *J. Electrochem. Soc.*, vol. 138, no. 10, pp. 2897–2907, Oct. 1991.

[26] E. G. Dafft, K. Bohnenkamp, and H. J. Engell, "Investigations of the hydrogen evolution kinetics and hydrogen absorption by iron electrodes during cathodic polarisation," *Corros. Sci.*, vol. 19, no. 9, pp. 591–612, 1979.

[27] T. Bellezze, G. Giuliani, and G. Roventi, "Study of stainless steels corrosion in a strong acid mixture. Part 1: cyclic potentiodynamic polarisation curves examined by means of an analytical method," *Corros. Sci.*, vol. 130, pp. 113–125, 2018.

[28] M. Bettayeb, V. Maurice, L. H. Klein, L. Lapeire, K. Verbeken, and P. Marcus, “Nanoscale Intergranular Corrosion and Relation with Grain Boundary Character as Studied In Situ on Copper,” *J. Electrochem. Soc.*, vol. 165, no. 11, pp. C835--C841, 2018.

[29] M. Orłowska, E. Ura-Bińczyk, L. Olejnik, and M. Lewandowska, “The effect of grain size and grain boundary misorientation on the corrosion resistance of commercially pure aluminium,” *Corros. Sci.*, vol. 148, pp. 57–70, 2019.

[30] L. C. Yule, V. Shkirskiy, J. Aarons, G. West, C. L. Bentley, B. A. Shollock, P. R. Unwin, “Nanoscale Active Sites for the Hydrogen Evolution Reaction on Low Carbon Steel,” *J. Phys. Chem. C*, vol. 123, no. 39, pp. 24146–24155, 2019.

Part C

The influence of phases constituents on corrosion and passivity properties

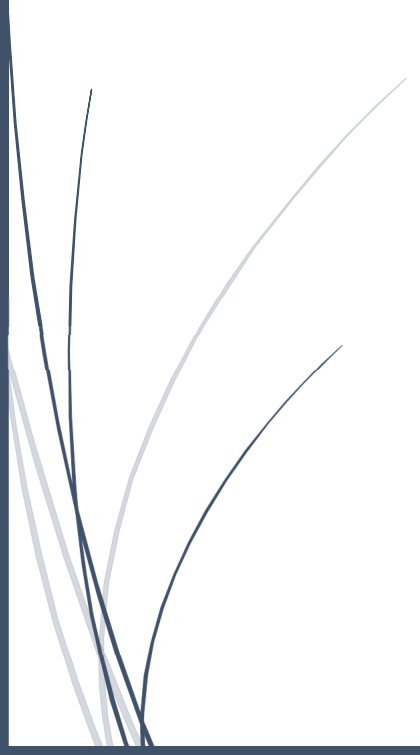

CHAPTER 7

Properties of Passive Films formed on Dual- Phase Ferrite-Martensite and Ferrite-Pearlite Microstructures

This chapter is based on the scientific paper:

A. Yilmaz, C. Ozkan, J. Sietsma, Y. Gonzalez-Garcia, Properties of Passive Films formed on Dual-Phase Ferrite-Martensite and Ferrite-Pearlite Microstructures, *Metals,* vol. *11*(4), p. 594, 2021.

Abstract

The effect of ferrite-pearlite and ferrite-martensite phase combinations on the passive layer properties of a low carbon steel is investigated in a 0.1 M NaOH solution. Heat treatments were designed to obtain ferrite-pearlite and ferrite-martensite microstructure with similar ferrite volume fractions. The microstructure of samples was obtained through scanning electron microscopy and optical images. Potentiostatic polarisation and electrochemical impedance spectroscopy (EIS) results exhibit the lower barrier properties of passive films on ferrite-martensite microstructure compared to the one formed on ferrite-pearlite microstructure. This is attributed to the passive layer's higher donor density on ferrite-martensite samples, measured with Mott-Schottky analysis.

Keywords: *Martensitic steels, grain-size, passivity, EIS, Mott-Schottky, XPS*

7.1 Introduction

A wide range of industries such as aerospace, automotive, oil and gas have been employing high strength low alloy (HSLA) steels due to their mechanical properties to reduce weight in structures and save energy in transportation applications. A wide range of industries such as aerospace, automotive, oil and gas have been employing high strength low alloy steels due to their mechanical properties to reduce weight in structures and save energy in transportation applications. The exceptional mechanical properties of HSLA steels (the optimal combination of strength, ductility, and plasticity) often result from a multi-phase microstructure created combination of strength, ductility, and plasticity) often result from a multi-phase microstructure created through a precise balance between kinetic and thermodynamic processes [1]. Therefore, pearlite and martensite, in combination with ferrite, are widely used in two-phase HSLA steels. Although the role of pearlite and martensite with a combination of ferrite in two-phase steels on mechanical properties is understood relatively clearly [2], [3], their passivity behaviour is not well understood [4], [5]. This is mainly due to the fact that the complex interaction of many microstructural features - grain sizes, phase fractions, dislocation densities,

crystallographic orientations, phase morphologies - dictates the properties of the passive layer of steels. Therefore, it is often challenging to isolate pearlite and martensite's role in combination with the ferrite on passive layer properties of two-phase HSLA steels.

It should be emphasized that the contribution of pearlite and martensite in two-phase steel on the passive layer properties can only be determined with the localised experiments and/or simplified model alloys. Fushimi et al. [4] compared the passive layer properties formed on ferrite and pearlite through local nanoscopic techniques. They reported a larger passive current density and smaller ionic/electronic resistance for the pearlite structure and related this behaviour to the differences between conductivities and phase structures of $FeCO_3$ and Fe_2O_3. With well-controlled microstructures, Yanagisawa et al. [5] investigated the role of martensite volume fraction of low-alloyed and simplified model alloys that minimised microstructural changes features other than martensite volume fraction. They reported that the barrier properties of passive film deteriorate with increasing martensite volume fraction of the substrate. Furthermore, a higher conductivity for the passive film formed on the martensite phase of the dual-phase steel was observed. This was attributed

to a higher fraction of Fe_3O_4 in the passive film formed on the martensite phase. Therefore, the passivity of the dual-phase ferrite-martensite steel is proposed to be controlled by the inferior passive properties of the martensite phase. However, controlled ferrite-martensite and ferrite-pearlite microstructures created through precise heat treatments of the same alloy composition and the resultant passive layer properties of the microstructures have not been previously investigated.

In this study, the effect of pearlite or martensite with ferrite in two-phased HSLA on passive layer properties is investigated in 0.1 M NaOH solution. Two well-controlled distinct microstructures - ferrite-martensite and ferrite-pearlite - with the same ferrite volume fractions were employed to minimise the possible differences between microstructural features. Samples are created through dilatometry and characterised by optical microscopy and SEM analysis. The phase constituents' contribution to the development of passive films is analysed by potentiostatic polarisation, electrochemical impedance spectroscopy, and capacitance measurements with Mott-Schottky analysis. Finally, the passive layers' nature is discussed in light of microstructural features of the phases and passive layer properties

7.2 Experimental

7.2.1 Material

As-received steel sheets (provided by Tata Steel, IJmuiden, the Netherlands) of 2 mm thickness were used. The sheets were laser-cut to the dimensions of 5 x 10 mm^2 coupons. The samples' chemical composition was obtained through wavelength dispersive spectroscopy with an electron beam energy of 10 keV and a beam current of 100 nA. A JEOL JXA 8900R microscope was used to obtain the chemical composition of the samples. The steel grade was chosen

due to its low-alloyed chemical composition. The chemical composition of the samples is presented in table 7.1.

	Fe	***C***	***Si***	***Mn***	***P***	***S***	***Al***	***Cr***	***Cu***	***Ni***	***Ti***
wt. %	Bal.	0.14	0.05	2.15	0.01	0.01	0.04	0.58	0.01	0.02	0.03

Table 7.1 Chemical composition (wt.%) of cold-rolled DP1000 dual-phase steel

7.2.2 Microstructure Characterisation

Dilatometry - A Bähr DIL 805 A/D dilatometer was employed to perform the heat treatments. Various heat treatments were applied to create different two-phase microstructures, a ferrite-pearlite microstructure, and a ferrite-

martensite microstructure, with similar ferrite volume fractions for both microstructures. Heat treatments are graphically presented in figure 7.1.

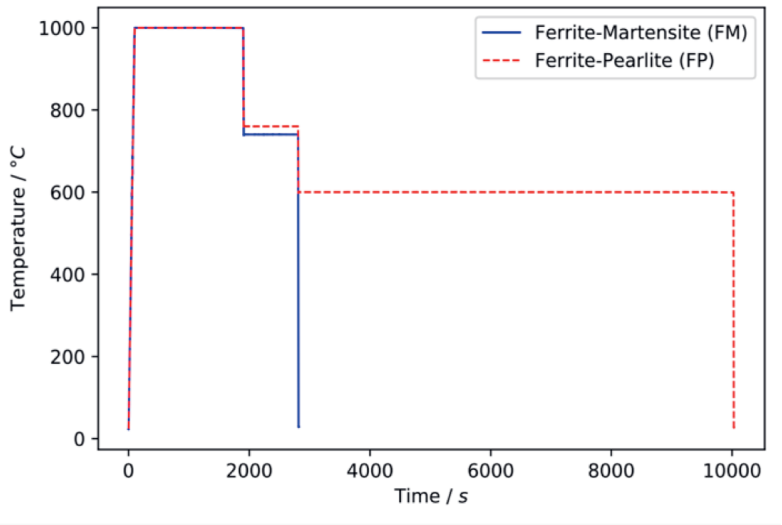

Figure 7.1 Graphical summary of the employed heat treatments

The ferrite-martensite (FM) microstructure was created by heating the samples to 1000°C with a rate of 10°C/s, austenitising at 1000°C for 30 minutes, quenching to the intercritical annealing temperature 740°C at a rate of 30°C/s, holding the sample at 740°C for 15 minutes and quenching to the room temperature with a rate of 30°C/s. The ferrite-pearlite (FP) microstructure was obtained by heating the sample to 1000°C with a rate of 10°C/s, austenitising at 1000°C for 30 minutes, quenching to the intercritical annealing temperature 760°C at a rate of 30°C/s, holding the sample at 760°C for 15 minutes, cooling to the sub-Ac_1 temperature of 600°C at a rate

of 30°C/s, isothermally holding the sample at 600°C for 2 hours and quenching to the room temperature with a rate of 30°C/s. The value of volume fractions of ferrite-martensite and ferrite-pearlite were obtained with the line interception method.

Sample Preparation - Samples were prepared for further microstructure characterisation by embedding them in an epoxy resin (Struers ClaroCit) and curing them for 1 hour under 2 bar pressure. The samples were ground with SiC sanding paper from 80 to 4000 grit and subsequently polished using a fine diamond suspension (Struers DiaDuo-2) with 3 and 1 µm particle sizes. Later, the samples were cleaned in an ultrasonic bath with isopropanol for 10 minutes after polishing and afterwards dried with compressed air. A 2% Nital solution was used for etching.

Optical Microscopy and SEM - An optical microscope (Keyence VHX-500) was employed to characterise the microstructure with optical micrographs. A scanning electron microscope (Jeol JSM-IT100) was used for a more detailed secondary phase determination. Micrographs were examined for the phase constituents and the volume fractions of the respective phases. The volume fraction of each phase of the samples was determined by analysing the contrast difference between the phases from optical

micrographs. Analysis areas of 0.1 mm^2 taken from four different locations per sample were investigated with ImageJ software.

7.2.3 Electrochemical Measurements

Sample Preparation - The grinding and polishing steps used for microstructure characterisation were followed to obtain a mirror-like polished surface for the electrochemical experiments. The gap between the steel specimen and the epoxy resin was covered with an insulating lacquer (Electrolube BLR) to prevent possible crevice corrosion during measurements.

Electrochemical Experiments - All electrochemical experiments were conducted at ambient room temperature in aerated 0.1 M NaOH solution (pH 12.6), prepared with Sigma-Aldrich NaOH pellets and Milli-Q® ultrapure water. A three-electrode electrochemical cell consisting of stainless-steel mesh as the counter electrode, Ag/AgCl, KCl(satd.) as the reference electrode, and the specimens as the working electrodes were employed. A Biologic VSP-300 potentiostat and EC-lab v11.33 software were utilised for the electrochemical measurements and data analysis.

Open circuit potential (OCP) was recorded for 1 hour, during which it had stabilised. Subsequently, the samples were passivated with potentiostatic

polarisation, carried out at a potential of 0.2 V (vs. Ag/AgCl) for 6 hours. After the passivation of the samples, electrochemical impedance spectroscopy (EIS) measurements were conducted by applying an AC perturbation with a peak-to-peak amplitude of 10 mV in the frequency range from 30 kHz to 10 mHz. The equivalent electrical circuit (EEC) fitting of electrochemical impedance spectroscopy data was done by Zview 3.5h software. Capacitance measurements (Mott-Schottky analysis) were performed to examine the corresponding effect of martensite and pearlite structures in two-phase steel on the passive layer's electronic properties. Capacitance measurements were conducted at a frequency of 1 kHz with a peak-to-peak AC voltage of 10 mV. At this frequency, the capacitance of the iron oxide is not considerably affected; as a result, the electronic part of the space charge region contribution to the capacitance can be evaluated [6]. A potential step size of 50 mV is used to sweep a potential range from 0.6 V to -1.0 V (vs. Ag/AgCl).

All electrochemical measurements were repeated at least three times to ensure reproducibility.

7.3 Results & Discussion

7.3.1 Microstructure Characterisation

Table 7.2 shows the austenite transformation start (A_{c1}) and austenite transformation finish (A_{c3}) temperatures, martensite start (M_s) and martensite finish (M_f) temperatures for the heat treatments in the dilatometer. Heat treatments for creating ferrite-martensite and ferrite-pearlite dual-phase microstructures are determined from these values obtained through dilatation responses of the samples . It is seen that samples annealed at 1000°C, a temperature significantly higher than the Ac_3 temperature, resulted in homogenised grain structures. This uniform grain distribution throughout the microstructure and lack of segregation of different phases result in structures suitable for subsequent electrochemical experiments. Intercritical annealing treatment allows partial stabilisation of some of the austenite into ferrite before the remaining austenite was transformed into martensite for the case of quench process and pearlite for the case of isothermal holding at 600°C.

Critical Temperatures	***Ac_1***	***Ac_3***	***M_s***	***M_f***
°C	720	840	400	140

Table 7.2 Critical temperatures for the heat treatments of DP1000 dual-phase steel

Optical images of both microstructures and SEM images, highlighting the distinct secondary phases of the microstructures, are presented in figure 7.2. In figures 7.2a and 7.2b, the optical images show the ferrite-martensite and ferrite-pearlite microstructures obtained after undergoing heat treatments at the dilatometry, respectively. Lighter areas correspond to ferrite phases, and darker ones correspond to martensite and pearlite phases for ferrite-martensite and ferrite-pearlite microstructures. In figures 7.2c and 7.2d, SEM images show the respective martensite and pearlite secondary phases in more detail, where red arrows demonstrate different martensite/pearlite grains. The martensite phase's complex morphology is seen to be composed of laths and blocks and displays a needle-like morphology. It consists of a lamellar structure of ferrite and cementite phases, shown in figure 7.2d. The samples were created on the basis that they had similar ferrite volume fractions of 50%, while having ferrite-martensite and ferrite-pearlite phase combinations. The heat treatments lead to a ferrite-martensite dual-phase microstructure with 50 ± 2% ferrite volume fraction and a ferrite-pearlite dual-phase microstructure with 56 ± 5% ferrite volume fraction.

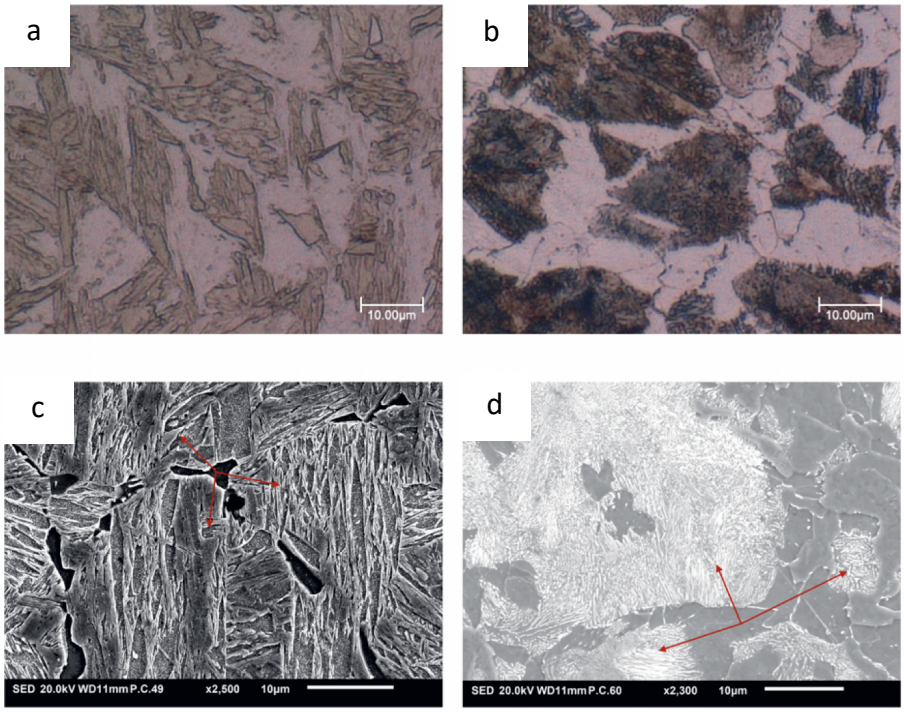

Figure 7.2 Optical and SEM micrographs taken from ferrite-martensite and ferrite-pearlite dual-phase microstructures. a) Ferrite-martensite microstructure, b) ferrite-pearlite microstructure, (c) detail from the martensite phase, d) detail from the pearlite phase

7.3.2 Electrochemical Characterisation

Potentiostatic Polarisation at 0.2 V is employed in a 0.1M NaOH (pH 12.6) environment for 6 hours, ensuring a passive layer's formation due to the alkaline environment. Figure 7.3 displays the change in current density in time during the potentiostatic polarisation experiment. Initially, for the first seconds, both samples' current densities decreased exponentially due to the formation of a passive film layer. The current changes correspond to the growth of the passive layer. After the sharp decrease in the first few

seconds, until around 100 seconds, the logarithmic slope (-dlog | *j* | / dlog *t*) of FM and FP samples has a value of 0.87 and 0.82, respectively, and decreases as the potentiostatic polarisation continued. A slope of 1 is associated with a perfect anodic passive film growth under a high electric field with negligible dissolution reactions of the oxide, where all of the current is consumed for the passive film growth [6]–[9]. In this case, slopes of 0.87 and 0.82 indicate some of the current can be attributed to other processes. In the beginning, the passive layer grew almost perfectly as a large part of the current was consumed for oxide growth. Afterwards, the current was also distributed to other processes, such as the transformation of ferrous oxides into ferric oxides. After 6000 seconds for the FM sample and 8000 seconds for the FP sample, the currents start to stabilise. The most interesting observation is that the samples presented different steady-state currents. The current densities for the steady-state are measured as 0.17 ± 0.02 μAcm^{-2} for the FP sample and 1.1 ± 0.04 μAcm^{-2} for the FM sample. Therefore, the passive film's conductivity developed on the FM sample is demonstrated to be 6½ times the FP sample passive layer conductivity. The

differences indicate the differences in the ionic and/or electronic conductivity of the formed passive layers.

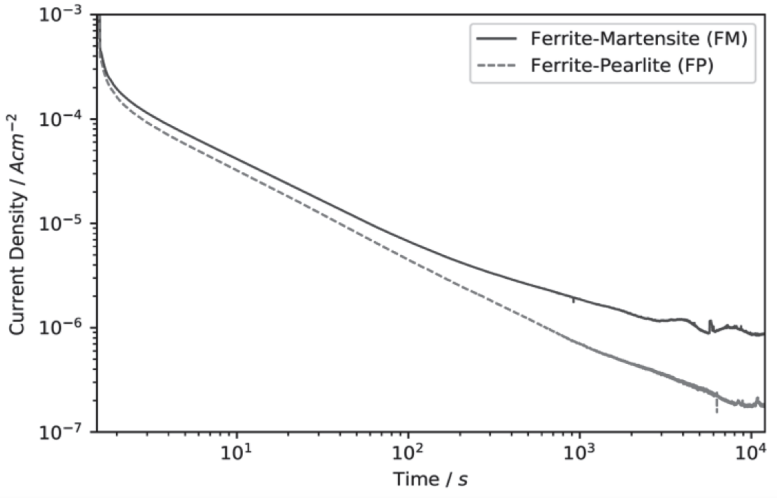

Figure 7.3 Double logarithmic time-current density plots of dual-phase steels during potentiostatic polarisation at 0.2 V (vs. Ag/AgCl) in 0.1 M NaOH solution with pH of 12.6

Electrochemical Impedance Spectroscopy (EIS) investigations are demonstrated in figure 7.4, which shows selected Nyquist and Bode plots of the FM and FP samples after potentiostatic polarisation. In the Nyquist plots, the FP samples exhibit a larger arc diameter than the FM samples. A second smaller semi-circle found at higher frequencies is only visible after zooming in the graph. From the EIS spectra inspection, the higher impedance value for the FP sample is clearly observed. The larger arc in the Nyquist plots and the higher impedance modulus values for the FP samples indicate a higher barrier property for the passive layer formed on the FP

samples. This agrees with the current transient trends observed at steady-state in potentiostatic polarisation curves.

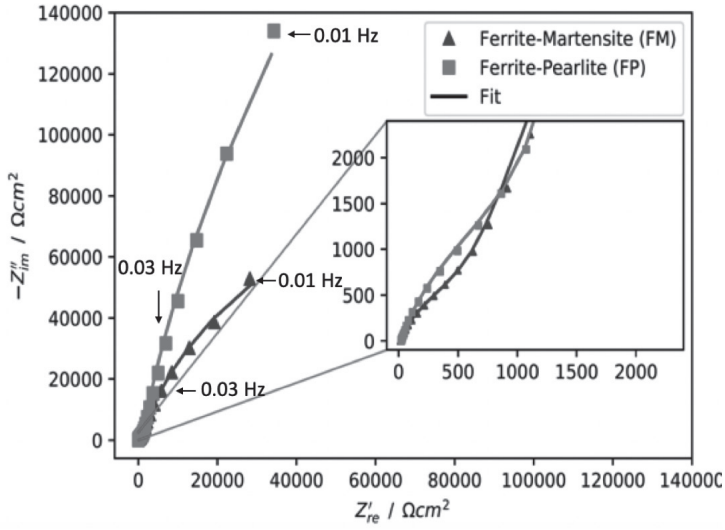

Figure 7.4 Nyquist plots of dual-phase microstructures obtained with EIS after potentiostatic polarisation at 0.2 V (vs. Ag/AgCl) in 0.1 M NaOH solution for 6 hours

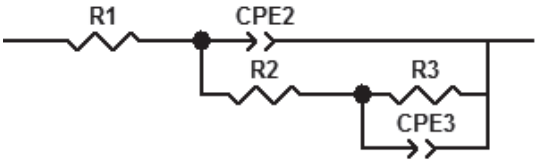

Figure 7.5 Equivalent circuit proposed for modelling the electrochemical response of dual-phase microstructures

The EIS results are fitted to an electrical equivalent circuit (EEC) shown in Fig 7.5. The chosen circuit with two-time constants was previously

used in literature for fitting the EIS response of low carbon steels in an alkaline NaOH environment to EEC [10], [11]. R_1 represents the electrolyte's resistance, R_2 and CPE_2 the resistance and capacitance of the double layer, R_3 the passive layer resistance, and CPE_3 the capacitance of the passive film. Constant phase elements (CPE) are employed instead of capacitors due to the deviation from the ideal capacitive behaviour. Capacitance (C) values are calculated by using the resistance and constant phase element values with the Hsu and Mansfeld approach [12]:

$$C = R^{\frac{(1-n)}{n}} Q^{\frac{1}{n}} \qquad \text{[Eqn. 7.1]}$$

where R is the resistance, n is the CPE coefficient, and Q is the CPE constant. Calculated equivalent resistance and capacitance values after the equivalent circuit fit are given in table 7.3.

	R_2 (Ωcm^2)	C_2 ($Fcm^{-2} \times 10^{-5}$)	CPE_2-Q ($\Omega^{-1} s^n cm^2 \times 10^{-5}$)	CPE_2-n	R_3 ($\Omega cm^2 \times 10^5$)	C_3 ($Fcm^{-2} \times 10^{-5}$)	CPE_3-Q ($\Omega^{-1} s^n cm^2 \times 10^{-5}$)	CPE_3-n
FM	85±30	13.1±0.7	2.3±1.2	0.87±0.04	2.02±0.12	3.2±0.5	2.2±0.5	0.82±0.03
FP	250±110	1.3±0.5	1.91±0.13	0.85±0.02	11.0±1.5	1.3±0.4	1.1±0.4	0.88±0.08

Table 7.3 The fitting values of the equivalent circuit components for ferrite-martensite (FM) and ferrite-pearlite (FP) microstructures

Passive layer resistance R_3 is considerably higher for the FP sample, with a fivefold increase from the FM sample's resistance value. This agrees with the behaviour seen in potentiostatic measurements. It indicates that the ferrite-pearlite microstructure forms a better passive layer with greater barrier properties.

Capacitance values of the double layers were in close proximity to one another. The ferrite-martensite passive film's average capacitance was slightly higher than the passive film of the ferrite-pearlite sample.

The calculated capacitance values can be used to estimate the thickness of the passive layer. The relation between the capacitance value and the thickness is given by [13]:

$$d_f = \frac{\varepsilon \varepsilon_0}{C_f} \qquad \text{[Eqn.7.2]}$$

where d_f is the thickness of the passive layer, ε = 40 [14], [15] the dielectric constant of the passive films formed on carbon steels, ε_0 the permittivity of vacuum, and C_f the capacitance of the passive film, the calculated thickness values are 1.10 ± 0.17 nm for ferrite-martensite and 2.2 ± 0.8 nm for ferrite-pearlite respectively.

The Mott-Schottky analysis is carried out to measure the effect of different phase constituents on the passive film's electronic properties. Figure 7.6 shows the Mott-Schottky plots of the passivated samples. The positive slopes of both samples indicate an n-type semiconductor behaviour of the passive layer [16]. This behaviour arises from point defects in the oxide structure, such as O^{2-} vacancies and Fe^{2+} ions in a Fe^{3+} matrix [17].

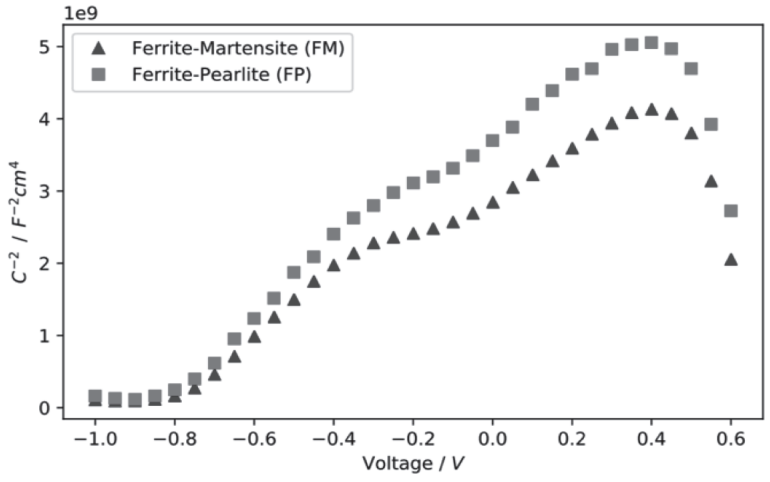

Figure 7.6 Mott–Schottky plots for the passive film formed on different microstructures for 6 h at 0.2 V in 0.1 M) NaOH solutions at a frequency of 1 kHz

A non-linear behaviour is observed in Mott-Schottky plots. The decreasing slopes at higher potentials suggest that Fe^{3+} vacancies start contributing to the total doping concentration with increasing potential [17]. The existence of a second linear positive slope indicates a change in

donor type or the presence of a second donor level in the band gap that corresponds to the ionisation of a deeper donor [18]. The (hydr)oxide film's capacitance is composed of the Helmholtz layer of the electrolyte and the space charge region of the semiconductor. The capacitance of the passive film is the combined capacitances of both layers connected in series. In the case of the passive film, the capacitance of the Helmholtz layer is much higher, and the capacitance can be regarded as the capacitance of the space charge layer. In such a case, the Mott-Schottky relationship can be used to quantitatively analyse the donor density of the oxide [19][20]:

$$\frac{1}{C^2} = 2(E - E_{FB} - kT/q) \,/\, \varepsilon\varepsilon_0 q N_d \qquad \text{[Eqn. 7.3]}$$

where C is the capacitance, E_{FB} the flat band potential, k the Boltzmann constant, T the temperature, q the electron charge, ε_0 the permittivity of vacuum, ε = 40 previously measured dielectric constant of the passive films formed on carbon steels [reference], and N_d is the donor density. The donor density is inversely correlated with the Mott-Schottky slope.

The calculated donor densities of both FM and FP samples were on the order of 10^{21} cm^{-3}. This order of magnitude is typical for the disordered

heavily doped passive films [5], [9], [18], [21], [22]. The donor density values were calculated from the linear slopes in the more positive potential range. The donor densities were calculated to be $2.4 \pm 0.3 \times 10^{21}$ cm^{-3} for the FM and $1.49 \pm 0.08 \times 10^{21}$ cm^{-3} for the FP sample. The FM sample's donor density is 1.6 times the FP sample's donor density, showing that the passive layer of the FM sample is notably more defective. Furthermore, the flatband potential for the FP and FM samples are 0.81 ± 0.01 and 0.73 ± 0.02 V. This difference in flatband potential indicates differences in the fraction of iron oxides in the passive film and is in line with previously reported values for passive layers developed on multi-phase steel substrates [5].

Electrochemical experiments exhibit that the ferrite-pearlite microstructure has a more resistant passive layer with better barrier properties. Superior barrier properties of the ferrite-pearlite microstructure are attributed to decreased donor density of the developed passive film. The defect density is an essential factor responsible for the electronic and ionic conductivity of the passive oxide layer. An increase in the donor density decreases the band gap of the oxide [23], facilitating the transfer of electrons and resulting in increased electronic conductivity. On the other hand, an increase in ionic defect concentration also allows easier ionic

access through the oxide film, increasing the ionic current [5]. As a result, both ionic and electronic resistances become essential factors in determining the barrier properties of the developed passive layer.

The FM sample's higher donor density can be explained by the complex microstructure morphology of the martensite phase. The passive film's overall quality is depreciated by the disordered surface resulting from the displacive diffusionless martensite transformation. The distorted microstructure has high surface energy due to the increased dislocation density and a higher number of ferrite-martensite boundaries. The ferrite-martensite grain boundaries are composed of a significant amount of lattice mismatch. Intricate lath and grain boundaries disturb the passive layer's packing structure, therefore resulting in a more defective passive film. Furthermore, it has been shown that the donor density of the pure martensite is higher than both dual-phase ferrite-martensite and pure ferrite microstructures, highlighting the harmful governing effect of martensite on passivity [5]. The increased donor density could also be facilitating the formation of Fe_3O_4, which results in a more conductive passive layer with a higher amount of oxygen vacancies [17].

It has been shown that the electronic resistance of bulk γ-Fe_2O_3 (in the order of 10^{16} Ωm [25]) is significantly larger than Fe_3O_4 (in the order of 10^{10} Ωm [24]). The band-gap of γ-Fe_2O_3 2.3 eV [18] is significantly higher than that of Fe_3O_4 (0.1 eV [26]). Electronic conduction is further affected by the continuous exchange of electrons between Fe^{+2} and Fe^{+3} ions. The logarithmic slope of the potentiostatic experiments decreases faster for the FM sample, indicating that an increasing part of the current is directed towards conversion between different forms of iron oxide. This would introduce higher Fe^{+2} concentration due to an increased Fe_3O_4 ratio, potentially increasing the current density by facilitating the exchange of electrons between Fe^{+2} and Fe^{+3} ions. Meanwhile, irregular and open structures such as porous FeO(OH) permit easier access to corrosive species such as oxygen to the substrate under the protective oxide film, causing minimal resistance [27]. The relative fraction of such species undoubtedly results in different corrosion resistivities for different microstructures. Future XPS analysis would illuminate this behaviour.

7.4 Conclusions

In this paper, phase constituents' role on the passivity behaviour of two-phase high strength low alloy steels is investigated in a 0.1 M NaOH

environment. The effect of phase contribution on the passivity behaviour of two-phase steels is analysed with potentiostatic polarisation, electrochemical impedance spectroscopy, and Mott-Schottky analysis. The following results are drawn from the electrochemical measurements:

- The current density during steady-state potentiostatic polarisation is higher for ferrite-martensite microstructure. The evolution of the logarithmic slopes with time indicates an immense amount of ferric-ferrous transformation of the ferrite-martensite microstructure, resulting in a more disorderly passive film.
- EIS measurements of the passive layers show a similar electrochemical response with two-time constants for both microstructures; however, the passive layer of the ferrite-pearlite microstructure displays a distinctly more resistive behaviour.
- Ferrite-martensite microstructure passive layer has a higher donor density, which results in a more defective film.

The presented results demonstrate that passive electrochemical behaviour is strongly dependent on the microstructure and phase constituents. For passivated two-phase ferrite-martensite and ferrite-pearlite microstructures with an equal amount of ferrite volume fraction, barrier

properties of the passive layer of ferrite-pearlite microstructure are determined to be superior to ferrite-martensite.

7.5 References

[1] J. Sietsma, “Physical modelling the microstructure formation in advanced high-strength steels,” *Mater. Sci. Forum*, vol. 762, pp. 194–209, 2013.

[2] A. Kalhor, M. Soleimani, H. Mirzadeh, and V. Uthaisangsuk, “A review of recent progress in mechanical and corrosion properties of dual-phase steels,” *Arch. Civ. Mech. Eng.*, vol. 20, no. 3, 2020.

[3] E. G. Astafurova, G. G. Zakharova, E. V Naydenkin, G. I. Raab, and S. V Dobatkin, “Structure and mechanical properties of low-carbon ferrite-pearlite steel after severe plastic deformation and subsequent high-temperature annealing,” *Phys. Mesomech.*, vol. 14, no. 3, pp. 195–203, 2011.

[4] K. Fushimi, R. Nakagawa, Y. Kitagawa, and Y. Hasegawa, “Micro- and Nano-Scopic Aspects of Passive Surface on Pearlite Structure of Carbon Steel in pH 8.4 Boric Acid-Borate Buffer,” *J. Electrochem. Soc.*, vol. 166, no. 11, pp. C3409–C3416, 2019.

[5] K. Yanagisawa, T. Nakanishi, Y. Hasegawa, and K. Fushimi, “Passivity of dual-phase carbon steel with ferrite and martensite phases in pH 8.4 boric acid-borate buffer solution,” *J. Electrochem. Soc.*, vol. 162, no. 7, pp. C322–C326, 2015.

[6] Y. Takabatake, Y. Kitagawa, T. Nakanishi, Y. Hasegawa, and K. Fushimi, “Grain Dependency of a Passive Film Formed on

Polycrystalline Iron in {pH} 8.4 Borate Solution," J. Electrochem. Soc., vol. 164, no. 7, pp. C349--C355, 2017.

[7] D. D. Macdonald, "Passivity: the key to our metals-based civilization, " Pure Appl. Chem. vol. 71, no. 6, 1999.

[8] G. T. Burstein and A. J. Davenport, "The Current-Time Relationship during Anodic Oxide Film Growth under High Electric Field," *J. Electrochem. Soc.*, vol. 136, no. 4, pp. 936–941, Apr. 1989.

[9] T. Yamamoto, K. Fushimi, S. Miura, and H. Konno, "Influence of Substrate Dislocation on Passivation of Pure Iron in pH 8 . 4 Borate Buffer Solution," *J. Electrochem. Soc.*, vol. 157, no. 7, pp. 231–237, 2010.

[10] L. Freire, X. R. Nóvoa, M. F. Montemor, and M. J. Carmezim, "Study of passive films formed on mild steel in alkaline media by the application of anodic potentials," *Mater. Chem. Phys.*, vol. 114, no. 2–3, pp. 962–972, 2009.

[11] S. Joiret, M. Keddam, X. R. Nóvoa, M. C. Pérez, C. Rangel, and H. Takenouti, "Use of EIS, ring-disk electrode, EQCM and Raman spectroscopy to study the film of oxides formed on iron in 1 M NaOH," *Cem. Concr. Compos.*, vol. 24, no. 1, pp. 7–15, 2002.

[12] C. H. Hsu and F. Mansfeld, "Concerning the conversion of the constant phase element parameter Y0 into a capacitance," *Corrosion*, vol. 57, no. 9, pp. 747–748, 2001.

[13] A. J. Bard and L. R. Faulkner, *Electrochemical Methods: Fundamentals and Applications*, 2nd. ed. John Wiley & Sons, 2001.

[14] K. Azumi, “Mott-Schottky Plot of the Passive Film Formed on Iron in Neutral Borate and Phosphate Solutions,” *J. Electrochem. Soc.*, vol. 134, no. 6, p. 1352, 1987.

[15] K. Azumi, T. Ohtsuka, and N. Sato, “Impedance of Iron Electrode Passivated in Borate and Phosphate Solutions,” vol. 27, no. 5, pp. 382–392, 1986.

[16] J. H. Kennedy and K. W. Frese, “Flatband Potentials and Donor Densities of Polycrystalline α -Fe2O3 Determined from Mott-Schottky Plots,” *J. Electrochem. Soc.*, vol. 125, no. 5, pp. 723–726, 1978.

[17] J. Wielant, V. Goossens, R. Hausbrand, and H. Terryn, “Electronic properties of thermally formed thin iron oxide films,” *Electrochim. Acta*, vol. 52, no. 27, pp. 7617–7625, 2007.

[18] L. Hamadou, A. Kadri, and N. Benbrahim, “Characterisation of passive films formed on low carbon steel in borate buffer solution (pH 9.2) by electrochemical impedance spectroscopy,” *Appl. Surf. Sci.*, vol. 252, no. 5, pp. 1510–1519, 2005.

[19] P. Schmuki and H. Böhni, “Illumination effects on the stability of the passive film on iron,” *Electrochim. Acta*, vol. 40, no. 6, 1995.

[20] W. Schottky, “Halbleitertheorie der Sperrschicht,” *Naturwissenschaften*, vol. 26, no. 52, p. 843, 1938.

[21] A. Yilmaz, K. Traka, S. Pletincx, T. Hauffman, J. Sietsma, and Y. Gonzalez-Garcia, “Effect of microstructural defects on passive layer properties of interstitial free (IF) ferritic steels in alkaline environment,” Corros. Sci., vol. 182, p. 109271, 2021.

[22] A. Yilmaz, K.Traka, S. Pletincx, T. Hauffman, J. Sietsma, Y. Gonzalez-Garcia, “The effect of grain size on passive layer properties of pure iron,” *To be Publ.*

[23] J. Wang *et al.*, “Oxygen vacancy induced band-gap narrowing and enhanced visible light photocatalytic activity of ZnO,” *ACS Appl. Mater. Interfaces*, vol. 4, no. 8, pp. 4024–4030, 2012.

[24] Y. Takabatake, K. Fushimi, T. Nakanishi, and Y. Hasegawa, “Grain-Dependent Passivation of Iron in Sulfuric Acid Solution,” *J. Electrochem. Soc.*, vol. 161, no. 14, pp. C594–C600, 2014.

[25] Y. Takabatake, Y. Kitagawa, T. Nakanishi, Y. Hasegawa, and K. Fushimi, “Heterogeneity of a Thermal Oxide Film Formed on Polycrystalline Iron Observed by Two-Dimensional Ellipsometry,” *J. Electrochem. Soc.*, vol. 163, no. 14, pp. C815--C822, 2016.

[26] R. M. Cornell and U. Schwertmann, *The iron oxides; Structure Properties, Reactions, Occurrences and Uses*. 2003.

[27] A. P. Moon, S. Sangal, S. Layek, S. Giribaskar, and K. Mondal, “Corrosion Behaviour of High-Strength Bainitic Rail Steels,” *Metall. Mater. Trans. A*, vol. 46, no. 4, pp. 1500–1518, 2015.

CHAPTER 8

The Influence of Phase Constituents on the Corrosion Response of Ferrite-Martensite and Ferrite-Pearlite Microstructures in acidic environments

This chapter is based on the scientific paper:

A. Yilmaz, C. Ozkan, J. Sietsma, Y. Gonzalez-Garcia, The Influence of Phase Constituents on the Corrosion Response of Ferrite-Martensite and Ferrite-Pearlite Microstructures in acidic environments, (To be submitted).

Abstract

The effect of ferrite-martensite and ferrite-pearlite phase combinations on the corrosion behaviour of a low carbon dual-phase steel is investigated in 0.1 and 0.01 M H_2SO_4 solutions. Various heat treatments in dilatometry are employed to obtain ferrite-martensite and ferrite-pearlite microstructures with similar ferrite fractions. The obtained microstructure is analysed through optical microscopy and scanning electron microscopy (SEM). The electrochemical properties of dual-phase microstructures are investigated with potentiodynamic polarisation and electrochemical impedance spectroscopy (EIS). The potentiodynamic measurements show that the corrosion current density is higher for ferrite-martensite microstructure than ferrite-pearlite microstructure. EIS measurements exhibit a higher resistivity for ferrite-martensite microstructure than the one for ferrite-pearlite microstructure. Therefore, the results reveal that the ferrite-martensite microstructure has a lower corrosion resistance than the ferrite-pearlite microstructure. The lower corrosion resistance in ferrite-martensite microstructure is attributed to the martensite phase's distorted structure, leading to a higher degree of micro-galvanic coupling between phases than ferrite-pearlite microstructure. Moreover, the influence of phase

constituents on corrosion response becomes stronger with the decreasing pH of the environment.

Keywords: *Martensite, pearlite, ferrite, micro-galvanic coupling, corrosion rate*

8.1 Introduction

Multiphase steels have been the centre of attention of various industries over the last decades due to their superior strength-ductility combination than their single-phase counterparts [1]. However, despite their good mechanical properties, the complex electrochemical properties arising from the coupling of the distinct phases have yet to be understood. Each phase of multiphase steels has different microstructural properties, such as crystal structure, chemical composition, and dislocation density. These result in distinct electrochemical properties for individual-phases, which determine the self-corrosion rate of those phases [2]–[5]. When two or more phases are present together in steel, the phases are electrochemically coupled, leading to the selective corrosion of a phase over the other through micro-galvanic coupling between the phases [2]. Therefore, the overall corrosion behaviour of a material can be influenced both by self-corrosion and selective corrosion mechanisms.

The role of ferrite-martensite and ferrite-pearlite phase combinations on the corrosion behaviour of low alloyed steels has been investigated in the past decades. Fushimi et al. [2] study the role of martensite volume fraction on corrosion behaviour of dual-phase steels

with both macro-and micro- electrochemical techniques in 0.1 M sulphuric acid solution. Their research employs well-controlled model microstructures with the same chemical composition of martensite while changing the martensite volume fractions. They show that the self-corrosion rate of the martensite phase is three times higher than that of the ferrite phase by measuring the individual electrochemical response of individual-phases. Moreover, they also present that the ferrite and martensite phases act as anode and cathode sites, respectively. Therefore, the ferrite phase selectively dissolves when combined with martensite, and the corrosion rate increases with increasing martensite volume fraction due to increasing cathodic area. Another research also investigates the effect of the volume fraction of martensite on corrosion behaviour of dual-phase carbon steels in 5% NaCl solution [5]. It exhibits an increase in corrosion rate with increasing martensite volume fraction in a ferrite-martensite microstructure. The authors hypothesize that an increase in martensite phase volume fraction would result in a higher cathode-to-anode ratio and increase the interfacial areas within the martensite structure due to the fibre structure of the martensite, exacerbating corrosion. Another study investigates the influence of different martensite volume fractions and

morphologies on corrosion behaviour of low alloyed steel (composed of ferrite-martensite structure with varying volume fractions of martensite) in a 3.5% NaCl solution [6]. Moreover, the authors compare the corrosion behaviour of ferrite-martensite and ferrite-pearlite phase combinations. They also show that decreasing volume fractions of martensite in a ferrite-martensite microstructure results in a lower corrosion rate, with island martensite morphology resulting in a more corrosion-resistant structure. Moreover, the ferrite-martensite steels have higher corrosion rates compared to the ferrite-pearlite steel. However, the ferrite volume fraction was also lower in all ferrite-martensite steels than the ferrite-pearlite steels. Schultze et al. [3] study the role of pearlite volume fraction in low alloy steels composed of ferrite-pearlite microstructure with various pearlite volume fractions on corrosion behaviour in 20 wt.% NaCl solution. They report the increased dissolution rate of steel with increasing pearlite volume fraction, attributed to the enhanced micro-galvanic coupling between cementite and ferrite. Kumar et al. [7] also studied the effect of martensite volume fraction on corrosion behaviour of low alloyed steels in 3.5% NaCl solution. In contrast to the studies mentioned above, the authors report an initial increase and then decrease in corrosion rate with increasing

martensite volume fraction. This is attributed to the microstructural features such as dislocation density and chemical composition being entangled with one another, complicating the overall electrochemical behaviour.

8.2 Experimental

8.2.1 Material

As-received dual-phase DP1000 steel samples (provided by Tata Steel, IJmuiden, the Netherlands) are selected based on their low-alloyed chemical composition. 5 x 10 mm^2 coupons are created from 2 mm thick steel sheets by laser-cutting. With wavelength dispersive spectroscopy, an electron beam with an energy of 10 keV and a beam current of 100 nA was used to obtain the chemical composition of samples. Chemical analysis was carried out with a JEOL JXA 8900R microscope.

8.2.2 Microstructure Characterisation

Dilatometry - A Bähr DIL 805 A/D dilatometer was employed to perform the heat treatments. Two dual-phase microstructures, a ferrite-martensite and a ferrite-pearlite microstructure, were created through various heat treatments. Heat treatments for the microstructures were designed to

result in similar ferrite phase volume fractions with distinct secondary phases, either pearlite or martensite. Details of the microstructure creation process are given in Chapter 7.

Sample Preparation – For microstructural characterisation, samples were embedded in a Struers ClaroCit epoxy resin and cured under 2 bar pressure for 1 hour. After embedding, the samples were ground with 80 to 4000 grit SiC sanding paper, and subsequently, they were polished with Struers DiaDuo-2 diamond suspensions with 3 and 1 µm sized particles. After polishing, the samples were cleaned with ethanol in an ultrasonic bath for 10 minutes. The samples were dried with compressed air and etched with a 2% Nital solution (nitric acid in anhydrous methanol).

Optical Microscopy and SEM - The microstructure was characterised with optical micrographs by a Keyence VHX-500 optical microscope. The phase constituents and the respective phase volume fractions were determined from the optical micrographs. Volume fraction analysis of the phases was performed through the ImageJ software. The secondary phases are analysed more elaborately by a Jeol JSM-IT100 scanning electron microscope (SEM) with a 13 mm working distance.

8.2.3 Electrochemical Measurements

Sample Preparation - The samples were embedded in epoxy resin, ground, and polished with the same procedures used for the microstructure characterisation. This resulted in a mirror-like polished surface. Electrolube BLR insulating lacquer was used to cover the space between the steel sample and the epoxy resin. This was carried out to prevent potential crevice corrosion during the electrochemical measurements.

Electrochemical Experiments - The electrochemical characterisation was conducted to understand the role of ferrite-pearlite and ferrite-martensite phase combinations on corrosion behaviour in 0.1 and 0.01 M sulphuric acid solutions with pH values of 1.0 and 1.9, respectively. Electrochemical experiments were performed at ambient conditions in solutions prepared with Milli-Q® ultrapure water. Before the electrochemical experiments, the solutions are deaerated for 1 hour by passing nitrogen gas. The electrochemical cell consists of three electrodes. Steel samples were used as the working electrode, stainless steel mesh was used as the counter electrode, and Ag/AgCl,KCl (saturated) electrode as the reference electrode. A Biologic VSP-300 potentiostat combined with EC-lab v11.33 software was used for data acquisition of the electrochemical experiments.

Firstly, open circuit potential (OCP) was measured for 1 hour. Afterwards, electrochemical impedance spectroscopy (EIS) experiments were carried out by applying an AC perturbation in the frequency range from 30 kHz to 10 mHz with a peak-to-peak amplitude of 10 mV. Zview software (v3.5) was employed to analyse the EIS data. Following the EIS measurements, potentiodynamic polarisation experiments were carried out in the potential range of ±0.25 V vs. OCP with a scan rate of 0.167 mV/s.

All tests were repeated three times to estimate the uncertainty of the experiments.

8.3 Results & Discussion

8.3.1 Microstructure Characterisation

The chemical composition of the steel samples is presented in Table 8.1. Heat treatments resulted in dual-phase ferrite-pearlite (FP) and ferrite-martensite (FM) microstructures with similar ferrite volume fractions. The different microstructures were created to have similar ferrite phase volume fractions of 50 %, but they would have distinct secondary phases. Ferrite-martensite microstructure consisted of 50 ± 2 % ferrite, while ferrite-pearlite microstructure consisted of 56 ± 5% ferrite. The ferrite phase grain

size was similar for both of the microstructures. The microstructure of the samples is presented in a more detailed manner in section 7.3.1 (Figure 7.2).

	Fe	***C***	***Si***	***Mn***	***P***	***S***	***Al***	***Cr***	***Cu***	***Ni***
wt%	Bal.	0.001	0.003	0.04	0.003	0.003	0.004	0.014	0.007	0.012

Table 8.1 Chemical composition (wt.%) of cold-rolled low alloyed steel samples

8.3.2 Electrochemical Characterisation

Electrochemical Impedance Spectroscopy (EIS) –Figure 8.1 and figure 8.2 show the Nyquist plots of the microstructures in 0.1 M and 0.01 M sulphuric acid solutions after immersion of 1h at the open circuit conditions, respectively. The Nyquist plots of samples (Fig. 8.1 and 8.2) exhibit a depressed semicircle and an inductive loop at the low-frequency region in both environments. These inductive loops indicate that adsorption of H^+ and HSO_4^+ occurs at the surface of the samples due to the lack of oxygen in the sulphuric acid environment [9], [10]. The absorbed layer is probably composed of iron sulphide and oxide species such as FeS, $FeSO_4$, $Fe_2(SO_4)_3$, Fe_2O_3, and FeO(OH) in sulphuric acid solutions [11], [12].

The ferrite-pearlite (FP) samples exhibit a larger arc diameter than the ferrite-martensite (FM) samples in the Nyquist plots of both environments. This is an indication that the FP samples have higher corrosion resistance in comparison to the FM samples in both 0.1 M and

0.01 M sulphuric acid solutions. Moreover, the arc diameters and impedance modulus values at low-frequency regions are higher for both samples in 0.01 M H_2SO_4 solution in comparison to the higher concentration solution. This indicates that the samples have higher corrosion resistance in a more diluted environment.

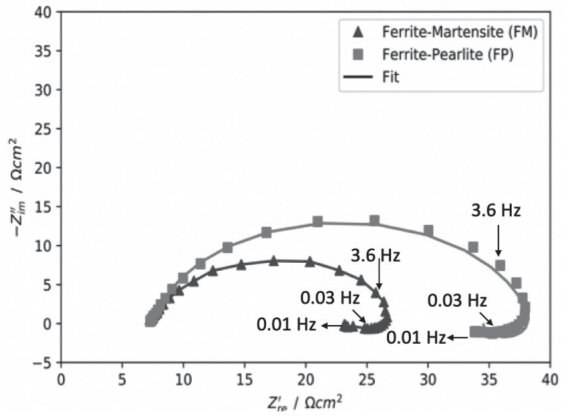

Figure 8.1 Nyquist plots of dual-phase microstructures obtained with EIS in 0.1 M sulphuric acid solution

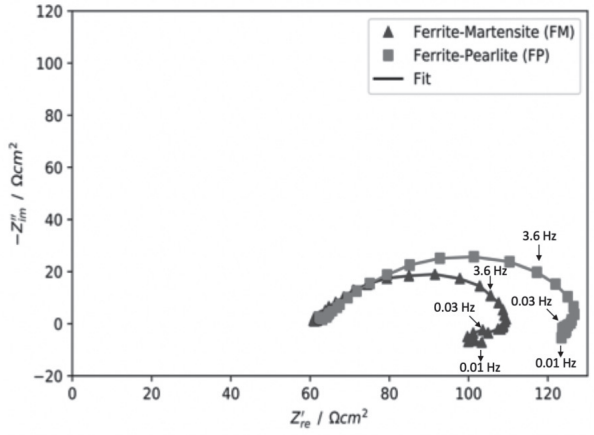

Figure 8.2 Nyquist plots of dual-phase microstructures obtained with EIS in 0.01 M sulphuric acid solution

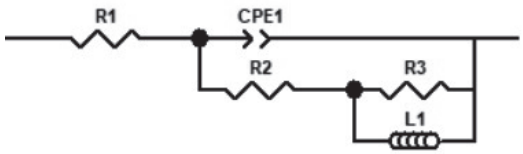

Figure 8. 3 Equivalent circuit proposed for modelling the electrochemical response of dual-phase microstructures

The electrical equivalent circuit (EEC) employed to fit the EIS data is given in figure 8.3. R_2 represents the charge transfer resistance, *CPE* the double layer capacitance, R_3 the resistance and inductance of the adsorbed species, *L* is the equivalent inductance stemming from the relaxation process of the absorbed species [11]. Constant phase elements (CPE) are employed because of the non-ideal capacitive behaviour. The capacitance (*C*) values are calculated by using the resistance and CPE values with the Hsu and Mansfeld approach [13]:

$$C = R^{\frac{(1-n)}{n}} Q^{\frac{1}{n}} \qquad \text{[Eqn. 8.1]}$$

where *R* is the resistance, *Q* is the constant phase element, and *n* is the CPE coefficient. Calculated equivalent resistance, capacitance, and inductance

values for the equivalent circuit fit are given in table 8.2 for concentrated and diluted acidic environments, respectively.

Sample	***Solution***	***R_2 (Ωcm^2)***	***CPE_2-Q ($\Omega^{-1} s^n cm^2$ x10^{-5})***	***CPE-n***	***R_3 (Ωcm^2)***	***L (Hcm^2)***
FM	0.1 M H_2SO_4	21±4	2.3±0.8	0.88±0.02	9±3	49±10
FP		36±3	2.2±0.7	0.89±0.02	14±4	143±48
FM	0.01 M H_2SO_4	146±9	2.1±0.03	0.86±0.02	16±9	7±3
FP		103±12	1.8±0.3	0.81±0.03	32±7	11±4

Table 8.2 The fit values of the equivalent circuit components for ferrite-martensite (FM) and ferrite-pearlite (FP) microstructures in 0.1 M and 0.01 M sulphuric acid solution

The charge transfer resistance R_2 values of the FP microstructure are approximately 50% higher in both concentrated and diluted acidic environments than for the FM microstructure. This shows the higher corrosion resistance of the FP microstructure in both environments. The capacitance fit values (*C* and *CPE-n*) of both microstructures are similar to one another. High CPE coefficients ($n > 0.8$ for all samples) of the microstructures indicate an almost ideal capacitance behaviour, where a value of 0 describes a perfect resistor and a value of 1 describes a perfect capacitor. The solution resistance values R_1 are the same for both samples in identical conditions and decrease with increasing solution concentration.

This was expected as the carrier ion concentration increases with increasing solution concentration.

Potentiodynamic Polarisation - Figures 8.4a and 8.4b display the potentiodynamic polarisation plots of the microstructures in 0.1 M and 0.01 M sulphuric acid solutions, respectively. The cathodic branches of potentiodynamic polarisation exhibit the cathodic hydrogen evolution reactions (HER), while the anodic branches show the metal's anodic dissolution kinetics. In both environments, the cathodic and anodic branches are shifted towards the higher current density values for the FM samples in comparison to the FP samples. This indicates faster kinetics in the FM samples, showing that HER and anodic metal dissolution kinetics is depended on substrate microstructure. In contrast, the slopes in the cathodic and anodic branches of samples do not show a significant difference between samples within the same environment. This shows that the mechanisms of HER and anodic dissolution are independent of the microstructure of the substrate.

Corrosion potentials and corrosion current densities calculated through Tafel slope analysis are presented in table 8.3. Tafel analysis reveals that FM microstructure has a higher corrosion current density in both

concentrated and diluted sulphuric acid environments. In the concentrated solutions, the FM samples have 2.5 times faster corrosion current density than the FP samples, while in the diluted solution, FM samples have 40% higher corrosion current density faster than the FP samples. This agrees with the EIS results and shows that the FM samples corrodes faster than the FP samples. Moreover, the influence of the microstructure becomes more prominent with increasing acidity of the environment. This is to be expected, as the electric field developed from the double layer at the metal-electrolyte interface would be stronger with an increase in dissolved carrier ion (H^+) concentration.

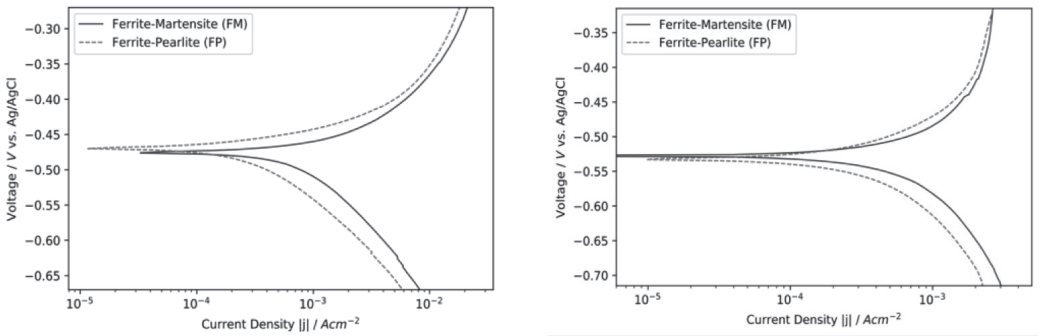

Figure 8.4 Potentiodynamic polarisation plots of dual-phase ferrite-martensite (FM) and ferrite-pearlite (FP) microstructures in a) 0.1 M , (b) 0.01 Msulphuric acid solutions

	Solution	***j_{corr} (A.cm^{-2} x 10^{-4})***	***E_{corr} (mV vs. Ag/AgCl)***
FM	0.1 M H_2SO_4	9.2±1.0	-470±6
FP		3.8±0.5	-467±6
FM	0.01 M H_2SO_4	3.8±1.0	-527±1
FP		2.8±0.3	-534±2

Table 8.3 Corrosion current density (j_{corr}) and corrosion potential (E_{corr}) values of ferrite-martensite (FM) and ferrite-pearlite (FP) microstructures calculated from the potentiodynamic polarisation experiments in 0.1 M and 0.01 M sulphuric acid solutions

To obtain an unambiguous identification of pearlite and martensite's effect on the corrosion behaviour of two-phased steel, it is crucial to isolate the differences between the microstructures of samples on solely the phases. Moreover, it is also important to keep the ferrite phase volume fraction constant to avoid the effect of the anode to cathode ratio on corrosion behaviour. Therefore, two distinct dual-phase microstructures with very similar ferrite volume fractions with different secondary phase constituents (ferrite-martensite and ferrite-pearlite) are created through heat treatments. The low-alloyed nature of samples minimises the formation of inclusions and alloy segregation. Furthermore, applying heat treatments to vary phases within the microstructure allows avoiding the

introduction of dislocations and texture through thermomechanical processing [1], [14], [15]. Therefore, the effect of these features is limited, allowing the investigation of the role of the phase constituents on corrosion behaviour.

Electrochemical experiments reveal that the ferrite-pearlite microstructures corrode slower than the ferrite-martensite microstructures in both concentrated (0.1 M) and diluted (0.01 M) sulphuric acid environments. The corrosion of metal with multiple phases, such as the ferrite-martensite and ferrite-pearlite microstructures used in these experiments, progresses through the self-corrosion of the phases and the preferential corrosion of the more anodic phase that stems from the micro-galvanic coupling between the phases [2]. As aforementioned, the contribution of the self-corrosion of the ferrite phase is kept constant by keeping the ferrite volume fraction constant in the ferrite-martensite and ferrite-pearlite microstructures. Therefore, the differences in the overall corrosion behaviour originate from the self-corrosion of the martensite and pearlite phases and the micro-galvanic coupling formed between the different phases.

The displacive transformation mechanism of the martensite phase substantially increases the dislocation density throughout the microstructure. The diffusionless transformation traps interstitial carbon as the austenite lattice transforms from a face centred cubic into body-centred tetragonal martensite. As a result, the structure is strained and has higher free energy. Amplified strain and dislocation density exacerbate corrosion by decreasing the activation energy related to the corrosion processes. This modification in free surface energy also impacts the rate of electrochemical reactions by facilitating atomic and/or ionic transport. Moreover, a strong micro-galvanic coupling occurs between ferrite and martensite phases because of the high ferrite-martensite boundary area that has its origins in the needle-like morphology of the martensite phase. Therefore, the strained structure of the martensite phase creates a less dense and more active surface with increased dislocation density, which increases the corrosion rate by facilitating cathodic reactions for galvanic corrosion and by exacerbating the self-corrosion in comparison with the more relaxed ferrite phase.

In contrast, the diffusive transformation mechanism of the pearlite brings about different electrochemical properties. The carbon is able to

diffuse during the austenite to pearlite transformation, generating lamellar plates of ferrite and cementite. The lamellar structure of the pearlite phase resulting from this diffusive transformation could potentially be causing a weaker galvanic interaction with the bulk ferrite phases, decreasing corrosion severity in the process. For this reason, understanding the micro-galvanic coupling between the phases is essential. Local micro-galvanic interaction between the phases can be identified more clearly with localised electrochemical experiments.

8.4 Conclusions

In this work, the role of phase constituents on the corrosion behaviour of two-phase high strength low alloy steels is studied in 0.1 M and 0.01 M sulphuric acid solutions. The following conclusions were drawn.

- The samples with ferrite-martensite and ferrite-pearlite microstructure are obtained after various heat treatments while limiting the variations in other microstructural features such as elemental segregation, crystallographic texture, and grain size. Moreover, the ferrite phase ratio in both microstructures is very similar, allowing to avoid the effect of the anode to cathode ratio on corrosion behaviour.

- The electrochemical impedance spectroscopy measurements show that both microstructures have similar capacitive properties, but ferrite-martensite microstructure displays lower charge transfer resistance. Both microstructures exhibit an inductive behaviour, resulting from the surface iron sulphide and/or oxide corrosion products.
- The corrosion potentials of the microstructures are very similar during potentiodynamic polarisation experiments. However, the ferrite-martensite microstructure exhibits a significantly higher corrosion current density than the ferrite ferrite-pearlite microstructure.
- The values of resistivity (EIS measurements) and current density (potentiodynamic polarisation) differences between ferrite-martensite and ferrite-pearlite microstructures increase with decreasing pH values.

From the results given above, it is concluded that the ferrite-martensite microstructure has a higher corrosion rate than the ferrite-pearlite microstructure due to the higher degree of galvanic coupling in the ferrite-martensite microstructure. Moreover, the effect of microstructure on

corrosion behaviour is more pronounced with decreasing the pH of the solution.

8.5 References

[1] C. Tasan, M. Dieh, D. Yan, M. Bechtold, F. Roters, L. Schemmann, C. Zheng, N. Peranio, D. Ponge, M. Koyama, K. Tsuzaki, and D. Raabe "An Overview of Dual-Phase Steels: Advances in Microstructure-Oriented Processing and Micromechanically Guided Design," *Annu. Rev. Mater. Res.*, vol. 45, no. 1, pp. 391–431, 2015.

[2] K. Fushimi, K. Yanagisawa, T. Nakanishi, Y. Hasegawa, T. Kawano, and M. Kimura, "Microelectrochemistry of dual-phase steel corroding in 0.1 M sulphuric acid," *Electrochim. Acta*, vol. 114, pp. 83–87, 2013.

[3] T. Haisch, E. J. Mittemeijer, and J. W. Schultze, "On the influence of microstructure and carbide content of steels on the electrochemical dissolution process in aqueous NaCl-electrolytes," *Mater. Corros.*, vol. 53, no. 10, pp. 740–755, 2002.

[4] T. V. Shibaeva, V. K. Laurinavichyute, G. A. Tsirlina, A. M. Arsenkin, and K. V. Grigorovich, "The effect of microstructure and non-metallic inclusions on corrosion Behaviour of low carbon steel in chloride containing solutions," *Corros. Sci.*, vol. 80, pp. 299–308,

2014.

[5] R. Nadlene, H. Esah, S. Norliana, and M. A. Mohd Irwan, “Study on the effect of volume fraction of dual phase steel to corrosion behaviour and hardness,” *World Acad. Sci. Eng. Technol.*, vol. 50, no. 2, pp. 564–567, 2011.

[6] P. P. Sarkar, P. Kumar, M. K. Manna, and P. C. Chakraborti, “Microstructural influence on the electrochemical corrosion behaviour of dual-phase steels in 3.5% NaCl solution,” *Mater. Lett.*, vol. 59, no. 19–20, pp. 2488–2491, 2005.

[7] S. Kumar, A. Kumar, Vinaya, R. Madhusudhan, R. Sah, and S. Manjini, “Mechanical and Electrochemical Behaviour of Dual-Phase Steels Having Varying Ferrite–Martensite Volume Fractions,” *J. Mater. Eng. Perform.*, vol. 28, no. 6, pp. 3600–3613, 2019.

[8] K. D. Ralston and N. Birbilis, “Effect of grain size on corrosion: A review,” *Corrosion*, vol. 66, no. 7, pp. 0750051–07500513, 2010.

[9] K. H. Kim, S. H. Lee, N. D. Nam, and J. G. Kim, “Effect of cobalt on the corrosion resistance of low alloy steel in sulfuric acid solution,”

Corros. Sci., vol. 53, no. 11, pp. 3576–3587, 2011.

[10] Z. Panossian, N. L. de Almeida, R. M. F. de Sousa, G. de Souza Pimenta, and L. B. S. Marques, "Corrosion of carbon steel pipes and tanks by concentrated sulfuric acid: A review," *Corros. Sci.*, vol. 58, pp. 1–11, 2012.

[11] L. Jinlong and L. Hongyun, "The effects of cold rolling temperature on corrosion resistance of pure iron," *Appl. Surf. Sci.*, vol. 317, pp. 125–130, 2014.

[12] X. Q. Cheng, F. L. Sun, S. J. Lv, and X. G. Li, "A new steel with good low-temperature sulfuric acid dew point corrosion resistance," *Mater. Corros.*, vol. 63, no. 7, pp. 598–606, 2012.

[13] C. H. Hsu and F. Mansfeld, "Concernng the conversion of the constant phase element parameter Y0 into a capacitance," *Corrosion*, vol. 57, no. 9, pp. 747–748, 2001.

[14] M. Eskandari, A. Najafizadeh, and A. Kermanpur, "Effect of strain-induced martensite on the formation of nanocrystalline 316L stainless steel after cold rolling and annealing," *Mater. Sci. Eng. A*,

vol. 519, no. 1–2, pp. 46–50, 2009.

[15] J. Lv and H. Luo, “Effects of strain and strain-induced α’-martensite on passive films in AISI 304 austenitic stainless steel,” *Mater. Sci. Eng. C*, vol. 34, no. 1, 2014.

Part D

Relationship between localised corrosion and crystallographic texture

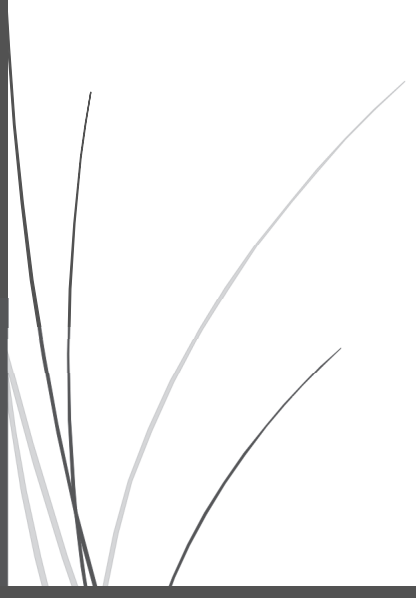

CHAPTER 9

The role of crystallographic orientation on the corrosion behaviour of interstitial free (IF) steels

This chapter is based on the scientific paper:

A. Yilmaz, C. Örnek, K. Traka, J. Sietsma, Y. Gonzalez-Garcia, Effect of crystallographic orientation on localised corrosion behaviour of interstitial free (IF) steels (To be submitted)

Abstract

In this study, the effect of crystallographic orientation on localised corrosion behaviour of an interstitial free (IF) steel is studied. The microstructure analysis was carried out through electron backscatter diffraction (EBSD) to investigate the grain crystallographic orientation and dislocation density distribution. Scanning Kelvin probe force microscopy (SKPFM) measurements show Volta-potential distribution gradients between the grains in (001), (111), and (101) crystallographic orientations parallel to the surface. The grains in (001) orientation show more cathodic (noble) behaviour than the ones in (111) and (101) orientations. In-situ atomic force microscopy (AFM) topography measurements show that the corrosion resistance in 0.02 M NaCl solution decreases in the order of (001), (101), and (111) crystallographic orientations.

Keywords: *crystallographic orientation, corrosion, Volta-potential, in-situ AFM*

9.1 Introduction

Over the last decades, interstitial free (IF) steels have been widely used in the automotive industry to produce car body panels due to their very high levels of formability [1], [2]. Their good formability is achieved by controlling their microstructural features such as interstitial content, grain size, and crystallographic texture [3]–[6]. Significant advances have been achieved in understanding the role of crystallographic texture on formability and drawability [1], [7]. However, the effect of crystallographic texture on corrosion behaviour is yet to be advanced. Several studies have investigated the role of crystallographic texture on the corrosion behaviour of ferritic ferrous materials [8]–[15]. Although these studies show that the crystallographic orientation of grains affects corrosion behaviour, there is no consensus on the trend of corrosion resistance. One reason for establishing a clear trend is the interaction between the crystallographic orientation and other microstructural features such as dislocation density and elemental segregation. The complex interaction between crystallographic orientation and dislocation density as well as elemental segregation on corrosion behaviour brings difficulties in understanding the effect of each feature on corrosion behaviour. Another reason for no unified

view on the relation between crystallographic orientation and corrosion behaviour is the limitations in the resolution of the techniques. The studies generally were conducted on single crystal materials with conventional electrochemical methods with centimetre scale resolution [9], [10] or localised electrochemical techniques with micrometre scale resolution on a single grain of polycrystalline ferrous materials [11], [12], [16]. These approaches provide valuable information on the corrosion behaviour of grains in specific crystallographic orientations. The solution is applied on a single grain with these approaches. However, the neighbouring grains with different crystallographic orientations might also affect the corrosion behaviour of one another. To include the role of these neighbouring grains on corrosion behaviour, it is crucial to employ localised electrochemical techniques that allow the application of a solution to numerous grains concurrently. Moreover, it is important to employ electrochemical characterisation techniques with nanoscale resolution to investigate the corrosion behaviour at the nanometre range.

Scanning Kelvin probe force microscopy (SKPFM) is a powerful technique that can yield the Volta-potential of surfaces on nanometre range. The Volta-potential is an electron-sensitive parameter and defines

the thermodynamic tendency of a metal surface to undergo electrochemical reactions [17]. Therefore, Volta-potential can be employed as a parameter to understand the corrosion susceptibility of surfaces [17]–[20]. Generally, a low (cathodic) potential indicates a low inclination for electron transfer, leading to low electrochemical reactivity, and therefore, higher corrosion resistance. This information can be employed to understand the differences in the local reactivity of metals since Volta-potential gradients indicate the formation of galvanic couplings. Several studies have employed Volta-potential to investigate the role of microstructural features such as inclusions [21] and dislocation density [22]. However, to the best of our knowledge, the effect of crystallographic orientation on Volta-potential was not revealed on steels. In-situ AFM is useful for monitoring the localised corrosion of metals in real-time with a spatial resolution on the nanoscale. It has been employed with a combination of SKPFM for investigating the role of several microstructural features. The results revealed the initial stages and progression of corrosion of grain boundaries, phases, and inclusions [23].

The present work investigates the effect of crystallographic orientation on localised corrosion behaviour of polycrystalline IF steels. Detailed

microstructure characterisation was conducted by electron backscatter diffraction (EBSD) analysis. SKPFM measurements were conducted to correlate the crystallographic orientation with Volta-potential distribution. In-situ liquid AFM measurements were performed to observe the corrosion process at different exposure times, to identify the initiation sites for localised corrosion, and to investigate the corrosion propagation, depending on the crystallographic orientation.

9.2 Experimental

9.2.1 Material

Low-alloyed hot-rolled interstitial free (IF) ferritic steels (provided by Tata Steel, IJmuiden, The Netherlands) were employed in this study. The hot-rolled sample sheets with a thickness of 0.76 mm were laser-cut to the dimensions of 10 mm x 10 mm. Wavelength dispersive spectroscopy (JEOL JXA 8900R) was employed to analyse the steel samples' chemical composition. With a 10 keV electron beam energy and 100 nA current. The chemical composition of samples is given in Table 9.1.

	Fe	***C***	***Mn***	***Al***	***N***	***Ti***	***S***	***Cr***
wt%	bal.	0.002	0.095	0.05	0.002	0.045	0.006	0.02

Table 9.1 The chemical composition (wt.%) of IF steel samples

9.2.2 Microstructure Characterisation

Electron backscatter diffraction (EBSD) analysis was conducted to characterize and quantify crystallographic orientation, phases and dislocation density of IF steel samples. To calculate the geometrically necessary dislocation density, EBSD data was analysed with OIM v7.3 software, employing the function described in ref. [24]. In this method, the dislocations are valued by summing the lattice curvature and the divergence of elastic strain tensor (as proposed by [25]).

For EBSD analysis, the samples were ground with SiC abrasive papers sequentially from 80 to 4000 grit. The grinding was followed by polishing with diamond particle slurries (Struers DiaDuo-2). Diamond slurries with 3 and 1 μm particle sizes were applied, respectively. A final polishing step was conducted with OPS suspension of 0.04 μm for 30 minutes. Afterwards, ultrasonic cleaning was undertaken in an ethanol bath for 10 min. Following the ultrasonic cleaning, the samples were rinsed with ethanol and dried with compressed air.

A JEOL JSM 6500F FEG-SEM microscope using an EDAX/TSL detector was employed for the EBSD measurements. A step size of 500 nm and a working distance of 17 mm were used. The geometrically necessary

dislocation (GND) density calculation with TSL-OIM v7.3 software and MTEX in Matlab [26] was conducted using the function described elsewhere [24]. This function calculates the dislocation density via the relationship between the dislocations and the dislocation tensor [27] and the divergence of elastic strain tensors.

9.2.3 Scanning Kelvin probe force microscopy (SKPFM) measurements

Scanning Kelvin probe force microscopy measurements were conducted to investigate the local surface nobility variations depending on the crystallographic orientations of grains. The samples were ground with SiC grind papers from 80 to 4000 grit. Following grinding, the samples were polished with 3, 1, and 0.25 µm alcohol-based polishing slurries (Struers DP-Suspension A) and polishing cloths Struers DP-Mol and Struers DP-Nap. The final surface finishing was then obtained after polishing with a standard colloidal silica suspension with 0.04 µm particle size. The samples were cleaned ultrasonically in ethanol bath for 10 minutes after polishing. A Bruker Dimension Icon© atomic force microscopy (AFM) was used for the SKPFM measurements. The measurements were conducted in the frequency modulation mode. The pixel resolution of Volta-potential maps is

256 x 256 points/line. The scan rate is 0.6 lines/s. The entire scan took approximately 10 min. The measurements were done in ambient air at a temperature of 22.4 °C and ~43% relative humidity. The SKPFM scans were done right after the polishing. An OSCM-Pt R3 n-Si doped Pt-coated tip was used. A bias voltage of 6V was applied to the sample. The Volta-potential values were not inverted due to applying the bias voltage on the samples as described elsewhere [17]. The calibration of the tip was performed as given in ref. [17]. Hence, the electrochemical nobility is proportional to the numerical sign and data variations of Volta-potential values. The higher potential values correspond to higher nobility, while the lower values mean lower nobility. To analyse the obtained data, the software Gwydion v2.56 was employed. To estimate the experimental uncertainty, the Volta-potential scans were repeated in three different areas, having grains with different crystallographic orientations. To obtain the average potential values for a particular crystallographic orientation, the mean potential values are calculated within grains with (111), (001) and (101) orientations. This calculation was repeated for three different grains, having a single crystallographic orientation.

9.2.4 In-situ atomic force microscopy (AFM) measurements

In-situ liquid AFM measurements were performed to monitor the local corrosion process, depending on the crystallographic orientation of grains. The measurements were conducted with a Bruker Dimension Icon© atomic force microscopy (AFM). An electrochemical cell was used for immersing the sample in 0.02 M NaCl solution. The sample was prepared by following the same sample preparation procedure as for SKPFM measurements. The measurements were done in ambient conditions. The topography of samples was acquired in contact mode. A ContAl-G probe (Si-probe with a reflex coating of Al) having an 8 nm tip apex was used. The scan rate and pixel resolutions were 0.41 lines/s and 256 x 256 points/line, respectively. An area of 19 µm x 19 µm was scanned, taking 10 min 40 s to acquire each topography map. The spatial resolution is approximately 75 nm. The first scan was conducted after 40 min of immersion to the electrolyte. This time was needed to set up the AFM and find the area of interest to be scanned. The Gwydion v2.56 software was used to analyse the data. A zero-order data levelling and 1st order data flattening were applied on the topography data, and the median line correction was conducted to remove the measurement artefacts. Following the line correction, horizontal artefacts

were removed. Data smoothing was not applied. The changes in the topography upon the immersion was used to evaluate the local corrosion. Line profiles in between grain with different crystallographic orientations were extracted, and the topographical changes along the line profiles were quantified by averaging three lines.

9.3 Results and Discussion

9.3.1 Microstructure analysis

High-resolution EBSD analysis was performed to investigate the grain crystallographic orientations of the polycrystalline IF steel samples. The geometrically necessary dislocation density (GND) distribution was also acquired through the local misorientations. In Figure 9.1a and 9.1b, the inverse pole figure (IPF) and geometrically necessary dislocation density maps in the Rolling Direction (RD) - Transverse Direction (TD) plane are given for an area of 180 x 640 μm^2, respectively. The measurements in RD – TD planes are shown since the SKPFM and in-situ AFM analysis were conducted on this plane, allowing to correlate the crystallographic orientation obtained through EBSD analysis with the SKPFM measured Volta-potential and localised dissolutions observed in-situ AFM analysis.

Figure 9.1a shows that the samples are composed of an equiaxed grain structure. The sample does not contain significant orientation gradients, stemming from the recrystallization after hot-rolling. Moreover, the sample microstructure shows only the body-centred cubic (BCC) crystal structure, indicating that the sample is composed of only ferrite structure. The formation of inclusions is also not observed. Figure 9.1b shows that the low density of geometrically necessary dislocations is uniformly distributed between grains, whereas the higher GND densities are observed at grain boundaries. The calculated average dislocation density over the sample surface is 3.6 ± 0.4 μm^{-2}. It should be noted that EBSD provides information on the spatially resolved crystallographic orientation. Therefore, the quantified dislocations are only related to the orientation gradient, while the total dislocations are composed of structural dislocations (GNDs) and Statistically Stored Dislocations (SSD).

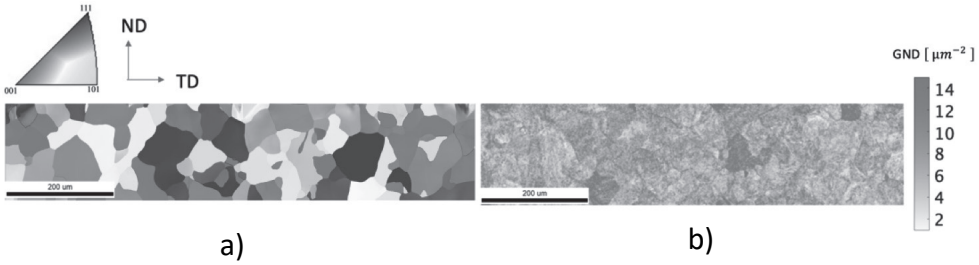

Figure 9.1 Microstructures obtained through EBSD for the samples. a) The inverse pole figure in show the spatially resolved crystal directions parallel to the sheet's normal direction (ND) in accord with the conventional colour coding. b) Geometrically Necessary Dislocations (GND)map calculated for a maximum angle $10°$ *and up to the 3rd neighbour pixel*

9.3.2 Assessing the localised nobility distribution

To demonstrate the effect of crystallographic orientation on the surface nobility, the Volta-potential map of IF steel samples with corresponding EBSD inverse pole figure (IPF) for the same region are given in Fig. 9.2. The potential maps present a good correlation with the EBSD IPF maps, permitting us to observe the variations depending on the crystallographic orientations. Figures 9.2a and 9.2b show EBSD and Volta-potential maps of the same area that includes grains in low-index crystallographic planes (101), (001) and (111), respectively, oriented parallel to the surface. In Figure 9.2b, the grains with different crystallographic orientations have distinctively different potential values. The grains in (111) and (101) crystallographic orientation show more anodic Volta-potential values than the ones in (001) orientation, whereas no significant differences are observed in terms of Volta-potential in between grains in (111) and (101) crystallographic orientation. Line profile 1 in Fig. 9.2c (indicated in Fig. 9.2b) shows the Volta-potential gradients in the grains in (001) and (111) crystallographic orientations. It is shown that the potential gradient across the grain boundary is about 45 mV, with the grains in (001) orientation being nobler with steep potential gradient across the grain boundary. In contrast,

leidt tot een verbetering van de barrière-eigenschappen van de passieve film vanwege de toename van de γ-Fe_2O_3 volumefractie. Deze verbetering wordt toegeschreven aan het dominante effect van veranderingen in de complexe martensietstructuur ten opzichte van verfijning van de voormalige austenietkorrels. Hoofdstuk 6 bestudeert het effect van korrelgrootte op het corrosiegedrag van ijzer. Er blijkt dat de korrelverfijning leidt tot een toename van de corrosiesnelheid. De kristallografische textuurvorming domineert echter het effect van korrelgrootte en leidt tot een afname van de corrosiesnelheid.

Deel C (hoofdstukken 7 en 8) vergelijkt de passiviteit en het corrosiegedrag van laaggelegeerde staalsoorten samengesteld uit ferriet-perliet en ferriet-martensiet microstructuren. Hoofdstuk 7 bestudeert het passiviteitsgedrag van ferriet-martensiet en ferriet-perliet microstructuren. Aangetoond wordt dat de passieve laag gevormd op de ferriet-martensiet microstructuur lagere barrière-eigenschappen heeft dan degene die gevormd is op de ferriet-perliet microstructuur. Dit komt voort uit de hogere donordichtheid van passieve film gevormd op ferriet-martensiet microstructuur. In hoofdstuk 8 wordt het corrosiegedrag van ferriet-perliet en ferriet-martensiet microstructuren onderzocht. De resultaten laten zien

The Volta-potential variation within each grain is minor (Fig. 9.2b and 9.2c). Considering that the differences in dislocation density influence the Volta-potential [29], the minor variance in potential within each grain is attributed to the uniform distribution of GND with no significant variations within each grain. Moreover, no noticeable Volta-potential hot spots (steep Volta-potential gradients in confined areas) are observed. The potential hot spots generally indicate susceptible spots for localised corrosion [30] (e.g., inclusions or intermetallic). The absence of localised hot spots in EBSD analysis agrees with the absence of inclusions in the samples as observed.

9.3.3 Selective dissolution of the grains

The in-situ liquid AFM topography measurements were conducted on samples immersed in 0.02 M NaCl solution to observe the localised corrosion behaviour depending on the crystallographic orientation. In figure 9.3, the EBSD IPF corresponding to the region where in-situ AFM measurements were conducted is given. It shows that the area is composed of grains in low-index crystallographic orientations (101), (001), and (111). In Figures 9.4, 9.5 and 9.6, the topography maps are given for several immersion times of 43 minutes, 160 minutes, and 281 minutes, respectively.

The topography map after 43 min of immersion (Fig. 9.4a) shows the topography differences between the grains in (001) and (101) as well as (101) and (111) orientations. This topography differences indicate the initiation of selective dissolution between these grains. No topography difference between grains (111) and (001) crystallographic orientations shows no selective dissolution between these grains. Moreover, the selective dissolution of grain matrix compared with certain grain boundaries is observed, indicating that the grain matrix dissolves faster than certain grain boundaries. The height profiles in Fig. 9.4b show the above-mentioned selective dissolution between grains and the local attacks at grain boundaries. The height profile 1 is obtained from the grain in (001) orientation towards the grain in (111) orientation. It shows no distinctive selective dissolution in between grains in (001) and (111) orientations. The height profile 2 is acquired from the grain with (001) orientation towards the (101) orientation. The grain in (101) orientation illustrates approximately 17-20 nm lower height than the one in (001) orientation, showing that the grain in (101) dissolves faster than the one in (001) orientation. The height profile 3 exhibits the topography variations from the grain in (111) orientation towards the one in (101) orientation. The grain in

(101) orientation also shows approximately 17-20 nm lower height than the grain in (111) orientation, indicating that the selective dissolution of (101) grain in comparison with the grain in (111) orientation.

In the height profiles 1, 2, and 3, the grain boundaries do not show a distinctive behaviour than the grain matrix. In contrast, the height profiles 4 and 5 show peaks (indicated by arrows in Figure 9.4b) of approximately 7 and 4 nm at the grain boundaries, showing that the neighbouring grains dissolve faster than certain grain boundaries. The quicker dissolution of certain grain boundaries than the grain matrix and the heterogeneous dissolution of grain boundaries along itself (the pronounced peak at height profile 4 and 5 and no distinctive peak at height profile 1, 2, and 3) indicates that the dissolution of grains appears to depend on the specific grain boundary character.

The average roughness (R_a) values within the grains in (001), (101), and (111) orientations are 4.69 nm, 6.72 nm, and 9.04 nm after 43 minutes of immersion, respectively. The largest average roughness within the grain in (111) orientation is attributed to the local attacks observed as pits in confined areas within only this grain. Therefore, the largest roughness within the grain in (111) orientation indicates that the local attacks are more

pronounced within the grain in this orientation in comparison to the ones in (001) and (101) orientations. These pits within the (111) grain are marked as Pit A, B, and C (Figure 9.4a), and the pits and their corresponding height profiles along these pits are given in Figures 9.4c and 9.4d, respectively. The height profiles A, B, and C in Fig. 9.4d show that the depth of pits A, B, and C are approximately 20, 15, and 7 nm, respectively. It is also worth mentioning that local height increases (observed as spikes) are seen within all grains. These local increases also lead to an increase in roughness within each grain. This increase in roughness probably stems from NaCl solution's deposition on the surface, in agreement with the previous studies conducted in-situ topography measurements in NaCl solution [31].

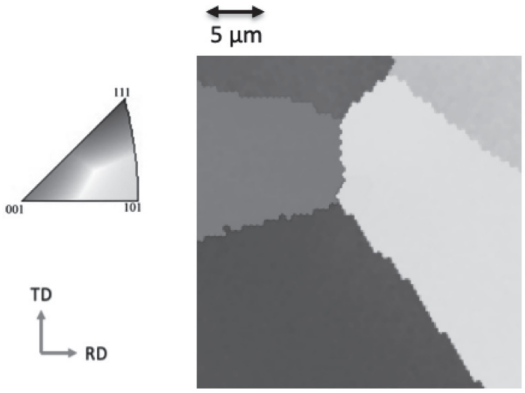

Figure 9.3 EBSD IPF corresponding to the area where in-situ AFM measurements were conducted

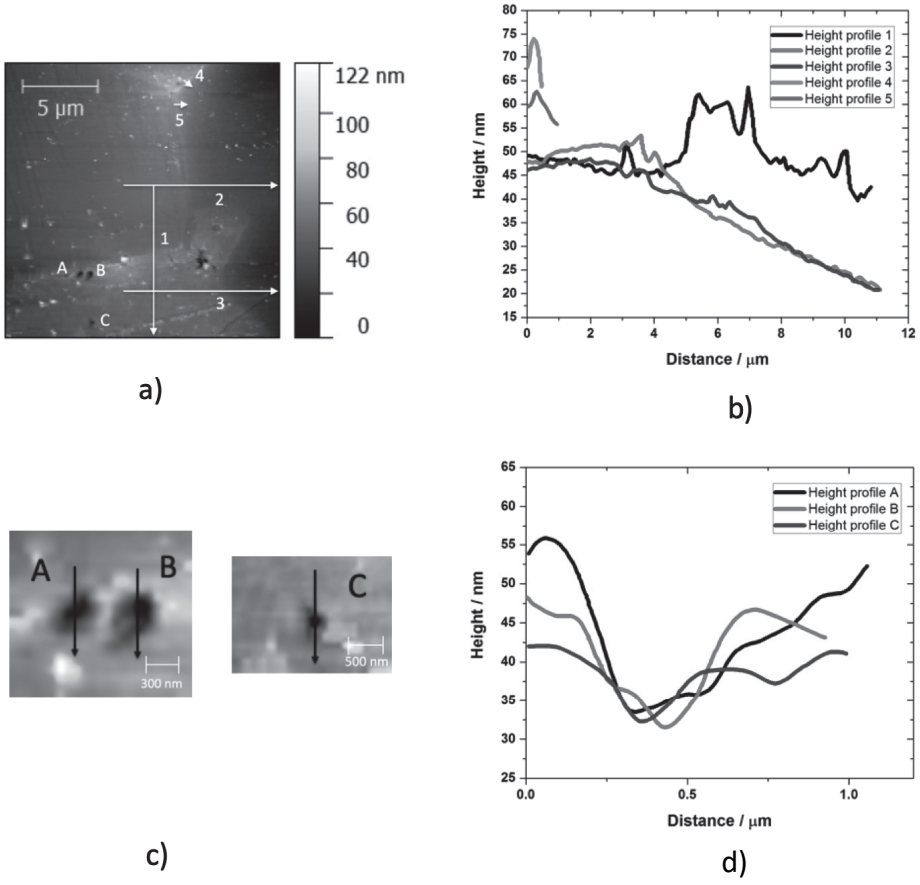

Figure 9.4In-situ AFM analyses after 43 min immersion in 0.02 M NaCl solution on the area corresponding to Fig 9.3: a) Topography map, b) Height profiles extracted between grains with different crystallographic orientations c) Topography map of the pits d) Height profiles extracted over the pits.

Fig. 9.5a shows the topography map after 160 minutes of immersion in NaCl solution. The topological differences between the grains in (001) and (101) as well as (111) and (101) orientations are not more pronounced than after 43 minutes of immersion, indicating no progression of selective

dissolution between these grains. Moreover, selective dissolution between the grains in (001) and (111) orientations is still not observed. The grain matrix's selective dissolution is nevertheless observed at the grain boundaries where the height profiles 4 and 5 are acquired. In the entire map, the spikes (height increases in confined areas) significantly diminish after 160 minutes of immersion compared with 43 minutes of immersion, indicating a diminished solution deposition.

Figure 9.5b shows the height profiles between grains after 160 minutes of immersion. The height profile 1 is acquired from the grain in (001) orientation towards the one in (111) orientation. It shows no height difference between the grains with these crystallographic orientations, indicating that no selective dissolution over these grains occurs after 160 minutes of immersion. Like the immersion of 43 minutes, the height profile 2 shows an approximately 17-20 nm lower height in the grain in (101) orientation than in (001) orientation. This shows no progression of selective dissolution after 160 minutes of immersion. The height profile 3 also shows a 17-20 nm lower height of the grain in (101) orientation than in the one in (111) orientation, similar to the behaviour after 43 minutes of immersion.

This indicates no selective dissolution progression between these grains with further immersion.

The height profiles 1, 2, and 3 still do not exhibit any distinctive behaviour across the grain boundaries. The height profiles 4 and 5 show that the height of the peak at grain boundaries is higher than the grain matrix. However, the height of these peaks decreases approximately 2 nm compared to the situation after immersion of 43 minutes. This indicates the faster dissolution of grain boundaries than the grain matrix during the immersion from 43 minutes to 160 minutes.

The average roughness (R_a) within the grains in (001), (101), and (111) crystallographic orientations diminishes to 3.86 nm, 7.35 nm, and 7.82 nm after 160 minutes of immersion, respectively. The average roughness decrease within the grains in (001) and (111) orientations is mainly attributed to the significant reduction of spikes stemming from the decreasing segregation of NaCl solution on the surface, in line with previously reported results [31]. This indicates that the segregation of solution diminishes with a longer duration of immersion.

The pits and their height profiles across pits A, B, and C are given in figures 9.5c and 9.5d after 160 minutes of immersion, respectively. The

height profiles A and B show that pits' depth does not display a distinct change from 43 minutes of immersion. This indicates no progression of local attacks in pits A and B from 43 minutes to 160 minutes of immersion. However, the height profile C shows that the depth of pit C increases further to approximately 15 nm, indicating the progression of local attacks inside of this pit.

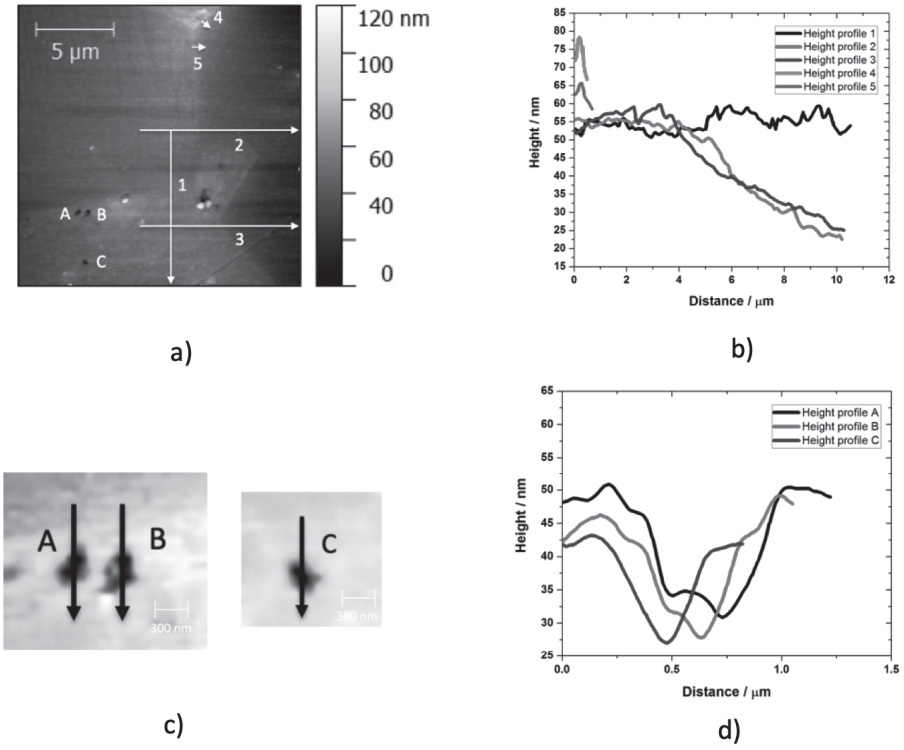

Figure 9.5 In-situ AFM analyses after 160 min immersion in 0.02 M NaCl solution on the area corresponding to the Fig 9.3: a) Topography map, b) Height profiles extracted between grains with different crystallographic orientations c) Topography map of the pits d) Height profiles extracted over the pits.

In Figure 9.6a, the topography map after 281 minutes of immersion is given. It is observed that the selective dissolution between the grains in (001) and (101) as well as (101) and (111) orientations are more pronounced than after 160 minutes of immersion. Moreover, a significant increase in the local roughness is observed within the grain in (111) orientation. Local increases in roughness are also observed within the grain in (101) and (001) orientation. These increases within the grains occur in the decreasing order of (111), (101) than (001) orientations, indicating more localised attacks inside of the grains in the same order.

The height profile 1 in Figure 9.6b shows that the grain in (111) orientation has a significant increase in height exceeding 70 nm in comparison with the one in (001) orientation. Moreover, significant variations of approximately 50-90 nm in the topography within the (111) grain are observed. The height profile 2 shows that the height difference between the grain in (001) orientation and the one in (101) orientation increases to approximately 50 nm after 281 minutes of immersion, indicating the significant progression of selective dissolution of (101) grain. The height profile 3 demonstrates that the grain in (111) orientation also has higher topography (approximately 100 nm) in comparison with the one

in (101) orientation. The average roughness values after 281 minutes immersion time are 9.31 nm for the grain in (001) orientation, 15.42 nm for (101) orientation, and 29.62 nm for (111) orientation.

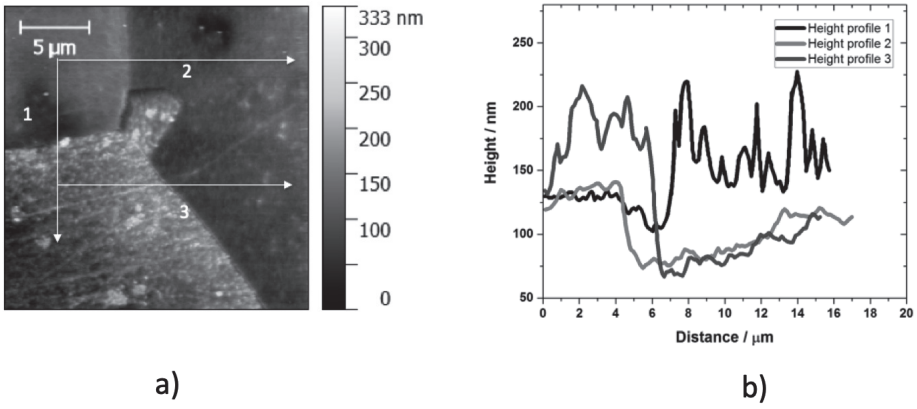

Figure 9.6 In-situ AFM analyses after 4 hours 41 min immersion in 0.02 M NaCl solution on the area corresponding to the Fig 9.3: a) Topography map, b) Height profiles extracted between grains with different crystallographic orientations

To understand the corrosion behaviour depending on crystallographic orientation, Volta-potential is a powerful material property that provides the electrochemical nobility of the surface. The higher algebraic Volta-potential values indicate more cathodic behaviour, implying a decrease in electrochemical reactivity [17], [22]. The grains in (001) orientation exhibits approximately more cathodic values than the grains in (111) orientation and (101) orientation. For the case of ferrite steel with BCC structure, the

surface atom density of (100) plane (1.2 x 1015 atoms cm-2) is significantly higher than (101) plane (1.7 x 1015 atoms cm-2) and (111) plane (1.9 x 1015 atoms cm-2). Considering the sequence of surface atom density, the carbon atoms might segregate more densely to the grains in (100) orientation in comparison with the grains in (111) and (101) orientations. This segregation probably leads to the more noble behaviour of the grains in (001) orientation in comparison with the ones in (111) and (101) orientations. The Volta-potential gradients between the grain in (001) and (111) orientations as well as (001) and (101) orientations indicate the possible formation of micro-galvanic coupling between grains. The formation of the micro-galvanic coupling is observed in in-situ AFM measurements between the grains in (001) and (101) orientation, in correlation with Volta-potential measurements. This shows that the corrosion resistance of grain in (001) orientation is higher than in (101) orientation. In contrast, no micro-galvanic coupling between (001) and (111) grains is observed, while Volta-potential differences are observed between these grains. Moreover, the formation of micro-galvanic coupling is observed between the grains in (111) and (101) orientations, whereas there are no significant Volta-potential differences between these grains. This inconsistency between the localised corrosion

behaviour and ex-situ measured Volta-potential values probably stem from that Volta-potential depends on the environment. The Volta-potential values might change upon the immersion in solution [18],[32], [34], leading to the alterations in the corrosion behaviour.

The initiation of selective dissolution of the grain with (101) orientation in comparison with the one in (111) orientation might initially indicate that the grain (101) orientation has a lower corrosion resistance than the one in (111) orientation. However, the significant progression of local attacks within the (111) grain is observed as pit formation and progression. The grain in (111) orientation exhibits higher surface roughness values than the one in (101) orientation and (001) orientation during the entire immersion. The drastic roughness increases in all grains are observed after 281 minutes of immersion, attributed to the accumulation of corrosion products due to the progression of local attacks. The largest average roughness within the (111) grain indicates that the most severe local attacks occur within this grain.

9.4 Conclusions

This work investigates the effect of crystallographic orientation on the localised corrosion behaviour of low-alloyed interstitial free (IF) steel through Volta-potential and in-situ topography measurements. Considering the results, the following conclusions are drawn:

- The Volta-potential distribution on the surface depends on the crystallographic orientation of grains. The grain in (001) crystallographic orientation (i.e. the (001) plane parallel to the surface) exhibits approximately 45 mV more cathodic (noble) behaviour than the ones in (111) and (101) orientations.
- The in-situ topography measurements show that the grains in (101) orientation selectively dissolves faster than the one in (001) orientation. The local attacks were observed in the later stages of immersion in (001) and (101) orientations, with (101) orientation having more local attacks in comparison to (001) orientation. On the other hand, the grain in (111) exhibits more local and severe attacks than the ones in (101) and (001) orientations, observed as pit formations and progressions in topography measurements.

From the results above, it is concluded that the corrosion resistance of grain increases in the order of (111), (101), and (001) crystallographic orientations in 0.02 M NaCl solution.

9.5 References

[1] S. Hoile, “Processing and properties of mild interstitial free steels,” *Mater. Sci. Technol.*, vol. 16, no. 10, pp. 1079–1093, 2000.

[2] R. Narayanasamy and C. S. Narayanan, “Forming, fracture and wrinkling limit diagram for if steel sheets of different thickness,” *Mater. Des.*, vol. 29, no. 7, pp. 1467–1475, 2008.

[3] E. A. Ariza, M. Masoumi, and A. P. Tschiptschin, “Improvement of tensile mechanical properties in a TRIP-assisted steel by controlling of crystallographic orientation via HSQ&P processes,” *Mater. Sci. Eng. A*, vol. 713, pp. 223–233, 2018.

[4] A. A. Gazder, S. S. Hazra, and E. V Pereloma, “Annealing behaviour and mechanical properties of severely deformed interstitial free steel,” *Mater. Sci. Eng. A*, vol. 530, pp. 492–503, 2011.

[5] S. Tamimi, M. Ketabchi, and N. Parvin, “Microstructural evolution and mechanical properties of accumulative roll bonded interstitial free steel,” *Mater. Des.*, vol. 30, no. 7, pp. 2556–2562, 2009.

[6] O. Saray, G. Purcek, I. Karaman, T. Neindorf, and H. J. Maier, “Equal-channel angular sheet extrusion of interstitial-free (IF) steel: Microstructural evolution and mechanical properties,” *Mater. Sci.*

Eng. A, vol. 528, no. 21, pp. 6573–6583, 2011.

[7] Y. H. Jin, M. Y. Huh, and Y. H. Chung, "Evolution of textures and microstructures in IF-steel sheets during continuous confined strip shearing and subsequent recrystallization annealing," *J. Mater. Sci.*, vol. 39, no. 16–17, pp. 5311–5314, 2004.

[8] A. Schreiber, J. W. Schultze, M. M. Lohrengel, F. Kármán, and E. Kálmán, "Grain dependent electrochemical investigations on pure iron in acetate buffer pH 6.0," *Electrochim. Acta*, vol. 51, no. 13, pp. 2625–2630, 2006.

[9] A. Schreiber, C. Rosenkranz, and M. M. Lohrengel, "Grain-dependent anodic dissolution of iron," *Electrochim. Acta*, vol. 52, no. 27, pp. 7738–7745, 2007.

[10] M. Seo and M. Chiba, "Nano-mechano-electrochemistry of passive metal surfaces," *Electrochim. Acta*, vol. 47, no. 1, pp. 319–325, 2001.

[11] M. Chiba and M. Seo, "Mechanoelectrochemical Properties of Passive Iron Surfaces Evaluated by an In Situ Nanoscratching Test," *J. Electrochem. Soc.*, vol. 150, no. 11, p. B525, 2003.

[12] K. Fushimi, K. Miyamoto, and H. Konno, "Anisotropic corrosion of iron in pH 1 sulphuric acid," *Electrochim. Acta*, vol. 55, no. 24, pp. 7322–

7327, 2010.

[13] K. Fushimi and M. Seo, “An SECM observation of dissolution distribution of ferrous or ferric ion from a polycrystalline iron electrode,” *Electrochim. Acta*, vol. 47, no. 1, pp. 121–127, 2001.

[14] G. P. Cammarota, L. Felloni, G. Palombarini, and S. S. Traverso, “Optical Microscopy Studies of Anodic Dissolution of Iron in Sulfuric and Hydrochloric Acid Solutions: Influence of Metal Purity, Structure, Heat Treatment,” *Corrosion*, vol. 26, no. 6, pp. 229–240, Jan. 2013.

[15] L.C. Yule, V. Shkirskiy, J. Aarons, G. West, B.A. Shollock, C.L. Bentley, P.R. Unwin, “Nanoscale electrochemical visualization of grain-dependent anodic iron dissolution from low carbon steel,” *Electrochim. Acta*, vol. 332, p. 135267, 2020.

[16] A. Schreiber, J. W. Schultze, M. M. Lohrengel, F. Kármán, and E. Kálmán, “Grain dependent electrochemical investigations on pure iron in acetate buffer pH 6.0,” *Electrochim. Acta*, vol. 51, no. 13, pp. 2625–2630, 2006.

[17] C. Örnek, C. Leygraf, and J. Pan, “On the Volta-potential measured by SKPFM–fundamental and practical aspects with relevance to corrosion science,” *Corros. Eng. Sci. Technol.*, vol. 54, no. 3, pp. 185–

198, 2019.

[18] M. Rohwerder and F. Turcu, “High-resolution Kelvin probe microscopy in corrosion science: Scanning Kelvin probe force microscopy (SKPFM) versus classical scanning Kelvin probe (SKP),” *Electrochim. Acta*, vol. 53, no. 2, pp. 290–299, 2007.

[19] V. Guillaumin, P. Schmutz, and G. S. Frankel, “Characterisation of Corrosion Interfaces by the Scanning Kelvin Probe Force Microscopy Technique,” *J. Electrochem. Soc.*, vol. 148, no. 5, p. B163, 2001.

[20] W. Li, M. Cai, Y. Wang, and S. Yu, “Influences of tensile strain and strain rate on the electron work function of metals and alloys,” *Scr. Mater.*, vol. 54, no. 5, pp. 921–924, 2006.

[21] C. Man, C. Dong, K. Xiao, Q. Yu, and X. Li, “The Combined Effect of Chemical and Structural Factors on Pitting Corrosion Induced by MnS-(Cr, Mn, Al)O Duplex Inclusions,” *Corrosion*, vol. 74, no. 3, pp. 312–325, Oct. 2017.

[22] C. Örnek and D. L. Engelberg, “SKPFM measured Volta-potential correlated with strain localisation in microstructure to understand corrosion susceptibility of cold-rolled grade 2205 duplex stainless steel,” *Corros. Sci.*, vol. 99, pp. 164–171, 2015.

[23] F. Zhang, J. Pan, and C. Lin, "Localised corrosion behaviour of reinforcement steel in simulated concrete pore solution," *Corros. Sci.*, vol. 51, no. 9, pp. 2130–2138, 2009.

[24] B. L. Adams and J. Kacher, "EBSD-based microscopy: Resolution of dislocation density," *Comput. Mater. Contin.*, vol. 14, no. 3, pp. 183–194, 2009.

[25] F. Nye, "Some geometrical relations in dislocated crystals," *Acta Metall.*, vol. 1, pp. 153–162, 1953.

[26] F. Bachmann, R. Hielscher, and H. Schaeben, "Texture analysis with MTEX- Free and open source software toolbox," *Solid State Phenom.*, vol. 160, pp. 63–68, 2010.

[27] P. J. Konijnenberg, S. Zaefferer, and D. Raabe, "Assessment of geometrically necessary dislocation levels derived by 3D EBSD," *Acta Mater.*, vol. 99, pp. 402–414, 2015.

[28] J. Jiang, T. B. Britton, and A. J. Wilkinson, "Measurement of geometrically necessary dislocation density with high resolution electron backscatter diffraction: Effects of detector binning and step size," *Ultramicroscopy*, vol. 125, pp. 1–9, 2013.

[29] A.Yilmaz, C.Örnek, K.Traka, J. Sietsma, Y.Gonzelez-Garcia "Combining

surface Volta-potential with electrochemical measurements to investigate the role of cold working on corrosion Behaviour of interstitial free (IF) steels," *To be Publ.*

[30] C. Örnek, M. Liu, J. Pan, Y. Jin, and C. Leygraf, "Volta-potential Evolution of Intermetallics in Aluminum Alloy Microstructure Under Thin Aqueous Adlayers: A combined DFT and Experimental Study," *Top. Catal.*, vol. 61, no. 9–11, pp. 1169–1182, 2018.

[31] K. H. Anantha, C. Örnek, S. Ejnermark, A. Medvedeva, J. Sjöström, and J. Pan, "In Situ AFM Study of Localised Corrosion Processes of Tempered AISI 420 Martensitic Stainless Steel: Effect of Secondary Hardening," *J. Electrochem. Soc.*, vol. 164, no. 13, pp. C810–C818, 2017.

[32] Y. Liew, C. Örnek, J. Pan, D. Thierry, S. Wijesinghe, and D. J. Blackwood, " In-Situ Time-Lapse SKPFM Investigation of Sensitized AA5083 Aluminum Alloy to Understand Localised Corrosion ," *J. Electrochem. Soc.*, vol. 167, no. 14, p. 141502, 2020.

[33] A. B. Cook, Z. Barrett, S. B. Lyon, H. N. McMurray, J. Walton, and G. Williams, "Calibration of the scanning Kelvin probe force microscope under controlled environmental conditions," *Electrochim. Acta*, vol.

66, pp. 100–105, 2012.

[34] M. Iannuzzi, K. L. Vasanth, and G. S. Frankel, “Unusual Correlation between SKPFM and Corrosion of Nickel Aluminum Bronzes,” *J. Electrochem. Soc.*, vol. 164, no. 9,2017.

CHAPTER 10

General Conclusions and Recommendations

10.1 Introduction

In the past decades, the microstructure of materials has been the centre of attention to improve the mechanical properties with only small adaptations of the chemical composition of low-alloy ferrous materials. Many studies aimed to improve the mechanical properties by changing the microstructure allowed to establish relationships between mechanical properties and microstructural properties [1]–[5]. Therefore, the design of ferrous and other alloys is primarily based on the control of the mechanical properties by the effective grain size, dislocation density, phase fractions and compositions, crystallographic texture, and size distributions of strengthening precipitates. Corrosion performance of the materials is usually not primarily considered in the design of the microstructure of materials. This mainly stems from the limited and contradictory knowledge in the literature on the microstructure and corrosion relationship. Researchers have reported conflicting results on the relationship between the microstructure of ferrous alloys and their corrosion relationship. This is mainly due to the complex interaction of microstructural features on corrosion resistance, the resolution limitations of techniques used for characterizing the corrosion performance, and the effect of many different

environments used for the research. This Ph.D. study aimed to come to a better understanding of the microstructural features and corrosion/passivity relationship of various ferrous materials.

10.2 Approach

In this thesis, the effect of several microstructural features (dislocation density, grain size/boundaries, phase combinations, and crystallographic orientation) on local and global corrosion and passivity behaviour has been studied. To establish the relationship between these microstructural features and corrosion behaviour, model microstructures were created through thermomechanical processes and heat treatments. This approach allowed controlling the changes in microstructural features and limiting the complications in the relationship between microstructural features and corrosion behaviour. The obtained microstructural features were analysed comprehensively through various surface characterisation techniques. The conventional and high-resolution local electrochemical characterisation was carried out on model alloys to understand the specific role of the aforementioned microstructural features on the electrochemical behaviour of the employed alloys.

10.3 General Conclusions and Discussion

The main focus of this thesis work was set to understand the specific role of microstructural features on local and overall corrosion and passivity behaviour. The results were obtained to bring a better understanding of the relationship between microstructural features and corrosion. The gained knowledge will allow improving the corrosion performance of low alloy ferrous materials without altering their chemical composition or applying additional corrosion protection methods. The important findings from this research are given in the following sections.

10.3.1 The effect of microstructural features on passivity behaviour

The effect of several microstructural features (dislocation density, grain size/boundary areas, and phases) on the passivation behaviour of low alloyed ferrous materials are investigated in this thesis. The effect of dislocation density and grain boundary density on passivity behaviour is studied in Chapter 2. The Mott-Schottky analysis of passive film's defect density shows that the donor density of passive films increases with an increase in substrate defect density. Moreover, XPS analysis shows that the volume fraction of protective γ-Fe_2O_3 in the passive film (composed of Fe_3O_4, γ-Fe_2O_3 and FeO(OH)) decreases with increasing substrate defect

density. It was also observed that the thickness of the passive film increases with increasing substrate defect density. Nevertheless, the electrochemical characterisation of passive films shows that the barrier properties of passive films deteriorate with increasing dislocation density and grain boundary density. The deterioration of barrier properties of passive films stems from the increasing donor density and lower γ-Fe_2O_3 volume fraction. This research thus shows how microstructural defects affect the barrier properties of the passive layer on ferrous materials and the reason.

After observing that the barrier properties of passive films worsen with increasing substrate defect density, the specific role of another defect was investigated for pure iron samples in Chapter 4. The grain sizes of the samples were manipulated by applying various heat treatments. Samples with 26, 53, and 87 μm grain sizes were obtained. The samples have no significant variations in dislocation density, and no inclusions, secondary phase formation and elemental segregation were observed. The overall electrochemical characterisation shows that the barrier properties of samples worsen with grain refinement. Similar to the microstructural defects and passivity relationship, the deterioration in barrier properties is attributed to the increasing donor density and the decreasing γ-Fe_2O_3

volume fraction in the passive films. To the best of the author's knowledge, there is currently no existing literature that controls and analyses the microstructural features while investigating the grain size and passivity relationship of ferrous materials. This work reveals the specific role of grain size in passivity behaviour. This knowledge can allow optimizing the passivity behaviour while designing alloys.

The effect of grain size on passivity behaviour is investigated in complex fully martensitic steels in Chapter 5. Several heat treatments were applied to vary the prior austenite grain sizes (PAGS) ranging between 5 to 66 µm. The refinement from 66 to 28 µm size leads to the deterioration of the barrier properties of the passive films due to an increase in the donor density and the decrease in the volume fraction of γ-Fe_2O_3 in the passive film. However, further refinement in prior austenite grain size leads to improvement in the barrier properties of the passive film. This is attributed to the increase in the volume of γ-Fe_2O_3 in the passive film while the donor density of passive film increases continuously with grain refinement from 66 to 5 µm. This indicates that the variations in the chemical composition of the passive film dominate the donor density effect on the barrier properties of the passive films. The improvement in barrier properties of the passive

layer with further PAGS refinement to 5 µm is attributed to the significant changes of lath structure (lath width to length ratio) within the complex martensite structure that occur while refining the prior austenite grain size from 28 to 5 µm dominate the PAGS refinement on passivity behaviour in this grain size range. This improvement in barrier properties with grain size refinement from 28 to 5 µm can allow improving the passive layer properties and mechanical properties of alloys simultaneously since the grain refinement leads to improvement in yield strength.

Considering that the increase in microstructural defect density (Chapter 2) and decrease in grain size (increase in grain boundary areas) (Chapters 4 and 5) lead to worsening in the barrier properties of the passive film, the defects in substrates' lattice structure deteriorate the barrier properties of the passive film. This is mainly due to the passive film formation on the sites of lattice defects that probably leads to a more defective passive layer. Moreover, the volume fraction of (hydr)oxides varies with the defects in the lattice structure of substrates.

The effect of phase combinations (ferrite-pearlite and ferrite-martensite) on the passivity behaviour of two-phase and low carbon steel is investigated in Chapter 7. Different heat treatments were employed to obtain ferrite-

pearlite and ferrite-martensite microstructure with similar ferrite volume fractions to avoid the effect of different phase ratios on passivity behaviour. The barrier properties of passive film formed on the ferrite-pearlite microstructure are significantly better than the ferrite-martensite microstructure. This stems from the higher donor density of the passive film formed on the ferrite-martensite microstructure. The martensite phase is highly distorted, with higher dislocation and boundary density. Therefore, the formation of the more defective passive film on martensite structure agrees with the above-mentioned discussion arguing that the lattice defects lead to the formation of the more defective passive film. This work deepens the understanding of the phases on passivity behaviour. It can contribute to the design of alloys including ferrite, pearlite, and martensite phases in terms of their corrosion performance.

All in all, the role of several microstructural features (dislocation density, grain size, and phases) on the passivity behaviour of ferrous materials is studied in this thesis. The gained fundamental knowledge deepens the understanding of the relationship between these microstructural features and the passivation behaviour of ferrous materials.

Moreover, it opens new scientific challenges, as discussed in section 10.4 in detail.

10.3.2 The effect of microstructural features on corrosion behaviour

The relationships between microstructural features (dislocation density, grain size/boundary areas, phases, and crystallographic orientation) and corrosion behaviour of low alloy ferrous materials are studied in this thesis. In chapter 3, the effect of dislocations induced by cold rolling is investigated by combining electrochemical characterisation and localised Volta-potential variations measured by SKPFM. It was observed that the corrosion rate increases by inducing dislocations by cold rolling. The Volta-potential variations are employed to understand the degree of galvanic coupling between grains. In recrystallized hot-rolled IF steel, the Volta-potential variations between grains are approximately 40 mV, depending on the crystallographic orientations. The Volta-potential variations between grains with different crystallographic orientations increase to about 130 mV, showing that the introduction of dislocations increases the degree of galvanic coupling. Therefore, the increase in corrosion rate is related to the higher degree of micro-galvanic coupling after cold rolling. This shows that

the dislocation density plays a dominant role in the corrosion behaviour in comparison to the crystallographic orientations in this study.

The effect of grain size on the corrosion behaviour of pure iron is investigated in Chapter 6. The grain refinement leads to an increase in grain boundary density, implying an increase in defect density. Considering that the dislocations (another defect in the lattice) lead to an increase in corrosion rate, the initial hypothesis was that grain refinement leads to an increase in corrosion rate due to higher defect density. To investigate the grain size effect on corrosion behaviour, it is crucial to minimize the changes in other microstructural features such as dislocation density, phases, inclusions, and elemental segregation that can contribute to the corrosion response. Therefore, several heat treatments were applied to obtain samples with grain sizes 26, 53, and 87 μm while limiting the changes in other above-mentioned microstructural features. The grain refinement from 87 to 53 μm leads to a decrease in corrosion resistance. Within this grain size range, there is no significant difference in terms of other microstructural features, including crystallographic texture. Therefore, it is concluded that the individual effect of grain refinement in the range of 53 and 87 μm leads to an increase in the corrosion rate. The grain refinement

temperature on corrosion behavior of E690 steel in 3.5 wt.% NaCl solution," *Mater. Res. Express*, vol. 8, no. 1, p. 16528, 2021.

[7] T. A. N. Remmerswaal, "The influence of microstructure on the corrosion behaviour of ferritic-martensitic steel,", Master Thesis, TU Delft, p. 106, 2015.

[8] Y. Shadangi, K. Chattopadhyay, S. B. Rai, and V. Singh, "Effect of laser shock peening on microstructure, mechanical properties and corrosion behavior of interstitial free steel," *Surf. Coatings Technol.*, vol. 280, pp. 216–224, 2015.

[9] W. R. Osório, L. C. Peixoto, L. R. Garcia, and A. Garcia, "Electrochemical corrosion response of a low carbon heat treated steel in a NaCl solution," *Mater. Corros.*, vol. 60, no. 10, pp. 804–812, 2009.

[10] P. K. Katiyar, S. Misra, and K. Mondal, "Corrosion Behavior of Annealed Steels with Different Carbon Contents (0.002, 0.17, 0.43 and 0.7% c) in Freely Aerated 3.5% NaCl Solution," *J. Mater. Eng. Perform.*, vol. 28, no. 7, pp. 4041–4052, 2019.

[11] Y. Raghupathy, A. Kamboj, M. Y. Rekha, N. P. Narasimha Rao, and C. Srivastava, "Copper-graphene oxide composite coatings for corrosion

The role of ferrite-pearlite and ferrite-martensite phase combinations on corrosion behaviour of low alloyed carbon steel is investigated in Chapter 8. Two-phase microstructures (ferrite-pearlite and ferrite-martensite) with similar ferrite fractions were obtained through heat treatments and employed for electrochemical characterisation. The electrochemical characterisation of samples shows that the corrosion resistance of ferrite-pearlite microstructure is higher than the ferrite-martensite microstructure. This is attributed to the highly distorted structure with high dislocation density and boundary density within the complex martensite structure, in agreement with the previous results on the effect of dislocation density and grain boundary areas on corrosion behaviour.

In Chapter 6, it is concluded that the grain's crystallographic texture affects the corrosion behaviour. To deepen the understanding of crystallographic orientation and localised corrosion behaviour in chapter 9, the Volta-potential and the dissolution rate variations between grain were characterised by SKPFM and in-situ liquid AFM measurements, respectively. The grains in (001) orientation (i.e. parallel to the surface) exhibit more cathodic behaviour than the ones in (101) and (111) orientation, indicating

a micro-galvanic coupling between grains. The effect of these micro-galvanic couplings can lead to the variation of dissolution rates. The grains in (101) orientation selectively dissolve faster than the ones in (001) orientation, whereas the grain in (111) orientation exhibits more localised and severe attacks than the ones in (101) and (001) orientations. These results obtained with high-resolution characterisation techniques bring a better understanding of the relationship between crystallographic orientation and corrosion behaviour.

10.4 General remarks and recommendations

An Austrian mathematician, Kurt Gödel, said in 1931, "No complex system could be known in its entirety, and any system that could be known in its entirety is merely a subset of a larger one". Considering this definition, the relationship between microstructural features and corrosion behaviour can be regarded as a complex system. Although the results obtained in this thesis provide fundamental knowledge on the relationship between several microstructural features and corrosion/passivity, there are still many questions to be investigated.

The knowledge obtained on the relation between microstructural features and passivity shows that the barrier properties of passive films

deteriorate with increasing microstructural defect density. This is due to changes in electronic properties (increase in overall donor density) and chemical composition (decrease in the volume fraction of protective γ-Fe_2O_3) of passive films. However, the local changes in the structural and electronic properties of passive films on the sites where the passive film forms on the substrate microstructural defects (e.g. dislocations and grain boundaries) are yet to be explored. Therefore, further research is needed to fully understand the underlying phenomena of the changes in passive films' electronic properties and chemical composition with alterations in substrate defect density. In-situ monitoring the structural and electronic properties of passive films with electrochemical scanning tunnelling microscopy (EC-STM) can help in revealing the passive films' donor density and structural changes on these sites during the formation and growth of the passive film. Moreover, the local reactivity of passive films around the areas formed on microstructural defects has also not been explored. This information can provide the local protective capacity of passive film formed on the microstructural defects and be obtained in high-resolution by AFM-SECM (atomic force microscopy - scanning electrochemical microscopy) measurements.

This thesis also shows that the barrier properties of passive film formed on ferrite-martensite are lower than of the film formed on ferrite-pearlite. However, the local differences in the protective capacity of passive films were not studied. SECM measurements would provide more insight into the protective capacity of passive films depending on the underlying substrate's phases.

On the side of grain size and corrosion behaviour, this research provides valuable information about the relationship between grain size and corrosion behaviour. However, a holistic quantitative relationship between corrosion rate and grain size has not been established for ferrous alloys. Further studies employing samples with a wide range of grain sizes (while avoiding the changes in other microstructural features) in various environments might enable establishing a statistical relationship between corrosion rate and grain size.

To gain more insight into the differences in the corrosion resistance of various phase combinations of two-phase steels, it is suggested to compare the (local) corrosion resistance of various phase combinations (e.g. ferrite-bainite, ferrite-austenite, austenite-martensite, etc.). This can be achieved with an investigation that combines (local) electrochemical

techniques (e.g. SECM, in-situ AFM) with surface characterisation tools. This can develop understanding of the corrosion resistance of a wide range of phases and the underlying phenomena leading to variations in the corrosion resistance of phases. Eventually, this information can provide guidelines in the design of the microstructure of alloys containing two or more phases to improve the corrosion resistance.

The aforementioned empirical studies would further deepen the understanding of a microstructural feature's individual role in corrosion behaviour. However, the environment is another phenomenon that affects the role of a microstructural feature on corrosion behaviour. Considering the very different variations between environments (e.g., solution concentration, the species in a solution, pH, temperature, etc.), it is practically not possible to conduct all experiments needed to understand the effects of a microstructural feature on the corrosion behaviour in such a range of environments. However, machine learning algorithms might help building models based on the experimental data on the relationship between a microstructural feature and corrosion in certain environments. In this way, the effect of microstructural features on corrosion behaviour can be modelled for every environment. Moreover, machine learning can

also be employed to understand the complex interaction between microstructural features on corrosion behaviour in different environments. This can be carried out using algorithms based on the empirical data on the individual role of a microstructural feature on corrosion behaviour.

10.5 References

[1] A. D.R., *Strain Hardening and Annealing. In: The Science and Engineering of Materials*. Boston, MA: Springer US, 1996.

[2] S. Zaefferer, J. Ohlert, and W. Bleck, "A study of microstructure, transformation mechanisms and correlation between microstructure and mechanical properties of a low alloyed TRIP steel," *Acta Mater.*, vol. 52, no. 9, pp. 2765–2778, 2004.

[3] K. L. Murty, M. D. Mathew, Y. Wang, V. N. Shah, and F. M. Haggag, "Nondestructive determination of tensile properties and fracture toughness of cold worked A36 steel," *Int. J. Press. Vessel. Pip.*, vol. 75, no. 11, pp. 831–840, 1998.

[4] J. P. Chu, J. M. Rigsbee, G. Banaś, and H. E. Elsayed-Ali, "Laser-shock processing effects on surface microstructure and mechanical properties of low carbon steel," *Mater. Sci. Eng. A*, vol. 260, no. 1–2, pp. 260–268, 1999.

[5] C. C. Tasan, M. Dieh, D. Yan, M. Bechtold, F. Roters, L. Schemmann, C. Zheng, N. Peranio, D. Ponge, M. Koyama, K. Tsuzaki, and D. Raabe, "An Overview of Dual-Phase Steels: Advances in Microstructure-Oriented Processing and Micromechanically Guided Design," *Annu.*

Rev. Mater. Res., vol. 45, no. 1, pp. 391–431, 2015.

[6] K. D. Ralston and N. Birbilis, “Effect of grain size on corrosion: A review,” *Corrosion*, vol. 66, no. 7, pp. 0750051–07500513, 2010.

Acknowledgements

The research presented in this dissertation was carried out under project number F41.3.14546a in the framework of the Partnership Program of the Materials innovation institute (M2i) and the Foundation for Fundamental Research on Matter (FOM), which is part of the Netherlands Organisation for Scientific Research (N.W.O.). I would like to thank these partners for their financial support and for their support in the track to becoming an independent researcher. A Ph.D. dissertation is a work of several years, and it is never the sole work of an individual. Therefore, I would like to express my gratitude to those who helped me directly or indirectly along the journey.

First of all, I would like to thank my co-promotor Assoc. Prof. dr. Yaiza Gonzalez-Garcia. You have always been available for scientific discussion and for providing valuable feedback. This roller coaster Ph.D. journey has been full of ups and downs. You have always supported me and provided me the guidance I needed to move forward throughout the entire journey in both scientifically and personally, especially during difficult times. I will always be grateful for it. Moreover, I truly appreciate the freedom that you gave me to choose my direction, helping me to find interesting research

topics and to develop myself as an independent researcher. Very importantly, I also would like to express my sincere gratitude to my promotor Prof. dr. ir. Jilt Sietsma for giving me this opportunity of developing myself as a scientist and for your guidance and support. It has been a great pleasure for me to work under your supervision and to learn from you. You have always pointed out the right direction to advance my research and myself as a scientist. Your outstanding commitment, enthusiasm, and passion for research have been a great motivation for me to develop as a scientist. Moreover, your modesty, kindness, approachability, and supportiveness have been a great inspiration for me as a human.

Furthermore, I would like to thank Dr. Erdni Batyrev, Dr. Berend Boelen, and Dr. Arnoud de Vooys from Tata Steel for always showing interest in the presented work and for supporting me whenever I faced a problem that could be solved within the company. The project benefited significantly from our close collaboration.

Over the years, other research groups warmly welcomed me during the journey. I am very grateful to Assoc. Prof. dr. Tom Hauffman from Vrije Universiteit Brussel (V.U.B.) for giving me the opportunity to conduct XPS

analysis at V.U.B. and the excellent help for the discussions on XPS data. I would also like to thank Dr. Sven Pletincx for conducting XPS measurements together, for many in-depth and fruitful discussions, your dedication to this work, and long scientific and non-scientific chats during the XPS measurements. The collaboration with V.U.B. tremendously significantly contributed to the quality of this work. I also would like to express my gratitude to Dr. Cem Örnek from the Royal Institute of Technology (KTH) for helping me tremendously with SKPFM, for your warm welcome during my stay in Stockholm, and long scientific and non-scientific discussions. Undoubtedly, everything related to SKPFM contributed significantly to the quality of this work. Moreover, your personal suggestions have had helped a lot me to become a better scientist.

I am very thankful to all my colleagues at the Materials Science and Engineering (M.S.E.) department, especially the ones in Corrosion Technology and Electrochemistry (C.T.E.) group. I would like to thank Prof. dr. Arjan Mol. Your approachability and leadership create a great atmosphere in the group. I also would like to acknowledge Assist. Prof. dr. Peyman Taheri, whose door was always open when I had any questions. Over the years, I had many colleagues within the group. They contributed

to this thesis directly or indirectly in many different ways. Therefore, I would like to thank my colleagues within the CTE group, Joost, Mirsajjad, Eszter, Shoshan, Peter, Laura-Lynn, Mats, Bala, Ali, Claire, Emina, Maria, Marta, Prakash, Ursa, Wojciech, Maxine, and Ziyu. A very special thank goes to Agnieszka, for always being very generous with your help which goes much further than technical support.

I also had the opportunity to work closely with numerous people from the microstructure group within the Materials Science and Engineering (M.S.E.) department. A very special thank goes to Konstantina Traka from the microstructure group. Your openness for collaboration, efforts, and dedication significantly made this project more interesting and comprehensive. I tremendously appreciate your contribution. I also want to thank Dr. Xiaolin Li for her contribution to the initial phase of the project. I would like to sincerely thank Prof. dr. Maria Santofimia Navarro for her availability whenever we needed her help. I also would like to thank Sudhindra, Carola, and Javier for your help with my many microstructure-related questions.

Throughout this project, I had the chance to work with many students, and each of them contributed to this project directly or indirectly. I thank all of

the students that I worked with for their contributions. To this end, I would like to specifically thank Can for his contributions in chapters 7 and 8 and to Satyakam for his contributions in chapter 6. Your contributions made this project broader. I am also grateful to the technical help from my colleagues Sander for the sample preparation, optical analysis, and nice talks, Kees for the S.E.M. analysis, and Nico for the dilatometry analysis.

I also would like to all my Delft friends, Alper, Cansel, Cenk, Cevdet, Fatma, Gozde, Hakan, and Muscan, who accompanied and supported me during the last years. Thanks for spending the constant support and fun times in Delft.

To obtain a Ph.D. degree, physical health is the first requirement. To this end, I would like to express my sincere gratitude to dr. P.P.J. van der Veek. I sincerely thank you for your close attention and for being very dedicated and thoughtful. Without your help, this Ph.D. could not be completed.

Roos, no words can describe how I am grateful for your support during this project. You have always supported me in my good and bad times. Your support always encouraged me to keep going on this project. Without you, I could never finish this Ph.D. thesis. I also genuinely appreciate that you have always tried to understand what I am doing for my Ph.D. I think you

could give the Layman's talk if it were possible. I also would like to express my gratitude to Ans and Andre for being enthusiastic about my project, the nice conversations, and their support.

Last but definitely not least, I would like to dedicate this book to my parents and my brother. I am very lucky to have you in my life. Without your constant support, I could not be here.

List of publications

Journal articles

A. Yilmaz, C. Ozkan, J. Sietsma, Y. Gonzalez-Garcia, ''The Influence of Phase Constituents on the Corrosion Response of Ferrite-Martensite and Ferrite-Pearlite Microstructures in acidic environments'', (tentative title), in preparation.

A. Yilmaz, S. Kar, J. Sietsma, Y. Gonzalez-Garcia, ''Role of grain size and crystallographic orientation on the corrosion behaviour of pure iron'', (tentative title), in preparation.

A. Yilmaz, C. Örnek, K. Traka, J. Sietsma, Y. Gonzalez-Garcia, ''Correlating Volta-potential with XPS measured chemical composition of oxide film to investigate the effect of crystallographic orientation on passivity behaviour of interstitial free (IF) ferritic steels'', (tentative title), in preparation.

Y. Gonzalez-Garcia, A. Yilmaz, L. Desvignes, V. Popovich ''The effect of microstructure on corrosion behavior of functionally graded Inconel 718 produced by additive manufacturing'', (tentative title), in preparation.

A. Yilmaz, C. Örnek, K. Traka, J. Sietsma, Y. Gonzalez-Garcia, ''Combining surface Volta-potential with electrochemical measurements to investigate the role of cold working on corrosion behavior of interstitial free (IF) steels'', submitted.

A. Yilmaz, K. Traka, S. Pletincx, T. Hauffman, J. Sietsma, Y. Gonzalez-Garcia, ''Role of grain size on passive layer properties of pure iron'', submitted.

A. Yilmaz, X. Li, S. Pletincx, T. Hauffman, J. Sietsma, Y. Gonzalez-Garcia, ''Effect of prior austenite grain size on passive layer properties of martensitic steels'', submitted.

A. Yilmaz, K. Traka, S. Pletincx, T. Hauffman, J. Sietsma, and Y. Gonzalez-Garcia, "Effect of microstructural defects on passive layer properties of interstitial free (IF) ferritic steels in alkaline environment", *Corros. Sci.*, vol. 182, 2021.

A. Yilmaz, C. Ozkan, J. Sietsma, Y. Gonzalez-Garcia, "Properties of Passive Films formed on Dual-Phase Ferrite-Martensite and Ferrite-Pearlite Microstructures", *Metals,* vol. *11*(4), p. 594, 2021.

L.I. Fockaert, M.V.E Ankora, J.P.B. Dam, S. Pletincx, A. Yilmaz, B. Boelen, T. Hauffman, Y. Garcia-Gonzalez, H. Terryn, J.M.C. Mol, ''Effect of organic additives in fluoacid-based Ti and Zr-treatments for galvanized steel on the stability of a polymer coated interface'', Progress in Organic Coatings. 146 (2020) 105738.

J.P.B. van Dam, S. Abrahami, A. Yilmaz, Y. Gonzalez-Garcia, H. Terryn, J.M.C. Mol, ''Effect of surface roughness and chemistry on the adhesion and durability of a steel-epoxy adhesive interface'', International Journal of Adhesion and Adhesives. 96 (2020) 102450.

D. Snihirova, S. Lamaka, Y. Gonzalez-Garcia, A. Yilmaz, N. Scharnagl, M. Montemor, M.I. Zheludkevich, ''Influence of inhibitor adsorption on

readings of microelectrode during SVET measurements'', Electrochimica Acta. 322 (2019) 134761

Y. Li, H. Jahr, K. Lietaert, P. Pavanram, A. Yilmaz, L. Fockaert, M. Leeflang, B. Pouran, Y. Gonzalez-Garcia, H.Weinans, J.M.C. Mol, J. Zhou, A.A. Zadpoor, ''Additively manufactured biodegradable porous iron'', Acta Biomaterialia. 77 (2018) 380–393

Conference presentations

A. Yilmaz, K. Traka, S. Pletincx, T. Hauffman, J. Sietsma, Y. Gonzalez-Garcia, ''The effect of grain size on passive layer properties of iron'', The European Corrosion Congress (EUROCORR) 2020, 7-11 September 2020, Brussels, Belgium (Virtual).

A. Yilmaz, K. Traka, S. Pletincx, T. Hauffman, J. Sietsma, Y. Gonzalez-Garcia, ''Application of localized electrochemical techniques to study the effect of crystallographic orientation on passive layer and corrosion behavior of IF ferritic steels'', The European Corrosion Congress (EUROCORR) 2020, 7-11 September 2020, Brussels, Belgium (Virtual).

A. Yilmaz, K. Traka, S.Pletincx, T. Hauffman, J. Sietsma, Y. Gonzalez-Garcia, ''The effect of microstructure on corrosion behaviour of steels'', 71st Annual Meeting of the International Society of Electrochemistry, 1-4 September 2020, Belgrade, Serbia (Virtual).

Y. Gonzalez-Garcia, L. Desvignes, A. Yilmaz, A. de Groot, E. Borisov, V. Popovich, ''Corrosion behaviour of functionally graded Inconel 718 produced by additive manufacturing'' 141th TMS Annual Meeting & Exhibition, 23-27 February 2020, San Diego, California, USA.

A. Yilmaz, K.Traka, S. Pletincx, T. Hauffman, J. Sietsma, Y. Gonzalez-Garcia, ''The effect of dislocation density on corrosion behaviour of IF ferritic steels'', Meeting Materials 2019, 9-10 December 2019, Noordwijkerhout, The Netherlands.

A. Yilmaz, K.Traka, S. Pletincx, T. Hauffman, J. Sietsma, Y. Gonzalez-Garcia, ''The role of microstructural defects on corrosion and passivity behaviour of steels'', The European Corrosion Congress (EUROCORR) 2019, 9-13 September 2019, Seville, Spain.

D. Snihirova, S. Lamaka, A. Yilmaz, Y. Gonzalez-Garcia, N. Scharnagl, M. Montemor, M.I. Zheludkevich, Influence of inhibitor adsorption on readings of microelectrode during SVET measurements, The European Corrosion Congress (EUROCORR) 2019, 9-13 September 2019, Seville, Spain.

A. Yilmaz, X. Li, S. Pletincx, T. Hauffman, J. Sietsma, Y. Gonzalez-Garcia, The effect of microstructure on localized corrosion behaviour of steels, Meeting Materials 2018, 11-12 December 2019, Noordwijkerhout, The Netherlands. (Best poster presentation)

A. Yilmaz, X. Li, S. Pletincx, T. Hauffman, J. Sietsma, Y. Gonzalez-Garcia, 'The role of prior austenite grain size on passive film properties of martensitic steels', The European Corrosion Congress (EUROCORR) 2018, 9 - 13 September 2018, Krakow, Poland.

A. Yilmaz, X. Li, S. Pletincx, T. Hauffman, J. Sietsma, Y. Gonzalez-Garcia, The effect of microstructure on localized corrosion behaviour of steels The European Corrosion Congress (EUROCORR) 2017, 3-7 September 2017, Prague, Czech Republic.

A. Yilmaz, X. Li, S. Pletincx, T. Hauffman, J. Sietsma, Y. Gonzalez-Garcia, The effect of microstructure on localised corrosion behaviour of steels, Meeting Materials 2017, Noordwijkerhout, 12-13 December 2017, Utrecht, The Netherlands.

About the Author

Aytac Yilmaz

Born on June 26th, 1989, in Mersin, Turkey

Professional Experience

2021 – Present	**Post-doctoral researcher**
	Materials Science and Engineering
	Delft University of Technology, Delft, The Netherlands
2016 – 2020	**Ph.D. researcher**
	Materials Science and Engineering
	Delft University of Technology, Delft, The Netherlands
2015 – 2016	**Research and Development Engineering Trainee**
	Gulfstream Aerospace Company, Georgia, U.S.A.

Education

2016 – 2020	**Ph.D., in Materials Science and Engineering**
	Delft University of Technology, Delft, The Netherlands
2014 – 2016	**MSc. in Materials Science and Engineering**
	University of Florida, Florida, U.S.A.
2015 – 2016	**BSc. In Mechanical Engineering**
	Bogazici University, Istanbul, Turkey